



STUDY OF THE FLUID-FLUID AND ROCK-FLUID INTERACTIONS: IMPACT
OF DISSOLVED CO₂ ON INTERFACIAL TENSION AND WETTABILITY FOR
THE BRAZILIAN PRE-SALT SCENARIO

Santiago Gabriel Drexler

Tese de Doutorado apresentada ao Programa de Pós-graduação em Engenharia Civil, COPPE, da Universidade Federal do Rio de Janeiro, como parte dos requisitos necessários à obtenção do título de Doutor em Engenharia Civil.

Orientador: Paulo Couto

Rio de Janeiro
Dezembro de 2018

STUDY OF THE FLUID-FLUID AND ROCK-FLUID INTERACTIONS: IMPACT
OF DISSOLVED CO₂ ON INTERFACIAL TENSION AND WETTABILITY FOR
THE BRAZILIAN PRE-SALT SCENARIO

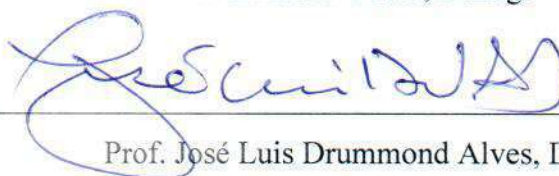
Santiago Gabriel Drexler

TESE SUBMETIDA AO CORPO DOCENTE DO INSTITUTO ALBERTO LUIZ
COIMBRA DE PÓS-GRADUAÇÃO E PESQUISA DE ENGENHARIA (COPPE) DA
UNIVERSIDADE FEDERAL DO RIO DE JANEIRO COMO PARTE DOS
REQUISITOS NECESSÁRIOS PARA A OBTENÇÃO DO GRAU DE DOUTOR EM
CIÊNCIAS EM ENGENHARIA CIVIL.

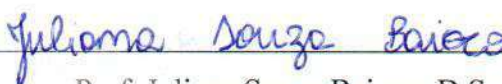
Examinada por:



Prof. Paulo Couto, D.Eng.




Prof. José Luis Drummond Alves, D.Sc.



Prof. Juliana Souza Baioco, D.Sc.



Prof. Aurora Perez Gramatges, Ph.D.



Prof. Ingebret Fjelde, Ph.D.

RIO DE JANEIRO, RJ-BRASIL

DEZEMBRO DE 2018

Drexler, Santiago Gabriel

Study of the fluid-fluid and rock-fluid interactions: Impact of dissolved CO₂ on the interfacial tension and wettability for the Brazilian Pre-Salt scenario/ Santiago Gabriel Drexler. – Rio de Janeiro: UFRJ/COPPE, 2018.

XXVI, 234 p.: il.; 29,7 cm.

Orientador(es): Paulo Couto

Tese (doutorado) – UFRJ/ COPPE/ Programa de Engenharia Civil, 2018.

Referências Bibliográficas: p. 189-211.

1. Interação rocha-fluido. 2. Tensão interfacial. 3. Injeção de CO₂. 4. Alteração da Molhabilidade. 5. Reservatórios carbonáticos. I. Couto, Paulo. II. Universidade Federal do Rio de Janeiro, COPPE, Programa de Engenharia Civil. III. Título.

I dedicate this work to my parents Cristina and Gustavo,
who are my role models as human beings and professionals
and to my mentors Profs. Susana Larrondo and Daniel Resasco,
who always inspired and supported me to become a researcher and a Professor.

ACKNOWLEDGEMENT

First, I would like to thank my advisor Prof. Paulo Couto for the opportunity to be the first researcher at the UFRJ EOR lab (LRAP). I feel blessed for being part of this from the very first steps. Also, the members of the committee Prof. José Luis Drummond, Prof. Juliana Souza Baioco, Prof. Aurora Perez Gramatges and Prof. Ingebret Fjelde for accepting the invitation to evaluate and contribute with their suggestions. I also want to thank my fellow researchers Thaís Márcia Silveira and Dr. Juliana Façanha for their contributions, but most importantly for their friendship and support during this journey making it easier to see the light at the end of the tunnel.

I'm grateful to my students, Nathália Dias, Elton Correia, Ana Jerdy, Felipe Pardini, Mariana Frias, Gabriel Sant'Anna and Lucas Cruz, who were a very important part of this work trusting my guidance and contributing with hard work. I would also like to acknowledge the engineers, technicians and students at LRAP who were part of this research somehow, particularly William Godoy, Fernanda Hoerle, Leandro Cavadas, Paula Reis, Tatiana Lipovetski, Fernanda Pedó, Thiago Saraiva, Bárbara Esteves, Anete Coelho, Daniela Costa, Dr. David Caetano, Dr. Denise Nunes and Dr. Edmilson Rios. I thank Dr. Frances Abbots, Dr. Claudia Amorim and Moisés Silva from Shell Brasil for the support throughout the years. Also, I am very grateful to Shaun Ireland, Adam Sisson, Pantelis Tsolis and Colin Flockhart from EOR CO₂ centre at Heriot Watt University coordinated by Prof. Mehran Sohrabi for the training, patience and friendship from the early days.

In addition, I acknowledge the following researchers and technicians from other laboratories and institutions who contributed carrying out several analysis employed in this work: the DR-X laboratory at CENPES/Petrobras managed by Vinicius Machado for the DRX analysis, Dr. Amal Elzubair and Mauro Wysard from the Protective Coatings Lab coordinated by Prof. Sérgio Camargo for the help in confocal microscopy and profilometer analyses, Heleno Souza da Silva from LabAFM coordinated by Prof. Renata Antoun for the AFM analysis, Victor Brandão and Prof. Luiz Carlos Bertolino from MCTIC/CETEM for the SEM/EDS and optical microscopy analysis, Adao Gonçalves from LIAP coordinated by Prof. Juliana Loureiro for the SEM analysis, Prof. Romildo Dias Tolêdo Filho from NUMATS for SEM/EDS analysis, Marcelo Queiroz from

Dopolab coordinated by Prof. Erika Nunes for the viscosity measurements and SARA analysis, Ms. Leonice Bezerra Coelho from the Instruments and Research Laboratory (IQ) for the infrared analysis, Dr. Simone Ribeiro from Flumat (IQ) coordinated by Prof. Regina Sandra Veiga Nascimento for the CHN analysis, Dr. Philip Jaeger from Eurotechnica for the support on the DSA equipment and the team of LAGESED coordinated by Prof. Borghi for the discussions.

This research was carried out in association with the R&D project registered as ANP19027-2, “Desenvolvimento de Infraestrutura para pesquisa e desenvolvimento em recuperação avançada de óleo - EOR no Brasil” (UFRJ/Shell Brasil/ANP) – setting-up an advanced EOR Lab facility for R&D in Brasil, sponsored by Shell Brasil under the ANP R&D levy as “Compromisso de Investimentos com Pesquisa e Desenvolvimento”. This study was financed in part by the *Coordenação de Aperfeiçoamento de Pessoal de Nível Superior- Brasil* (CAPES) - Finance Code 001.

Resumo da Tese apresentada à COPPE/UFRJ como parte dos requisitos necessários para a obtenção do grau de Doutor em Ciências (D.Sc.).

ESTUDO DAS INTERAÇÕES FLUIDO-FLUIDO E ROCHA FLUIDO: IMPACTO DO CO₂ DISSOLVIDO NA TENSÃO INTERFACIAL E MOLHABILIDADE NO CENÁRIO DO PRÉ-SAL BRASILEIRO

Santiago Gabriel Drexler

Dezembro/2018

Orientadores: Paulo Couto

Programa: Engenharia Civil

Os reservatórios carbonáticos do Pré-sal estão entre as principais descobertas das últimas décadas, sendo capazes de mudar a economia brasileira. Entretanto, eles apresentam desafios únicos para sua produção. Os dados publicados empregando rochas e fluidos análogos aos do Pré-sal são limitados e as interações rocha-fluido e fluido-fluido que governam o deslocamento ainda precisam ser compreendidas. Neste contexto, este trabalho apresenta dados experimentais confiáveis e promove discussões com o objetivo de melhorar os modelos dos reservatórios do Pré-sal. O escopo desta pesquisa é avaliar a molhabilidade inicial (MI) e a tensão interfacial (IFT) como pilares destas interações, com ênfase no impacto do CO₂. A customização de metodologias experimentais, adequadas às condições de reservatório, permitiu concluir que: as rochas do Pré-sal apresentam molhabilidade ao óleo e assim, o envelhecimento das amostras é necessário para atingir a molhabilidade inicial; as composições ácido/base e SARA do óleo são essenciais para o envelhecimento das amostras; a dissolução de CO₂ modifica a molhabilidade inicial para mais molhável à água e, portanto, reservatórios do Pré-sal que possuem alta concentração de CO₂ podem apresentar molhabilidade inicial intermediária; por fim, a presença de compostos surfactantes resulta em baixa IFT entre os óleos e a salmoura, logo a presença de CO₂ não contribui significativamente com o aumento do Número Capilar.

Abstract of Thesis presented to COPPE/UFRJ as a partial fulfillment of the requirements for the degree of Doctor of Science (D.Sc.)

STUDY OF THE FLUID-FLUID AND ROCK-FLUID INTERACTIONS: IMPACT OF DISSOLVED CO₂ ON INTERFACIAL TENSION AND WETTABILITY FOR THE BRAZILIAN PRE-SALT SCENARIO

Santiago Gabriel Drexler

December/2018

Advisor: Paulo Couto

Department: Civil Engineering

Pre-Salt carbonate fields are among the most important discoveries of the last decades representing economy game-changing assets in Brazil. Nevertheless, these reservoirs present unique challenges for their development. Literature data for fluids and rocks analogous to Pre-Salt conditions is limited, and the rock-fluid and fluid-fluid interactions remain to be understood. In this context, this work aims to contribute with reliable experimental results and discussions to improve the Pre-Salt reservoir models. The scope of this research is to evaluate initial wettability and interfacial tension as pillars of these interactions with focus on the impact of CO₂. Customizing experimental methodologies for material characterization, initial wettability and interfacial tension evaluation at reservoir conditions, it was possible to reach the following conclusions: Aged Pre-Salt rocks were oil-wet., and rock aging is required to achieve the initial wettability. Crude's acid/base and SARA compositions play an important role during the aging process; CO₂ dissolution rendered initial wettability towards water-wet. Thus, Pre-Salt reservoirs with elevated CO₂ concentration are likely to be intermediate to water-wet at initial conditions; finally, the presence surface-active compounds in the oils resulted in a low interfacial tension with brine, so the presence of CO₂ did not contribute to increase the Capillary Number.

CONTENTS

| | |
|---|------|
| LIST OF FIGURES | xii |
| LIST OF TABLES | xx |
| LIST OF SYMBOLS | xxii |
| LIST OF TABLES | xxiv |
| CHAPTER 1: INTRODUCTION | 1 |
| 1.1 Motivation | 1 |
| 1.2 The Pre-Salt reservoir environment | 3 |
| 1.3 Objective of this research..... | 10 |
| 1.4 Structure of the text..... | 12 |
| CHAPTER 2: THEORETICAL FRAMEWORK..... | 14 |
| 2.1 Reservoir production and Enhanced Oil Recovery | 14 |
| 2.2 Interfacial tension..... | 25 |
| 2.3 Wettability..... | 34 |
| CHAPTER 3: LITERATURE REVIEW | 59 |
| 3.1 Status of CO ₂ flooding | 59 |
| 3.2 Analysis of the interfacial tension of the oil-brine-CO ₂ system | 63 |
| 3.3 Analysis of the solid-fluid interactions | 64 |
| 3.4 Effect of CO ₂ on the physical properties of the fluids | 68 |
| 3.5 Considerations for CO ₂ injection in the Pre-Salt reservoirs..... | 72 |
| CHAPTER 4: METHODOLOGY | 75 |
| 4.1 Experimental Methods | 75 |
| 4.2 Computational Methods | 89 |
| 4.3 Data analysis methods..... | 90 |
| CHAPTER 5: MATERIALS CHARACTERIZATION | 92 |
| 5.1 Brines | 92 |

| | |
|---|-----|
| 5.2 Oils | 92 |
| 5.3 Rocks..... | 96 |
| CHAPTER 6: STUDY OF INITIAL WETTABILITY EVALUATION | 109 |
| 6.1 Development of the initial wettability evaluation technique | 109 |
| 6.2 Wettability of pure minerals..... | 120 |
| 6.3 Wettability of carbonate outcrops and Pre-Salt reservoir rock | 122 |
| 6.4 Discussion: Initial wettability of different minerals and rocks under Pre-Salt reservoir conditions | 124 |
| 6.5 Effect of asphaltenes and resins on changing initial wettability | 131 |
| 6.6 Initial wettability under injection brine..... | 134 |
| 6.7 Highlights of this chapter | 135 |
| CHAPTER 7: CO ₂ EFFECT ON INITIAL WETTABILITY..... | 137 |
| 7.1 CO ₂ injection method | 137 |
| 7.2 Pre-equilibration of the gas cap..... | 145 |
| 7.3 Effect of CO ₂ concentration | 149 |
| 7.4 Effect of pressure | 151 |
| 7.5 Discussion: Effect of CO ₂ on the wettability of the different rocks | 153 |
| 7.6 Effect of CO ₂ on wettability of synthetic Model Oil..... | 167 |
| 7.7 Effect of CO ₂ dissolution on wettability using injection brine | 168 |
| 7.8 Highlights of this chapter | 170 |
| CHAPTER 8: CO ₂ EFFECT ON THE FLUID-FLUID INTERACTIONS..... | 171 |
| 8.1 Validation of the technique | 171 |
| 8.2 Dynamic behavior of IFT | 173 |
| 8.3 Effect of CO ₂ for different oils..... | 178 |
| 8.4 Effect of pressure and CO ₂ concentration..... | 180 |
| 8.5 Highlights of this chapter | 182 |

| | |
|---|-----|
| CHAPTER 9: CONCLUSIONS AND FUTURE WORK..... | 183 |
| CHAPTER 10: BIBLIOGRAPHY..... | 189 |
| APPENDIX A: EQUATIONS INVOLVED IN THE DROP SHAPE ANALYSIS METHOD | 212 |
| APPENDIX B: SIMULATIONS OF FLUID’S PROPERTIES | 215 |
| APPENDIX C: MINERAL COMPOSITIONS AND DESCRIPTIONS..... | 229 |
| APPENDIX D: Asphaltene Characterization..... | 230 |
| APPENDIX E: Alkane-water IFT results | 232 |

LIST OF FIGURES

| | |
|---|----|
| Figure 1.1. Diagram of the Pre-Salt cluster area (FORMIGLI FILHO; CAPELEIRO PINTO; ALMEIDA, 2009)..... | 4 |
| Figure 1.2. Production history for Lula field (BOYD et al., 2015)..... | 10 |
| Figure 2.1. Capillary pressure curve (AHMED, 2010)..... | 17 |
| Figure 2.2. Relative permeability curve (AHMED, 2010)..... | 19 |
| Figure 2.3. Areal sweeping of a displaced fluid. Left: formation of fingers. Right: homogeneous front. (SHENG, 2010). | 20 |
| Figure 2.4. Capillary desaturation curve for a water-wet rock (SCHRAMM, 2000). | 22 |
| Figure 2.5. Scheme of the application of a WAG process (SHENG, 2013)..... | 25 |
| Figure 2.6. Representation of bulk and interfacial molecules for two liquids in contact (ROSEN; KUNJAPPU, 2012). | 27 |
| Figure 2.7. Experiment showing the physical meaning of the surface tension (BUTT; GRAF; KAPPL, 2006)..... | 27 |
| Figure 2.8. Geometrical analysis of the drop profile used the method of the selected plane (ANDREAS; HAUSER; TUCKER, 1937)..... | 31 |
| Figure 2.9. Contact angle for different wetting tendencies (AHMED, 2010)..... | 37 |
| Figure 2.10. Forces acting on the interfaces of drop of water resting on a solid surrounded by oil (DONALDSON; ALAM, 2008)..... | 38 |
| Figure 2.11. Scheme of the experiment by Leach et al. (1962) to study the advancing and receding contact angles (DONALDSON; ALAM, 2008). | 39 |
| Figure 2.12. Model curve of the potential of interaction of two spherical atoms as a function of separation (BARTA, 2008)..... | 41 |
| Figure 2.13. Scheme of the electrical double layer (DONALDSON; ALAM, 2008). | 45 |
| Figure 2.14. Scheme representing repulsive electrostatic interactions of the double layer and the attractive van der Waals interactions (DONALDSON; ALAM, 2008).... | 46 |
| Figure 2.15. Reaction scheme for silica surface in contact with water..... | 48 |

| | |
|--|----|
| Figure 2.16. Drainage and imbibition cycles for a water-wet porous medium (DONALDSON; ALAM, 2008)..... | 51 |
| Figure 2.17. Capillary pressure curves. Left: intermediate-wet system. Right: oil-wet system (DONALDSON; ALAM, 2008)..... | 53 |
| Figure 2.18. Effect of wettability on the relative permeability curves for different types of samples (DONALDSON; ALAM, 2008)..... | 54 |
| Figure 3.1. Viscosity as a function of pressure for different oils saturated with CO ₂ (HOLM, 1982)..... | 68 |
| Figure 3.2. Phase diagram for the Wasson crude/CO ₂ system at 105 °F (GARDNER; ORR; PATEL, 1981). | 70 |
| Figure 3.3. Swelling factor versus CO ₂ fraction (SIMON; GRAUE, 1965)..... | 71 |
| Figure 3.4. Pore pressure versus depth for Campos (red) and Santos (blue) basins (MATIAS et al., 2015). | 73 |
| Figure 4.1. Excess bulk oil cleaning by centrifugation..... | 76 |
| Figure 4.2. Excess bulk oil cleaning by applying solvent (cyclohexane). | 76 |
| Figure 4.3. Flowchart summarizing the steps for contact angle measurement. | 77 |
| Figure 4.4. Scheme of the Drop Shape Analyzer equipment setup (adapted from (PARDINI DE SOUZA, 2018)). | 78 |
| Figure 4.5. Picture of a droplet showing the baseline and the measured contact angle..... | 79 |
| Figure 4.6. Scheme representing “Gas cap” and “Pre-equilibrated fluids” experiments..... | 82 |
| Figure 4.7. Image drop profile on DSA analysis software..... | 83 |
| Figure 4.8. Flowchart with the steps for interfacial tension measurement. | 84 |
| Figure 5.1. Optical microscope images of calcite with magnifications of 1.25, 2.5 and 5. | 97 |
| Figure 5.2. Optical microscope images of dolomite calcite with magnifications of 1.25, 2.5 and 5. | 98 |

| | |
|--|-----|
| Figure 5.3. Optical microscope images of coquina sample with magnifications of 1.25, 2.5 and 5. | 98 |
| Figure 5.4. Optical microscope images of D rock sample with magnifications of 1.25, 2.5 and 5. | 99 |
| Figure 5.5. Thin layer microscopic analysis of calcite (A) and dolomite (B) minerals. | 100 |
| Figure 5.6. Thin layer microscopy of coquina x (A), y (B) and z (C) cores. | 100 |
| Figure 5.7. Thin layer microscopy of D reservoir rocks showing optical calcite (A) and spherulites (B). | 101 |
| Figure 5.8. SEM images of calcite (top) and dolomite (bottom). | 102 |
| Figure 5.9. SEM images of coquinas samples. Last image shows EDS results showing calcium (red), silicon (blue) and sulfur (green) as main elements. | 103 |
| Figure 5.10. SEM/EDS images of D reservoir rocks. | 104 |
| Figure 5.11. EDS analysis of a single D rock sample showing primary and secondary elements. | 105 |
| Figure 6.1. Contact angle measurements for three minerals using solvents and centrifuge for bulk oil removal. Aging time: 1-3. Conditions: 60 °C and 1000 psi. | 110 |
| Figure 6.2. Relative GC areas on the analysis of the rinsing with toluene, cyclohexane and n-hexadecane. | 114 |
| Figure 6.3. Relative GC areas of rinsing with cyclohexane with and without centrifugation. | 115 |
| Figure 6.4. Contact angle measurement for minerals and coquinas using 1 day aging in Brine B and different aging times in Oil B. Conditions: 60 °C and 1000 psi. | 116 |
| Figure 6.5. Images of Oil B drops surrounded by Brine B on coquinas slab using 1 day aging in brine and 3,15 and 30 days aging in oil. No aged slab is also included. . | 117 |
| Figure 6.6. Contact angle measurements versus pressure using the same drop and a new drop for coquina with Field B fluids and 15 days aging in oil. Conditions: 60 °C and 1000 psi. | 118 |

| | |
|--|-----|
| Figure 6.7. Effect of reutilization of the aging oil in the contact angle between Oil B and Brine B on calcite and coquinas aged 1 day in brine and 15/30 days in oil..... | 119 |
| Figure 6.8. Contact angle measurements for pure minerals using Field B and Field D fluids and 15 and 30 days aging in oil. Conditions: 60 °C and 1000 psi..... | 120 |
| Figure 6.9. Images of Oil B drops in Brine B on different substrates. Aging: 1 day in Brine B 30 days in Oil B. | 121 |
| Figure 6.10. Contact angle measurements for calcite and coquina outcrops using Field B and Field D fluids and 15 and 30 days aging in oil. Conditions: 60 °C and 1000 psi..... | 123 |
| Figure 6.11. Contact angle measurements for Indiana limestone, coquina outcrops and Field D rock using Field D fluids 15 and 30 days aging in oil. Conditions: 60 °C and 1000 psi..... | 124 |
| Figure 6.12. SEM images of calcite aged 1 day in Brine B and 30 days in Oil B after centrifugation and rinsing with cyclohexane..... | 125 |
| Figure 6.13. EDS analysis of the selected image showing concentration maps of calcium, carbon and oxygen. | 126 |
| Figure 6.14. Spot EDS analysis of aged calcite showing the %wt. of the detected elements. | 127 |
| Figure 6.15. SEM images of coquina aged 1 day in Brine B and 30 days in Oil B after centrifugation and rinsing with cyclohexane. | 128 |
| Figure 6.16. EDS analysis of the selected image showing concentration maps of calcium, carbon and oxygen. | 129 |
| Figure 6.17. Spot EDS analysis of aged coquina showing the %wt. of the detected elements. | 129 |
| Figure 6.18. Contact angle measurements for calcite and coquina using Oil B / Model Oil and Brine B. Conditions: 60 °C and 1000 psi and 30 days aging in oil..... | 132 |
| Figure 6.19. Contact angle measurements for calcite and coquina using Oil B and Brine B / DSW. Conditions: 60 °C and 1000 psi and 30 days aging in oil..... | 134 |
| Figure 7.1. Effect of different CO ₂ injection methods for calcite using Field B fluids at 60 °C. Top: 15 days aging in oil. Bottom: 30 days aging in oil. | 138 |

| | |
|---|-----|
| Figure 7.2. Effect of different CO ₂ injection methods for calcite using Field D fluids at 60 °C and 30 days aging in oil..... | 139 |
| Figure 7.3. Effect of different CO ₂ injection methods for dolomite using Field B fluids at 60 °C and 30 days aging in oil..... | 140 |
| Figure 7.4. Effect of different CO ₂ injection methods for quartz using Field B fluids at 60 °C and 30 days aging in oil..... | 141 |
| Figure 7.5. Effect of different CO ₂ injection methods for coquinas using Field B fluids at 60 °C. Top: 15 days aging in oil. Bottom: 30 days aging in oil. | 142 |
| Figure 7.6. Effect of different CO ₂ injection methods for coquinas using Field D fluids at 60 °C and 30 days aging in oil..... | 143 |
| Figure 7.7. Effect of different CO ₂ injection methods for Field D Pre-Salt rock using Field D fluids at 60 °C and 30 days aging in oil. | 144 |
| Figure 7.8. Effect of carbonated water injection for Field D Pre-Salt rock using Field D fluids at 60 °C and 15 days aging in oil. | 144 |
| Figure 7.9. Contact angle on 30 days aged calcite measured for CO ₂ injection using separate drops at different pressures or varying the pressure on the same drop. Field B fluids at 60 °C..... | 146 |
| Figure 7.10. Contact angle on 30 days aged coquina measured for CO ₂ injection using separate drops at different pressures or varying the pressure on the same drop. Field B fluids at 60 °C. | 147 |
| Figure 7.11. Contact angle versus pressure for 30 days aged calcite (in reutilized oil) using Field B fluids at 60 °C..... | 149 |
| Figure 7.12. Contact angle versus pressure for 30 days aged coquina (in reutilized oil) using Field B fluids at 60 °C..... | 150 |
| Figure 7.13. Contact angle versus CO ₂ concentration in brine for 30 days aged (in reutilized oil) calcite and coquina using Field B fluids at 60 °C and 1000 psi. | 150 |
| Figure 7.14. Contact angle versus pressure for tests with pre-saturated fluids using the same drop (line) or a new drop (bars). Conditions: 1 day aging (Brine B), 15 days aging (Oil B) and 60 °C. Top: calcite. Bottom: coquina. | 152 |

| | |
|--|-----|
| Figure 7.15. Effect of CO ₂ injection on the wettability of different rocks using Field B fluids. Aging time: 15 or 30 days. Field B fluids at 60 °C and 1000 psi. | 154 |
| Figure 7.16. Effect of CO ₂ injection on the wettability of pure minerals using Field D fluids. Aging time: 15 days. Field D fluids at 60 °C and 1000 psi..... | 154 |
| Figure 7.17. Effect of CO ₂ injection on the wettability of pure minerals using Field D fluids. Aging time: 30 days. Field D fluids at 60 °C and 1000 psi..... | 155 |
| Figure 7.18. Oil B drop in Brine B on 15 days aged coquinas using dead fluids and CO ₂ saturated fluids..... | 157 |
| Figure 7.19. Confocal microscopy showing surface topography of new calcite slab. | 159 |
| Figure 7.20. Confocal microscopy showing surface topography of calcite slab after test with carbonated brine..... | 159 |
| Figure 7.21. Confocal microscopy showing surface topography of new coquina slab..... | 160 |
| Figure 7.22. Confocal microscopy showing surface topography of coquina slab after test with carbonated brine..... | 160 |
| Figure 7.23. Confocal microscopy showing surface topography of new Field D rock slab..... | 161 |
| Figure 7.24. Confocal microscopy showing surface topography of Field B slab after test with carbonated brine..... | 161 |
| Figure 7.25. Optical microscope of a calcite sample. Top: new sample. Bottom: sample after test with carbonated brine. | 162 |
| Figure 7.26. Optical microscope of a coquina sample. Top: new sample. Bottom: sample after test with carbonated brine. | 163 |
| Figure 7.27. Optical microscope of a Pre-Salt Field D rock sample. Top: new sample. Bottom: sample after test with carbonated brine..... | 163 |
| Figure 7.28. SEM images of calcite. Top: new sample. Bottom: sample after test with pre-saturated carbonated brine. | 164 |
| Figure 7.29. SEM images of coquinas. Top: new sample. Bottom: sample after test with pre-saturated carbonated brine. | 165 |

| | |
|---|-----|
| Figure 7.30. SEM images of Pre-Salt Field D sample. Top: new sample. Bottom: sample after test with pre-saturated carbonated brine. | 166 |
| Figure 7.31. Contact angle values for experiments using Model Oil and Oil B. Full bars are tests with no CO ₂ and patterned bars are pre-saturated tests. Conditions: 60 °C, 1000 psi, 1 day aging in Brine B, 30 days aging in oil..... | 168 |
| Figure 7.32. Contact angle values for experiments using DSW / Brine B and Oil B. Conditions: 60 °C, 1000 psi, 1 day aging in brine, 30 days aging in Oil B..... | 169 |
| Figure 8.1. Surface plots showing the interfacial tension (IFT) dependence on Temperature (T), Alkane Carbon Number (CN) and Pressure (P). Top: IFT as a function of T and CN at fixed 1200 psi. Bottom: IFT as a function of P and CN at 60°C..... | 173 |
| Figure 8.2. Interfacial tension between Oil B and Brine B as a function of time with no CO ₂ and with CO ₂ saturated fluids. Conditions: 60 °C, 1000 or 5000 psi. | 176 |
| Figure 8.3. Interfacial tension between Model Oil and Brine B as a function of time with no CO ₂ and with CO ₂ saturated fluids. Conditions: 60 °C, 1000 or 5000 psi. | 177 |
| Figure 8.4. CO ₂ effect on the dynamic and equilibrium interfacial tension between Oil B and Brine B. Conditions: Conditions: 60 °C, 1000 or 5000 psi. | 178 |
| Figure 8.5. CO ₂ effect on the dynamic and equilibrium interfacial tension between Model Oil and Brine B. Conditions: Conditions: 60 °C, 1000 or 5000 psi..... | 179 |
| Figure 8.6. CO ₂ effect on the dynamic and equilibrium interfacial tension between Oil D and Brine D. Conditions: Conditions: 60 °C, 1000 or 5000 psi..... | 180 |
| Figure 8.7. Interfacial tension versus pressure using dynamic and equilibrium measurements in Oil B and Brine B with and without CO ₂ . Temperature: 60 °C. | 181 |
| Figure 8.8. Interfacial tension between Oil B and Brine B for different CO ₂ concentrations. Conditions: 60 °C, 1000 or 5000 psi..... | 182 |
| Figure A.1. Scheme of the parameter used to characterize the equations involved in DSA measurements. | 213 |
| Figure B.1. pH of Brine B, D and DSW with no CO ₂ and CO ₂ saturated at 60 °C. | 216 |
| Figure B.2. pH for Brine B at 60 °C with different concentrations of CO ₂ used in this work. | 217 |

| | |
|--|-----|
| Figure B.3. Density of crude B and CO ₂ saturated mixture..... | 219 |
| Figure B.4. Solubility of CO ₂ in crude B at 60 °C and pressures up to 10000 psi. | 221 |
| Figure B.5. Density of crude D and CO ₂ saturated mixture at 60 °C. | 222 |
| Figure B.6. CO ₂ solubility in crude B at 60 °C and pressures up to 7000 psi. ... | 223 |
| Figure B.7. Density of Model Oil and CO ₂ saturated mixture at 60 °C..... | 223 |
| Figure B.8. CO ₂ solubility in Model Oil at 60 °C and pressures up to reaching a critical mixture..... | 224 |
| Figure B.9. Phase diagram for dead Oil B. | 224 |
| Figure B.10. Phase diagram for mixture L1..... | 225 |
| Figure B.11. Phase diagram for mixture L2..... | 225 |
| Figure B.12. Phase diagram for mixture L3..... | 226 |
| Figure B.13. Phase diagram for mixture L4..... | 226 |
| Figure B.14. Phase diagram for dead Oil D. | 227 |
| Figure B.15. Phase diagram for mixture with equivalent volumes to L4 using Oil D. | 227 |
| Figure B.16. Phase diagram for dead Model Oil. | 228 |
| Figure B.17. Phase diagram for mixture with equivalent volumes to L4 using Model Oil. | 228 |
| Figure D.1. FTIR spectra of asphaltene sample from Oil B. | 230 |
| Figure D.2. . FTIR spectra of asphaltene sample from Oil D. | 231 |

LIST OF TABLES

| | |
|---|-----|
| Table 5.1. Ionic composition (ppm), total dissolved solids TDS, and pH and density (ρ) for the different brines used in this work. | 93 |
| Table 5.2. SARA analysis of the Pre-Salt crude oils used in this work (wt.%).... | 94 |
| Table 5.3. Total Acid and Base Numbers (TAN and TBN) and API of the Pre-Salt crudes..... | 94 |
| Table 5.4. Gas chromatography composition (wt.%) of the crude oils used in this work..... | 95 |
| Table 5.5. Profilometer average roughness and standard deviation of clean rock slabs..... | 106 |
| Table 5.6. AFM root mean square roughness and standard deviation of clean rock slabs..... | 107 |
| Table 5.7. XRD results for different rocks. Results in wt%. | 108 |
| Table 6.1. Maximum solvent volume fraction that can be mixed with crude B without asphaltene precipitation..... | 112 |
| Table 6.2. CHN (wt.%) for asphaltene samples of Oils B and D. | 133 |
| Table 7.1. Effect of CO ₂ on average roughness of different rocks. | 158 |
| Table 8.1. Comparison of IFT measured at atmospheric pressure with the results in the literature (ZEPPIERI; RODRÍGUEZ; LÓPEZ DE RAMOS, 2001)..... | 172 |
| Table B.1. CO ₂ solubility in the brines used in this work at 60 °C. | 215 |
| Table B.2. Density (g/ml) of the brines used in this work with no CO ₂ and CO ₂ saturated. Temperature = 60 °C..... | 217 |
| Table B.3. Concentration and simulated density data for brine B recombined with CO ₂ | 218 |
| Table B.4. Volumes injected for each recombination at 1000 psi and 25 °C. | 219 |
| Table B.5. Composition (mol%) of the phases after recombination at 25 °C and 1000 psi..... | 220 |
| Table B.6. Density (g/ml) of the liquid oil phase at 60 °C after recombination flash at 25 °C and 1000 psi..... | 220 |

| | |
|---|-----|
| Table B.7. Composition (mol%) of the phases after recombination of 50 ml Oil D and 18.8 ml CO ₂ at 25 °C and 1000 psi..... | 222 |
|---|-----|

| | |
|--|-----|
| Table E.1. Interfacial tension measurements between n-alkanes and water..... | 232 |
|--|-----|

LIST OF SYMBOLS

| | |
|-----------|---|
| A | Cross section area |
| A_{ii} | Potential energy between molecules of species “i” |
| B | Drop shape parameter |
| Bo | Bond Number |
| C | Constant |
| d_e | Diameter at the drop’s plane of Equator |
| D_n | Needle diameter |
| d_s | Drop diameter at a d_e vertical distance |
| E_{ij} | Free energy of interaction between phases “i-j” |
| F | Force |
| H | Mineral hardness |
| k | Absolute permeability |
| L | Distance in the direction of flow |
| M | Mobility ratio |
| N_c | Capillary Number |
| N_{cri} | Critical Capillary Number |
| P | Pressure |
| P_d | Displacement pressure |
| q | Volumetric flow rate |
| r | Distance |
| R | Roughness |
| R_i | Main radii of curvature |
| r_m | Critical separation of negative potential |
| R_n | Needle radius |
| S_i | Saturation |

| | |
|---------------|---|
| S_{or} | Residual oil saturation |
| S_{wi} | Connate water saturation |
| v | Sweeping fluid's velocity |
| V | Volume |
| V_d | Dimensionless volume |
| W | Work |
| W_o | Worthington Number |
| x | Axis coordinate perpendicular to gravity acceleration |
| z | Axis coordinate parallel to gravity acceleration |
| β | Ratio between gravity and interfacial tension forces |
| γ | Interfacial tension |
| γ_{ii} | Energy of interaction between species "i" |
| δ | Solubility parameter |
| ΔP | Pressure difference |
| θ | Contact angle |
| μ | Dynamic viscosity |
| μ_w | Sweeping fluid's viscosity |
| ρ | Density |
| φ | Angle of rotation |
| ψ_i | Potential energy at the point "i" |

LIST OF ABBREVIATIONS

| | |
|-------|---|
| AFM | Atomic Force Microscopy |
| ANOVA | Analysis of Variance |
| API | American Petroleum Institute |
| ASTM | American Society for Testing and Materials |
| Ave. | Average |
| bbl | Barrels |
| bopd | Barrels of oil per day |
| BSCF | Billion Standard Cubic Feet |
| CA | Contact Angle |
| CHN | Carbon, Hydrogen and Nitrogen |
| CT | Computed Tomography |
| DLVO | Deerjaguin, Landau, Verwey, Overbeek Theory |
| DSA | Drop Shape Analysis |
| EDS | Electron Dispersive Microscopy |
| EOR | Enhanced Oil Recovery |
| EWT | Extended Well Test |
| FS | Stabilization Frequency |
| FTIR | Fourier-Transform Infrared Spectroscopy |
| GC | Gas Chromatography |
| GDP | Gross Domestic Product |
| GOR | Gas to Oil Ratio |
| HCPV | Hydrocarbon Pore Volume |
| HPHT | High Pressure and High Temperature |
| IFT | Interfacial Tension |
| IOR | Improved Oil Recovery |

| | |
|-------|--|
| IP | Institute of Petroleum |
| LPG | Liquefied Petroleum Gas |
| LWD | Logging While Drilling |
| MME | Minimum Miscibility Enrichment |
| MMP | Minimum Miscibility Pressure |
| MMSCF | Million Standard Cubic Feet |
| MSCF | Thousand Standard Cubic Feet |
| NMR | Nuclear Magnetic Resonance |
| OECD | Organization for Economic Co-operative Development |
| OOIP | Original Oil in Place |
| OPEC | Organization of Petroleum Exporting Countries |
| pI | Isoelectric point |
| PID | Proportional, Derivative and Integral |
| PVT | Pressure, Volume and Temperature |
| pzc | Point of zero charge |
| RCAL | Routine Core Analysis |
| RDA | Reservoir Data Acquisition |
| RF | Recovery Factor |
| RMS | Root Mean Square |
| RSD | Relative Standard Deviation |
| SCAL | Special Core Analysis |
| SCF | Standard Cubic Feet |
| SD | Standard Deviation |
| SEM | Scanning Electron Microscopy |
| SF | Swelling Factor |
| STB | Stock Tank Barrel |

| | |
|------|----------------------------------|
| TAN | Total Acid Number |
| TBN | Total Basic Number |
| TDS | Total Dissolved Solids |
| USA | United States of America |
| USBM | United States Bureau of Mines |
| USD | United States Dollars |
| UV | Ultraviolet |
| VBA | Visual Basic Applications |
| WAG | Water Alternated with Gas |
| WOR | Water to Oil Ratio |
| WTI | West Texas Intermediate |
| XPS | X-ray Photoelectron Spectroscopy |
| XRD | X-ray Diffraction |

CHAPTER 1: INTRODUCTION

1.1 Motivation

The Oil and Gas Industry is complex and the revenues, profits, geographical distribution and main expenses depend on both human interventions (such as historical, political and economic factors) and natural factors (environmental aspects, reserves discoveries among others). As a result, the level of investment in the industry is cyclic. There are periods of considerable growth that bring a favorable job market, advances in infrastructure and the possibility of exploration of more complex reserves. In contrast, when the industry is in period of low income, the budgets tighten up and the companies and other institutions need to shorten their expenses leading to a more difficult scenario to produce the fields that represent a greater economic challenge. With this in mind, a brief introduction about the actual situation of the Oil and Gas Industry in the world and in Brazil is necessary to set the scenario for the motivation of this work. This will be discussed in the following paragraphs.

According to the Organization of Petroleum Exporting Countries (“2017 OPEC World Outlook”, 2017), the global energy demand will continue to increase up to 35% in 2040 reaching 372 million barrels of oil equivalent per day (mboe/d). Due to industrialization, population growth and increase in consumption the developing countries, which represented 52.1% of the demand in 2015, are expected to represent 62.4% of the total demand. Nevertheless, the countries that belong to the Organization for Economic for Co-operation and Development (OECD) are expected to increase their energy demand in less than 2% for the same period of time.

The document also states that, although the renewables and alternative sources of energy are increasing their importance in the energy matrix, fossil fuels will continue to be the dominant sources of energy with a share of 52.2% of the total demand. The global demand of oil is expected to increase 16.4%, and this trend is set particularly by the developing countries. Thus, Brazil is one of the key players for this trend meaning that the demand of oil will be a determinant factor for the development of the country and its economy,

In addition to an increased oil demand, the actual scenario of the Oil and Gas Industry is marked by the instability of the crude oil price. According to the United States Energy Information Administration (“US Energy Information Administration Spot Price”, [s.d.]), the Oklahoma WTI crude price decreased to less than 50% in two years (from US\$ 105 a barrel in July 25th 2014 to US\$42 for the same day in 2016), reaching an intermediate value of 67.87US\$ in July 2018. The same trend is observed for Europe Brent crude. The sociopolitical factors that influence the price of oil are beyond the scope of this text. Nevertheless, it is of paramount importance determining the viability of exploration and activities including research in laboratory and field scales.

The Pre-Salt province represents up to 58% of Brazil’s Gross Domestic Product (GDP). Therefore, it represents the most important resources of the country. Following the oil price reduction of 2014, operators in Brazil, focused on reducing the capital cost index as a driver for lowering the breakeven price (BUCKLEY; UEHARA, 2017). The exploration of Brazilian Pre-Salt follows the trend of other ultra-deep water fields that show a decrease in breakeven values from US\$70 to 40 between 2014 and 2018 (D’SOUZA et al., 2018). This is a key to re-activate E&P activities in the Pre-Salt. Accordingly, a demand in research must support these operations to plan and execute the projects adequately and to maximize the profit increasing the Recovery Factor.

Proved oil reserves at a specific time represent the resources that could be produced in the following years considering the technology and economic production limits available at that time. The proven world reserves for December 2017 were 1,482 billion barrels (“OPEC Share of World Proven Reserves”, 2018). However, although the proved reserves increase over the time, the production from reservoirs for long periods of times leave the most difficult to obtain part of the resources behind. For these type of fields, referred to as mature fields, more complex (and expensive) type of processes are required to obtain the required production rates. In addition, some of these “new” proven reserves correspond to unconventional scenarios that were not considered recoverable in the past. The Brazilian Pre-Salt belongs to this group, and the characteristics that make these reservoirs a unique challenge will be described in the following section. Moreover, the amount of CO₂ produced from these fields encourages the operators to evaluate the injection of this gas as a method to improve oil recovery.

To sum up this brief discussion, Pre-Salt fields are the most important assets for the economy of Brazil, and they will play a key role to supply the increase of the energy

demand. The actual crude oil price raises the challenge of exploring these resources. Therefore, the development of technologies to learn about the behavior of the rocks and fluids for each specific production strategies and its impact on oil recovery is very relevant for the Brazilian Oil and Gas Industry. Nevertheless, there are few publications available in the literature describing rock-fluid and fluid-fluid interactions from an Enhanced Oil Recovery point of view. This scenario encourages the experimental research to understand behavior of the components of the reservoir under different conditions including the presence of CO₂, which sets the goals of this work discussed later in this chapter.

1.2 The Pre-Salt reservoir environment

1.2.1 General characteristics of the Pre-Salt fields

The structure known as Pre-Salt was formed 160 million years ago during the separation of the African and American continents. Seawater filled the spaces formed as the separation advanced, and rifting allowed the existence of a series of interconnected lacustrine basins. Stratigraphic evidence that indicates the sediments in the southern rift Santos, Campos and Espirito Santo basins are lacustrine (THOMPSON; STILWELL; HALL, 2015). These sediments consist of flood basalt deposits that allowed the formation of reservoirs after oil migration. Due to climate changes in the planet, the salts dissolved in the seawater precipitated in forming the salt layer that acted as a seal allowing the accumulation of hydrocarbons in the reservoir rock (FORMIGLI; CAPELEIRO PINTO; ALMEIDA, 2009).

Some general features of the Pre-Salt rocks were described in the literature. First, the rock matrix in Pre-Salt reservoirs is a very heterogeneous carbonate (PEPIN et al., 2014). Other challenges present in the Pre-Salt fields include a water depth of up to 2,250 meters, internal (pressures higher than the ones found in post-salt fields) that result in gas injection lines at pressures up to 8000 psi, 300 km to the coast and a content of CO₂ up to 20% of the produced gas. Since CO₂ is a greenhouse gas, venting excessive amounts of this gas to the atmosphere is not a possibility due to environmental reasons. So, Petrobras has adopted a membrane system to separate CO₂ from the produced gas (CEZAR et al., 2015).

The Santos Basin Pre-Salt cluster is located at approximately 290 km from the Rio de Janeiro coast in the southeastern region of Brazil. It is under ultra-deep waters with a water depth of 1900 to 2400 meters (FORMIGLI FILHO; CAPELEIRO PINTO; ALMEIDA, 2009). A diagram of this region presented in the literature is showed in Figure 1.1.

Lula field, which was discovered in September 2006, was the second discovery in the Santos Basin Pre-Salt Cluster. The estimated reserves from Lula field, which was formerly known as Tupi field, are 8,3 billion barrels of oil equivalent (boe) making it the first supergiant field in Brazil.

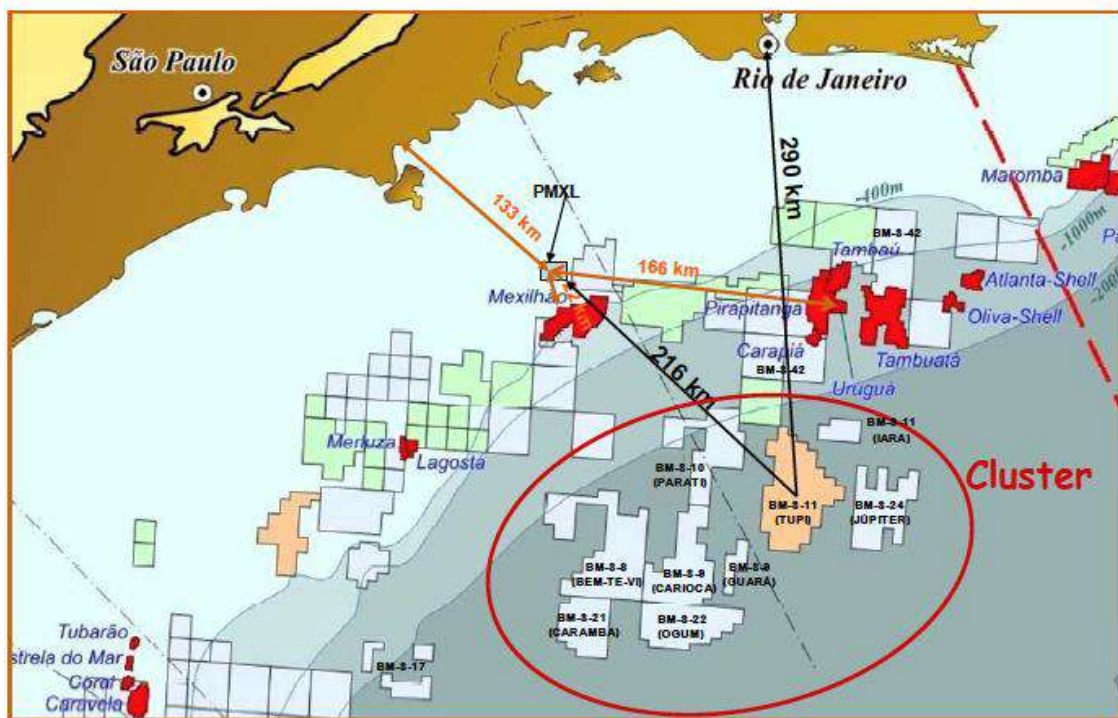


Figure 1.1. Diagram of the Pre-Salt cluster area (FORMIGLI FILHO; CAPELEIRO PINTO; ALMEIDA, 2009).

The main characteristics of Lula field, presented by Vianna Filho and de Oliveira (2015), are the following. Ultra-deep waters (around 2,200 meters) and salt layer of around 2,000 meters result in well depths that can reach 5,500 meters, which represent a challenge for drilling and well construction. The reservoirs, considered unconventional, are extremely heterogeneous with a wide distribution of porosities and permeabilities. The gas to oil ratio (GOR) is considered high (greater than 150 to std m³ / std m³), and

the concentration of non-hydrocarbons (specially CO₂) is particularly high (GONÇALVES REIS VIANNA FILHO; NAVEIRO; DE OLIVEIRA, 2015).

1.2.2 The rock

Pre-Salt reservoirs consist of two types of formations: the upper sag is characterized by what was called microbial carbonates, and the lower sag is represented by the coquinas. It is known that these formations are extremely heterogeneous with interbedded microbial and volcanic rocks that have been affected by different geological processes, such as hydrothermalism (MATIAS et al., 2015).

Due to the difficulty and cost of obtaining rock samples from the reservoir, most studies were carried out using samples from analogue formations. The coquinas gained interest for this reason due to the availability of samples in different parts of Brazil. Some works in the literature describe these formations ((CAMARA et al., 2014; CORBETT; BORGHI, 2013)).

Pepin et al. (2014) studied the coquinas formations as the best analogues from Pre-Salt rocks. They obtained samples from quarry in the Morro do Chaves formation in the Sergipe – Alagoas basin in northeastern Brazil. The samples were cleaned and submitted to routine core analysis tests, such as, porosity and permeability measurement, X-ray diffraction (XRD), scanning electron microscopy with X-Ray spectroscopy (XRD/EDX), nuclear magnetic resonance (NMR) and X-Ray transmission microtomography (μ CT). In addition, they performed core flood tests to analyze the response of the samples to stimulation treatments.

The researchers measured the porosity and air permeability using the unsteady-state pulse-decay method. The results show a very heterogeneous distribution of porosity and permeability that not necessarily followed any trend among the consecutive layers. The values obtained for the permeability ranged from 0,001 to 358 mD. Furthermore, the porosity showed a variation from 2,57% to 22,5% (PEPIN et al., 2014).

The lithology was analyzed by the XRD technique. Although calcite was, as expected, the most abundant mineral in all of the samples, heterogeneities were found among the distribution of the secondary minerals in the samples. Quartz and microcline (feldspar) appear, in different proportions, as the secondary minerals, and illite is present in less abundance. The average of the 13 samples analyzed by Pepin et al. (2014) gives

the following distribution (in weight %): 89,41% calcite, 8,02% quartz, 1,70% microcline and 0,87% illite. A list of the minerals used in this work with their chemical formulas and descriptions is showed in Appendix C.

The presence of different lithological groups was analyzed quantitatively using the SEM/EDX technique. The results obtained by Pepin et al. for the average of the 13 samples that were tested showed that oxygen, calcium and carbon are the elements found in higher concentrations with concentrations in weight % of 35.18, 34.72 and 13.57 respectively. This is consistent with their previous results that show calcite as the most abundant mineral. In addition, the tests indicated silicon, in agreement with the presence of quartz, as the fourth richest element with 11.25 wt%. Finally, the concentration of magnesium reported was 1.27 wt%. This is relevant because the ratio of calcium to magnesium elements characterize the ratio of calcite to dolomite.

The authors classified the quarry as “thick massive limestone beds with large cross stratifications and hummocky cross stratifications corresponding to shallow-water shoal environments dominated by waves”. Quartz was only found above the transgressive surfaces (prominent flooding surfaces). Calcitic shells and calcitic cement dominate the lithology. Nevertheless, dolomite was not common and it was found as isolated crystals.

Terra et al. presented a classification for a wide variety of carbonate facies present in Brazilian basins (TERRA et al., 2010). This classification was the base for Corbett and Borghi (2013) to report the identification of the key facies that, having the best characteristics to be reservoir rocks, are associated with Pre-Salt formations. These key facies are the following (BOYD et al., 2015):

- Tufa and travertine: They contain a great degree of layering and vugs are very frequent. Their formation is associated with CaCO_3 precipitation due to pH changes in spring waters (tufa) or geothermal waters containing calcium (travertine).
- Stromatolites: They correspond to shallow lacustrine environments where algal mats trap carbonate sediments. Since they present convex bedding, they have dome-shaped formations. In addition, their vuggy porosity can benefit the flow of fluids through them.

- Coquinas: They are formed from the deposition of shells from molluscs from fresh or low salinity water. They good intergranular porosity and permeability give them satisfactory properties as reservoir rocks.

Corbett and Borghi (2013) analyzed the lacustrine carbonates from a reservoir characterization point of view. The main idea of the work is to identify similarities and differences, regarding Reservoir Engineering, between lacustrine carbonates and other types (and more studied) carbonates. They address experimental procedures 3-D modeling methodologies to study the porosity and permeability of this type of samples. In addition, they characterize the capillary pressure and relative permeability curves, which are fundamental for Reservoir Engineering, for these formations. They outlined that, since lacustrine carbonates developed from a range of chemical to microbiological processes under a variety of environmental conditions, their matrix can be composed of a broad distribution of elements. However, the authors distinguished that the broad pore distribution and complexity of the pores found in lacustrine carbonates is similar to that reported for other carbonate rocks.

Tavares et al. (2015) discussed the geological facies present in the coquinas from the Morro do Chaves formation. In agreement with the previous studies, calcite, which is in most cases composed of mollusk shells, is identified as the major mineralogical component. Quartz, micrite, clay and lithoclasts of igneous, sedimentary and metamorphic rocks were reported as components of the matrix. The facies described (TAVARES et al., 2015) are listed as follows:

- Fragmented coquina with no micrite (Cf): coquina with more than 80% of fragmented shells, less than 10% micrite and less than 10% siliclastics.
- Impure fragmented coquina with no micrite (Cfi): coquina with more than 40% of fragmented shells, less than 10% of micrite and more than 10% of siliclastics.
- Non-fragmented coquina with micrite (Cm): coquinas with more than 20% of non-fragmented shells, more than 10% of micrite and less than 10% of siliclastics.
- Impure non-fragmented coquina with micrite (Cmi): coquina with more than 20% of non-fragmented shells, more than 10% of micrite and less than 10% of siliclastics.
- Green shale (Fv): laminated green mudstone.
- Black shale (Fp): laminated black mudstone / siltstone.

Boyd et al. (2015) presented a procedure for the petrophysical analysis of Pre-Salt formations. It is based on wireline logging and logging-while-drilling (LWD), formation testing tools for fluid sampling, geochemical mud logging and core sampling followed by routine core analysis and special core analysis (RCAL and SCAL). Briefly, the workflow reported consists of three main steps:

- Determination of lithology and porosity using neutron logging and nuclear magnetic resonance (NMR) tools.
- Permeability determination using NMR and borehole imaging tools.
- Fluids' saturations and relative permeabilities analyses by combining dielectric logs with NMR and correlating the results with SCAL analysis.

The authors show the application of this procedure for Pre-Salt field examples. The petrophysical properties and the identification of the different layers are explained from the results of logging and NMR tests. Their results were in agreement with the characterization of analogue rocks, showing calcite, dolomite and quartz as the main mineral constituents. The authors present a petrophysical characterization of reservoir samples; however, further research is required to relate these results to the prediction of the production from reservoir simulation.

1.2.3 The fluids

Since Pre-Salt reservoirs have been discovered relatively recently and due to the early stage of exploration and production of most of the active fields, there is not too much data available from the fluids contained in Pre-Salt reservoirs in the literature. Some information collected from recently published papers is commented in the following paragraphs.

De Almeida et al. (2010) reported medium to light oil with API gravity around 28°-30° in the Santos Basin Pre-Salt cluster. In addition, they informed that the gas to oil ratio (GOR) is high (from 200 to 300 m³ std / m³ std) containing high contents of CO₂. As an example, they mention the Lula Field (formerly Tupi field) that has a CO₂ concentration of 8 to 12% in the produced gas. The authors relate the formation of CO₂ in Pre-Salt fields to organic and inorganic processes. The former are reactions that occur during kerogen maturation, oil decomposition by microorganisms and biochemical

reduction of sulfate. The later are present during the metamorphism of carbonate rocks and coals (DE ALMEIDA et al., 2010).

Other works (CEZAR et al., 2015) stated that the CO₂ content in the produced gas from Pre-Salt reservoirs is extremely variable ranging from 0 to more than 20%. Due to environmental reasons, the CO₂ produced from the fields in operation is not vented; so, the production unites are equipped with membranes to separate large volumes of CO₂. Then, the CO₂ is re-injected in the reservoir for EOR and CO₂ storage applications. As a result, the CO₂ concentration in the produced fluids may reach higher values, such as 45%, after recirculation of this component. The injected gas is rich in CO₂ with concentrations up to 85%. In addition, the authors report variable concentration of H₂S in some areas. However, it is not a principal component of the gas, and these formations are considered particularly rich in sour gas.

Matias et al. (2015) remarked that, while fields with more than 15% of CO₂ content are considered rare, the average CO₂ content in Santos and Campos basins is around 19%. The great content of CO₂ was related to the accentuated geothermal gradient, igneous intrusions among others, and its origin is believed to be from the mantle (SANTOS NETO; CERQUEIRA; PRINZHOFER, 2012). Nonetheless, carbon dissolution could be another source of CO₂ in the Pre-Salt environment.

Considering the Lula field, Boyd et al. (2015) expressed similar values (28 to 30) of oil API gravity. Furthermore, its viscosity is around 1 cp at reservoir conditions, resulting in great flowing properties. They also informed that the GOR is between 140 and 240 std m³ / std m³ with CO₂ contents from 8 to 18%. Later research (DE MORAES CRUZ et al., 2016) indicated an API gravity of 28 and GOR value of 250 std m³ / std m³ for the Lula field with the presence of CO₂.

The main Pre-Salt fields are Lula, Libra and Franco. In 2015 twelve fields were producing reach around 648000 barrels of oil per day (bopd) (MATIAS et al., 2015). De Moraes Cruz et al. (2016) reported an updated greater value of up to 900000 bopd from the Santos and Campos basins. According to Boyd et al. (2015), the sum of the 15 producing wells in Lula field give a total of 450000 bopd. Furthermore, when the associated gas is included, each well produces 30000 barrels of oil equivalent per day (boepd). The production history of Lula field is showed in Figure 1.2.

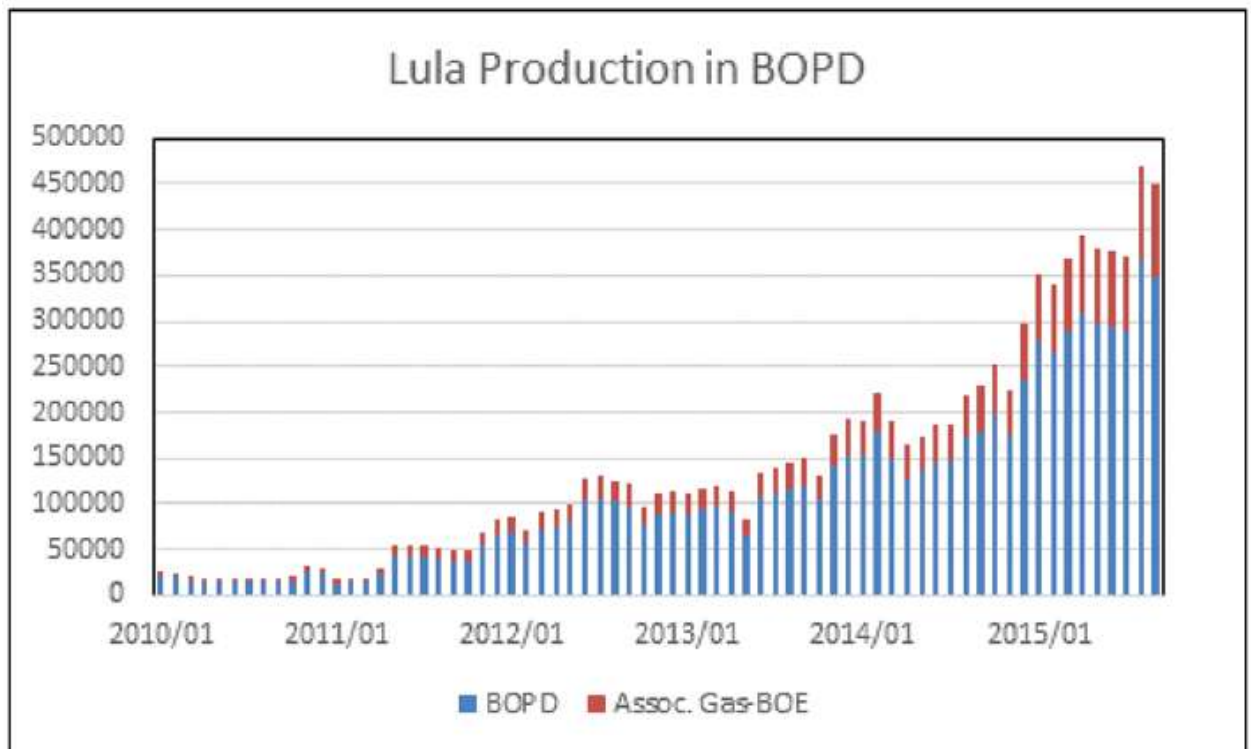


Figure 1.2. Production history for Lula field (BOYD et al., 2015).

De Moraes Cruz et al. (2016) described the first megaproject applied in Lula field. The objective of this pilot project was to gain experience in secondary recovery for the Pre-Salt fields, to acquire data for these reservoirs and to achieve ways to increase the total production of the Pre-Salt while generating short-term revenues. The strategies for reservoir data acquisition (RDA) and the extended well tests (EWT) performed are discussed. In addition, the facilities and the different subsea and surface equipment and operating units are described in detail. Since this is out of the scope of this text, it will not be discussed here. However, the reader is advised to consult this reference for further information.

1.3 Objective of this research

The last sections discussed the importance of the Pre-Salt fields for the Brazilian Oil and Gas Industry. However, these formations represent unprecedented challenges for the production of oil, and reliable experimental data under representative reservoir conditions is not present in the literature. The acquisition and publication of this data is

of paramount importance for the planning and success of recovery technologies in the Pre-Salt fields.

For the economic and environmental reasons exposed before, the injection of CO₂ in the reservoirs appears as a sensible recovery method for the Pre-Salt fields. Nevertheless, the fundamentals of the fluid-fluid and fluid-solid interactions of the oil-gas-brine-rock system are still not understood for these reservoirs. These interactions are key to understand the behavior of the different phases under different recovery scenarios, and therefore, to construct reservoir models that are representative of the Pre-Salt and design a recovery method successfully. The properties considered to characterize these phenomena are divided in two main groups briefly mentioned as follows:

1) Fluid-fluid:

- The study of the interfacial tension between brine and oil under different pressure and compositional conditions.
- The effect of CO₂ dissolution on the physical properties of oil and formation brine.

2) Rock-fluid:

- The effect of each phase composition (particularly CO₂ concentration) on the tendency of the rock to be preferentially wet by oil or brine.
- The changes on the rock properties as a result of the contact with the fluids.

The scope of this work is, based on the properties listed above, to characterize interfacial tension and wettability under the conditions expected for Pre-Salt reservoirs containing CO₂. With this goal, the first part of this study looks to develop adequate experimental techniques to measure meaningful parameters under reservoir conditions. In addition, this research will study how compositional and pressure conditions affect these properties. Finally, it will conclude about how the changes on these conditions may influence the recovery of oil.

The ultimate goal of this research is to gain basic knowledge about the behavior of the different phases under the conditions expected for the Pre-Salt reservoirs considering also dissolved CO₂ in the. The understanding of this behavior allows the analysis of initial wettability and capillary forces, identifying the most favorable conditions for oil recovery.

This study therefore aims to provide reliable experimental results to aid in the development of representative reservoir models.

1.4 Structure of the text

This text is divided in 9 chapters. To simplify the organization of the text, the scope of each chapter is briefly explained below:

- Chapter 1 sets the scenario and the motivation for this research. In addition, it describes the main characteristic of the Pre-Salt environment. Also, it specifies the goals of this work, and it shows the relevance of the results in the present context.
- Chapter 2 contains the theoretical framework to describe the physical and chemical concepts that govern the fluid-fluid and fluid-solid interactions. The principal phenomena covered in this chapter are interfacial tension and wettability.
- Chapter 3 contains the literature review. It considers the state of the art of techniques applied in this work.
- Chapter 4 describes the methodology carried out in this experimental research. It briefly covers the experimental procedures, and the data analysis methods. It also includes the experimental techniques applied for rock and fluid characterization and the computational techniques used to complement the experimental results.
- Chapter 5 shows the characterization of the reservoir fluids and types of rocks used in this work.
- Chapter 6 considers the experimental and discussions on the study of initial wettability for pure minerals, outcrops and reservoir rocks. Two Pre-Salt reservoir scenarios are considered, and a model oil is included for comparison.
- Chapter 7 focuses on the impact of CO₂ on the initial wettability for the different minerals and rocks. The methodology to feed CO₂ in the system and the causes for wettability alteration are discussed.
- Chapter 8 is about the fluid-fluid interactions in the Pre-Salt reservoir conditions. The effects of CO₂ on the action of surface-active components present in Pre-Salt oils is discussed.

- Chapter 9 contains the final remarks and recommendations for future works.
- Chapter 10 is the bibliography.

CHAPTER 2: THEORETICAL FRAMEWORK

The scope of this chapter is to describe the physical and chemical concepts that rule the fluid-fluid and solid-fluid interactions in Reservoir Engineering, more specifically regarding fields with high concentration of CO₂. It is divided in three sections that discuss the theory behind each phenomenon and the techniques associated to the experimental measurement of the most relevant variables.

The first section is a short review of the fundamentals of Reservoir Engineering and Enhanced Oil Recovery, including definitions that will be employed throughout the text. The second part covers the surface and interfacial tension from a chemical and a thermodynamic point of view. The main equations and properties affecting the interfacial tension are discussed. Finally, the wettability, as a characterization of the interaction between the rock and the fluids, is reviewed. This last section includes the fundamentals of wettability for reservoir engineering and the measurement of the contact angle as a tool to study the wettability quantitatively.

2.1 Reservoir production and Enhanced Oil Recovery

2.1.1 Definitions

The previous chapter discussed that fossil fuels are still the primary source of energy, and that this trend is expected to continue for, at least, the following 20 years. The global demand of energy is expected to keep increasing due to the expanded economies and the population growth of the emerging regions. For this, maximizing the production of the oil fields is one of the most important present objectives of the Oil and Gas Industry. Being an emerging economy with a large volume of unconventional reserves, Brazil has great interest in studying and developing methods to increase the production of both mature and newly discovered fields.

The Recovery Factor (RF) is defined as the recoverable fraction of the Original Oil in Place (OOIP) measured in standard conditions. In this text, the internationally accepted

standard conditions in the Oil and Gas Industry (15.6 °C and 14.7 psi) will be considered. Present research reviewed the history of the recovery factor in different types of reservoirs and different regions of the world (LU; SUN; DODDS, 2016). An average Recovery Factor of 35% was reported (THAKUR, 2012). In addition, for offshore fields the numbers are even lower: only 5% of the fields reach a Recovery Factor of 60% (ROELOFSEN; BASTIAN, 2008). These facts show that for most oil reservoirs a majority of the reserves remain unrecovered after production. The development of methods to increase the production is the objective of Enhanced Oil Recovery.

Before discussing Enhanced Oil Recovery, primary, secondary and tertiary oil recoveries need to be addressed. A common definition for primary recovery is the production of oil based solely on the primary source of energy (pressure) present in the reservoir. In addition, secondary recovery is referred to as the injection of external fluids, such as brine or natural gas, for pressure maintenance. Tertiary oil recovery is any additional production method that is applied after secondary production when the water-to-oil ratio (WOR) is no longer economically favorable (DONALDSON; CHILINGARIAN; YEN, 1989).

Enhanced Oil Recovery (EOR) is the addition injection of fluids to interact physically or chemically with any of the phases present in the reservoir (SHENG, 2010). These fluids can be sources of chemicals or thermal energy and their purpose is to increase the amount of oil that is recovery. In addition, the term Improved Oil Recovery (IOR) has been widely used to describe any operation carried out to raise the production. This includes different types of operations that do not consist in the injection of fluids, such as drilling horizontal wells and reservoir characterization among others. Thus, IOR is a broader term that includes the EOR techniques as a subset of methods to increase the production of oil.

The application of EOR methods has two main objectives: to augment the productivity of specific wells to increase the short-term profit and to maximize the ultimate recovery to increment the long-term revenue of a field (THAKUR, 2012). Previous research reported increments of up to 25% of the OOIP for EOR applications (CHANG et al., 2006). In addition, previously disclosed projects claimed the possibility of achieving Recovery Factors as high as 70% with the application of EOR methods (LU; SUN; DODDS, 2016).

2.1.2 Capillary pressure

The pores in the reservoir contain more than one phase. The presence of two or more fluid phases confined in the pore volume gives place to capillary forces that result in a pressure difference between these phases that is defined as capillary pressure. The capillary forces are governed by the surface or interfacial tension between the fluids, the surface or interfacial tension between each fluid and the solid (wettability) and the geometry of the pore. The capillary pressure produces the curvature of the interface between the fluids. The pressure difference at both sides of the interface is a function of the main radii of curvature and the interfacial tension between the phases as defined by the Young-Laplace Equation showed in Equation 2.1 (BUTT; GRAF; KAPPL, 2006).

$$\Delta P = \gamma \left(\frac{1}{R_1} + \frac{1}{R_2} \right) \quad (2.1)$$

where ΔP is the capillary pressure, γ is the interfacial tension between the fluids and R_1 and R_2 are the main radii of curvature.

Equation 2.1 shows that the greater the interfacial tension between the fluids or the smaller the radius of confinement, the higher the action of capillary forces at the interface. The importance of the role of capillary pressure on the recovery of oil will be discussed later in this chapter.

To displace a drop of a phase that is trapped in a pore by capillary forces, the pressure difference through the pore must exceed the capillary pressure. It is evident (from Equation 2.1) that the smaller pores will result in more curved interfaces with higher radii of curvature. Thus, the capillary pressure is greater for the smaller pores, and so is the pressure required to remove the trapped phase from the interior of the pores.

The extraction of a phase from the porous medium by another is classified depending on which phase (wetting or non-wetting) is the displaced phase. Imbibition occurs when the non-wetting fluid is the displaced phase. On the other hand, drainage is the displacement of the wetting fluid by a non-wetting phase. In other words, imbibition is a process in which the saturation of the wetting fluid increases, and drainage is a process that consists of an increase in the saturation of the non-wetting fluid (DONALDSON; ALAM, 2008).

A capillary pressure curve represents the capillary pressure as a function of the wetting fluid's saturation. A typical capillary pressure curve (AHMED, 2010) is showed in Figure 2.1. This curve shows an increase in the pressure required for displacement when the saturation decreases. This is a consequence of Equation 2.1 because for the lower the saturation values the fluid is retained in the smaller pores that result in higher capillary pressure values. The asymptotic behavior at the minimum saturation value represents the connate or irreducible water saturation, which is the fraction of the pore volume that remains trapped in the smaller pore throats. The capillary pressure that corresponds to the initial decrease in the saturation (indicated as p_d) is the minimum pressure required to displace the fluid from the biggest pores.

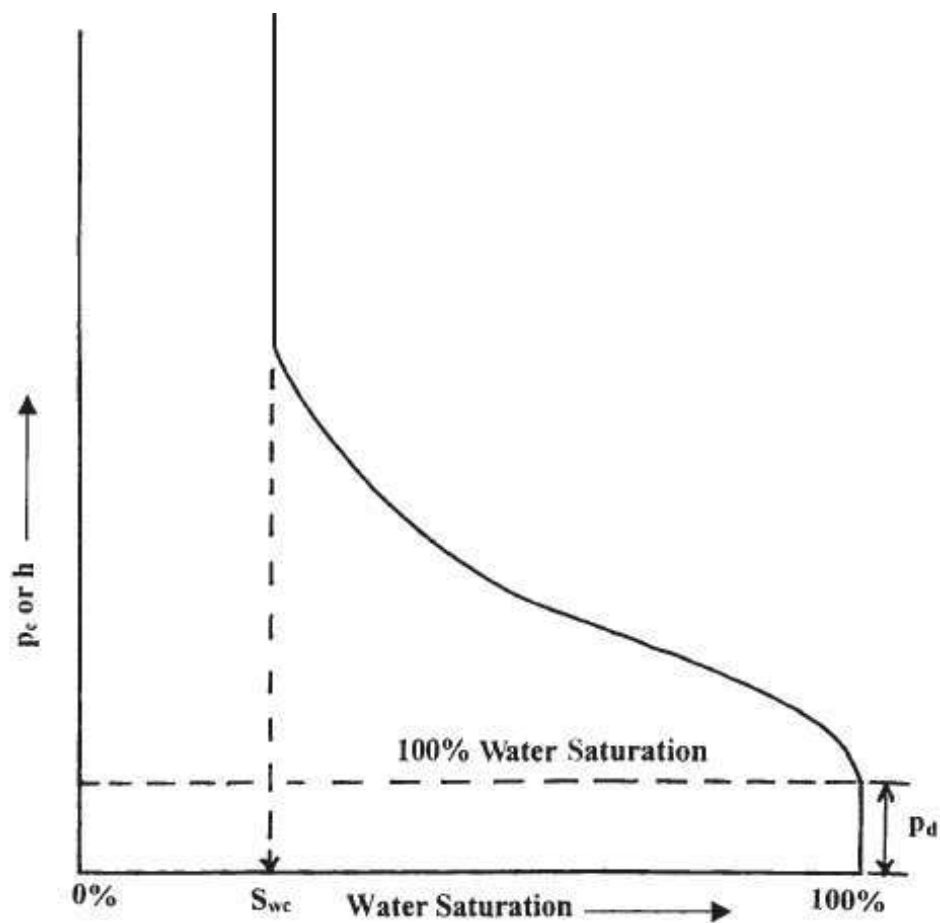


Figure 2.1. Capillary pressure curve (AHMED, 2010).

2.1.3 Relative permeability

The most widely equation used to describe the flow through porous media is the Darcy's law showed in Equation 2.2. In this expression, which corresponds to horizontal flow, the flow rate is proportional to the pressure gradient, the absolute permeability of the porous medium and the cross-section area and inversely proportional to the viscosity of the fluid. When the action of gravity needs to be considered, the hydraulic potential gradient must be used. The absolute permeability is a property of the porous medium alone, and it does not depend on the fluid (PINDER; GRAY, 2008).

$$q = - \frac{kA}{\mu} \frac{dP}{dL} \quad (2.2)$$

where q is the flow rate, k is the absolute permeability of the porous medium, A is the cross-section area, dP/dL is the pressure gradient and μ is the viscosity of the fluid.

When more than one phase saturates the porous medium the effective permeability towards each phase must be considered. The relative permeability to a phase (usually identified as k_{ri} for the i phase) is the ratio between the effective permeability to that phase and the absolute permeability. It considers the fluids' distribution in the pores according to the differences in wettability. Since, the non-wetting fluid locates in the biggest pores to minimize its contact with the solid, it occupies the regions of the pore volume that contribute the most to the flow. The relative permeability accounts for the flow capacity of each phase in the porous medium according to its distribution in the porous volume (AHMED, 2010).

The relative permeability curves represent the relative permeabilities to each phase as a function of the wetting fluid's saturation. A typical curve is showed in Figure 2.2 (AHMED, 2010). Three regions (A, B and C) are identified in the curve showing the saturation values where oil, biphasic and water flow occur. It can be noted that the non-wetting phase has higher values of relative permeability for the broader range of saturations, indicating that it flows with less resistance than the wetting fluid.

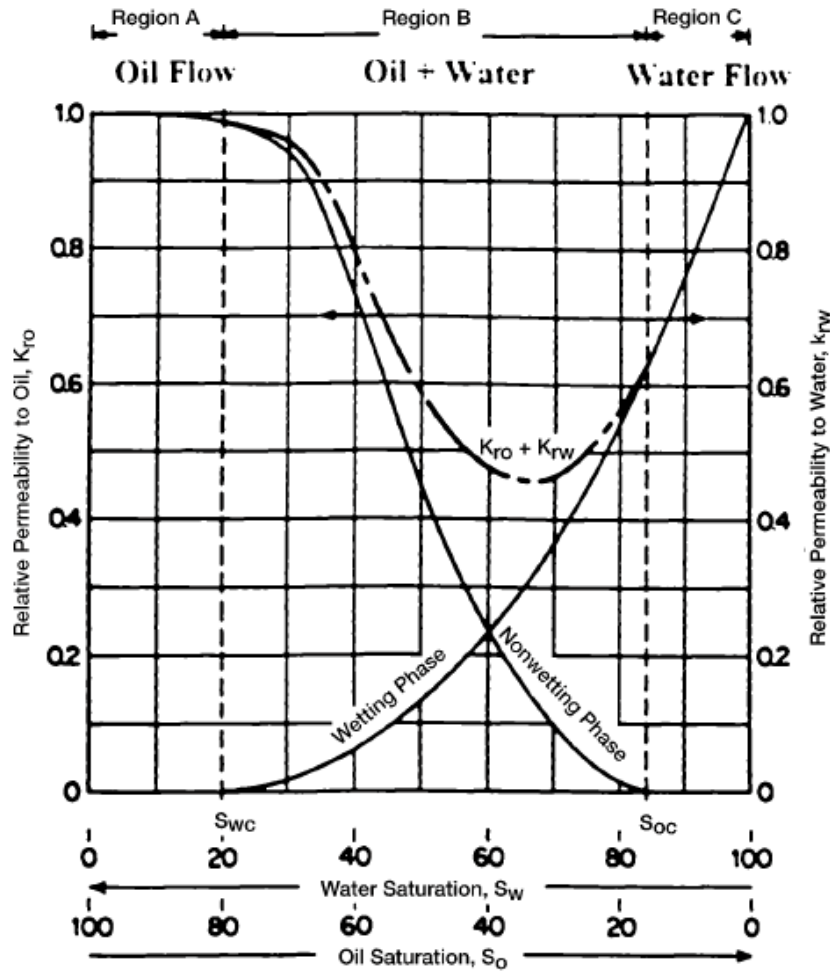


Figure 2.2. Relative permeability curve (AHMED, 2010).

2.1.4 Mobility ratio

The mobility of a phase in the porous medium is defined as the effective permeability to that phase divided by its viscosity. When a sweeping fluid (i.e. water) displaces a mobile fluid (such as oil), the ratio between the mobility of both fluids determines the homogeneity of the displacement front. To evaluate this, the Mobility ratio (M) is defined as the ratio between the mobility of the displaced fluid and the sweeping fluid. If the displaced fluid is more (or equally) mobile than the sweeping fluid ($M < 1$), the front is considered homogeneous. In contrast, if the mobility of the displaced fluid is lower than that of the sweeping fluid, the front is dominated by the formation of fingers (SHENG, 2010). It is important to remark that, to obtain the Mobility ratio, the water relative permeability is calculated at the average water saturation behind the water front,

and the oil relative permeability is calculated at the water saturation in the oil bank ahead of the front (CRAIG, 1971).

The effect of the homogeneity of the sweeping front is showed in Figure 2.3. The image on the left shows a displacement characterized by the formation of fingers; on the other hand, the front in the image on the right is homogeneous.

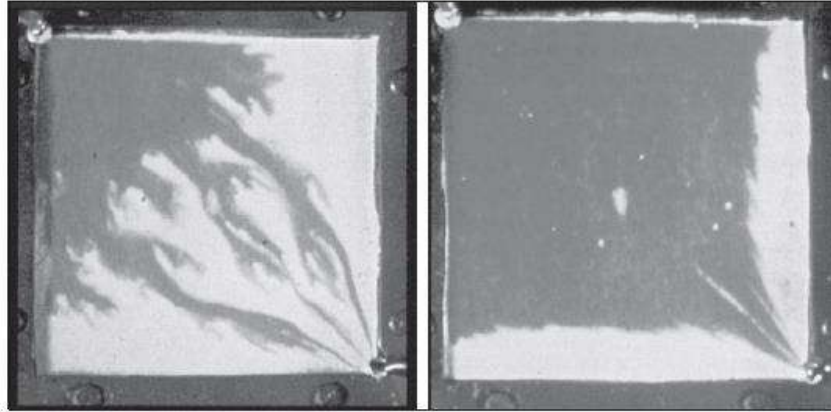


Figure 2.3. Areal sweeping of a displaced fluid. Left: formation of fingers. Right: homogeneous front. (SHENG, 2010).

It is evident, from Figure 2.3, that the fluid on the right is sweeping the porous medium more efficiently than the one on the left. The areal sweeping efficiency is strongly related to the formation of fingers. Sweepings carried out with a Mobility ratio greater than 1 are likely to form fingers and preferential channels of flow resulting in lower sweeping efficiencies (WILLHITE, 1986). The sweeping efficiency is also referred to as Macroscopic Efficiency.

2.1.5 Capillary Number

In the displacement of a phase (i.e. oil) by another (i.e. brine) in the porous medium, the viscous forces must exceed the capillary forces acting on an oil blob trapped in the pore throat. The Capillary Number (N_c) represents the ratio of viscous to capillary forces. The most accepted expression of the Capillary Number that takes into consideration the wettability preference of the rock is showed in Equation 2.3 (SCHRAMM, 2000).

$$N_c = \frac{v\mu_w}{\gamma\cos(\theta)} \quad (2.3)$$

where N_c is the Capillary Number, v is the displacing fluid's velocity (flow rate divided by the effective area), μ_w is the displacing fluid's viscosity, γ is the interfacial tension between both fluids and θ is the three-phase contact angle measured through the fluid of higher density.

In section 2.2.2 it was discussed that, for an imbibition process, the capillary pressure increases as the saturation of the displaced phase increases because the fluid remains trapped in the smallest pores. In a similar fashion, for the commonly studied water-wet reservoirs, when oil is displaced by water it is removed from the largest pores first. As waterflooding proceeds oil remains in the smallest pores which offer more resistance by the increase in capillary pressure. The oil that cannot be removed from the pores by water injection under normal pressure gradient conditions is called residual oil. The residual oil saturation is the fraction of the pore volume that remains trapped in the pores by the action of capillarity after sweeping the pore volume with water (DONALDSON; CHILINGARIAN; YEN, 1989).

When the oil saturation approaches to the residual value, the capillary forces increase over the oil blobs trapped in the smaller pores. The Capillary Number represents this demand in a quantitative way. The capillary desaturation curve represents the Capillary Number required to obtain different values of residual oil saturation. An example of this type of curve is showed in Figure 2.4.

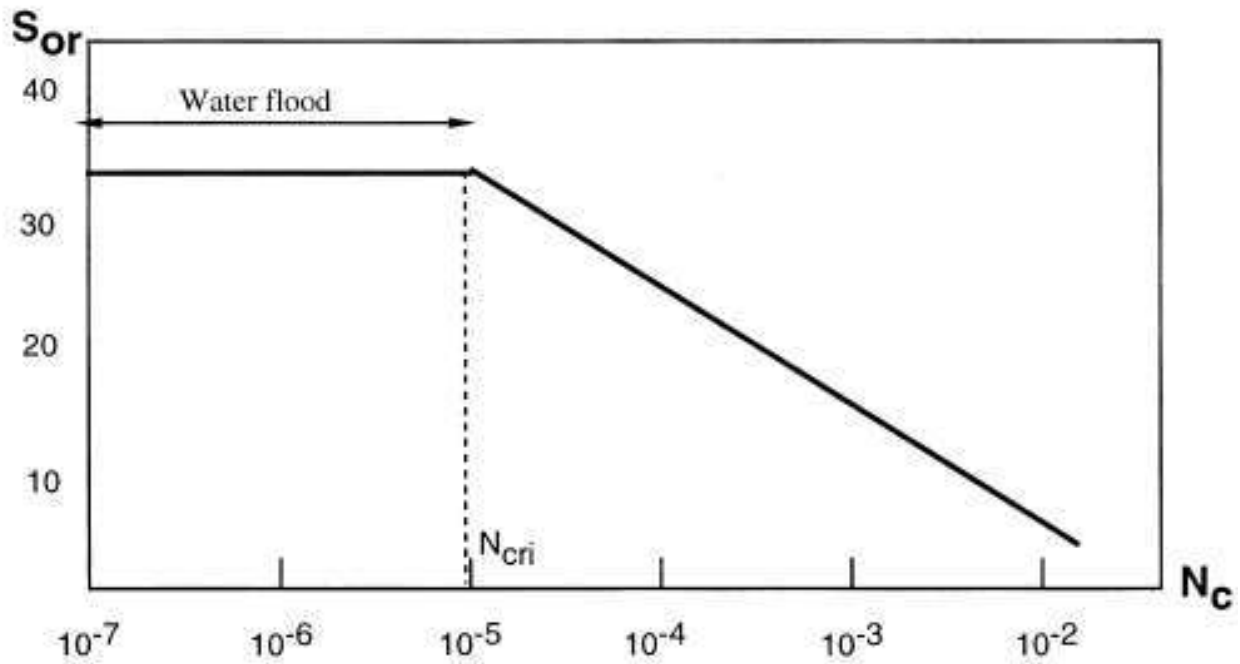


Figure 2.4. Capillary desaturation curve for a water-wet rock (SCHRAMM, 2000).

The plot shows that there is a critical value of the Capillary Number up to which the residual oil saturation remains unaffected. In another words, once the system achieved the residual oil saturation, the Capillary Number must be increased above this critical value to displace any additional oil. Typical values of N_c after waterflooding are in the range of 10^{-7} to 10^{-5} , and a reasonable range for the critical N_c is 10^{-5} to 10^{-4} . In addition, to reduce the residual oil saturation considerably, an N_c in de order of 10^{-2} may be required. This means that, to increase the amount of oil produced after the residual oil saturation was reached, an increase of 10^3 to 10^4 times in the N_c may be required (SCHRAMM, 2000).

The displacement efficiency considers the production of oil from the reduction in the residual oil saturation associated to changes in the magnitude of capillary forces (SHENG, 2010). It is often referred to as Microscopic Efficiency because it is related to the acting forces at the pore scale.

The Recovery Efficiency (or total efficiency) is the product of both Macroscopic and Microscopic Efficiencies. Consequently, both efficiencies need to be considered when designing a recovery strategy. If the Macroscopic Efficiency is poor, the injected fluid will bypass most of the oil. However, the operation achieves saturations close to residual, additional production requires an increase of the Microscopic Efficiency.

To sum up, the objective of Enhanced Oil Recovery is to improve the production of oil by increasing the Macroscopic and the Microscopic Efficiencies. Most of the times, combined EOR techniques are applied to improve both efficiencies simultaneously. In the next section, the different techniques of EOR will be briefly described focusing on the way they act to improve the Recovery Efficiency.

2.1.6 CO₂ flooding

Miscible methods consist in the injection of substances, usually called “solvents”, that are partially or totally miscible with the oil in the reservoir. The dissolution of the injected substance in the oil increases its mobility improving the sweeping efficiency. The main mechanisms attributed to these effects are summarized here from a previous publication (HOLM, 1982).

- Oil swelling: The increase of the formation volume factor, which represents the volume of a unit mass of live oil at reservoir conditions over its volume at standard conditions, is a direct consequence of CO₂ dissolution. It increases the oil saturation increasing, as discussed in Section 2.2.3, the relative permeability of oil. This clearly increases the mobility of the oil phase.
- Viscosity reduction: The increase of CO₂ concentration in the oil phase reduces its viscosity. Thus, the mobility ratio is reduced and the sweeping efficiency is improved.
- Solution gas drive: The volume of dissolved gas increases, acting in the primary recovery mechanism of solution gas drive described elsewhere (AHMED, 2010).
- Miscibility effects: The mass transfer between the oil and gas phases decreases the capillary effects until a single-phase is formed and the interface is vanished. In addition, the mobility of the oil phase is increased. These effect impact on both the Microscopic and Macroscopic efficiencies.

The contribution of each mechanism depends on several factors such as the composition of the oil and solvent injected, the thermodynamic conditions and the volume of the injected slug. Nonetheless, these mechanisms are expected to occur, at certain degree, for CO₂ injection under conventional reservoir conditions. At Pre-Salt reservoir conditions, the CO₂ is in supercritical state; thus, its physical properties and interaction

with the reservoir fluids could affect the mechanisms described in the previous paragraph, particularly regarding the swelling of the oil phase.

Different types of solvents have been applied, such as, fractions of the oil (i.e. LPG), natural gas, CO₂ and nitrogen. For the last years, CO₂ flooding has gained more interest due to the properties and relative low cost of CO₂ and the environmental advantages of avoiding the emission of this gas.

Miscibility, which can be achieved in single or multiple contacts, is a key factor for these methods. It can be achieved by vaporization of the light components of the oil in the gas, condensation of the gas to the oil phase or a combination of both. The thermodynamic conditions (minimum miscibility pressure or MMP) and composition of the injected gas (minimum miscibility enrichment or MME) are fundamental to assure that total miscibility will be achieved and that a single phase will be formed. Miscible displacement results in higher recovery efficiencies (HOLM, 1982).

The application of Miscible methods consists in the injection of slugs of gas. Typically, the volume of the slugs is a fraction of the pore volume that will be attained. Since the viscosity of the injected gas is lower than the viscosity of oil, the Mobility ratio is not favorable for effective sweeping. To correct the Mobility ratio, gas slugs are typically injected alternated with water slugs in a process called Water Alternated with Gas (WAG). The gas slug solubilizes with the oil facilitating its mobility and the water slug corrects the frontal advance. Consequently, this process has the same benefits than gas flooding and an improved sweeping efficiency. A scheme of the application of WAG is showed in Figure 2.5.

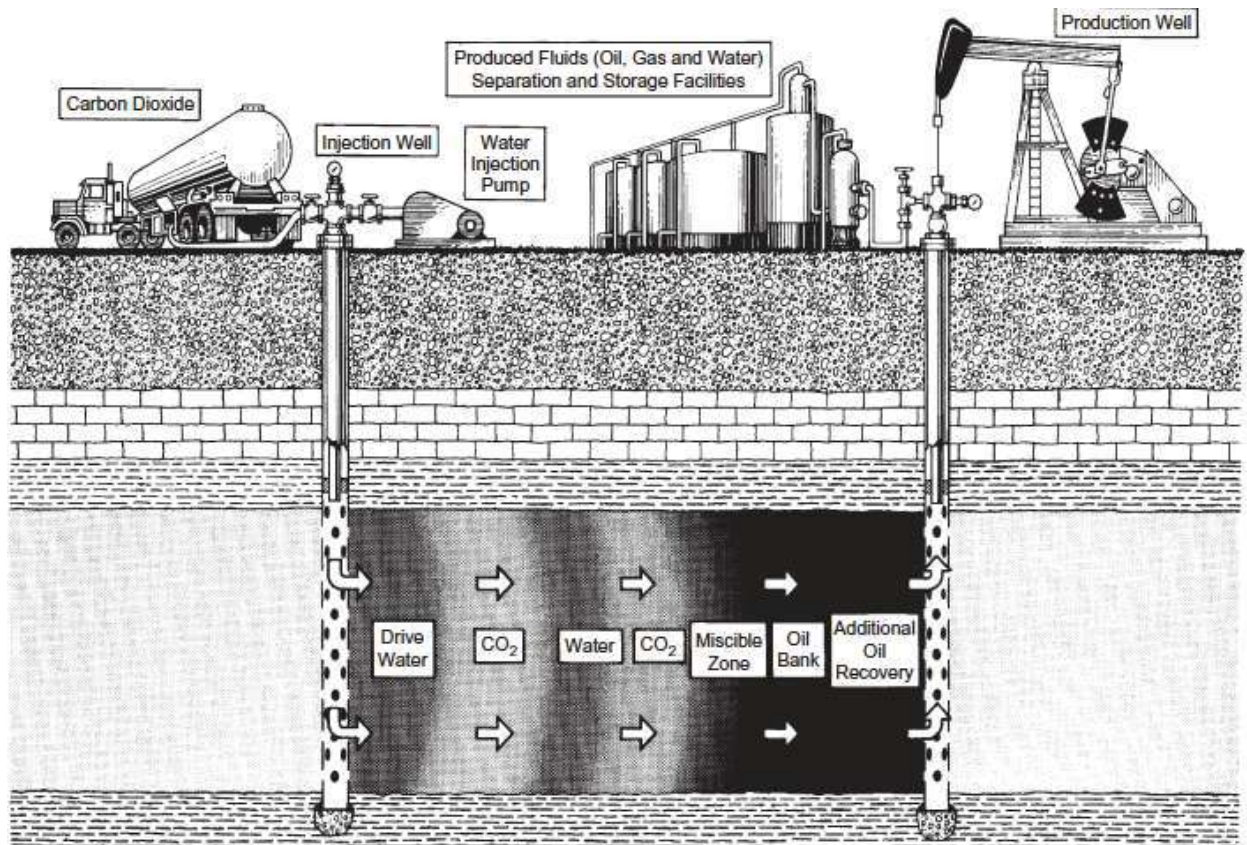


Figure 2.5. Scheme of the application of a WAG process (SHENG, 2013).

2.2 Interfacial tension

2.2.1 Theory

The molecules in the bulk of a liquid have lower potential energy than the molecules of the same liquid located at the interface with another fluid. The reason for this is that the intermolecular forces between the similar (and more closely located) molecules in the bulk are greater than those between molecules of two different fluids with different chemical natures. As a result, to bring a molecule from the bulk to the surface, its potential energy must be increased, so potential work must be applied on the system. The interfacial tension is the amount of energy required to increase the surface of the fluid a unit area (ROSEN; KUNJAPPU, 2012).

This concept, exemplified by Rosen and Kunjappu (2012), will be described as follows. The interface between two liquids “a” and “b” is shown in Figure 2.6. The interaction energy between the molecules of the liquid “a” and the adjacent molecules of the same liquid is represented by A_{aa} . Similarly, the interaction energy of “a” molecules

at the interface with the “b” molecules on the other side of the interface is A_{ab} , and the interaction energy between “b” molecules is A_{bb} . The molecules in the bulk interact only with molecules of the same species nearby. In contrast, the molecules at the interface interact with molecules of both species at the different sides of the interface. Thus, the difference in potential energy between the molecules of liquid “a” at the interface and the molecules of the same liquid at the bulk is $(A_{aa}-A_{bb})$. Analogously, the difference in potential energy between “b” molecules at the interface and similar molecules in the bulk is $(A_{bb}-A_{ab})$. If the energy per unit area is γ , the total energy difference per unit area between molecules at the interface and molecules in the bulk the sum of these interactions for both “a” and “b” molecules, as showed in Equation 2.4.

$$\gamma = \gamma_{aa} + \gamma_{bb} - 2\gamma_{ab} \quad (2.4)$$

where γ_{ii} represents the energy interaction per unit area between molecules of “i” species.

The value of γ showed in Equation 2.4 corresponds to the interfacial tension between the fluids “a” and “b”. It should be noted that the interfacial interactions between each type of molecules per unit area is greater for similar types of molecules. Then, γ_{aa} and γ_{bb} are expected to be greater than γ_{ab} , which depends on the similarity of the chemical nature between “a” and “b” that will determinate the strength of the intermolecular forces between both species. As a result, the more similar the liquids (for example water and a short-chain alcohol which are both small molecules with –OH groups), the greater the value of γ_{ab} and the lower the interfacial tension between the fluids. Nevertheless, if both liquids are very different in nature, such as water and a long chain non-polar alkane, the interfacial tension between the fluids will be greater.

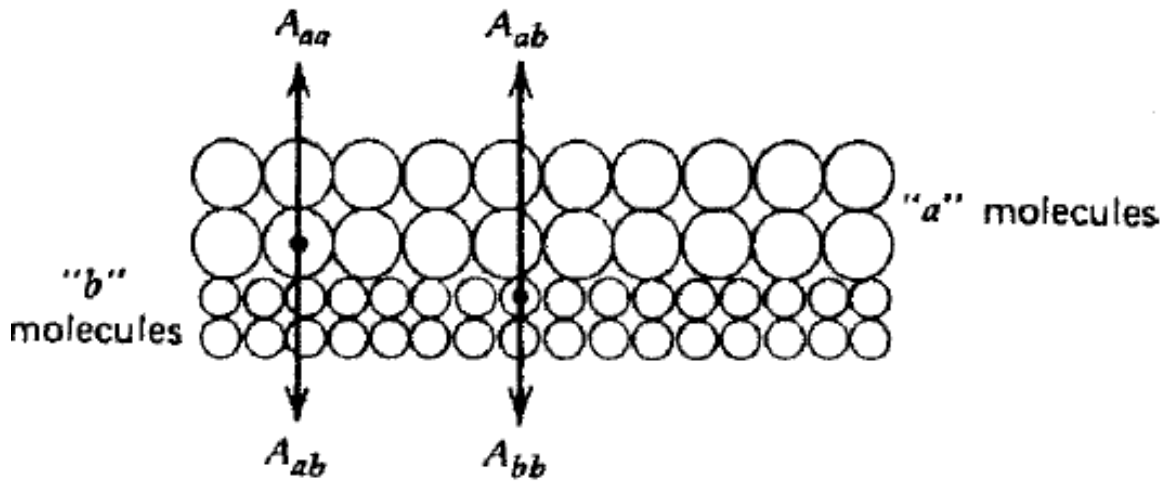


Figure 2.6. Representation of bulk and interfacial molecules for two liquids in contact (ROSEN; KUNJAPPU, 2012).

The surface tension is also referred to as the force applied on a surface per unit length. To explain the physical meaning of this definition, an example from the literature (BUTT; GRAF; KAPPL, 2006) will be reviewed. Let us assume that there is a frame with a mobile side over which a film of a liquid of surface tension γ is spread as showed in Figure 2.7. If the mobile side is displaced a distance dx , the area of the surface liquid film will be increased by $dA = 2b dx$ (since the film has two surfaces). According to the previous discussion, work (dW) must be applied on the system to achieve this, and the proportionality constant between the work applied and the increment of area is the surface tension.

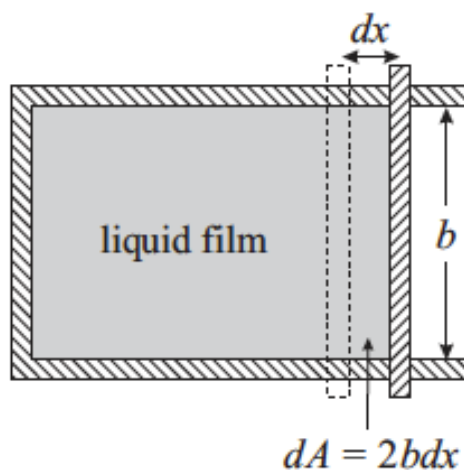


Figure 2.7. Experiment showing the physical meaning of the surface tension (BUTT; GRAF; KAPPL, 2006).

From this example, it is evident that a force F is needed to keep the loose side from retracting back to minimize the exposed area of the film. Since the work equals the force times the displacement distance, it follows that:

$$dW = \gamma dA$$

$$F = -\frac{dW}{dx} = -2\gamma b$$

$$\gamma = -\frac{F}{2b} \quad (2.5)$$

It should be noted that in Equation 2.5, the negative sign represents that the applied force has the opposite direction than the interfacial tension, which tends to minimize the exposed area. In addition, the factor of two in the denominator results from the fact that the liquid film has two surfaces.

The terms surface and interfacial tension have been widely used to refer to the physical property described before. However, to distinguish the different types of systems, the term surface tension is commonly used for systems where one of the phases is a gas and the term interfacial tension refers to interfaces between two non-gaseous phases (SHAW, 1992).

2.2.2 Relevance for Reservoir Engineering

The interfacial tension is one of the most important parameters for Reservoir Engineering and Enhanced Oil Recovery since it affects the magnitude of the capillary forces into the pores as reviewed in Section 2.1.2. The capillary pressure increases as the interfacial tension increases, as shown in the Young-Laplace Equation (Equation 2.1). This means that, the higher the interfacial tension between the fluids, the larger the pressure requirement the driving fluid must overcome to displace the fluid that is trapped in the pores. Thus, when the interfacial tension between the reservoir oil and the formation brine is large, it is a greater challenge to remove the oil by injecting a fluid to promote immiscible displacement.

This effect is implied in the definition of the Capillary Number shown in Equation 2.3. For larger values of the interfacial tension, the Capillary Number is reduced

showing that capillary forces overcome viscous forces. It is clear that this situation is unfavorable for the displacement of oil. Thus, the EOR techniques that improve the Capillary Number seek to increase it above a critical number by reducing the interfacial tension between the oil and the brine phases.

To conclude, when a reservoir has achieved its residual oil saturation after being efficiently swept by the displacing fluid, the removal of the residual oil only occurs if the Capillary Number exceeds a critical value. In other words, the action of the capillary forces must be diminished to reduce the residual oil saturation. Then, the interfacial tension plays a major role in determining the fluid distribution in the pores and the pressure requirement as a function of saturation.

2.2.3 Measurement

Several methods to measure the surface and interfacial tension were developed. The discussion in this text will only include the Drop Shape Analysis (DSA) technique, which is the method that will be used in this work. A description of the other methods commonly used (such as the du Noüy ring, the Wilhemy plate, the capillary rise, drop weight, oscillating jet and the spinning drop methods) can be found elsewhere (HIEMENZ; RAJAGOPALAN, 1997; SHAW, 1992).

The measurement of the surface or interfacial tension by the analysis of the shape of sessile or pendant drops is based on the balance between the interfacial tension and the gravity forces. The former induce the drop to a spherical shape to minimize its surface area, thus, minimizing the surface energy. In contrast, the latter tend to stretch the droplet, flattening its interface and increasing its surface area.

Bashforth and Adams (1883) solved the equations that result from the expression of the pressure difference at a point on the interface of the drop considering the interfacial and gravity forces. Yakhshi-Tafti et al. (2011) described this derivation and the method used for its resolution. The original publication and the steps to reach the equation that describes the profile of the drop are available in the literature (BASHFORTH; ADAMS, 1883; YAKHSHI-TAFTI; KUMAR; CHO, 2011). To illustrate the physical balance involved in the measurement of the interfacial tension using the DSA technique, the mathematical derivation of the differential equation to be solved in this method (Equation 2.6) to obtain the profile of the pendant drop is covered in Appendix A.

$$\frac{d^2z}{dx^2} + \left[1 + \left(\frac{dz}{dx} \right)^2 \right] \frac{1}{x} \frac{dz}{dx} = (2 + \beta z) \left[1 + \left(\frac{dz}{dx} \right)^2 \right]^{3/2} \quad (2.6)$$

$$\beta = \frac{\Delta\rho g b^2}{\gamma} \quad (2.7)$$

where β is defined in Equation 2.7, x and z are the axis coordinates of the drop profile, $\Delta\rho$ is the density difference between the fluids, g is the acceleration of gravity, b is the radius of curvature at the apex of the drop and γ is the interfacial tension. The parameter β represents the ratio between gravity and interfacial tension forces, and it corresponds to the Bond Number using a b as a characteristic length.

Bashforth and Adams solved this equation by relating the coordinates of the profiles (x and z) to the angle ϕ for systems with different Bond Numbers (β) in the range from 0,125 to 100. To obtain the Bond Number, the density of both phases and the interfacial tension between them must be known. Furthermore, the radius of curvature at the apex (b) must be obtained using geometric relations from the coordinates of the profile of the drop. They compiled and published these results as sets of that relate the angle ϕ to the dimensionless coordinates x/b and z/b for different Bond Numbers. Posterior research (PADDAY; PITT, 1972) updated this work by using computer solutions and increasing this compilation. From these tables, a drop profile can be drawn and linked to a specific Bond Number. It should be remarked that, as showed in Equation 2.6, the drop profile depends solely on the Bond Number.

Since the Bond Number determines the drop profile, if an image of the profile of a real drop is acquired it could be compared to the profiles that were published to identify which one of them best fits the profile of the real drop. Consequently, the Bond Number and the radius of curvature associated to that profile are obtained. If the density difference is known, the interfacial tension between both phases can be calculated from Equation 2.7.

Another consideration that should be introduced is that for low values of the Bond Number, the interfacial tension dominates the shape of the drop over the body forces. In fact, the spherical profile corresponds to a density difference of zero that means no action of the buoyant forces.

Andreas, Hauser and Tucker (1938) proposed a different approach to calculate the interfacial tension between two fluids from the graphical analysis of their profiles on

images taken experimentally. They used different geometrical measurements, as showed in Figure 2.8, to calculate dimensionless parameters that were used to relate the drop profile to the interfacial tension. The length identified as d_e is the diameter of the drop at the plane of its equator, which corresponds to the maximum diameter. The value of d_s is the diameter of the drop measured at a vertical distance from the apex equal to d_e . The reason to use these parameters is that both of them could be calculated in a simple and objective way from the analysis of the images of the profiles without the use of computational systems.

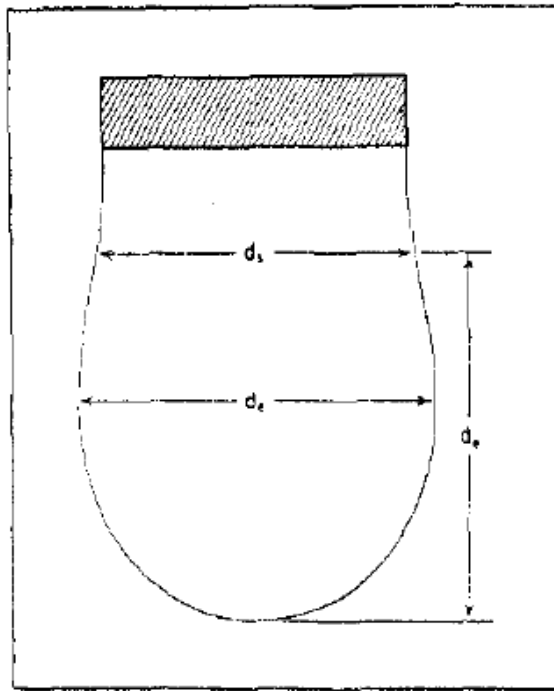


Figure 2.8. Geometrical analysis of the drop profile used the method of the selected plane (ANDREAS; HAUSER; TUCKER, 1937).

The authors presented a tabular relation between dimensionless numbers that contained d_e and d_s from the analysis of the profiles of water droplets formed in air at 25 °C, a system that has a surface tension of 72.0 dyn/cm. For systems of unknown interfacial tension, images of a droplet could be acquired allowing the measurement of d_e and d_s . The interfacial tension was obtained from and the tables published by the authors (ANDREAS; HAUSER; TUCKER, 1937).

The advance of computerized systems allowed the resolution of numerical methods using powerful tools that were not available when the DSA technique was introduced. The images obtained by cameras have increased their quality significantly. In

addition, there are programs that analyze these images digitally identifying the drop profile based on the contrast obtained by the two phases and the line that delimits the interface. The algorithm in these programs identifies the profile of the drop and finds the solution of Equation 11 that best fits it. Using a numerical method the program calculates the value of the interfacial that minimizes the error between the measured and the theoretical (also called laplacian) profiles. Usually, an objective function to measure the distance between both profiles is defined. Saad *et al.* (2010) discussed in detail the determination of the best fit for the drop profile using an objective function that is the sum of the squares of the distance between the experimental and the calculated curves.

There has been concern about the range of validity of the DSA technique to calculate accurate results for the interfacial tension. When the interfacial tension forces dominate over the gravitational forces, the drop will be spherical and the variations of the interfacial tension will not affect the drop of the profile significantly (SAAD *et al.*, 2010). In contrast, for well-deformed drops, small changes in the interfacial tension will modify the shape of the drop dramatically. Thus, spherical drops should be avoided to obtain interfacial tension measurements with an adequate sensitivity (HOORFAR; KURZ; NEUMANN, 2005).

The approach used to identify the droplets that allow an accurate calculation of the interfacial tension consists in the definition of a shape parameter that measures the deformation of a drop profile when compared to a spherical profile. The simplest definition for this parameter consisted of the difference in area between the projection of the drop profile and a circle of the radius equal to the radius of curvature at the apex on the numerator and the projected area of the drop on the denominator. Saad *et al.* (2010) reported that there is a critical value above which the error of the measurement by the DSA technique is lower than 0.1 mN/m. In addition, they found that this critical value does not depend on the Bond Number. It is sensible to compare the area of the drop to the area of a circle; however, the authors explained some drawbacks of this definition of the shape parameter. First, the circle of radius equal to the radius of curvature at the apex is not necessarily the best fit for the drop profile. This represents that a circle of a different radius could have a profile more similar to that of the drop if overlapped correctly. In addition, they reported that when the volume of the drop is very small, the shape parameters obtained were excessively large. Finally, the fact that the critical value of the

shape parameter does not depend on the Bond Number is against the physics that govern this phenomenon.

To address these difficulties, the authors proposed a new definition of the shape parameter that compares the profile of the drop with the best-fit circle, independently of its radius. They used an algebraic method to find the best-fit circle that minimizes the sum of the distances with the real profile for a specific number of points. The shape factor is defined as the sum of the distances between the real profile and the fitted circle for the n considered points divided by the radius of the needle used to generate the drop.

The radius of curvature at the apex defines the shape of the drop. Moreover, this radius of curvature is a function of two dimensionless numbers: the Bond Number (B_o) and the dimensionless drop volume (V_d) (SAAD et al., 2010). The authors adapted these dimensionless parameters using the diameter of the needle used to form the drop (R_n) as the characteristic length as shown in Equations 2.8 and 2.9.

$$B_o = \frac{\Delta\rho g R_n^2}{\gamma} \quad (2.8) \quad V_d = V/R_n^3 \quad (2.9)$$

where $\Delta\rho$ is the density difference between the fluids, g is the acceleration of gravity, R_n is the radius of curvature at the apex of the drop, γ is the interfacial tension and V is de drop volume.

The authors used these numbers to develop a map that shows the drop profiles and the best-fit circles for different systems where the radius of the needle (R_n), the interfacial tension (γ) and the Bond Number (B_o) are defined. They used the axisymmetric liquid fluid interface (ALFI) program (DEL RÍO; NEUMANN, 1997) to determine the Laplacian profiles of the drops for each set of values. They concluded that, even if the independent γ and R_n values are different, droplets with similar B_o and V_d values result in measurements with comparable sensitivity. The technique performed best for droplets that differ from the spherical shape (greater B_o and V_d).

Critical values of the shape parameters can be found for certain values of the Bond Number that correspond to the conditions used in the experiments. These critical values correspond to the minimum dimensionless volume that the drop must have to achieve a well-deformed profile that is distant to the best-fit circle. The DSA technique offers a poor sensitivity when the Bond Number tends to zero because the interfacial tension forces overcome the gravity forces, and the slight changes in the interfacial

tension will not affect the profile of the drop. Moreover, very small drops should always be avoided because, even for large Bond Numbers, they result in profiles with low deformation compromising the accuracy of the measurements.

Berry et al. analyzed the factors that affect the accuracy of the measurements of the surface tension between water and air using the DSA technique. They proposed the application of a different dimensionless number that represents the volume of the drop divided by the theoretical maximum volume that can be formed with the capillary in use. They defined it as the Worthington Number (W_o) and derived its expression as shown in Equation 2.10. In this expression, the Worthington Number is equivalent to the Bond Number considering a characteristic length equal to $(V/\pi D_n)^{0.5}$ where V is the drop volume and D_n is the diameter of the needle.

$$W_o = \frac{\Delta\rho gV}{\gamma D_n} \quad (2.10)$$

The reader should note that while V_d and W_o represent a similar ratio of volumes, the former does not account for drop deformation due to gravity forces. On the other hand, W_o considers the effect of both gravity and interfacial forces. The Worthington Number ranges from 0.1 to 1. The authors concluded that higher values of this number are associated with measurements with higher precision. Nevertheless, no such studies regarding reliability of the DSA measurements for the interfacial tension between liquid hydrocarbons and water are present in the literature.

2.3 Wettability

2.3.1 Physical description

The term wettability represents the attraction or repulsion of a fluid to a porous medium in the presence of other immiscible fluids. This difference between the attractive / repulsive forces determines the way fluids will distribute in the porous medium. So, the fluid with greater attractive interactions with the rock will maximize the contact between these two phases. On the other hand, the fluid with the greatest repulsion will minimize the contact with the rock (HONARPOUR; KOEDERITZ; HARVEY, 1986).

When two immiscible fluids saturate a porous medium, the tendency to adhere or spread on the solid's surface that each fluid presents is determined by the wettability. This

leads to four different states of wettability for a solid surface (DONALDSON; ALAM, 2008):

a) Water - wet

The system is considered water-wet when most of its surface is covered by water. Since the porous medium has greater affinity towards water, this phase will locate on the smaller pores maximizing its contact with the solid. Therefore, water forms a film that extends throughout the pore volume as a continuous phase. In contrast, oil remains as globules forming a discontinuous phase in the biggest pores surrounded by the water films.

This tendency remains even at extreme conditions, such as when water saturation is decreased to the irreducible value (connate water saturation). However, when this is the case, oil saturation is high enough to also form a continuous phase. Due to its tendency to wet the rock, water will spontaneously imbibe the rock displacing some of the oil located in the pore volume. As the water saturation increases, the oil phase will again become discontinuous forming blobs immersed in the water phase.

The spontaneous imbibition of the water phase will continue until the surface and capillary forces are balanced. At this point, a pressure differential must be supplied in order to increase the water saturation in the porous medium.

On the other hand, if the rock is saturated with water, oil will not enter the pore volume spontaneously. A displacement pressure is needed to force the non-wetting phase into the porous medium. This process, in which the saturation of the wetting phase is reduced, is called drainage.

b) Fractionally-wet

These systems are defined as heterogeneous porous media with scattered regions of varying wettability. This is mainly attributed to the uneven distribution of minerals with different chemical properties on the rock's surface (BROWN; FATT, 1956).

c) Mixed-wet

In these systems water wets the small pores and oil preferentially contacts the rock matrix in the bigger pores. The main reason for this is the presence of surface active agents in the oil which may have adsorbed in the rock's surface gradually changed its wettability with time after the oil has migrated to the reservoir rock and located in the biggest pores.

These systems have been associated with low residual oil saturations due to the formation of continuous oil paths through the larger pores that promote the flow of oil through the porous medium (SALATHIEL, 1973).

d) Oil-wet

This condition represents the opposite distribution of the fluids in the formation rock. Thus, in oil-wet systems water locates in the center of the bigger pores surrounded by a film of oil. In addition, the smaller pores are filled with oil, which forms a continuous phase throughout the formation.

As a result, water will only form a continuous phase for very high saturations. If oil is injected, reducing the water saturation to lower levels, this continuity will be lost, and water will remain as drops (or blobs) inside the oil phase. On the other hand, oil will typically form a continuous phase for any saturation value greater than the residual oil saturation.

In contrast to the displacement described for water-wet systems, in an oil-wet system water will not imbibe the porous media spontaneously. To force water into the oil-saturated rock, a pressure difference must be applied. However, oil will go under spontaneous imbibition due to its greater tendency to contact the rock surface and to saturate the porous medium.

The two most typical types of rock found in oil reservoirs are sandstones and carbonates. General knowledge considers sandstones as water-wet systems with different degrees of wettability (neutral or strongly water-wet). On the other hand, carbonates are acknowledged as neutral to oil-wet systems. However, the contact with the formation fluids may result in the adsorption of surface-active species that change rock's wettability. For instance, many oil-wet sandstone systems were reported in the United States (KATZ, 1942; MARSDEN; KHAN, 1962; NUTTING, 1934). This discussion will be continued in more detail in the next chapter.

When a drop of a liquid contacts a solid surface surrounded by an outer fluid, the drop will spread on the surface to certain degree determined by the balance between adhesion and fluid-fluid interfacial tension forces. The contact angle is defined as the angle between the line tangent to the solid surface and the tangent to the drop profile at the three-phase contact. It is usually measured towards the liquid of higher density, as shown in Figure 2.9, and it gives information about the wettability of the solid by each

fluid phase. For extreme cases, if the drop wets the surface completely the contact angle is 0° , but if the outer fluid wets the surface completely, the angle is 180° . It is generally accepted that when the contact angle (measured towards the denser phase) is lower than 90° , the denser phase wets the surface (AHMED, 2010). On the other hand, when the contact angle is greater than 90° , the lighter phase wets the surface preferentially. For applications in oil-brine-rock systems, contact angles measured towards the brine lower than 90° are associated with water-wet (hydrophilic) rocks and positive the capillary pressure. For neutral wettability the contact angle is close to 90° and the capillary pressure is approximately zero. Finally, for oil-wet systems the contact angle is greater than 90° (DONALDSON; ALAM, 2008). Nevertheless, as it will be discussed in the following sections, the reservoir rock and fluids are complex systems, so wettability is more frequently associated to trends in the contact angle more than to these exact values (i.e. the neutral-wet behavior could be accepted to values between 70° and 110° the lower indicating more tendency towards water-wet).

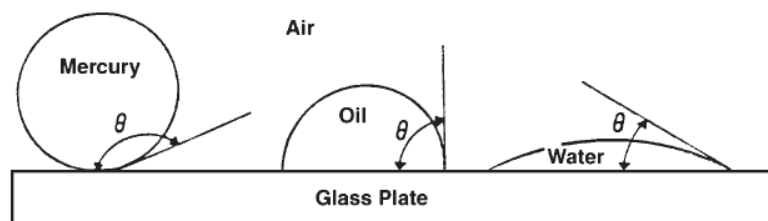


Figure 2.9. Contact angle for different wetting tendencies (AHMED, 2010).

Lowell and Shields described the three forces acting on the interfaces when a water drop is resting on a solid surface surrounded by oil. The oil-water interfacial tension acts in the direction tangent to the oil-water interface, and its horizontal component pulls the circumference (projection of the contact surface) towards the center. In addition, the water-solid interfacial tension, which acts on the interface between these two phases, also pulls the contact towards in the inward direction. To balance these forces, the oil-solid interfacial tension pulls the circumference away from its center. These forces applied on a drop of water deposited on a solid when oil is the external fluid are represented in Figure 2.10 (LOWELL; SHIELDS, 1981).

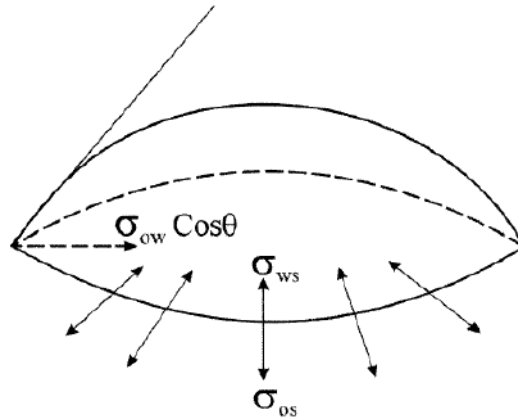


Figure 2.10. Forces acting on the interfaces of drop of water resting on a solid surrounded by oil (DONALDSON; ALAM, 2008).

Young (1855) developed an equation that relates the forces acting on the droplet in the system showed in Figure 4. This equation, which is a function of the different interfacial tensions and the contact angle, is presented in Equation 2.11 (YOUNG, 1855).

$$\gamma_{os} - \gamma_{ws} = \gamma_{ow} \cos(\theta) \quad (2.11)$$

In this equation, γ represents the interfacial tension and θ represents the contact angle. The subscripts o, w and s represent the different phases: oil, water and solid respectively. Later research by Gibbs introduced the effect of the spreading of each phase on the solid surface obtaining a more general form called the Gibbs-Young Equation (showed in Equation 2.12):

$$\cos(q) = \frac{E_{ws} - E_{os}}{g_{ow}} \quad (2.12)$$

The E terms are the derived free energies, which are calculated by subtracting the interfacial tension between the solid and the water (to calculate E_{ws}) or oil (to calculate E_{os}) to the surface free energy of the solid in vacuum (GIBBS, 1948).

The hysteresis of the contact angle was introduced using the following experiment: a drop of oil surrounded by water was located between two solid plates; then, one of the plates was moved in the parallel direction towards the other as shown in Figure 2.11:

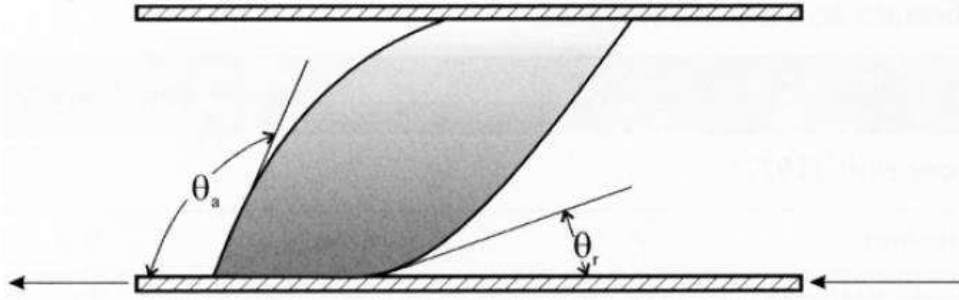


Figure 2.11. Scheme of the experiment by Leach et al. (1962) to study the advancing and receding contact angles (DONALDSON; ALAM, 2008).

Due to the movement of the bottom plate, the oil droplet was forced to advance with respect to the water on the front side. At the same time, the drop was allowed recede to (or was advanced by) the water on the back side. Leach *et al.* measured both the advancing and receding contact angles with time, reaching the stabilization time between 1 or 2 days. The values obtained for both angles, as indicated qualitatively in Figure 2.11, were different for each system (LEACH et al., 1962).

The different values between the advancing and receding contact angles can be as high as 75° (DONALDSON; ALAM, 2008). It is accepted that this difference is one of the causes of the hysteresis observed in the capillary pressure curves. A reason for this is that the aging changes the wettability according to which phase contacted the porous medium first. Thus, the forces acting on the interfaces are different depending on which phase saturated the porous medium first and which phase invaded the porous medium afterwards. Therefore, the existence of an advancing and a receding contact angle is a very important factor when determining the wettability of a system for a specific set of rock and fluids and a defined displacement process. The hysteresis showed by the contact angle is particularly relevant when analyzing the changes in wettability due to the flow of different fluids in the porous medium. In this case, water advancing should be considered as the best representation of the imbibition process.

Another factor that determines the wettability of a system is the history of saturation or aging time (i.e. time of contact with each phase). Treiber et al. (1972) determined that the equilibrium contact angle was a function of the composition of the oil phase because the asphaltene and surfactant type compounds may adsorb on the solid surface and produce a wettability change on the system with time. By calculating the equilibrium contact angle as a function of aging time for several reservoir systems, the

authors proved that aging up to certain time increases the oil-wet behavior. In some cases, the aging time needed was up to 60 days (DONALDSON; ALAM, 2008; TREIBER; OWENS, 1972).

2.3.2 Intermolecular interactions involved in the oil-water-rock system

Wettability is governed by surface interactions which consist in different types of intermolecular forces that can be either repulsive or attractive. The relative strength of each of these forces will determine the tendency of the rock surface to be wet by the oil or water phase. This section will present a brief discussion about these interactions and its role in the wettability. It is not intended to be an extensive review containing a complete description of the phenomena nor the mathematical expressions that correspond to each of them. This type of review can be found elsewhere (ATKINS; DE PAULA, 2010; CASTELLAN, 1971; ISRAELACHVILI, 2015; STEPHANOS; ADDISON, 2017; STONE, 2013).

Two atoms that are located extremely far away do not interact with each other; thus, their energy is solely associated with the kinetic contribution from the movement of each atom. As they get closer to each other, an attractive force between them becomes relevant. The potential energy of the system now includes the energy of interaction between both elements. This means that to bring to particles together from infinite separation work must be applied to the system. The work applied corresponds to the potential of interaction between the elements. In addition, attractive forces are considered negative, and repulsive forces are positive. Since the potential of interaction is the integral of the force over the distance, negative potentials are associated with attractive interactions with decreasing absolute values with the separation distance. A characteristic plot of the interaction potential as a function of separation distance for two spherically symmetric atoms is shown in Figure 2.12. It can be observed that for large separations, the attractive forces bring the atoms together, as represented by the decrease of the interaction potential. This continues up to a critical separation (r_m) which corresponds to the minimum negative potential (or maximum absolute value). Any further approximation will result in vanishing attractive force and the appearance of short-range repulsive forces that raise the positive interaction potential to infinity. When molecules are brought close together, these repulsive forces avoid further approximation. An example of these

interactions is the lower compressibility of liquids and solids, in which molecules are closer to each other, compared to that of gases. In summary, the interaction is governed by long-range attractive forces and short-range repulsive forces.

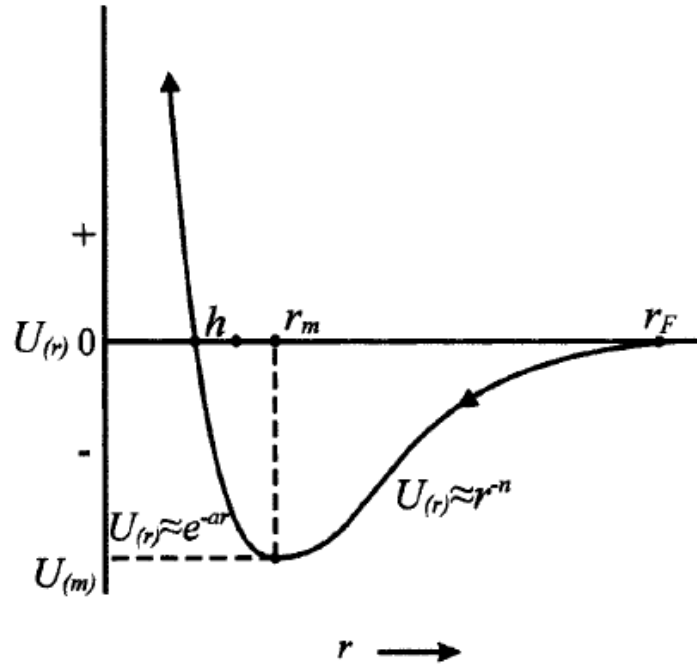


Figure 2.12. Model curve of the potential of interaction of two spherical atoms as a function of separation (BARTA, 2008).

Electrostatic interactions are the forces between charged elements that are the result of the electric field exerted by these elements. The magnitude of the force is proportional to the electric charges and inversely proportional to the dielectric constant of the medium and the the square of the separation between the elements as expressed by Coulomb's law (STEWART, 2001). For ionic elements, the charge absolute value corresponds to the valence (i.e. 1 for monovalent cations or anions) multiplied by the elementary charge of the electron e (1.602×10^{-19} C considering four significant figures). Obviously, the charge associated to anions is negative and to cations is positive. In addition, alike charges present repulsive forces, which result in positive free energy of interaction (in agreement with the convention presented in the previous paragraph). On the other hand, unlike charges exert attractive forces characterized by negative free energy of interaction (ISRAELACHVILI, 2015).

As discussed in the previous paragraph, the dielectric constant of the medium is important as it affects the electrostatic interaction between charged elements. In addition,

it determines the capability of a medium to dissolve species that contain net or induced charge (i.e. ions or polar compounds). Solvents with high dielectric constants tend to keep charged species in solution. The opposite behavior is expected for solvents with low dielectric constants. Some examples of dielectric constants of substances related to reservoir systems are: water (78.5), methanol (32.6), cyclohexane (2.00) at 25 °C (WEAST, 1968), n-hexane (1.88), n-decane (1.99) at 20°C (SCAIFE, 1972). Moreover, the presence of ions dissolved in an aqueous phase, for example in seawater or formation brine, reduce its dielectric constant. As a reference, values lower than 50 were reported for 6M solutions of NaCl at 21°C (GAVISH; PROMISLOW, 2016).

The intermolecular forces that have effect on the wettability are based on electrostatic interactions. Donaldson and Alam (2008) used the following classification based on the charge originating the interaction and the range of separation:

a) Short-range forces

The short-range forces correspond to separations below a nanometer lower than r_m , as indicated in Figure 2.8. As discussed before, as the particles approach at molecular level a repulsive effect is produced by the distortion of their electron clouds. This is due to Pauli Exclusion Principle as electrons with the same spin cannot occupy the same quantum space (i.e. the same orbital simultaneously) (TIPLER; LLEWELLYN, 2007). On the other hand, electrons with opposite spin can lead to attractive forces between the nuclei and the overlapped electron cloud due to the increased electron density. In this case, the short-range interactions analogously to the formation of covalent bonds (MAITLAND, 1981).

b) London dispersion forces

The dispersion forces are considered short-range and are present in all types of particles. However, they are the only intermolecular forces between large non-polar molecules (such as long-chain hydrocarbons). Although they are weaker than permanent dipole and hydrogen bonds, they play an important role in the physical behavior of non-polar substances. The origin of these forces is the instantaneous dipole moment that appears at a given time due to the charge distributions in the molecules caused by the oscillation of the negative charge around the positive charged nuclei. This momentary orientation of the instantaneous dipoles leads to an attractive interaction which results in a decrease of the molecule's energy (LONDON, 1937).

c) Dipole forces

When the dispersion of the electrons in the covalent bonds that hold the atoms in a molecule together are not symmetric, there is an uneven distribution of the charges resulting in a permanent dipole moment. The electrostatic interaction between the permanent dipoles, also called as Keesom forces, can result in attractive and repulsive forces. However, as discussed in the beginning of this section, the attractive interactions result in the lower (negative) potential; thus, the molecules orient for these interactions to prevail. The interaction energy is inversely proportional to the separation elevated to cube. Nevertheless, when the three dimensions are taken into account, the rotation of the dipoles and alternation between attractive and repulsive interactions has to be considered to calculate the averaged interaction energy (ISRAELACHVILI, 2015).

Dipoles can be induced in non-polar molecules by the action of permanent dipoles from surrounding polar molecules on their electron clouds. This happens when the electron cloud in a non-polar molecule is deformed by the action of electrostatic forces. The forces involved induced dipoles are also known as Debye forces. The degree at which dipoles can be induced in a non-polar molecule is called polarizability. For hydrocarbons, polarizability increases with the molecular weight (i.e. 4.48 \AA^3 for ethane and 11.78 \AA^3 for hexane) and is greater for small aliphatic hydrocarbons than for aromatics with the same number of carbons (9.87 \AA^3 for benzene) (BHAUMIK; JAFFÉ; MARK, 1982). Long-range molecules (London, Keensom and Debye) are commonly grouped into van der Waals forces. The three components of these forces are inversely proportional to the distance elevated at a power of 6.

d) Hydrogen bonds

Hydrogen bonds are a particular case of permanent dipoles as the small size of water molecules and the great electronegativity difference between oxygen and hydrogen makes these interactions stronger than other dipole forces but still weaker than covalent bonds. Water molecules interact among them and with other polar species, such as alcohols, through hydrogen bonding being the natural solvent for polar compounds. In addition, due to its high dielectric constant, water (as opposed to nonpolar substances) dissolves salts effectively.

The formation of hydrate complexes between water and charged surfaces by hydrogen bonding is responsible for hydration forces. Water adsorbs on the surface (or

ion) forming a film that can have several layers. As disruption of this film requires the distortion of the ordered water molecules, hydrated surfaces tend to exert repulsion among each other. In order to displace the water film, and increase the hydrophobicity of the surface, the energy of interaction of a solute must overcome the energy associated with the network of hydrogen bonds on the hydrated surface.

2.3.3 Electrostatic surface interactions

The electrons in the elements that compose a solid surface are not evenly distributed. For example, two different metals in contact will have a redistribution of their surface electrons resulting in a charge difference between them. Several factors can affect this charge, such as the presence of physically adsorbed species, dissolution of species from the surface, reactivity of the atoms on the solid with the aqueous phase and formation of chemical bonds between components in the solid and aqueous phases. When a liquid is in contact with the solid, there is a potential gradient in solid-liquid interfaces known as the electrical double layer, which is illustrated in Figure 2.13. At molecular distance, the charge is balanced by the Stern layer, in which counterions are strongly adsorbed forming an immobile layer where the potential gradient ($\psi_s - \psi_\zeta$) is linear. Between the Stern layer and the bulk of the aqueous phase, the potential decays exponentially in what is called “diffuse layer”. The thickness of the diffuse layer is called the Debye length, and it is greater for monovalent than for bivalent ions. In addition, the Debye length is inverse to the square root of the ionic concentration (RUSSEL et al., 1991). If the potential in the bulk aqueous phase (ψ_ω) is taken as zero, the potential at the Stern layer (ψ_ζ) is defined as “zeta potential” (DONALDSON; ALAM, 2008; HUNTER, 1988). The adsorption of ions and polar molecules by non-electrostatic interactions can cause the formation of an additional layer, the Helmholtz layer, formed by mobile charged species. The length of this layer depends on the molecular size of the adsorbed species (GRAHAME, 1947).

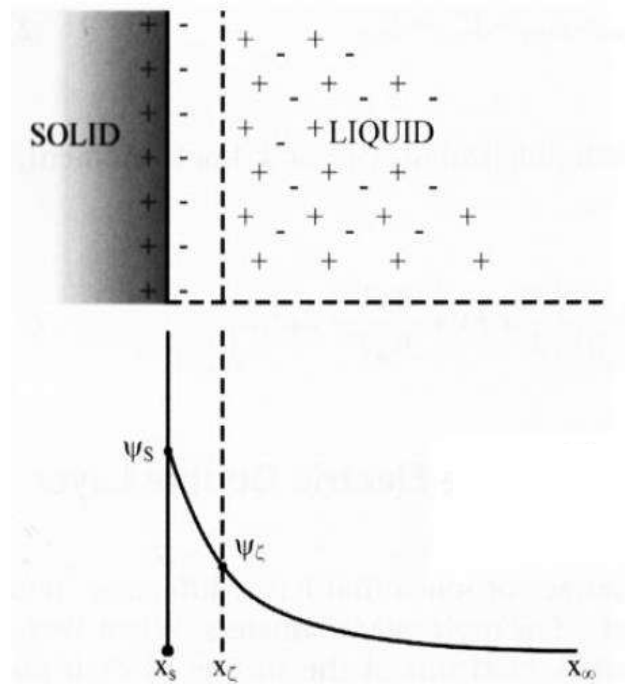


Figure 2.13. Scheme of the electrical double layer (DONALDSON; ALAM, 2008).

In aqueous solutions, pH affects the surface charge. Typically, lower pH induces positive charges due to the excess of H^+ species. On the other hand, basic solutions are more likely to result in negative charges induced by the higher concentration of OH^- . The point of zero charge (pzc) is the pH at which the zeta potential is zero. Another important definition is the isoelectric point (pI) which corresponds to the pH at which a molecule, atom or other species are electrically neutral or have their charges balanced. Due to the difference in the electronic configurations between silicon oxide and calcium carbonates, sandstones and carbonate reservoir rocks present great difference in isoelectric potential. Experimental works using brines with salinities up to 5M reported isoelectric points lower than 3 for sandstone rocks and higher than 9 for carbonate rocks (JAAFAR; NASIR; HAMID, 2014). These results indicate that, since the pH of formation brines of most reservoirs is between 5.5 and 7.5, sandstone rocks have negative charge and carbonates present positive charge at reservoir conditions.

The competition between the attractive van der Waals forces and the repulsive forces associated to the electrical double layer determines whether a particle will be stable in suspension or of coalescence will occur. This is the matter of the DLVO theory, which is named after its developers Derjaguin, Landau, Verwey and Overbeek (DERJAGUIN;

CHURAEV; MULLER, 1987; VERWEY; OVERBEEK; VAN NES, 1948). The theoretical concepts behind this theory are out of the scope of this text; thus, only a summary is included here. The reader can consult the cited references for a more detailed description.

Charged surface will be subject of repulsion that arises from the charge induced by the electrical double layer. However, species adsorbed on the surfaces and other molecules on the medium are subject to attractive van der Waals forces that are not dramatically dependent on the pH and the ionic force of the solvent. These interactions are represented in Figure 2.14. The solid curves show the isolated effects of one type of interactions in the absence of the others. For example, curve “1” is the pure repulsive electrostatic repulsions when no van der Waals forces are present. In contrast, curve “4” is the attractive van der Waals forces alone. The dashed curves represent the combined effect of both types of interactions. In curve “2”, the surface electrostatic repulsions are strong enough to avoid coalescence of the particles. The opposite case is showed in curve “3” where the attractive van der Waals forces overcome the double layer interactions resulting in further approximation that may lead to different particle association mechanisms.

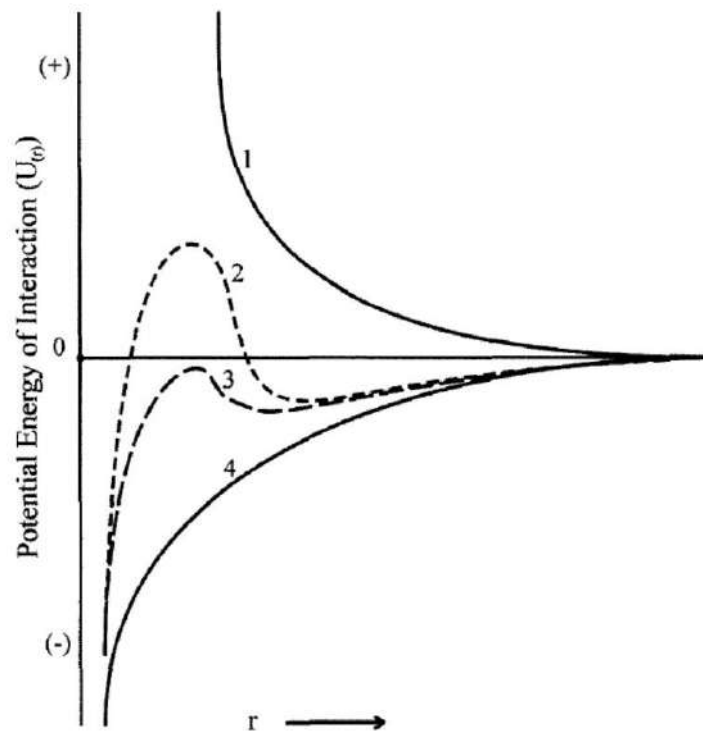


Figure 2.14. Scheme representing repulsive electrostatic interactions of the double layer and the attractive van der Waals interactions (DONALDSON; ALAM, 2008).

Although the DLVO was developed for colloidal stability, it considers phenomena relevant to wettability as under reservoir conditions, the rock-fluid and oil-brine interfaces have charges which are affected by the pH and the salinity of the aqueous phase. In addition, polar species such as asphaltenes interact with charged surfaces; also, nonpolar substances will be subject to van der Waals forces. However, concern regarding the applicability of the DLVO theory to complex electrolyte solutions with high salinity was raised (MANCIU; RUCKENSTEIN, 2001). In the presence of divalent ions (with monovalent counterions), the double layer repulsion is decreased by the adsorption of the divalent counterions (EDERTH; CLAESSON, 2000). This could even lead to surface charge reversal (SZILAGYI; SADEGHPOUR; BORKOVEC, 2012), indicating that repulsion could exist between surfaces which were originally oppositely charged. For high salinity brines composed of multivalent ions, non-DLVO effects affect the quantitative results of the theory (ISRAELACHVILI, 2015). An extended DLVO theory that accounts for ionic correlations and finite ionic radius improved the prediction of quantitative values (DANOV; BASHEVA; KRALCHEVSKY, 2016).

Hydration forces are also a cause of deviation from the predictions of the DLVO theory. At high electrolyte concentrations, the electrical double layer is compacted reducing the Debye length, thus reducing the separation that corresponds to the potential barrier. In this situation, hydrate forces, which act at separations in the order of nanometers, gain importance. In consequence, the effect of increasing electrolyte concentration is complex. At lower salinities, as the electrolyte concentration increases, the surface repulsion decreases due to the compression of the electrical double layer. At higher salinities, if hydration forces are high enough, the repulsion increases with increasing electrolyte concentration due to the repulsive effect of hydration forces. In this case, the repulsive forces undergo through a minimum as electrolyte concentration is increased (MANCIU; RUCKENSTEIN, 2001).

2.3.4 Acid-base interactions

Quartz is the main constituent of sandstone rocks. The surface of this mineral contains positive Si^+ and negative O^- sites balancing their charges. In the presence of water, silanol groups form by the adsorption of negative OH^- groups. Silanol is a weak acid that can release a proton giving the negative surface charge found for quartz at neutral

pH. Therefore, the surface of quartz is considered to be acidic in nature (CUIEC, 1975). This mechanism is summarized in the reactions below (Figure 2.15). The acidity of quartz was evidenced by showing that a base (oactadecylamine) was strongly adsorbed on a glass surface. Nevertheless, stearic acid showed little or no adsorption at all on the same surface (BLOCK; SIMMS, 1967). Other studies came to similar conclusion using pure quartz mineral (MCCAFFERY; MUNGAN, 1970).

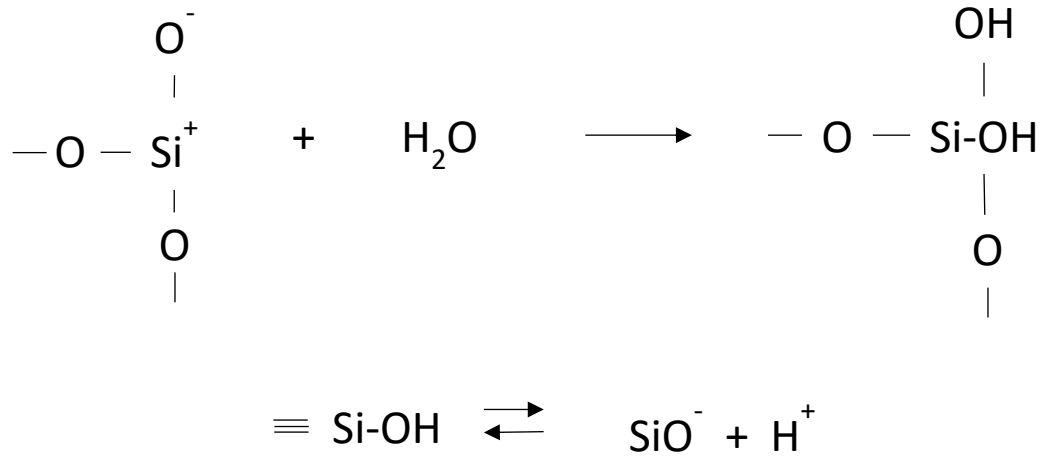


Figure 2.15. Reaction scheme for silica surface in contact with water.

The previous de discussion is relevant to wettability as basic compounds contained in the oil phase, typically nitrogen compounds such as quinolines (LOCHTE, 1952), can adsorb on quartz's surface altering its wettability. This was previously reported in the literature (GRETTIE; WILLIAMS, 1928). In contrast, organic acids in the oil will interact weakly with the acid sites on the surface.

On the other hand, the surface of carbonate rocks in contact with water has basic characteristics and interact with acid compounds in the oil phase, such as aliphatic and aromatic naphthenic acids (LOCHTE, 1952). Studies of steric acid adsorption on calcite were in agreement with this trend (MCCAFFERY; MUNGAN, 1970). Another study evaluated the chemical adsorption of acid compounds in the crude oil on the surface of calcium carbonate (LOWE; PHILLIPS; RIDDIFORD, 1973). The authors found that this process consists in the diffusion of surface-active acidic compounds in the oil to reach the rock surface. It can happen through the water phase in the case of an existent water layer on the rock's surface. However, the increase in salinity can affect this process reducing

the adsorbed mass. If the rock was previously immersed on purely paraffinic oil, the adsorption of acidic compounds on its surface is hindered.

Other work (MORROW; CRAM; MCCAFFERY, 1973) addressed the wettability alteration of dolomite using basic nitrogen and sulfur compounds and octanoic acid. For the basic compounds, low contact angles were obtained showing weak interactions between the base and the surface. In contrast, the presence of octanoic acid resulted in higher advancing contact angles of up to 155° . Strong wettability towards oil could only be assumed for angles greater than 140° , above which oil imbibed spontaneously in the dolomite packings. Nevertheless, interaction of dolomite with the organic acid was considered weak since rocks showing initial intermediate wettability would shift towards water-wet after immersion in formation brine.

These results indicate that acid compounds in crude oils could be adsorbed on basic sites on carbonate rock surfaces making it more oil-wet. In contrast, basic compounds in the crude interact with acid sites on sandstone rocks shifting their wettability towards the same behavior. However, acid-base are not the only type of interactions causing adsorption on rock surfaces. Other electrostatic and intermolecular forces, such as the ones discussed in the previous sections, also play important roles. Paraffins and naphthenes only interact through van der Waals forces, which are considered weak. Aromatic and naphtheno-aromatics are more active due to the formation of π bonds with the solids. Finally, asphaltenes and other heteroatoms containing species, such as resins, are the most active compounds regarding adsorption on the rock. They can be acid, basic or polar, so they may interact with the surface in many ways. Thus, they can form covalent bonds, hydrogen bonds or present dipole or electrostatic interactions.

Therefore, the acid and basic numbers (TAN and TBN) cannot be employed as the unique parameter to characterize wettability alteration after surface contact with the oil. The results in previous works (CUIEC, 1975) showed that the oil with higher TAN had a stronger interaction with the limestone rock surface. Nonetheless, for experiments using sandstone rocks, the expected trend was not followed. The authors concluded that a series of complex interactions take place and, in addition of TAN and TBN values, the nature of the acid and basic species on the oil are important in determining the interactions with the rock surface.

2.3.5 Disjoining pressure

If a liquid is allowed to spread on a solid surface surrounded by gas, the advance of a film of the liquid will depend on its physical properties, such as viscosity, the van der Waals attractive forces and the electrostatic surface interactions. The disjoining pressure represents the pressure required to counterbalance the interaction between the liquid film and the solid, thus, removing the film from the solid surface. The main components of the disjoining pressure are the van der Waals (represented by the Hamaker constant (HAMAKER, 1937), electrostatic and hydration forces.

2.3.6 Relevance for Reservoir Engineering

Donaldson and Alam (2008) describe wettability as one of the most relevant properties of the reservoir system because it affects the following characteristics: the distribution of oil and water in the pores, the capillary pressure curves, the value of the residual oil saturation and the flow properties of each phase (relative permeabilities). The effect of wettability on capillary pressure and relative permeabilities will be discussed as follows.

a) Effect on capillary pressure

Capillary pressure is a function of the saturation. The hysteresis between the drainage and imbibition processes can be observed in the capillary pressure curves. One of the most important reasons for this is the difference that exists between the advancing and receding contact angles. When the wetting fluid is being injected (imbibition), the advancing contact angle dominates during the displacement. In contrast, when the wetting phase is being replaced by the non - wetting fluid (drainage) the receding angle is more representative ((DONALDSON; ALAM, 2008)). Thus, the drainage and imbibition capillary pressure curves go through different paths. This can be noticed in Figure 2.16: curves (2) and (3) correspond to the imbibition process, and curves (4) and (5) represent a drainage process.

Closer analysis of Figure 2.16 allows the understanding of the different curves presented. The trends correspond to a water - wet porous medium. Curve (1) is the primary drainage process, where after the application of the displacement pressure (P_T) the oil is forced into the rock reducing the water saturation. As the capillary pressure is increased, the water saturation continues to be reduced until the irreducible water

saturation is reached (S_{wi}). Curve 2 is the spontaneous imbibition of water into the porous medium. Indeed, the water saturation is increased as soon as the capillary pressure is decreased showing that no displacement pressure requirement exists for water to enter the pores. The water saturation is increased until the zero capillary pressure is reached. This represents that to further increase the water saturation, negative capillary pressure values are required. This is, the water injection pressure must be higher than the pressure in the oil phase. This is shown in curve (3) which extends until the water saturation that corresponds to the residual oil saturation (S_{WOR}). Curves (4) and (5) are for the secondary drainage process. Again, a displacement pressure must be applied as to reduce the water saturation. It must be observed that the pathways of curves (1), (2) - (3) and (4) - (5) are different, which is a result of the hysteresis existent between the successive cycles of drainage and imbibition processes.

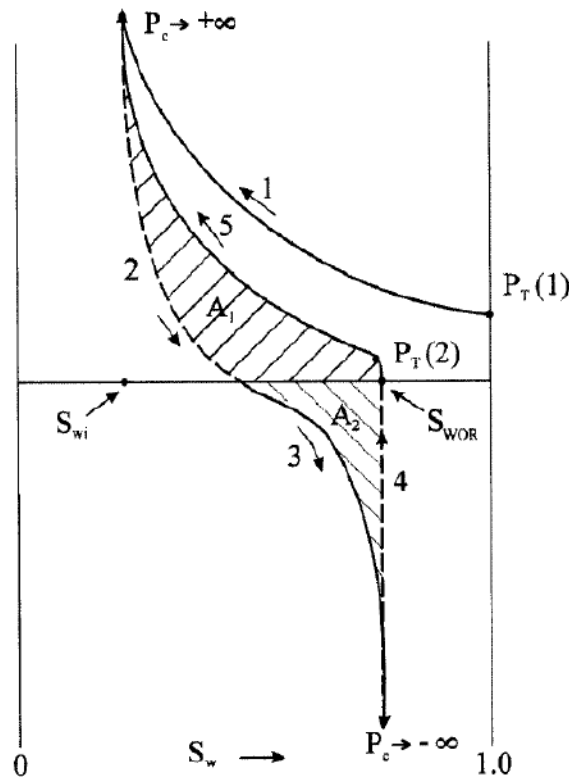


Figure 2.16. Drainage and imbibition cycles for a water-wet porous medium (DONALDSON; ALAM, 2008).

The areas below the curves represent the work required to displace one fluid by the other. By the analysis of Figure 4.21, it can be seen that for a water - wet system a greater work is required to remove the water from S_{WOR} to S_{wi} when compared to the work needed to increase the water saturation from S_{wi} to S_{WOR} . This is, in the figure the area A_1 is greater than the area A_2 . This is in agreement with the fact that while water

imbibes spontaneously into the porous medium, oil requires a threshold pressure limit even when the rock is fully saturated with water.

An analogous analysis can be made for intermediate - wet and oil - wet systems. In the former, the work required for the displacement of oil with water is similar to the work required to displace water with oil. Thus, the areas A_1 and A_2 in Figure 31 would be similar for a rock with intermediate wettability. Nevertheless, an oil - wet system has the opposite behavior of that showed in Figure 4.21. Oil imbibe spontaneously into the porous medium, and water needs a threshold pressure to enter the pores even when the water saturation is at its minimum value. In addition, the work required to displace oil with water is greater than the work required to imbibe the rock with oil. Therefore, it is expected a contrary fashion than that presented in Figure 4.21: the area identified as A_2 is greater than the area identified as A_1 .

The capillary pressure curves for intermediate and oil - wet porous media are showed in Figure 2.17. The graph on the left represents the intermediate - wet system initially saturated with water. Curve (1) represents the initial displacement of water by oil. It should be noticed that no threshold pressure is needed to introduce the oil for a 100% water saturation value. At position (2), water starts to be injected. A little amount of water will enter spontaneously. However, this is a much lower value than the one obtained at the water - wet system. After that, pressure must be applied and curve (3) occurs for negative capillary pressure values. Curves (4) and (5) represent similar behavior than curves (2) and (3). So, a little amount of oil will enter the porous medium. Next, a positive capillary pressure is needed to force the oil into the rock. It must be distinguished that the areas below the curves (A_1 and A_2) are approximately equal, meaning that the same amount of work is required to displace oil with water, than to displace water with oil.

Donaldson and Alam (2008) sum up the three particular characteristics for a intermediate-wet system: First, no threshold pressure is needed to inject either water or oil at the extreme saturation conditions. Also, a little amount of water will enters at S_{wi} spontaneously, and a little amount of oil will go into the pores spontaneously at S_{or} . Finally, the work required for the displacement of oil with water is approximately the same than the work needed to remove water by injecting oil.

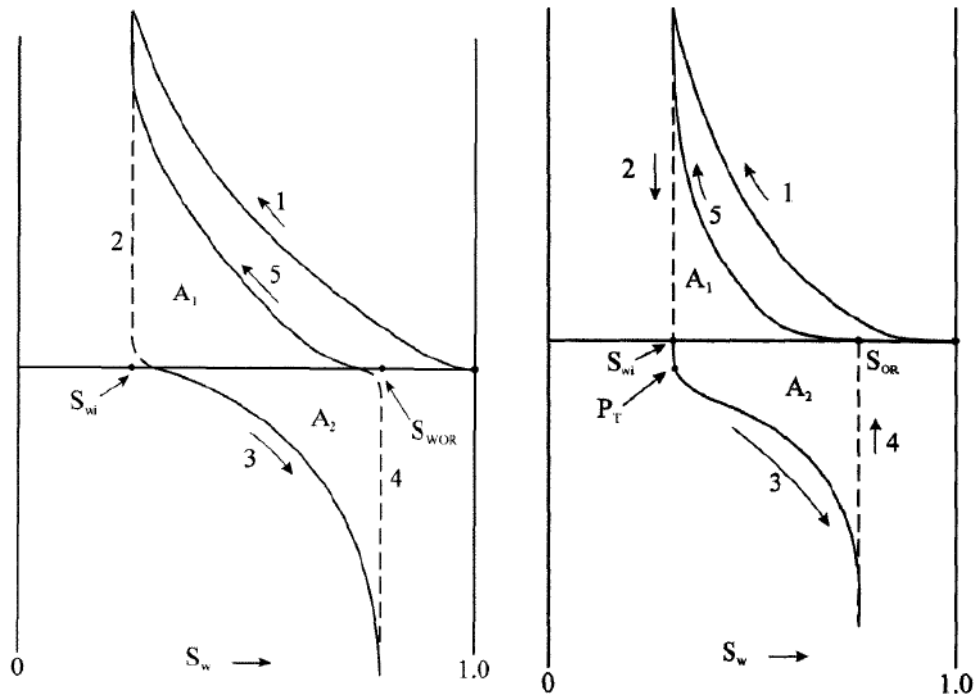


Figure 2.17. Capillary pressure curves. Left: intermediate-wet system. Right: oil-wet system (DONALDSON; ALAM, 2008).

The right plot in Figure 2.17 represents an oil-wet system. The behavior observed in this curve is clearly the opposite than the one presented in Figure 2.16 for a water-wet system. If the rock is initially saturated with water, oil will spontaneously imbibe into the pores with no threshold pressure as showed in curve (1). After reaching the irreducible water saturation (S_{wi}) a displacement pressure is needed to drain the oil and introduce some water volume in the rock. This is evidenced in curve (2) because even though the capillary pressure is being modified, the water saturation remains constant at S_{wi} . After applying a water injection pressure higher than the displacement pressure, water will invade the pores displacing the oil until reaching the residual oil saturation (that corresponds to a water saturation equal to S_{wOR}). Curves (4) and (5) show that no threshold pressure is needed to start injecting the oil phase, as it will spontaneously imbibe the oil-wet rock. Finally, the ratio of the areas A_1/A_2 demonstrates that less work is required to imbibe the oil when the rock is saturated with water than to drain the oil with water from a rock at S_{wi} . This is, the area A_2 is bigger than the area A_1 for an oil-wet system.

b) Effect on relative permeability

The impact of wettability on relative permeability is based on the difference in the distribution of the fluids. As stated in 4.4.1, when a system is water-wet the water tends to locate in the smaller pores and oil in the bigger pores. The former present a more severe restriction to flow while the latter have a greater contribution to the total flow. Thus, the more water-wet behavior the system presents, the smaller the water relative permeability and the bigger the oil relative permeability. The opposite is valid for oil-wet systems (DONALDSON; ALAM, 2008). The effect of wettability on the relative permeability curves can be observed in Figure 2.18.

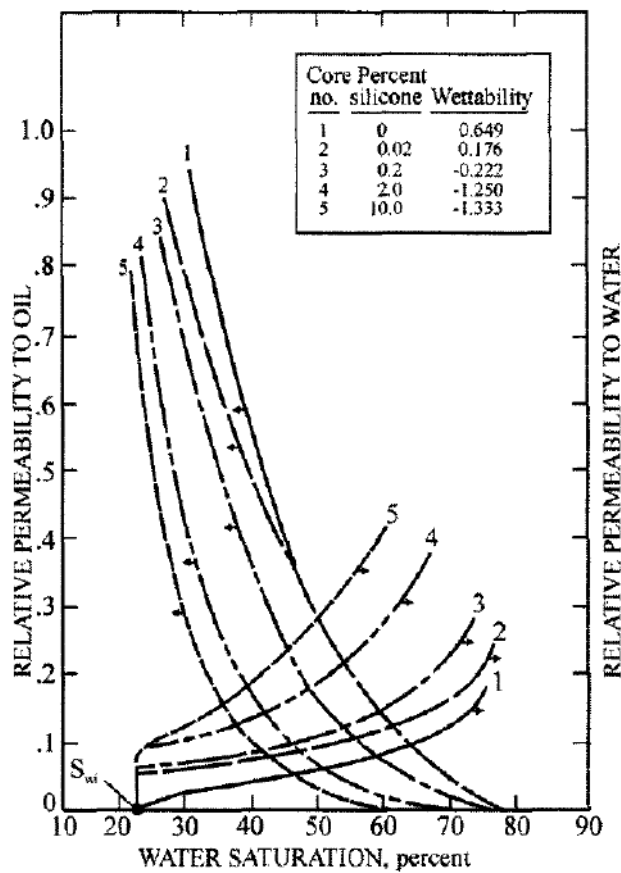


Figure 2.18. Effect of wettability on the relative permeability curves for different types of samples (DONALDSON; ALAM, 2008).

It can be observed that core (1) is the most water-wet core, and core (5) is the less water-wet core. Two different parameters indicate this: the end-point relative permeability ratio and the saturation of the intersection, and they will be discussed in the following paragraphs.

The end point relative permeability of a phase corresponds to the value when the saturation of the other phase minimum. For example, the end point relative permeability to oil is measured at the connate water saturation (S_{wi}). This specific relative permeability is used to analyze the flow capacity when the phase is at its maximum saturation. When the ratio of the end point relative permeabilities to water and oil is low it means that the flow capacity of water is low, even when it is at its maximum saturation. Thus, this indicates the porous medium is mainly water-wet. It can be noticed that in Figure 2.18 core (1) has the lowest ratio of end point relative permeabilities indicating that it is the most water-wet core.

The water saturation at the intersection represents the fraction of the pore volume that is filled with water when the flow capacity of both phases is the same. If the intersection is located at higher water saturations it indicates that a greater proportion of water is needed to achieve the same flow capacity than the oil phase. As a result, the porous medium is more water-wet because the flow capacity of the water is reduced because it will be located in the smaller pores. This is the case of core (1) in Figure 2.18.

2.3.7 Measurement

Wettability can be analyzed qualitatively by observing the shape of the capillary pressure and relative permeability curves. In addition, quantitative methods exist. In this work, the contact angle is used the parameter that defines the wettability as presented in Section 2.3.1. Moreover, the two other quantitative methods that are more accepted and implemented in the Oil and Gas Industry are presented.

a) Amott Index

Amott (1959) proposed this index, which is based on the analysis of the capillary pressure curves. For each phase, a parameter is calculated that represents the saturation difference that corresponds to spontaneous imbibition of that phase over the saturation difference of the total imbibition (spontaneous and forced). The closer this parameter is to 1 means that most of that phase enters the porous medium spontaneously indicating greater wettability by that phase. For example, in Figure 2.16 the parameter corresponding to water is the ratio of $S_2 - S_{wi}$ divided by $S_4 - S_{wi}$.

The Amott Index is the calculated subtracting the parameter of the oil phase to that of the water phase. As expected, if the Amott Index is positive the system is water-wet. In contrast, negative values indicate an oil-wet system, and values close to zero indicated neutral wettability (or mixed wettability) (AMOTT, 1959).

b) USBM Index

Donaldson et al. (1969) developed this method from the integration of the capillary pressure curves. As discussed in Section 4.4.3.1 the area under the forced imbibition region of the curve represents the work needed to introduce a phase into the porous medium after spontaneous imbibition. Then, a large area represents more work needed to force the phase in the porous medium indicating a lower wettability towards that phase. For instance, in Figure 4.21 the area corresponding to forced imbibition of oil is the area A_1 , and the area corresponding to the forced imbibition of water is the area A_2 .

The USBM Index is calculated as the logarithm of the ratio between the area that corresponds to the forced imbibition of oil divided by the area that corresponds to forced imbibition of water. Thus, a positive index represents water-wet rock that requires greater work to allow the forced injection of oil than the forced injection of water (DONALDSON; THOMAS; LORENZ, 1969).

c) Contact angle

The application of Young's Equation (Equation 2.11) determines a single value of the contact angle as a function of the interfacial tensions between each of the three phases that form the system. This applies to stabilized systems where the solid surface is flat and homogeneous. When the interface that separates the solid, the liquid(s) and/or the gas(es) is moving, the contact angle is not static, and it is not represented by a single value. Thus, a dynamic contact angle must be measured. When the angle is measured by expanding the liquid, it is called the "advancing contact angle". In contrast, when the angle is measured by contracting the liquid, it is called "receding contact angle" (YUAN; LEE, 2013). This classification used for the measured contact angles is analogue to the one described in Section 2.3.1.

The advancing contact angles usually give the maximum values, and the receding contact angles the minimum values. The difference between both angles is called contact angle hysteresis. It is accepted that this phenomena is closely related to the presence of

heterogeneities on the solid surface, which can be either a rough surface or a solid with areas of different composition (YUAN; LEE, 2013). For example, these heterogeneities may act as barriers to oppose to the movement of the liquid. As a result, they can raise the level of the liquid as it advances, increasing the angle measured. On the other hand, they can pull the liquid back when the front is receding, reducing the angle measured. Previous works (GAO; MCCARTHY, 2007; SCHWARTZ; GAROFF, 1985) explained the contact angle hysteresis phenomena by analyzing the deformation of the three-phase contact line and the activation energy required for the advancing and receding displacement of the contact line. They concluded that the hysteresis is a result of the activation energy that depends on the changes on the interfacial area. Yuan and Lee (2013) reviewed several works and reported that, for a rough surface, the measured contact angles vary significantly when compared to the values predicted by Young's Equation. On the other hand, for smooth surfaces with chemical heterogeneities, the measured advancing contact angle gives values that approximate to the one obtained by Young's Equation. However, for the receding contact angle, the measured values differ from the ones obtained by the application of Equation 2.11. According to the authors liquid sorption and the swelling of the solid phase is the cause for this.

Shedid and Ghannan (SHEDID; GHANNAM, 2004) studied the main factors affecting CA measurements on real carbonate reservoir oil-brine-rock systems. They evaluated the effect of drop volume, oil total acid number (TAN), temperature and brine salinity. The authors affirmed that there is a critical salinity at which, the drop volume has no effect on the measured CA. In addition, they found that increasing the TAN of the oils results in a more water-wet behavior of the carbonate rocks used in this work. Finally, the increase of temperature also shifted wettability towards more water-wet.

For rough surfaces, Wenzel (1936) defined the theoretical contact angle at the thermodynamic equilibrium (WENZEL, 1936, 1949). In addition, Cassie (1948) studied the theoretical contact angle for surfaces with chemical heterogeneities (CASSIE, 1948). Both these values differ considerably from the contact angle predicted by Young's Equation ((YUAN; LEE, 2013)). It is expected that for surfaces with roughness below 1 μm , the apparent contact angle on a rough hydrophilic surface is lower than the Young contact angle. On the other hand, for a rough hydrophobic surface, the apparent contact angle is higher than the Young contact angle (BUTT; GRAF; KAPPL, 2006; QUÉRÉ,

2002). A similar effect is observed for surface heterogeneity where the clusters of different minerals can act as barriers or valleys for the advancing of the liquid drop.

Another concern regarding contact angle measurement is the difference between the macroscopic (visible with optical methods) and microscopic (at the molecular level below 1 nm). The intermolecular interactions affect the microscopic contact angle, which differs from the macroscopic one (BUTT; GRAF; KAPPL, 2006). The microscopic contact angle can be obtained by the Young Equation when all the surface tensions are known. Nevertheless, this is rarely the case.

There is no general agreement regarding the assessment of wettability and the prediction of valid models to relate measured contact angles, spontaneous imbibition tests and core flooding experiments. Contact angles are used to identify wettability trends, and to qualitatively analyze the initial wettability under specific reservoir conditions. In this work, the purpose of contact angle measurement is to establish the trends in the interactions between different solid surfaces and reservoir fluids under different conditions such as oil and brine composition and pressure. The reported measurements are not intended to be representative of water imbibition or forced flooding displacements in reservoir cores.

CHAPTER 3: LITERATURE REVIEW

The objective of this chapter is to review the development and the latest advances in the techniques that will be used in this work. The application of these techniques to environments concentrated in CO₂ is summarized here as a review previous knowledge in the analysis of CO₂ effects in the complex Pre-Salt environment.

First, past and actual field and lab projects involving CO₂ injection are described. Then, the most relevant works analyzing wettability and interfacial tension in oil reservoirs, particularly considering the presence of CO₂, are reviewed.

3.1 Status of CO₂ flooding

The first applications of miscible flooding at field scale started in the decade of 1950 and consisted in the injection of slugs of LPG and natural gas. The elevated cost and physical properties that reduced the sweep efficiency of these solvents led to an increased interest in the use of CO₂ as a solvent.

CO₂ has relatively low critical conditions (31.1 °C and 1073 psi (ONISHI et al., 2009)), so in most EOR applications it will be injected as a supercritical fluid. As a result, it presents low viscosity (similar to that of a gas) and high density (similar to that of oil). This means the Mobility Ratio is still a concern, but the potential for gravity override is lower increasing the contact between the solvent and the oil. In addition, the use of CO₂ is more favorable for economic reasons when there is a source for this gas available nearby. In the last decades, the raise of awareness regarding the environment brought another advantage of using CO₂ as a solvent. Since it is a greenhouse effect gas, the injection of CO₂ can be combined with geologic sequestration to reduce the emissions of this gas.

The first CO₂ flooding pilot scale project with published results was in the SACROC unit in the Permian Basin (GRAUE; BLEVINS, 1978). The project started in 1973 and was evaluated for four years. The reservoir is an algal carbonate reef, and the area considered for the pilot had a thickness up to 200 ft with a net pay up to 100 ft. Six water-injector wells were converted to CO₂ injectors, and two producer-wells were drilled

in the middle resulting in two normal five-spot patterns. Adding up both producers, tertiary production was 64,000 STB and CO₂ production was 421 MMSCF. The volume of CO₂ injected was 2.3 BSCF. The sweep efficiency was estimated to be 33%. Tertiary oil recovery was calculated to be 5.75% of the original oil in place (OOIP). However, this value could be underestimated since one of the wells was stopped when the production was still increasing. In spite of the fact that the field represented a positive response, the pilot project was not considered economically favorable to move forward to the field scale due to economic reasons due to the low oil price at the time (14.85 USD/bbl). A minimum price of 20 USD/bbl was indicated as the threshold value. Another important effect that was evidenced in this project was the acidic dissolution of calcium carbonates by the dissolution of CO₂ in water.

Brock and Bryan (1989) summarized the results of the most important miscible and immiscible CO₂ projects from 1972 to 1987. This was the period in which CO₂ flooding grew exponentially and acquired great relevance as an EOR technique. The type of projects considered varied from single-well immiscible stimulation to continuous miscible flooding and WAG applications. The compilation included miscible (9 pilots and 12 field scale) and immiscible (2 pilots and 2 field scale) projects. Rock types varied from sandstone to carbonates including dolomitic formations. The greatest depth was 13,000 ft and the highest temperature 118°C. The increment on the Recovery Factor ranged from 5 to 22% of the OOIP. The gas utilization measures the volume of CO₂ injected per stock tank barrel of oil produced. The values of CO₂ utilization ranged from 2.4 to 13 MCF/STB. This shows that the conditions of the reservoir, the type of project and the strategies for injection and production (time of the cycles, CO₂ management, volume of the slugs among others) affect the efficiency of the project considerably (BROCK; BRYAN, 1989).

In 2006 an overview of the EOR projects in carbonate fields in the United States was presented. At the time of their study, there were 143 active EOR projects in carbonates in the USA, and CO₂ flooding projects represented the majority of them. CO₂ injection accounted for 52% (345,514 bbl/d) of the EOR production in the USA at that time. CO₂ injection represents the most widely used EOR technique in carbonate reservoirs, and at the time of the publication there were 48 active projects of this type. Most of these projects are located in the Permian Basin. The authors relate the growth of CO₂ flooding in the USA to several factors including the availability of CO₂ as a natural

resource, the developed structure for the transport and the economic attractiveness, since an oil price of breakeven price was 18 USD/bbl for the Permian Basin at the time (MANRIQUE; MUCI; GURFINKEL, 2006).

Sheng (2013) reviewed the application of CO₂ flooding in the Slaughter Estate Unit in the West Texas Permian Basin. The formation is dolomite rich with an average permeability of 4 mD and a depth of 5000 ft. The oil is light (32 °API) and the average reservoir pressure at the time was around 2000 psi. The injected gas consisted of a sour gas with a composition of 72 mol% CO₂ and 28 mol% H₂S. For this gas and oil, the minimum miscibility pressure was determined to be 1000 psi, so it was a miscible flooding. The process was applied as WAG with a water to gas volume ratio of 1. The pilot project included the injection of a gas slug of 25% of the hydrocarbon pore volume (HCPV). Tertiary recovery was 19% of the OOIP which, added to primary and secondary recoveries, resulted in a Recovery Factor of 79% of the OOIP. The pilot was considered a success and was extended to the field scale.

The author also presents an overview of CO₂ field experiences. The average incremental oil recoveries including miscible and immiscible projects ranges between 5 and 20% of the OOIP. However, miscible flooding usually gives recoveries 10% higher than immiscible flooding. The latter, when applied as tertiary recovery, has an average incremental oil recovery of 6% OOIP (SHENG, 2013).

The main drawback for CO₂ application is the high mobility of the injected gas that leads to low sweep efficiency, gas channeling and premature breakthrough. Mobility control mechanisms, such as WAG or foaming, could improve the Recovery Factors of these methods. In addition, corrosion of both injection and producing facilities is a frequent problem due to the decrease of the pH when CO₂ dissolves in water. Also, flow assurance issues, such as asphaltenes deposition, hydrates formations or scales precipitation are commonly reported. Studying phase behavior and carefully planning the conditions of the operation can reduce these obstacles. However, in some cases fixed conditions such as reservoir temperature and pressure may lead to these restrictions. So, a flow assurance-mitigating plan (mechanical, chemical or thermal) needs to be implemented in all CO₂ flooding field projects. Moreover, water injectivity problems when WAG or a sweeping-water slug is applied are frequently observed. The main cause of this is the effect of the three-phase flow and hysteresis due to the injection of alternating fluids on the relative permeability curves. On the other hand, gas injectivity is not an issue

especially for carbonates where the carbonated water dissolves part of the matrix increasing its permeability.

At the present time, most of the CO₂ flooding projects are WAG. The water to gas ratio is usually around 1, with CO₂ slugs between 0.1 to 0.3 pore volumes. The most important parameter to measure the efficiency of the project is the gas utilization, defined previously in this section. The author indicates that the projects that have gas utilizations lower than 10 MCF/STB are considered efficient (SHENG, 2013).

A recent project considered the injection of CO₂ in the Bakken formation in the Williston Basin in the north of the US. This formation is one of the largest non-conventional reserves, and a very promising tight-oil play with 7.4 billion of barrels of recoverable reserves. The formation consists of three blocks: the upper and lower ones are organic-rich shales. The middle block is organic-poor but presents largest porosity (5 to 8%) and permeability (less than 50 μD). Thus, the production is carried out through horizontal wells in the middle member that present conditions that are more favorable. At reservoir temperature and pressure, the injection of CO₂ is a miscible process (ZHANG, 2016). Previous modeling analysis for this formation indicated that EOR flooding is required to aid in the mobilization of oil due to the low permeability. In addition, continuous flooding through horizontal wells showed to be more effective than cyclic injection or vertical wells (SHOAIB; HOFFMAN, 2009). Being an unconventional field, the application is still in the laboratory and modeling phase. The authors obtained an increment of the Recovery Factor of more than 50% OOIP from a 1 HCPV slug of CO₂ in their simulations from history marching from the data obtained in core flood experiments. However, since the formation is so tight, fractures are needed to allow efficient diffusion of the CO₂. So, hydraulic fracture and horizontal wells are needed prior to the application of miscible flooding. They concluded that the governing mechanism for the application of CO₂ in this tight oil is vaporization of the light hydrocarbons with some contribution of swelling, re-pressurization, viscosity and interfacial tension reduction.

In Brazil, CO₂ is already being reinjected in offshore Pre-Salt fields as stated in Chapter 1. Two technologies are used to separate CO₂ from the produced gas to increase the concentration of the CO₂ in the injected gas. The surface and subsurface equipment were already planned considering the challenges of CO₂ injection discussed before (DE

ALMEIDA et al., 2010). Few results from these tests are available since this application is considered recent and in stage of development.

3.2 Analysis of the interfacial tension of the oil-brine-CO₂ system

The number of published papers containing experimental data for the oil-CO₂-brine system is limited due to the difficulty of carrying out meaningful measurements. Some of the complications include high sensitivity to impurities which cause dynamic effects and the need to know the density of all phases at test conditions considering CO₂ partitioning between the oil and brine (GEORGIADIS et al., 2010, 2011).

An experimental study (GU; YANG, 2004) analyzed the behavior of the interfacial tension between CO₂ and crude oil at reservoir conditions for a heavy-oil field scenario in Saskatchewan, Canada. They found a similar behavior than for most gas-liquid systems: the dynamic interfacial tension decreases until reaching an equilibrium value. In addition, the interfacial tension decreases with pressure and increases with temperature. This is associated with the fact that the solubility of the CO₂ in brine increases with pressure and decreases temperature. In addition, they found that there is a pressure above which the solubility does not increase with further increases of pressure. Above this maximum solubility the brine drops cannot be formed in CO₂ to measure the interfacial tension by the DSA technique. They reported that the interfacial tension between oil and brine in systems containing a fixed concentration of CO₂ decreases with both pressure and temperature. The effect of pressure is related to the increase in solubility of CO₂ in both oil and brine phases. On the other hand, the reduction of the interfacial tension with temperature is explained because the fact that the intermolecular forces that cause the interfacial tension are weakened at higher temperatures is more important than the solubility effects for this system.

Another experimental work studied the effect of CO₂ concentration on the interfacial tension between live oil and brine for a Chinese reservoir with low salinity brine (below 3,000 ppm) and heavy live oil (90% C₁₁₊) (SUN; CHEN, 2005). The CO₂ was dissolved in the live oil to obtain the desired concentration, and the mixtures were injected above its bubble point to avoid the release of dissolved gas. The interfacial tension between the live oil and brine phases was measured as a function of pressure for different CO₂ concentrations. The interfacial tension decreased with CO₂ concentration reaching

30% of its initial value for 65 mol% of CO₂. For a fixed CO₂ concentration pressure had minor effect on the interfacial tension. It is interesting to remark that no asphaltene, resin or other surface-active species were reported in the crude oil employed.

A study considering decane-CO₂-water was carried to observe the effects of CO₂ dissolution on the interfacial tension (GEORGIADIS et al., 2011). The effects of impurities was critical causing dynamic effects that complicated obtaining accurate equilibrium values. The authors informed dynamic interfacial tension values which were considered to be less determined by concentration of impurities.

To the best of the author's knowledge, no published works considering the effects of CO₂ dissolution in Pre-Salt crude oils and brines on the interfacial tension are present in the literature. The effect of salinity on the interfacial tension between Pre-Salt crudes and oils was investigated (ALVES et al., 2014). The authors reported that the increase in salinity enhanced the interfacial activity of the surfactants present in the crude oil. Moreover, the greater ionic force resulted in an interfacial film which was more rigid.

3.3 Analysis of the solid-fluid interactions

Wettability affects the performance of a WAG or miscible flooding process. Tiffin and Yelling (1983) explained that the WAG recovery in water-wet rocks is poorer because CO₂ must diffuse through the continuous layer of water to reach the oil blobs, which are a discontinuous phase. On the other hand, in oil-wet reservoirs the oil phase is continuous, and the CO₂ will reach it more readily (TIFFIN; YELLIG, 1983).

A pilot-scale work assessed the effects of wettability on WAG at a larger scale (JACKSON; ANDREWS; CLARIDGE, 1985). The paper includes results for WAG recovery in two five-spots in different wettability rocks. The authors concluded that the recovery was higher in the oil-wet scenario because in the water-wet rock the displacement was governed by gravity override.

Moreover, severe oil-trapping was reported elsewhere (RAIMONDI; TORCASO, 1964; STALKUP, 1970). Another paper (HUANG; HOLM, 1988) presented a method to alter the wettability of Berea Sandstones by using different aging times. The final wettability was qualitatively assessed by X-ray photoelectron spectroscopy (XPS) of the crushed sand. The performance of WAG recovery was analyzed using coreflood tests. Again, the oil-wet cores showed lower oil trapping (5%) due to the WAG cycles, but not

necessarily resulted in the lowest residual oil saturations. For water-wet cores oil trapping was greater than 45% due to WAG injection. Finally, mixed-wettability showed a WAG trapping of 15%, but the residual oil saturation after miscible flooding was lower than in the oil-wet cores. Posterior work (LIN; HUANG, 1990) confirmed high oil trapping effects for WAG in water-wet cores and insignificant trapping for mixed-wet cores. The authors proposed diffusion mass transfer mechanisms as the main cause for trapped oil displacement in mixed-wet cores.

Later research (RAO; GIRARD; SAYEGH, 1992) studied the correlation between laboratory-scale and field-scale recoveries in three reservoirs with different wettabilities finding good agreement between both results. They found that waterflooding recoveries were lower for the oil-wet formation (Cross-field Cardium), followed by the water-wet (Beaverhill Lake), and the mixed-wet (Gilwood) showed the highest recovery. However, miscible flooding showed a different trend: the oil-wet had the highest recovery, followed by the mix-wet, and the water-wet had the lowest recovery. The authors attributed this to the fact that mixed-wettability show the best situation for WAG because it contains the continuous oil-phase in the largest pores that can be swept in waterflooding, and the effect of water films is diminished because it is mainly located in the smallest pores.

The same group studied interfacial phenomena in CO₂ injection considering the same reservoirs (RAO; GIRARD; SAYEGH, 1989). They measured contact angles in pure quartz, calcite and dolomite minerals using crude oil and reproduced formation brine. For the Beaverhill Lake reservoir fluids, the authors found increasing contact angles with CO₂ injection (from water to mix-wet) in both calcite and quartz. For the Crossfield Cardium and Gilmore reservoirs the contact angle remained invariant after CO₂ dissolution. They did not succeed at measuring the contact angles on dolomite substrates due to continuous rolling of the oil droplets. The study couldn't cross-match the results to core results for the same type of rocks. Several difficulties (i.e. asphaltene precipitation as CO₂ dissolved in the oil phase) compromised the representability and repeatability of the contact angle results.

The effects of CO₂ dissolution on the wettability of different minerals was evaluated (SEYYEDI; SOHRABI; FARZANEH, 2015). The authors assessed the wettability of unaged and aged samples of mica, quartz and calcite. They analyzed the effect of adding CO₂ in the fluid on the wettability of the rock sample. For the unaged minerals, the change in wettability by CO₂ addition was low, showing a maximum

increase of 6° for quartz. For the aged carbonates, the effect was more pronounced: a decrease from 89° to 63° for mica and 144° to 97° for calcite. This supports the idea that carbonated water reacts with aged carbonate mineral surfaced weakening the attractive forces that makes them oil-wet in the absence of CO_2 .

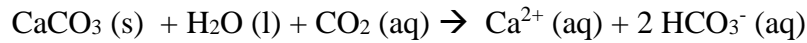
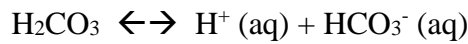
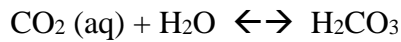
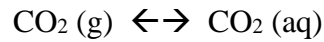
Wettability alteration by WAG injection in cores was studied in several publications. Potter (1987) studied the modification of wettability in CO_2 flooding in West Texas dolomitic formations. He found that the surface tends to become more water-wet after CO_2 flooding due to the extraction of compounds from the surface. Specifically, the author remarks the dissolution of anhydrite (CaSO_4) by the decrease in pH in the carbonated water formed in CO_2 flooding (POTTER, 1987). In addition, posterior research (FJELDE; ASEN, 2010) that the first cycle of WAG increased the water-wet behavior of fractured chalk reservoir rocks from the North Sea. The wettability was determined by the sulphate test (ASTM D516-07). CO_2 -WAG cyclic injection increased the water-wet area of the cores resulting in an increased oil recovery.

A more recent work (RUIDIAZ; WINTER; TREVISAN, 2018) considered the wettability alteration of dolomite and limestone cores and its effects on oil recovery using de-waxed and de-asphalted Pre-Salt crude and formation and injection brines (200,000 and 35,000 ppm salinities respectively) using the Amott-Harvey Index and spontaneous imbibition tests. The authors found that switching the brine salinity had a dramatic effect on the wettability of the dolomitic cores towards water-wet increasing oil recovery. In addition, it was found that carbonated resulted in lower oil recovery than alternating the salinity of the brine. These wettability trends may differ when crudes containing asphaltenes and waxes are considered.

Also, simulations have also contributed to experimental efforts to evaluate the wettability alteration during CO_2 injection in carbonate oil-wet cores (AL-MUTAIRI; ABU-KHAMSIN; HOSSAIN, 2012). The paper considered the injection of carbonated water in an immiscible displacement and measured the contact angle experimentally. The results were used to build a mathematical model based on Corey Equations for relative permeability (COREY, 1954). In agreement with the previous discussions, the effect of the dissolved CO_2 was to turn the core more water-wet. The authors indicated that this modification affected the relative permeability curves. They concluded that to include these changes in the reservoir model was relevant to calculate the oil recovery more

accurately. Nevertheless, in terms of simulations, carbonate reservoirs represent a much more complex scenario and other models are under development.

Finally, another rock-fluid effect that was observed in CO₂ flooding is carbonate dissolution. The presence of dissolved CO₂ in the water shifts the pH towards acid values due to the formation of HCO₃⁻ and H₂CO₃. As the water becomes more acidic, its capacity for dissolving carbonate minerals from the cores increases. This is the case, for example, for calcite. The main chemical reactions for calcite dissolution are shown below (SEYYEDI; SOHRABI; FARZANEH, 2015):



The solubility of calcite in carbonated water at temperatures up to 70° C and CO₂ partial pressures up to 725 psi was recently studied (BO; ZHANG; ZHANG, 2018). The results showed that the solubility of calcite increased with the partial pressure of CO₂ and decreased with temperature for the thermodynamic conditions considered in the experiments. In addition, the solubility of the natural existing carbonate rocks is lower than that of the pure calcite mineral (SVENSSON; DREYBRODT, 1992).

The overall effect of carbonate dissolution in oil recovery is not easy to be accounted for. On the one hand, it increases porosity and permeability by reducing the area of the rock blocking the pores. On the other, it could favor the transport of particles that could deposit blocking the thinner channels of the pores and decreasing permeability. Both these effects were reported in the literature (BACCI; KORRE; DURUCAN, 2011; IZGEC et al., 2005).

Recent research (DE FREITAS FILHO, 2017) studied the effects of carbonated water in the mineral dissolution, porosity and permeability of limestone from Morro do Chaves (Brazil) and dolomite from Silurian Formation (USA) rocks. The dissolution of carbonates was evaluated by measuring the concentration of calcium and magnesium ions in the carbonated water in contact with the rock as a function of time and pressure. The porosity and permeability was measured before and after the contact with the carbonated

water using bench equipment. The author found that the rate of limestone dissolution was greater than that of dolomite for one order of magnitude. In addition, mineral dissolution damaged the core due to fines transport and deposition, which reduced the permeability of the rocks.

3.4 Effect of CO₂ on the physical properties of the fluids

3.4.1 Viscosity reduction

The dissolution of CO₂ in the crude oil brings the additional advantage of reducing its viscosity. The reduction in viscosity improves the mobility of the oil increasing the Macroscopic Efficiency of the displacement process. Holm (1982) presented the viscosity of several crude oils saturated with CO₂ as a function of pressure. The results are shown in Figure 3.1. It can be observed that, since the solubility of CO₂ in oil increases with pressure at constant temperature, the viscosity is lower for the oils at higher pressures because they contain higher CO₂ concentrations. It should also be observed that CO₂ has a greater impact on the viscosity of heavy oils if the relative decrease of viscosity for the same increase in pressure is considered.

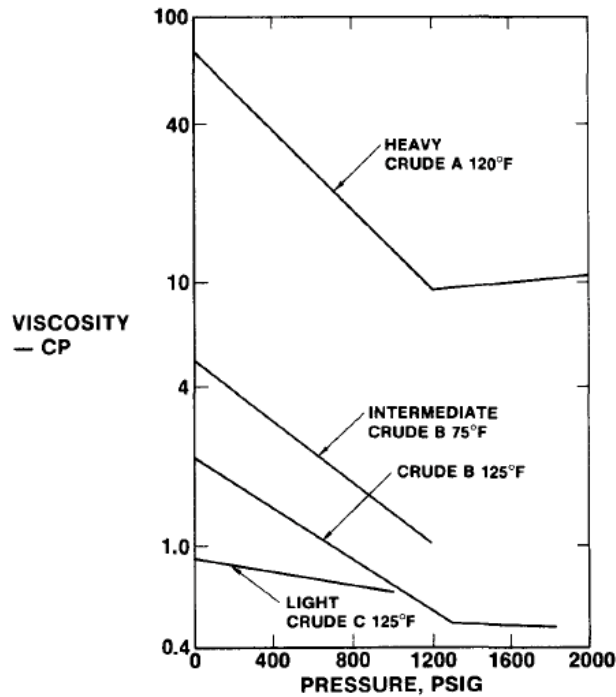


Figure 3.1. Viscosity as a function of pressure for different oils saturated with CO₂ (HOLM, 1982).

The effect of CO₂ on the viscosity of a light live oil from West Texas was analyzed under partially miscible conditions (LANSANGAN; SMITH, 1993). A reduction from 1 to 0.4 cp was observed for the oil-rich heavier phase at 1370 psi and 105°F for CO₂ molar fraction of 0.6. Under similar conditions, the viscosity of the CO₂-rich light phase was around 0.25 cp showing that CO₂ is actually partitioning into both phases, which become more similar to each other as CO₂ concentration increases.

The viscosity reduction of heavy oils in Alaska was reported elsewhere (NING et al., 2011). The authors carried out multi-contact experiments and studied the phase behaviors of the mixtures between CO₂ enriched natural gas and crude oil. The experimental results showed that the viscosity could be reduced from 120 to 17 cp for the CO₂ enriched natural gas and up to 6 cp for CO₂ injection. Moreover, the effect of CO₂ combined with steam injection was investigated for ultra-heavy oils in China (ZHU et al., 2018). By using a CO₂/oil ratio of 20, the researchers obtained a reduction in oil viscosity from 140000 to 20000 cp at 45 °C. When the temperature increased, this reduction was less pronounced, but lower viscosity values could be achieved using lower CO₂/oil ratios.

Similarly, the decrease in viscosity when heavy oil from the Waseca formation (Canada) where saturated with CO₂ was assessed (FREITAG, 2018). A reduction from 20000 to 1000 cp was obtained for an increment in equilibrium pressure from atmospheric to 4000 kPa at 21 °C. As indicated in the previous discussion, the latest research regarding the impact of CO₂ on oil viscosity is focused on heavy oils due to their greatest potential for viscosity reduction.

3.4.2 Swelling

Gardner et al. (1981) reported the effect of pressure and CO₂ mole fraction on the phase behavior of the Wasson crude (Texas) at 105 °F. The resulting phase diagram is showed in Figure 3.2. It is evident that for CO₂ concentrations below 60% the mixture forms a single phase at pressures above 1500 psia. At 60% CO₂ concentration there is a critical point where the bubble and the dew point curves intersect. For CO₂ concentrations above 60% the formation of a three-phase region is observed at lower pressures and two liquid phases in equilibrium appear at higher pressures. The phase behavior as a function of CO₂ concentration and pressure will depend on the composition of the crude and the

temperature. The study of the Wasson crude is presented in this work to show the complexity of the phase behavior of the mixtures between crude oil and CO₂.

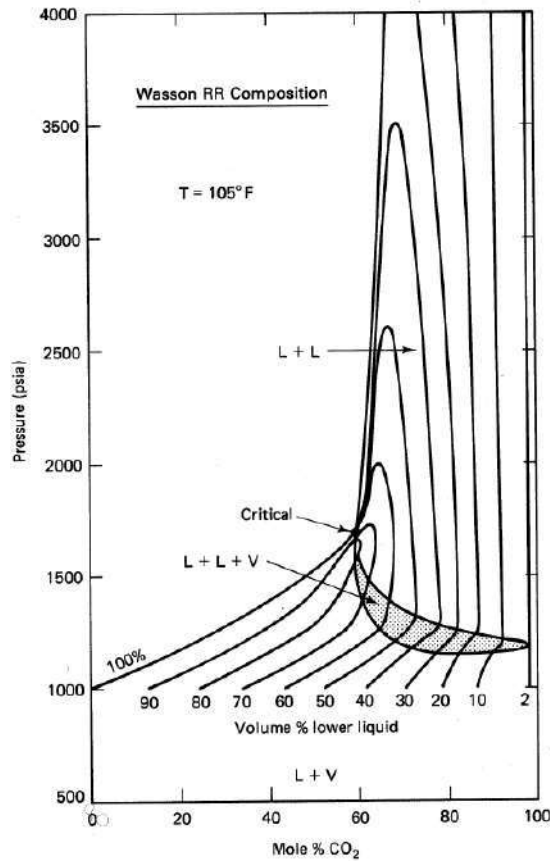


Figure 3.2. Phase diagram for the Wasson crude/CO₂ system at 105 °F (GARDNER; ORR; PATEL, 1981).

As CO₂ dissolves in the oil phase, it augments its volume giving resulting in swelling of that phase. The degree of swelling is characterized by a swelling factor (SF) that is the ratio between the volume of the oil saturated with CO₂ at the saturation pressure and a given temperature and the volume of the oil at a reference pressure (usually standard) and the same temperature.

The SF depends directly on the solubility of CO₂ in oil, so it follows the same behavior as a function of pressure. At higher pressures, a greater volume fraction of CO₂ is dissolved in the oil resulting in larger values of SF. An example of a curve of SF as a function of CO₂ concentration is shown in Figure 3.3.

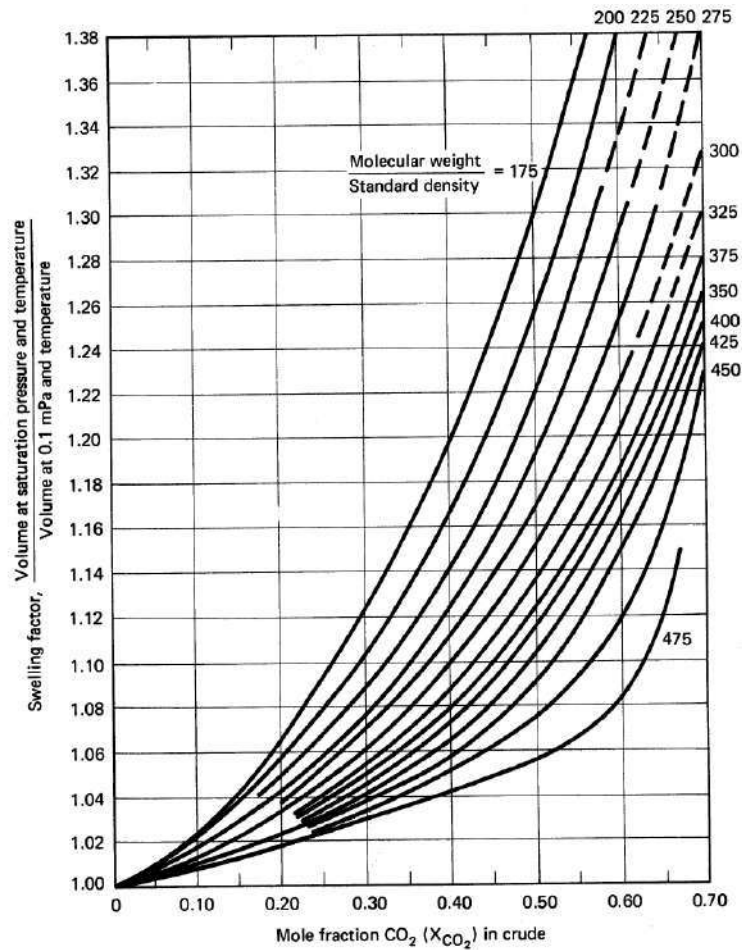


Figure 3.3. Swelling factor versus CO₂ fraction (SIMON; GRAUE, 1965).

A more recent study presented the comparison of the existing correlations for CO₂ solubility in oil, swelling factor and density for crudes containing dissolved CO₂ as a function of pressure and temperature (EMERA; SARMA, 2007). The authors used a genetic algorithm-based technique to enhance the representability of the system by including CO₂ liquefaction pressure. The results enhanced the existing correlations by reducing the error with published experimental data. The trends obtained indicate increase of oil swelling and density and reduction of viscosity with the dissolution of CO₂ in oil.

The PVT study of CO₂ injection for an onshore field was carried out (JHA et al., 2015). The authors extended the effect of saturating the crude oil with CO₂ at constant temperature (192.2 °F) and pressures up to 3000 psi. The results for the constant mass expansion experiments indicated that for pressures greater than 500 psi, the contribution of CO₂ produces a reduction in volume and increase of density of the saturated mixtures. This is more important for higher pressures over the critical point of CO₂.

Oil swelling contributes to its production in a similar fashion than the expansion of oil and gas in primary recovery mechanisms. In addition, swelling causes an increase in oil saturation that raises the relative permeability of oil as discussed in Section 2.1.3. Consequently, the increase in relative permeability improves the mobility of the oil phase improving the Macroscopic Efficiency. More importantly, swelling can result in the displacement of residual oil that remained trapped due to the increase of the saturation of oil in the porous medium. Swelling factors up to 1.7 may be achieved under reservoir conditions for specific oil compositions at certain thermodynamic conditions (SHENG, 2013).

3.5 Considerations for CO₂ injection in the Pre-Salt reservoirs

Some general characteristics of the Pre-Salt fields were introduced in Section 1.2.1. In terms of elevation and flow systems, the water depths of over 2000 m in combination with strong tides and big ocean waves represent a great challenge the mechanical resistance of risers. If CO₂ production and reinjection is expected, corrosion protection needs to be promptly addressed due to acidification of the water phase. In addition, the distance of around 300 km to the coast and the lack of previous local onshore infrastructure difficult the logistics for transportation of both equipment and production fluids (CEZAR et al., 2015). In this regard, CO₂ injection and WAG appear as a solution in the fields that have high CO₂ content, as this produced gas cannot be vented to atmosphere.

The water depth also affects flow assurance since extremely high heat losses are expected due to the low temperatures at the bottom of the sea; thus, adequate insulation is required. In addition, the wells are equipped with chemical injection devices to prevent asphaltene, scale or wax precipitation or hydrate formation. Special consideration should be given to asphaltenes as CO₂ injection was associated with asphaltene deposition in several studies (ADYANI et al., 2011; ALI; DAHRAJ; HAIDER, 2015; SRIVASTAVA; HUANG; DONG, 1999).

The internal pressures in the Pre-Salt reservoirs are higher than the ones in conventional fields from the Campos basin. Besides the exceptional challenges for drilling, the wells, pipelines and surface facilities must be prepared for these elevated pressures. This is critical for injection wells and lines that operate at pressures close to

8000 psi (500 bar) (CEZAR et al., 2015). The pore pressure distribution as a function of depth for wells in the Santos and Campos basins is shown in Figure 3.4. This indicates that supercritical state of CO₂ must be considered at reservoir conditions.

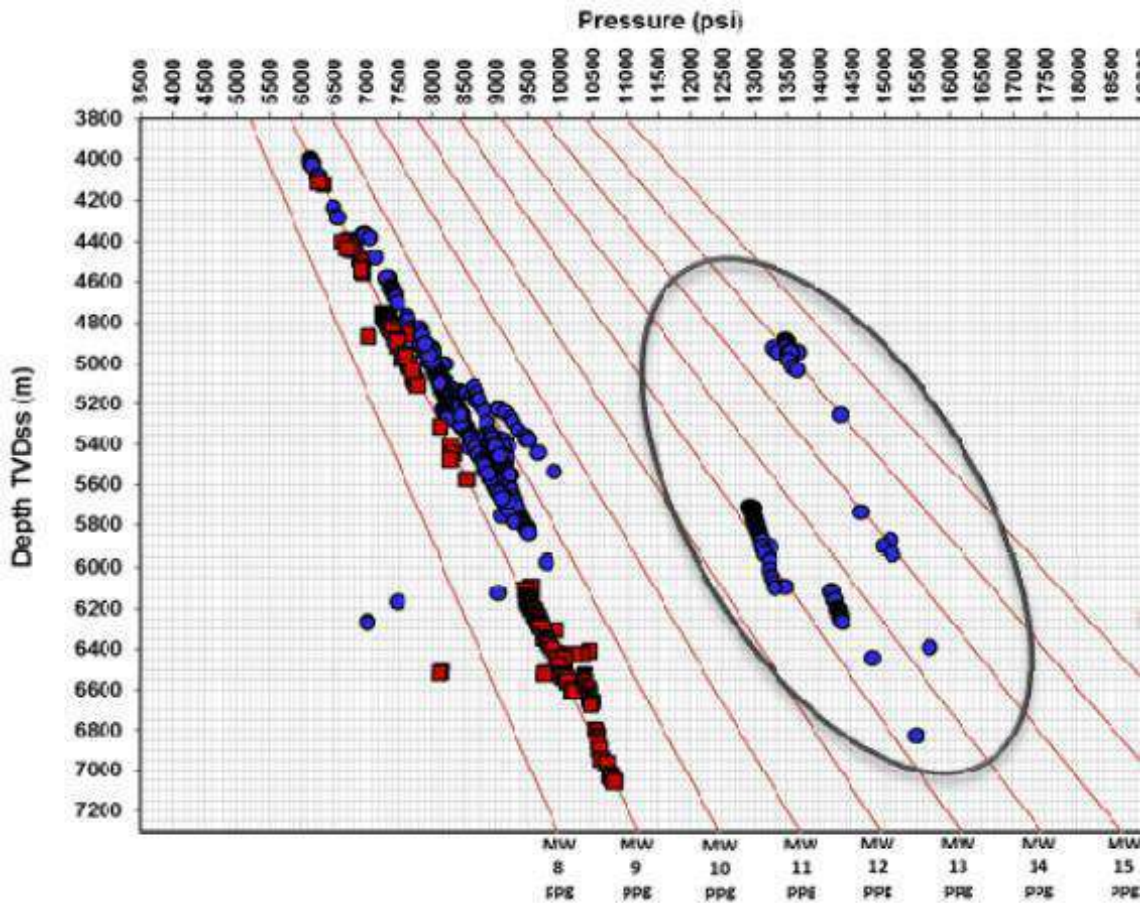


Figure 3.4. Pore pressure versus depth for Campos (red) and Santos (blue) basins (MATIAS et al., 2015).

The suitability of Lula field for the injection of CO₂ was discussed (PIZARRO; BRANCO, 2012). Besides the water depths commented before, the authors remark that the low temperatures (between 60 and 70 °C) and the oil properties (high API and low viscosity) represent good conditions for gas-oil miscibility. In addition, the equipment and facilities in the operating units have already been prepared for CO₂ production. Some of the preventive actions applied include: implementation of anti-corrosion protection, injection of chemicals for flow assurance and the use of CO₂ separation and re-injection units among others. The analysis of the first well-tests and the history matching of the first production pilots, where the produced CO₂ was re-injected, seek to improve the geomodel of the Lula field. The simulations were carried out using data obtained from equations of state and measurements from PVT and miscibility analyses. However, due

to confidentiality reasons, this data is not included in the publication. The results allowed identifying high-channeling areas, improving the injection pattern, confirming the absence of major flow assurance issues, observing good response to CO₂ injection and testing the adequate injectivity for the water.

The authors describe the pattern and sequences for gas injection keeping the CO₂ concentration in the injected gas was always above 50%. An increase in the rate of production of oil was associated with the cycle of gas injection. The authors remark that the continuous increase of oil production indicates that CO₂ injection is an effective method to improve the recovery of oil for the Lula field. In addition, no operational issues were reported. Finally, they encouraged further study of the WAG process in the Lula field. Nevertheless, the phenomena that govern the interactions between CO₂ and the fluids and rock in this scenario have yet not been studied in detail.

Even though the oil companies perform PVT analysis and characterization of Pre-Salt fluids considering the presence of CO₂, the data generated from these tests is not available in the literature. Consistent experimental data including physical properties, rock-fluid interactions, and the impact of CO₂ on them is necessary to improve the actual models that describe Pre-Salt reservoirs. In this respect, this work aims to report reliable experimental data and to discuss the physical and chemical phenomena relevant for oil production in the Pre-Salt scenario.

CHAPTER 4: METHODOLOGY

This chapter presents a summary of the experimental, analytical and computational methods used in this work. It presents the experimental techniques and procedures for data analysis and simulations and includes diagram fluxes showing the different steps involved for the contact angle and interfacial tension tests.

4.1 Experimental Methods

4.1.1 Contact Angle Measurement

The Contact Angle (CA) is measured to study the interactions between the solid surface (rock) and the different fluids. The test contains two fluids, an external phase (brine) in which the rock is immerse and the phase contained in the drop deposited on the rock surface (oil). Before the proper CA test, the rock has to be prepared to be representative of reservoir conditions. As explained in Section 3.3, rock preparation is a crucial part of wettability assessment as it has a great effect on the obtained results (BUCKLEY, 1998; BUCKLEY; LIU; MONSTERLEET, 1998; SEYYEDI; SOHRABI; FARZANEH, 2015; YU; BUCKLEY, 1997).

First, the rock sample needs to be cleaned, cut to corresponding slab sizes (25.4 x 25.4 mm and 3 mm thickness) and polished to minimize its roughness. This procedure was done by Solintec. Then, the rock needs to be aged to allow the surface interactions with the fluids. For this, the slabs were placed in closed recipient with the respective fluid and kept at constant reservoir (test) temperature. Initially, the slabs were aged in brine for a given period (usually 1 day), and then in crude oil for different aging times (1, 3, 5, 15, 30 and 40 days).

After aging, the rock surface is covered by an excess bulk oil film. CA cannot be measured on this surface as it is not representative of the solid surface. Different methods for removing excess oil were applied in the literature including the use of solvents and centrifugation (BUCKLEY, 1996; SEYYEDI; SOHRABI; FARZANEH, 2015). However, no systematic studies comparing the effects of different solvents and the volumes applied including centrifugation are available in the literature. The objective of

this is to remove the bulk oil without altering the composition of the rock nor the adsorbed oil on the surface. In this work, the cleaning of bulk oil on the surface was done by centrifugation in a tube filled with the test brine at 3000 rpm for 20 minutes. A rock slab after bulk oil removal by centrifugation is shown in Figure 4.1.

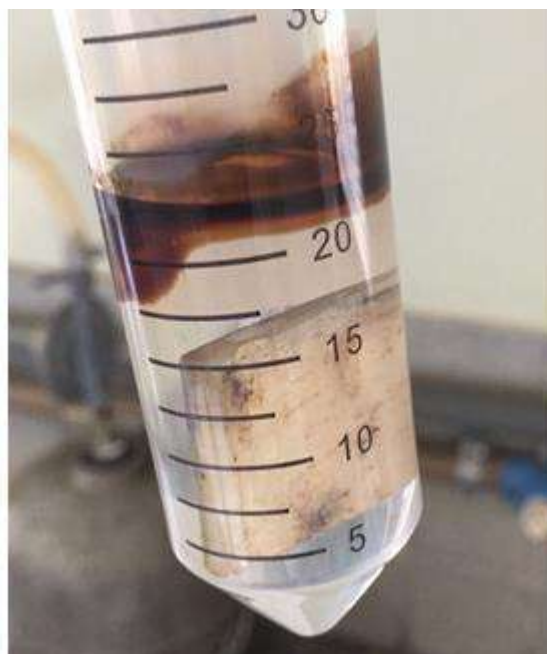


Figure 4.1. Excess bulk oil cleaning by centrifugation.

Furthermore, the effect of rinsing each surface with 1 ml of different solvents (*n*-hexane, cyclohexane, *n*-hexadecane and toluene) was evaluated. Depending on the viscosity and composition of the oil and on the aging time, both methods may need to be applied to remove the excess bulk oil as observed in previous works (SEYYEDI; SOHRABI; FARZANEH, 2015). An example of bulk oil cleaning by rinsing with solvent is shown in Figure 4.2.



Figure 4.2. Excess bulk oil cleaning by applying solvent (cyclohexane).

Finally, the slab is rinsed thoroughly with formation brine to remove any excess of solvent from its surface. After rock sample preparation, the slab is placed in a Teflon holder with the adequate size and taken to the Drop Shape Analyzer (DSA) to carried out the proper measurement. The experimental procedure for CA measurement is summarized in Figure 4.3. Each overall experiment including preparation and measurement required between 6 and 8 weeks due to the long aging times.

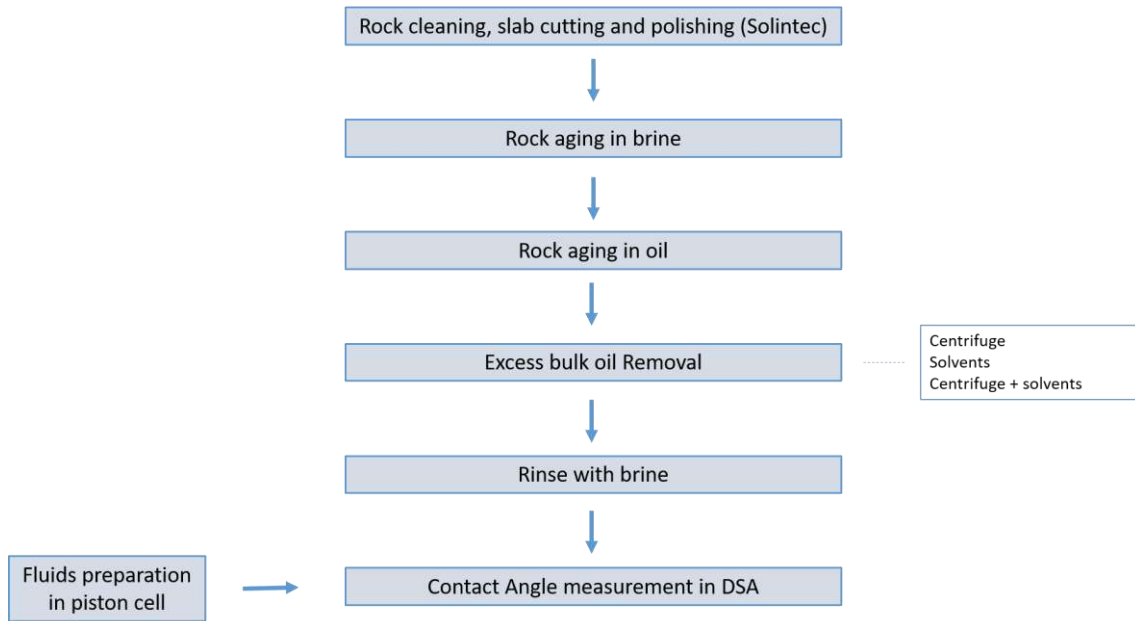


Figure 4.3. Flowchart summarizing the steps for contact angle measurement.

CA measurements were carried out using a Drop Shape Analyzer DSA 100E supplied by Kruss with a HPHT chamber designed by Eurotechnica. It consists of a goniometer with a high-resolution camera and sapphire glass windows capable of resisting temperatures up to 150 °C and pressures up to 7500 psi. All wetted parts are made of Hastelloy, making it appropriate for contact with high salinity brines and high concentrations of CO₂. The fluid can be injected from the top or bottom of chamber. The fluids to be used in the test are contained in a piston cell (or accumulator), and a high-precision positive-displacement pump is used to control the injection either at constant rate or constant pressure. A capillary tube of 1.6 mm external diameter is used for forming the droplets. The equipment has a PID temperature controller and a thermocouple that measures the internal fluid temperature with a resolution of 0.1 °C. The transducers that indicate the test pressure have a resolution of ±0.25%. The equipment is placed on an

anti-vibration containing a leveler to assure that the equipment is located on a flat surface minimizing the effects of tilting. A scheme of the setup is shown in Figure 4.4.

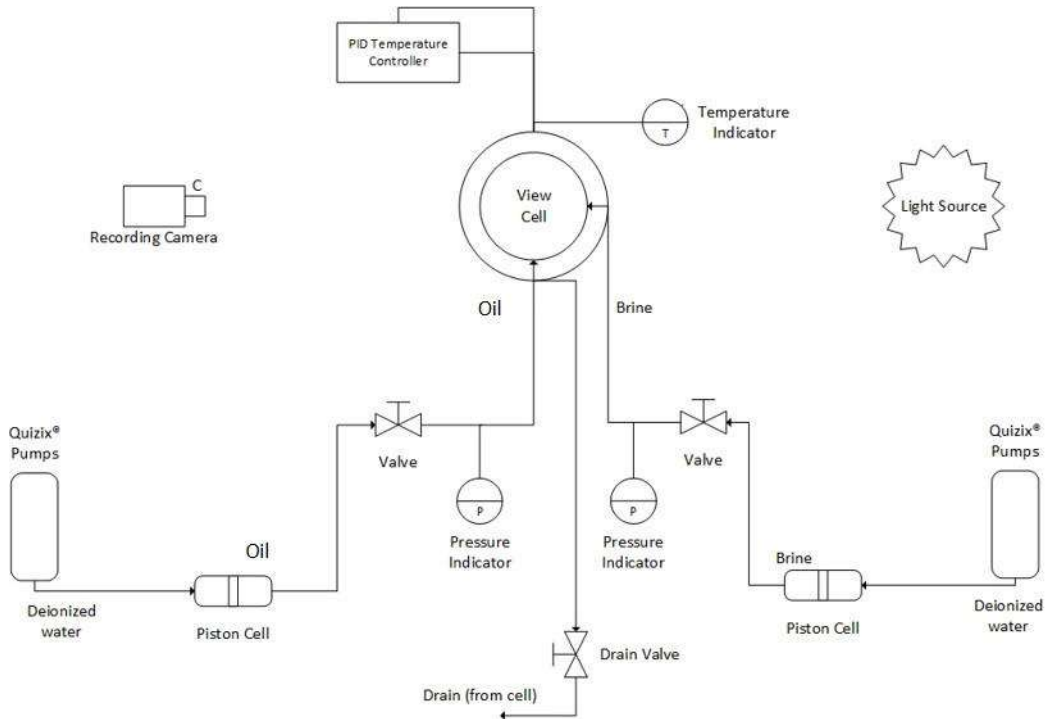


Figure 4.4. Scheme of the Drop Shape Analyzer equipment setup (adapted from (PARDINI DE SOUZA, 2018)).

a) Experiments with no CO₂

For CA measurement, the aged rock slab in the Teflon holder is placed in the high pressure chamber and adjusted to the horizontal position using the baseline provided by the software. Then the sapphire windows are tightened, and the chamber is filled with the external fluid (previously degassed brine). Every line in the system is bled to fully remove the air from the equipment. After this, the valves are closed and the fluid in the chamber is pressurized to the desired test pressure. When the pressure is stabilized, the heater is switched on increasing the fluid's temperature up to the test value. The pump used for brine injection is set to control the pressure at the desired value.

Since drop is the lighter phase, the oil drops are formed with the capillary tube from the bottom of the chamber. Once the temperature and pressure are stable, the drop fluid (oil) is pressurized in the accumulator to a pressure 10 psi higher than the pressure in the DSA chamber. This is to avoid water entrance in the accumulator containing the oil phase. The valve that allows the entrance of fluid by the capillary tube is then open.

Oil is then injected through the capillary at a controlled rate of 5 ml/h. When the first drop is delivered, its size is increased until it is detached by gravity forces. The valve is closed, and the zoom is set to improve the visualization. The baseline is then adjusted to the three-phase contact line and the image and data acquisition begins. The software includes the calculation of the drop profile Fitting Error using the Robust Digital Image Analysis (ANASTASIADIS et al., 1987; THIESSEN et al., 1996) that aids in placing the baseline to optimize the image processing. The CA is measured towards the denser phase (brine) as represented in Figure 4.5. Then, lower CA values represent a more water-wet surface and greater CA values represent a more oil-wet surface. Measurements are performed every 30 seconds for the complete experiment time. In this work, the following criteria to classify wettability is used (ANDERSON, 1986):

- $CA < 60^\circ$: water-wet
- $60^\circ < CA < 75^\circ$: weakly water-wet
- $75^\circ < CA < 105^\circ$: intermediate-wet
- $105^\circ < CA < 120^\circ$: weakly oil-wet
- $CA > 120^\circ$: oil-wet

The software contains different methods for CA calculation. “Tangent 1” assumes an elliptical drop shape and calculates the contact angle by finding the equation for the ellipse that best fits the drop profile. In contrast, “Tangent 2” obtains the angle by fitting the tangent lines at the intersection with the baseline. The former method is recommended for lower contact angles since droplets which do not wet the surface can be represented by elliptical shapes. On the other hand, “Tangent 2” should be used for intermediate and strongly wetting drops. The results can also be crosschecked by analyzing the images in digital image processor with angle measurement function, such as ImageJ®.

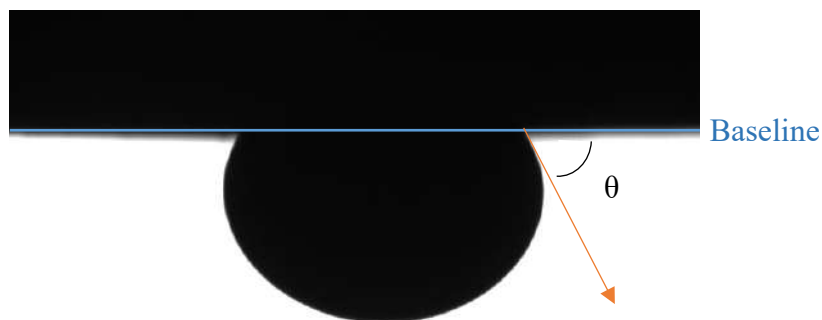


Figure 4.5. Picture of a droplet showing the baseline and the measured contact angle.

After the experiment is finished, the pressure and temperature in the chamber are decreased and the liquids are drained using the lines for that purpose. The rock slab is removed, cleaned and stored for characterization. The DSA equipment is then clean thoroughly flushing toluene and methanol in the chambers and all the lines until the effluents are clear of contamination. Finally, the equipment is dried using nitrogen gas to vaporize the residues of methanol from the chamber and lines.

b) Experiments with a CO₂ gas cap

In this type of experiment, CO₂ is added to the system forming a separate gas cap above the water phase. Even though the density of CO₂ at supercritical conditions can be higher than many liquids, the aqueous phase; thus, the CO₂ cap stays located on top.

The test is carried out in a similar fashion as the procedure described before. After depositing the drop, CO₂ is injected at a controlled rate with a pump by opening the valve on the top of the system. The pump connected to the brine phase retracts the flow to keep the pressure constant. Gas injection is carried out until reaching 20% of the internal volume of the chamber. Next, the valve on top is closed and the pressure is kept constant by the pump that injects the brine.

Typically, the gas cap is injected at the lowest test pressure (i.e. 1000 psi). The system is set to stabilize while CA values are acquired. After the stabilization time (see Section 4.3 for equilibrium values calculation), pressure is increased through brine injection. To avoid the dissolution of the gas cap, more CO₂ is injected to keep the gas cap volume constant. This procedure is repeated until reaching the highest test pressure (i.e. 5000 psi).

This method measures CA values while mass transfer is taking place from the gas to the brine phase and from the brine to the oil phase. This produces oil swelling during the test which may affect the measured CA leading to incorrect interpretations regarding wettability changes in the system. Another disadvantage of this method is that CO₂ is dissolved in the fluids after drop deposition. This could hinder the effects of wettability changes due to the pinning of the three-phase line (ANASTASIADIS et al., 1987).

Some modifications in this procedure were applied to analyze their effects on the results. The set of experiments identified as “New drop gas cap” were carried out in a similar manner as in the “Gas cap” procedure. The difference was that a new droplet was

deposited on a new substrate for each test pressure. The objective of these tests was to evaluate the effects of pressure on a new drop instead of increasing the pressure after the drop was already in contact with the solid and the three-phase line was pinned.

In the experiments identified as “Pre-equilibrated gas cap”, the gas cap was formed prior to drop deposition at the desired pressure. The substrate was kept immerse in the brine in contact with the gas cap for 24 hours. This was to allow time for CO₂ dissolution in the aqueous phase and reaction with the rock substrate. During this time, the oil phase was saturated with CO₂ at the test pressure and let to equilibrate in the piston cell. The purpose of this was to minimize CO₂ mass transfer between the oil and brine phases. Finally, the drop was formed and the measurements proceeded as described in the previous paragraphs. As for the previous procedure, in this test a new drop was formed on a different substrate for each test pressure.

c) Experiments with pre-equilibrated fluids

In these tests the corresponding volume of CO₂ to achieve the desired concentration is injected into the separate piston cells containing the brine and oil phases (see Section 4.1.4 for the experimental procedure). For the experiments with saturated fluids, an excess of three times the solubility at the highest test pressure was used. The recombined fluids with CO₂ are shaken in the piston cell and let to reach mass transfer equilibrium for at least 24 h.

To carry out the measurements, first the rock slab is placed in the chamber, and test brine with no dissolved CO₂ is injected to eliminate the air in the equipment and lines as in the previous procedures. Then, the system is pressurized and the temperature increased until reaching the test conditions. The pre-equilibrated brine with dissolved CO₂ is then injected at a low flowrate (i.e. 50 ml/h) at the top of the chamber while the brine with no dissolved CO₂ is retracted on the bottom keeping the test pressure constant. This exchange of fluids is continued until the total volume injected is greater than twice the volume of the system (including the dead volume of the lines). Finally, the pre-equilibrated oil with dissolved CO₂ is injected in the capillary tube at a flowrate of 5 ml/h as in the procedures described before. A schematic representation comparing the “Gas cap” and the “Pre-equilibrated fluids” experimental conditions is shown in Figure 4.6.

These experiments are the most consistent to analyze the interaction between carbonated brine and the different rocks. In addition, they give information about the initial wettability of the system when CO₂ is already present in the fluids in at different concentrations, such as in the case of some of the Pre-Salt reservoirs. It should be noted that, in this procedure, when the oil droplet is deposited on the rock surface, the carbonated brine has already contacted the surface. Thus, the initial wettability indicated by these tests is more representative of reservoir conditions where brine and oil have originally high CO₂ contents.

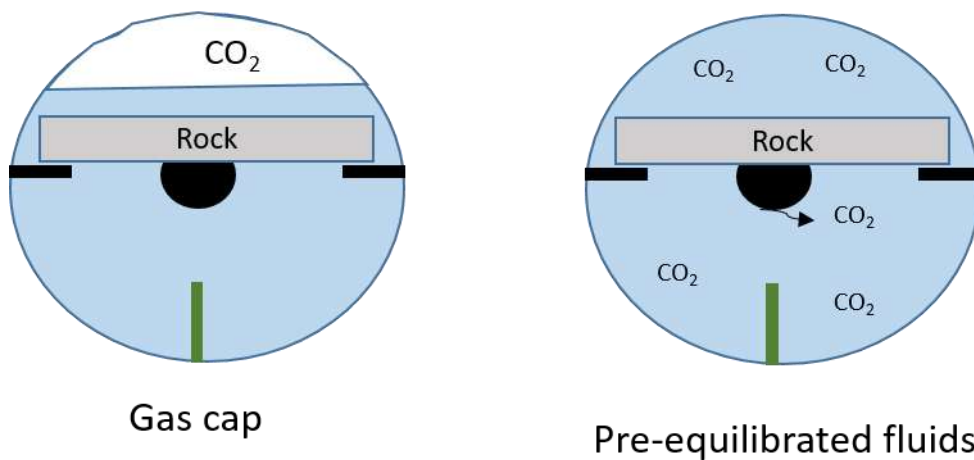


Figure 4.6. Scheme representing “Gas cap” and “Pre-equilibrated fluids” experiments.

4.1.2 Interfacial Tension Measurement

The interfacial tension (IFT) is measured to evaluate the interactions between the aqueous polar phase (brine) and the non-polar organic phase (oil) under different conditions. As discussed in Section 2.2, the IFT will be greater the more similar (in terms of polarity) the phases are. This is because similar molecules interact through stronger intermolecular forces reducing the energy difference between the molecules in the bulk and at the interface. Since the IFT is a surface property, as opposed to for example density, it is greatly influenced by small concentrations of surface-active components. Thus, depending on their molecular properties, asphaltenes and resins can affect the oil-brine IFT dramatically, even at low concentrations.

The IFT was analyzed using the DSA equipment using the method described in Section 2.2.3. The measurement consists in injecting a pendant drop of oil in the capillary

tube from the bottom of the equipment, which remains suspended due to the balance between gravity and interfacial forces. Before calculating the IFT value, the zoom needs to be adjusted to maximize the shape of the drop, and the magnification needs to be reset so the software can convert pixels into actual length values. The baseline needs to be adjusted above the tip of the needle to induce the software to neglect the lower part of the drop that has its shape affected by the contact with the needle. As pointed out in the CA measurement procedure, the Fitting Error function aids in the location of the baseline. Measurements are performed every 30 seconds for the complete length of the test (see Section 4.3 for data analysis and equilibrium IFT calculation). During each measurement, the software calculates the following output values: IFT, drop volume, drop surface area, drop shape parameter (B) and fitting error. The shape parameter, defined elsewhere (HOORFAR; KURZ; NEUMANN, 2005), represents the deformation from a spherical profile, and its expression is shown in Equation 4.1.

$$B = b \left(\frac{\Delta\rho g}{\gamma} \right)^{0.5} \quad (4.1)$$

where b is the radius of curvature at the apex, $\Delta\rho$ is the density difference between both fluids and γ is the interfacial tension. As discussed in Section 2.2.3, spherical drop shapes decrease the precision of the measurements. Therefore, shape parameters lower than 0.5 should be avoided to obtain reliable results. An image showing the measured and theoretical (HOORFAR; KURZ; NEUMANN, 2005) profiles for IFT calculation is shown in Figure 4.7.

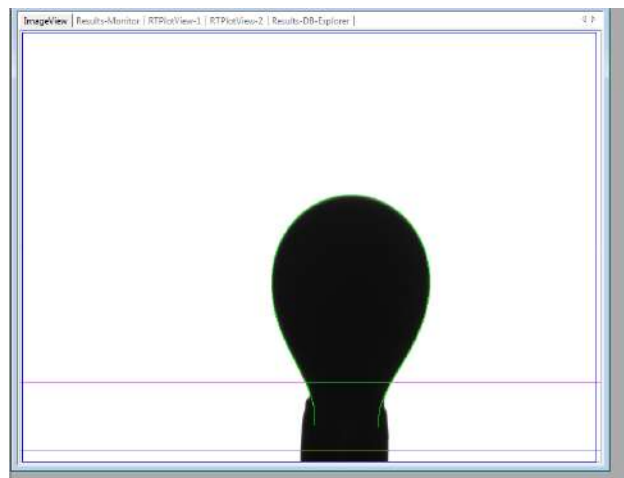


Figure 4.7. Image drop profile on DSA analysis software.

To calculate the IFT, the software solves the force balance that derives from the Young-Laplace Equation (Equation 2.6). It is evident that the density difference between both fluids at test conditions is a required input parameter in this method. For pure substances, density values at different thermodynamic conditions were retrieved from the NIST website (NIST, 2017). For reservoir oils and oils with dissolved CO₂, the densities were either calculated using PVTsim® (Section 4.2) or measured experimentally (Section 4.1.3). For brines and carbonated brines, densities were obtained either using OLI Studio® or measured experimentally using the same procedures than for oils.

As a new drop is created, IFT decays exponentially with time as the surface-active components diffuse to saturate the interface. The equilibrium value is obtained when mass transfer between phases reaches the steady state. Equilibrium time depends on the composition of the aqueous and organic phases, particularly with respect to the concentration and partitioning of surface-active components. The data analysis method to calculate the equilibrium IFT and to estimate the experimental error and repeatability is described in Section 4.3. A flowchart with the steps for IFT measurement is shown in Figure 4.8. Each overall experiment required 2 days for fluid equilibration.

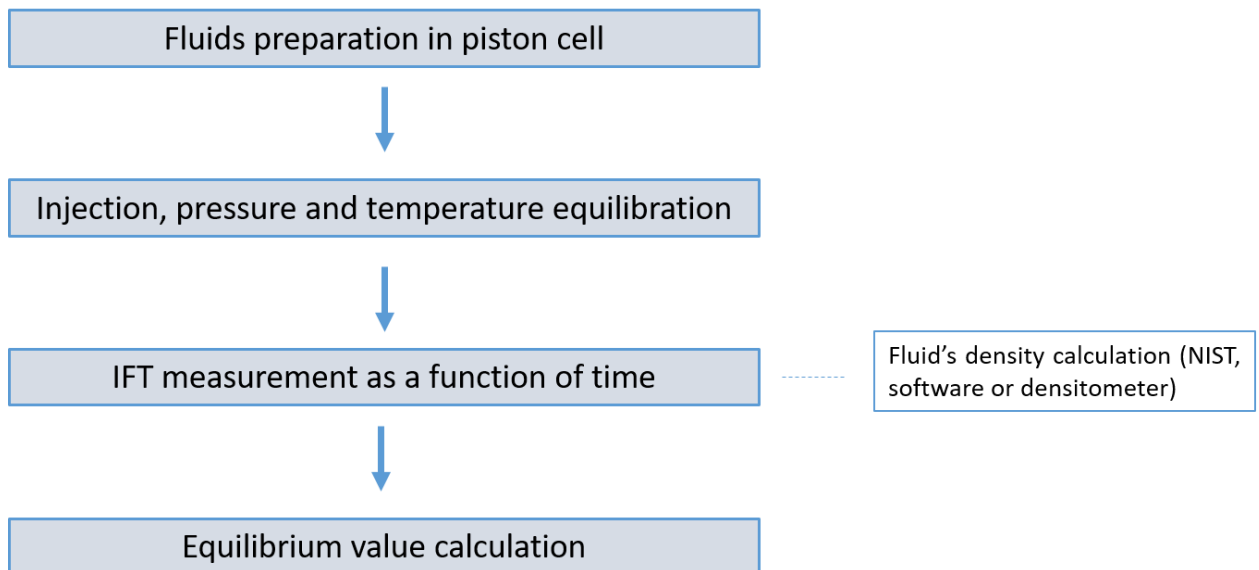


Figure 4.8. Flowchart with the steps for interfacial tension measurement.

As for the CA measurement, different types of experiments were carried out, which are briefly described as follows:

- a) Experiments with no CO₂

These tests study the IFT as a function of time at different pressures for the oil – brine systems in the absence of CO₂. Two different procedures were used. In the “New drop” experiments, a new droplet is formed for each measurement, and a series of drops at the same conditions are analyzed to assess repeatability.

In contrast, the “Same drop” experiments consist of analyzing the effect of pressure on the IFT for the same drop. After reaching equilibrium, the pressure is increased. To avoid a decreased volume due to the compression of the drop, oil is injected to keep the same drop volume for all the test pressures. The “Same drop” experiment seeks to evaluate the equilibrium IFT reducing the mass transfer diffusion time for the different pressure values considered in the test.

b) Experiments with a CO₂ gas cap

The procedure for injecting a gas cap is similar than the one explained in Section 4.1.1. In this procedure, mass transfer between the CO₂ gas cap produces carbonation of the brine phase. Moreover, CO₂ diffuses to the oil drop causing swelling. The augmented drop volume increases the effect of gravity forces, which eventually will cause the detachment of the drop. These experiments are interesting to observe the effects of swelling as CO₂ is dissolved in the aqueous and oil phases. Nevertheless, it cannot be used to calculate the equilibrium IFT value due to the premature detachment of the pendant drop.

c) Experiments with pre-equilibrated fluids

Using the same procedure as in Section 4.1.1, the measurement is carried out to obtain the IFT between fluids with dissolved CO₂. In this procedure, drop swelling is minimized as, when the drop is formed, both fluids have CO₂ dissolved. Using this method, the equilibrium IFT for different CO₂ concentrations can be obtained as a function of pressure.

4.1.3 Materials characterization

This section summarizes the techniques used to characterize the different materials used in this experimental work.

a) Brines

Characterization of the produced brines was done by measuring the pH and conductivity in a Mettler Toledo SevenExcellence™ benchtop meter. Total dissolved solids (TDS) values were obtained from conductivity measurements by performing calibration curves to obtain the TDS-factor for each type of brine as reported elsewhere (REBELLO; SIEPMAN, 2018). In addition, density measurements at ambient conditions (25 °C and 14.7 psi) were carried out in a Mettler Toledo DM40 densitometer.

b) Oils

SARA analysis was performed by IP 143 *n*-heptane precipitation method (asphaltenes) and medium pressure liquid chromatography (saturates, resins and aromatics). In addition, the total acid and basic numbers (TAN and TBN) were obtained by the procedure in ASTM D664, and API was measured in a Mettler Toledo DM40 densitometer. Water content of the crude oil samples were measured in a C20 Karl Fischer Coulometer.

High-pressure density measurements were performed using an Anton Paar DMA HPM densitometer with a thermostatic bath. Injection pressure was controlled by use of Quizix pumps. The fluid sample was initially pressurized in a piston cell. The pressure drop across the system was regulated adjusting both valves, and back pressure was controlled by connecting an evacuated piston cell controlled by an additional pump. More details about this procedure can be found elsewhere (PÉNELOUX; RAUZY; FRÉZE, 1982). In addition, dead oil viscosity at atmospheric pressure and different temperatures was measured with an Anton Paar SVM 3000.

Moreover, the composition of the crude oil samples and rock cleaning solvents was analyzed using Gas Chromatography (Agilent GC7890) using a DB-Petro (Agilent) column with a length of 50 m, a diameter of 0.2 mm and a 0.25 μm film.

Asphaltene fractions from Oils B and D were separated using *n*-heptane for precipitation following the procedure in the literature (FRANCO et al., 2013). The typical asphaltenes absorption bands of the dried extracted solids were confirmed by Fourier-transform infrared spectroscopy (FTIR) using a Nicolet 6700 spectrometer (Thermo Scientific) with a DTGS KBr detector. Carbon, hydrogen and nitrogen contents were obtained by elemental analysis with a Thermo Finnigan Flash EA1112 CHN analyzer. The temperature was 900 °C and helium and oxygen flows were 130 and 250 ml/min.

c) Rocks

Petrographic thin layer analysis was carried out by Solintec using the following procedure. First, samples were cleaned in a soxhlet system using toluene and chloroform until no fluorescence was detected under UV light. Then, methanol was used to remove excess salts until no reaction with silver nitrate was noticeable. Finally, they were dried at 90 °C. Then, the samples were impregnated with epoxy resin under vacuum followed by adherence to a glass sliver. Polishing reduced the thickness of the layer up to 30 microns, optimal for characterization of the minerals. Dying with S red alizarine and potassium ferricyanide in HCl 10% aided in the identification of carbonate minerals. Petrographic analysis was performed in a Zeiss A2 microscope with magnifications from 1.25X to 40X. In this work, a summary including the features more relevant to rock wettability are presented. In addition, rock surface texture, existence of pores, fractures, clusters of different minerals and other visual conditions were observed by analyzing their surfaces in a Zeiss Stereo Discovery V8 optical microscope.

Mineralogical composition of rock samples was characterized by X-ray diffraction XRD. First, rock samples were pulverized in an agate grinding mill followed by micronization in a McCrone mill. XRD analysis were carried out in a Bruker D8 Advanced diffractometer using the following test conditions: Cu tube, 40 kV nominal tension and 40 mA current, Soller slit 2.5°, primary slit 0.6 mm, secondary slit 5 mm, LINXEYE® linear detector with opening of 189 channels, Ni filters of 0.02mm, step size of 0.02 and speed of 1.1 °/min. Qualitative mineralogical analysis was done with Jade 9 software (with PDF-2 database). Quantitative analyses was done using the Rietveld Method in the TOPAS software.

Surface characterization by Scanning electron microscopy (SEM) was performed in a Hitachi TM3030 Plus under low vacuum atmosphere and an acceleration voltage of 1.5 kV with Energy dispersive X-ray spectroscopy (EDS) for identification of the elements composing the surface using a Bruker XFlash MIN SVE detector.

In addition, confocal microscopy for qualitative characterization of surface topography was performed in Zeiss Laser Scanning Microscope LSM 700 using an individual area of 1.2 x 1.2 mm and a tile scan of 6.5 x 5.1 mm and a depth ranging between 300 m and 700 µm.

Microscopic roughness was measured using Atomic force microscopy (AFM) using a WITec Alpha 300 microscope with a NCST-20 tip supplied by NanoWorld AG. The force constant was 7.4 N/m and the tip frequency 160 kHz using intermittent contact mode in an area of 15x15 μm . Five measurements were carried out for each sample.

Macroscopic roughness measurements were performed in a Bruker Dektak XT profilometer following the recommendations in ASME B46.1-1995. For each sample, six measurements at different parts of the surface were performed. Each measurement time was 60 seconds for an extension of 1 cm. The range was set to 6.5 μm with a radius of 12.5 μm , a force of 3 mg and a resolution of 0.555 μm .

4.1.4 Fluids preparation

This section describes the procedures used to prepare the brines and for CO₂ dissolution in both oil and brine phases.

a) Brine preparation

The salts used in brine preparation were purchased from Sigma Aldrich with purities over 99%. Deionized water (conductivity below 0,05 $\mu\text{S}/\text{cm}$) was produced in a Gehaka OS10LXE reverse osmosis system.

Brines were prepared dissolving the corresponding salts in deionized water using magnetic stirring and volume adjustment in volumetric flasks. Weighting of the required mass of salts was done in a Mettler Toledo MS3002S scale with a precision of 0.01 g. After preparation, brines were degassed using a vacuum pump.

b) CO₂ dissolution in oils and brines

Before combining with CO₂, oils and brines are degassed using a vacuum pump for 30 minutes. The corresponding fluid is then introduced in a piston cell containing a mixing ball, and the excess of air on top is eliminated by bleeding the cell. Then, the fluid is pressurized up to the recombination pressure (i.e. 1200 psi) using a positive displacement pump. 99.999% purity CO₂ (supplied by Praxair) is injected into a previously vacuumed piston cell and compressed up to recombination pressure using a Haskel booster compressor.

After the pressures in both fluids in the piston cells are stabilized, CO₂ is injected into the cell containing the test fluid (oil or brine) using a Quizix pump. The pressure in the cell containing the test fluid is kept constant by retracting on its water side with the other pump connected to it. The water volume that was removed from the cell, which is equal to the injected CO₂ volume, is recorded. The flow is continued until the required volume of CO₂ was injected into the test fluid. After that, the valves on the piston cell are closed isolating the test fluids, and the piston cells are shaken vigorously to favor the mixing.

The calculation of the volume that needs to be injected to achieve certain concentration was carried out by applying mass balances using the densities of the different fluids to convert masses into volumes at different thermodynamic conditions. For the case of saturated fluids, the solubility at the highest test pressure (i.e. 5000 psi) and lowest temperature (i.e. 25 °C) were used to assure that the fluid will be saturated at all pressure and temperature conditions considered the test. CO₂ solubility in oil and density of different mixtures were calculated in PVTsim. For the carbonated brines, solubility and densities were calculated in OLI Studio.

4.2 Computational Methods

The physical properties of brines with different concentrations of CO₂ were modelled using OLI Studio® software (OLI Systems Inc.). Input parameters include the concentration of the different salts and CO₂ and the thermodynamic conditions. Simulations are straightforward giving density, solubility pH and conductivity as outputs for the different conditions of pressure and temperature. A summary of the results obtained from this software are included in Appendix B.

Phase behavior of crude oils and mixtures with different concentrations of CO₂ was simulated in PVTsim® (Calsep). Soave-Redlich-Kwong equation of state with the volume correction presented by Peneloux (PÉNELOUX; RAUZY; FRÉZE, 1982). The CO₂ for EOR lumping model was applied. The composition of the crude oil was inputted from the gas chromatography data. Different mixtures corresponding to the volumes of each phase injected (according to the procedure in Section 4.1.4) were created. The phase behavior of these mixtures was studied using thermodynamic diagrams. Moreover, the physical properties of the corresponding liquid phase, which was the phase used in the

CA and IFT tests, were obtained. The volumes of the liquid and excess CO₂ phase were obtained by flashing the mixture at recombination temperature and pressure (i.e. 60 °C and 1000 psi).

Statistical analysis of CA and IFT data was carried out in Statsoft Statistica 7.0® to evaluate the impact of different variables (i.e. aging time) on the output values. Design of Experiments was used to obtain significant sets of experiments. The tools implemented to analyze the relevance of the different variables included Correlation Matrix, ANOVA and Pareto Chart of Effects. A more extensive discussion of these results can be found in the literature (DREXLER et al., 2018).

4.3 Data analysis methods

CA and IFT measurements result in an extensive dataset that needs to be processed adequately to obtain meaningful results. During the CA tests, data is continuously acquired for periods over 12 hours. The identification of the most stable value was achieved using Visual Basic for Applications (VBA) in Microsoft Excel®. The dataset was divided in groups of 10, and for each group stability was tested using three different criteria. First, the amplitude, which is the difference between the minimum and maximum values of the group, has to be lower than 1°. Also, the variance of the values in the group needs to be lower than 0.05. Last, the slope of the linear regression of the plot of the CA's versus time must be between -0.01 and 0.01 °/min. The stability frequency (FS) for each data point was defined as the number of preceding measurements that satisfied all three criteria. In addition, the standard deviation (SD) and relative standard deviation (RSD) were calculated to check the consistence of the results within each interval. Finally, the CA and the FS were plotted versus time to aid in the identification of the most stable CA value for each measurement. The reported value was the arithmetic mean of the values in the most stable interval.

IFT between oil and brine decays over time as, when a new drop is formed, surface active species diffuse towards the interface (GEORGIADIS et al., 2010). This results in a slow equilibration process which can take several hours depending on the composition of the phases and the thermodynamic conditions. In order to identify the stabilization time, the curves were fitted with a logarithmic function. Since this type of function does not converge to a final value at infinite time, a threshold value of 0.01 mNm⁻¹h⁻¹ for the

derivative of the fitted function was implemented to calculate the stabilized IFT value. In addition, dynamic were calculated as the mean of the values at 150 and 900 seconds, following the adopted values for the water-CO₂-decane system in the literature (GEORGIADIS; TRUSLER; BISMARCK, 2011).

To analyze repeatability and data consistency each type of experiment (both IFT and CA) was repeated a minimum of 3 times. The informed results are the mean values, and the standard deviation was calculated to assess data dispersion. The standard error of the mean is informed in tables or as error bars in plots to show the relevance of the changes in the different measured values.

CHAPTER 5: MATERIALS

CHARACTERIZATION

5.1 Brines

Brine with three different compositions were used in this work. Two of them (Brine B and D) correspond to the compositions of formation brine from producing wells in two Pre-Salt fields (Field B and D). The third one (DSW) corresponds to the desulfated injection water commonly used in Pre-Salt fields to avoid calcium, barium and strontium sulfate scaling problems. All three compositions were supplied by Shell Brasil. The ionic concentrations of these aqueous solutions, their total dissolved solids (TDS), pH and densities are presented in Table 5.1. The experimental techniques in Section 4.1.3 were used for the characterization of the produced brines.

Although Field B has a salinity 10% higher than Field B, both formation brines are considered of high salinity (above 200000 ppm). pH is slightly acidic being lower for brine B. DSW, on the other hand, has a salinity close to seawater (approximately 35000 ppm), low hardness and basic pH.

5.2 Oils

Dead crude oil samples from Fields B and D were supplied by Shell Brasil. SARA analysis was performed by IP 143 *n*-heptane precipitation method (asphaltenes) and medium pressure liquid chromatography (saturates, resins and aromatics). The results for the oils are shown in

Table 5.2. For Oil B, the analysis was also carried out for samples reutilized after the aging process, to evidence the effects aging at reservoir temperature on the properties of the oil.

Table 5.1. Ionic composition (ppm), total dissolved solids TDS, and pH and density (ρ) for the different brines used in this work.

| Ion | Brine B | Brine D | DSW |
|-------------------------------|---------|---------|-------|
| Na ⁺ | 57584 | 62250 | 12000 |
| Ca ²⁺ | 24260 | 17480 | 500 |
| Mg ²⁺ | 2121 | 1430 | 1700 |
| K ⁺ | 1201 | 5180 | 500 |
| Ba ²⁺ | 22 | 149 | - |
| Sr ²⁺ | 1269 | 1800 | 9 |
| Li ⁺ | - | 152 | - |
| SO ₄ ²⁺ | 54 | 15 | - |
| Cl ⁻ | 139900 | 121400 | 21347 |
| HCO ₃ ⁻ | - | 1094 | 101 |
| Acetate | - | 188 | - |
| Br ⁻ | - | 586 | - |
| TDS (ppm) | 226401 | 200319 | 35177 |
| pH* | 5.7 | 6.1 | 7.0 |
| ρ (g/ml)* | 1.18 | 1.11 | 1.03 |

* At 25 °C and 14.7 psi.

In addition, the total acid and basic numbers (TAN and TBN) were obtained by the procedure in ASTM D664, and API was measured in a Mettler Toledo DM40 densitometer. These properties are included in Table 5.3. Oils B and D correspond to lighter crudes. On the other hand, aged Oil B (Oil B2) represents a medium to heavy crude, this could be verified by its lower API and much higher viscosity at test temperature. All the Pre-Salts oils considered have low acid numbers and considerably higher basic numbers. Even though TAN/TBN ratio lower than 1 indicates greater amount of positive ions at the oil-brine and oil-solid interfaces (CAMARA et al., 2014; CORBETT; BORGHI, 2013; PEPIN et al., 2014; TELES et al., 2016), this information

alone is not enough to make conclusions regarding the wettability of different rocks. It should not be assumed that these oils have greater interaction with rocks having negative surfaces because, as discussed in Section 2.3.2, the interactions that control wettability are complex and different phenomena occur at the same time. To make such conclusions, the surface properties of the existing acids and bases in the oil need be considered as well. In addition, the divalent ions in the brine could also aid in the adsorption of positive/negative species on positive/negative surfaces. Furthermore, the presence of asphaltenes and resins on the oil could increase the interaction of the oils with positive-charged surfaces. These properties will be used throughout this text to support the results and discussions.

Table 5.2. SARA analysis of the Pre-Salt crude oils used in this work (wt.%).

| | Oil B | Oil B2(after aging) | Oil D |
|-------------|-------|---------------------|-------|
| Saturates | 64.06 | 40.00 | 56.65 |
| Aromatics | 25.98 | 20.00 | 30.11 |
| Resins | 8.46 | 32.50 | 10.95 |
| Asphaltenes | 1.50 | 7.50 | 2.29 |

Table 5.3. Total Acid and Base Numbers (TAN and TBN) and API of the Pre-Salt crudes.

| | Oil B | Oil B2 (after aging) | Oil D |
|-----------------|-------|----------------------|-------|
| TAN (mg KOH/g) | 0.37 | 0.37 | 0.40 |
| TBN (mg KOH/g) | 4.0 | 4.0 | 4.0 |
| API | 26.14 | 18.60 | 23.36 |
| Viscosity (cp)* | 14.5 | 83.2 | 27.4 |

* Measurements carried out at 60 °C, 14.7 psi using the procedures in ASTM D7042.

Table 5.4 shows the Gas Chromatography analysis (Section 4.1.3) results for the oils used in this work. Although a similar distribution is observed, Oil D presented a higher concentration of high molecular weight compounds.

Table 5.4. Gas chromatography composition (wt.%) of the crude oils used in this work.

| Component | Oil B | OIL B (after aging) | Oil D |
|--------------------------|-------|---------------------|-------|
| <i>i</i> -C ₄ | 0.01 | 0 | 0 |
| <i>n</i> -C ₄ | 0.01 | 0 | 0 |
| <i>i</i> -C ₅ | 0.12 | 0 | 0.03 |
| <i>n</i> -C ₅ | 0.18 | 0 | 0.06 |
| C ₆ | 0.48 | 0.03 | 0.26 |
| Mcyclo-C ₅ | 0.21 | 0 | 0.13 |
| Benzene | 0 | 0 | 0.01 |
| Cyclo-C ₆ | 0.19 | 0 | 0.12 |
| C ₇ | 0.94 | 0.03 | 0.37 |
| Mcyclo-C ₆ | 0.48 | 0 | 0.37 |
| Toluene | 0.03 | 0.01 | 0.06 |
| C ₈ | 1.72 | 0.01 | 1.31 |
| C ₂ -Benzene | 0.08 | 0 | 0.07 |
| <i>m&p</i> -Xylene | 0.09 | 0 | 0.12 |
| <i>o</i> -Xylene | 0.05 | 0 | 0.06 |
| C ₉ | 2.11 | 0.01 | 1.7 |
| C ₁₀ | 2.61 | 0.02 | 2.22 |
| C ₁₁ | 2.56 | 0.02 | 2.18 |
| C ₁₂ | 2.68 | 0.05 | 2.31 |
| C ₁₃ | 3.12 | 0.12 | 2.65 |
| C ₁₄ | 3.03 | 0.31 | 2.58 |
| C ₁₅ | 3.29 | 0.89 | 2.82 |
| C ₁₆ | 2.9 | 1.60 | 2.48 |
| C ₁₇ | 2.85 | 2.45 | 2.4 |
| C ₁₈ | 3.15 | 3.40 | 2.71 |
| C ₁₉ | 2.89 | 3.47 | 2.47 |
| C ₂₀ | 2.62 | 3.36 | 2.29 |
| C ₂₁ | 2.54 | 3.33 | 2.3 |
| C ₂₂ | 2.47 | 3.39 | 2.25 |
| C ₂₃ | 2.39 | 3.25 | 2.23 |
| C ₂₄ | 2.38 | 3.24 | 2.27 |
| C ₂₅ | 2.31 | 3.13 | 2.24 |
| C ₂₆ | 2.33 | 3.21 | 2.27 |
| C ₂₇ | 2.37 | 3.23 | 2.37 |
| C ₂₈ | 2.39 | 3.36 | 2.44 |
| C ₂₉ | 2.45 | 3.38 | 2.53 |
| C ₃₀₊ | 39.97 | 54.68 | 47.32 |

5.3 Rocks

This research employed different type of rocks as the solid phase to study systems with increasing degrees of complexity. The simplest type of solids were pure minerals, and quartz (UQG Optics Ltd), calcite and dolomite (Wards Science) were used to represent the main components of Pre-Salt carbonate rocks. The purpose of using pure minerals is to simplify the effects of heterogeneity and surface roughness to be able to isolate wettability effects on surface with uniform chemical behavior. In addition, it is interesting to compare wettability results obtained for pure minerals to that of complex rocks.

The second type of rocks in complexity are the Indiana Limestone (IL) samples (Kocurek Industries Inc.), which represent a carbonate rock with measured porosity and permeability and homogeneous or slightly heterogeneous surface properties. Limestone is mostly composed of calcite, but it can contain varying amounts of different minerals, such as quartz, clay or pyrite. This is more representative than the pure minerals since limestone samples are actual porous cores.

Coquinas outcrops from Morro de Chaves formation in Northeast Brazil, (Sergipe-Alagoas) were proposed as analogues of some of the Pre-Salt fields that contain coquinas in their rock composition (CAMARA et al., 2014; CORBETT; BORGHI, 2013; PEPIN et al., 2014; TAVARES et al., 2015). A summary of the main characteristics of this formation is included in Section 1.2.2, and a complete description can be found elsewhere (TAVARES et al., 2015). These rocks represent analogues of some sections of the Pre-Salt, but the mineralogy is less complex than that of subsurface reservoir rock.

Finally, rock samples (D1 to D4) of a Pre-Salt field were studied to evaluate wettability for actual reservoir components. These rocks contain a diverse mineralogical composition and heterogeneous surface and rock properties, such as porosity and permeability.

The following sections describe the characterization of these materials by different techniques.

5.3.1 Optical microscopy

Calcite and dolomite samples, as prepared for CA measurement, were observed in the optical microscope (see Section 4.1.3 for specifications) using magnifications from 1.25x to 6.3x. The images for these minerals are shown in Figure 5.1 and Figure 5.2. For calcite, the appearance is of a homogeneous mineral with no irregular spots, only the cleavage plane and lines from rock cutting are visible. For dolomite, the typical texture of this mineral is observed. However, other minerals (i.e. calcite) are present as shown in the irregularities on the surface. Figures 5.1-5.5 contain the images for coquinas, rock D and IL samples. The expected differences such as heterogeneous mineralogy, presence of pores in the micron scale and cementation are visible. Nevertheless, the polished flat surfaces indicate smooth topography to this degree of magnification.

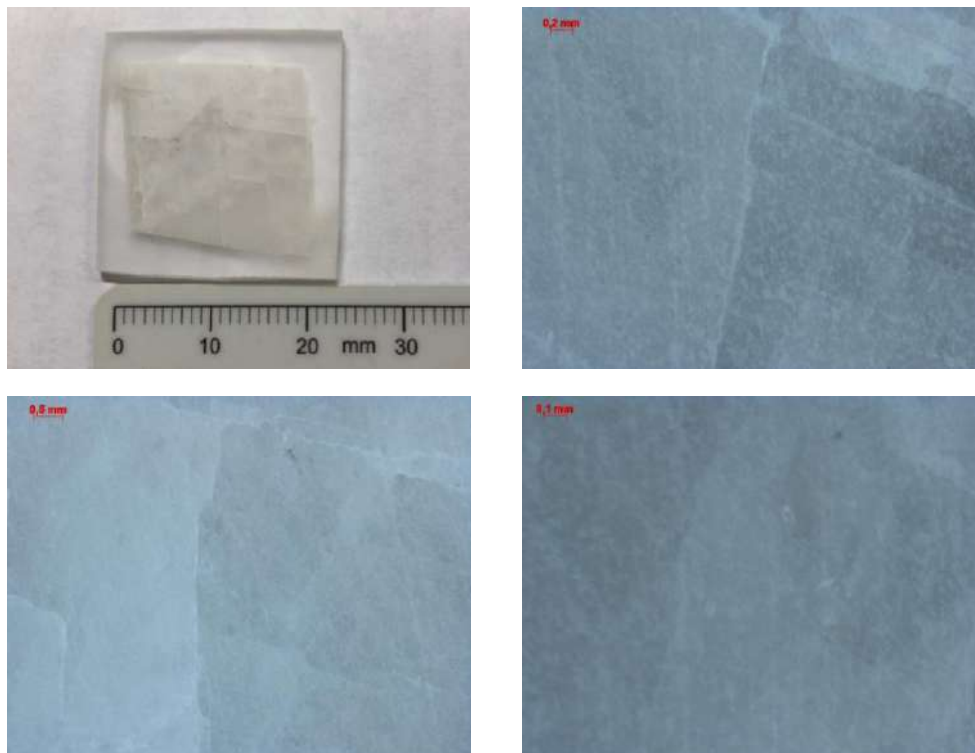


Figure 5.1. Optical microscope images of calcite with magnifications of 1.25, 2.5 and 5.

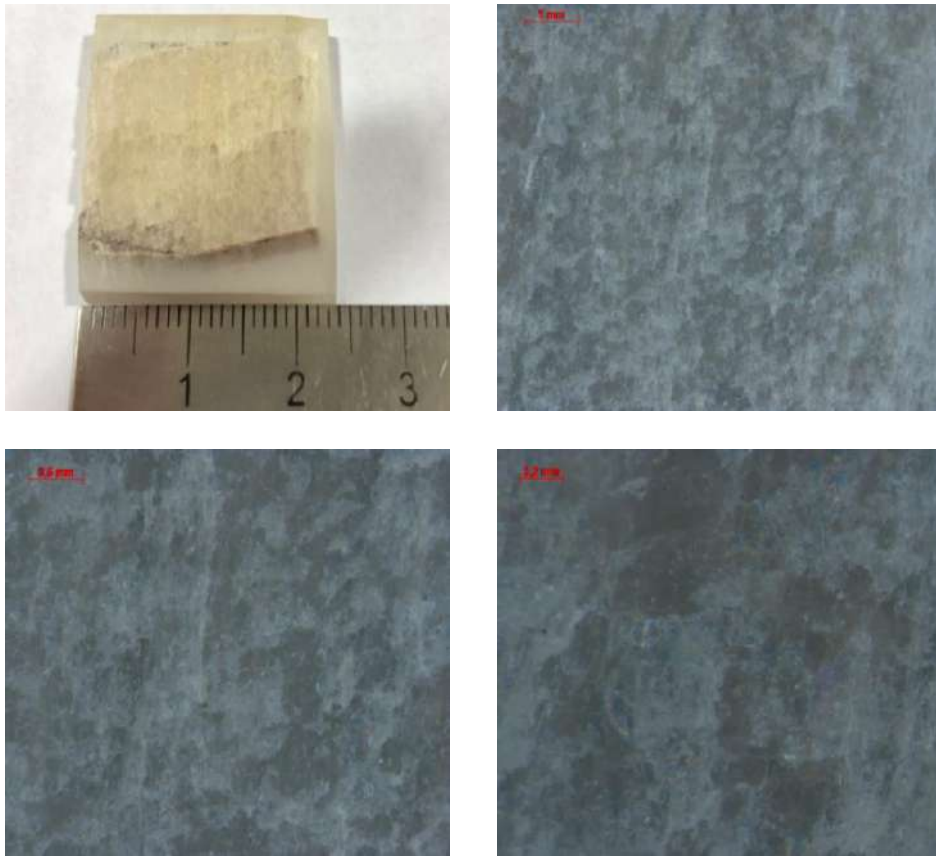


Figure 5.2. Optical microscope images of dolomite calcite with magnifications of 1.25, 2.5 and 5.

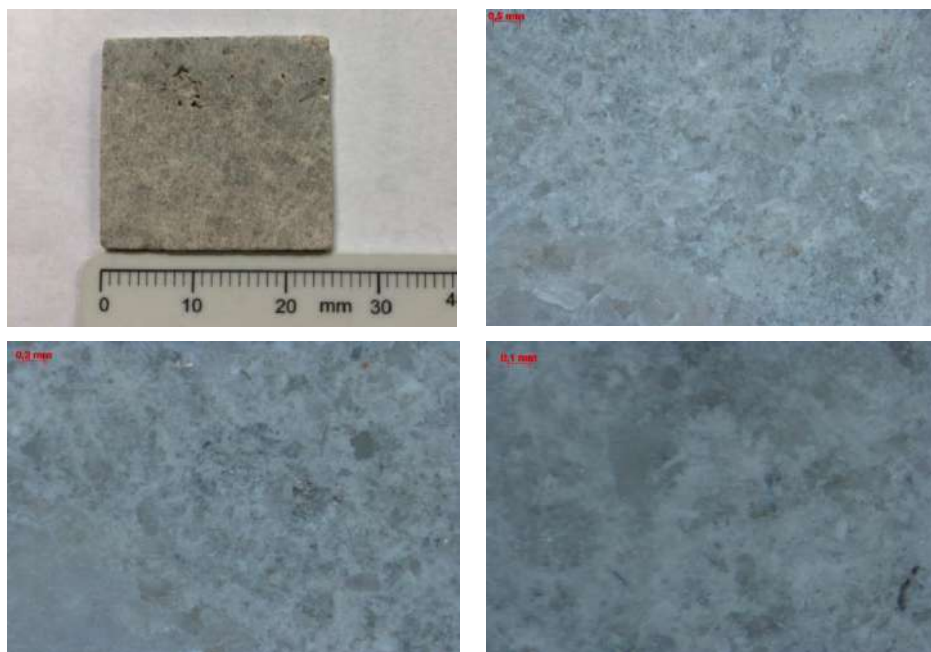


Figure 5.3. Optical microscope images of coquina sample with magnifications of 1.25, 2.5 and 5.

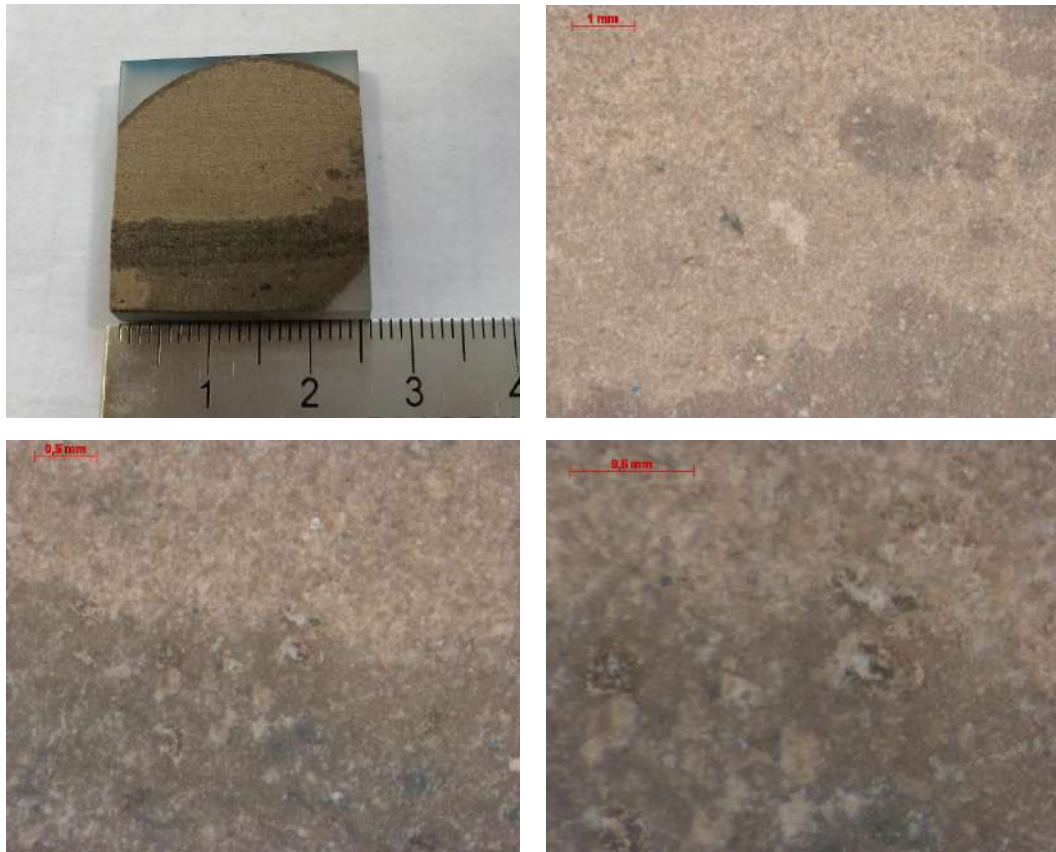


Figure 5.4. Optical microscope images of D rock sample with magnifications of 1.25, 2.5 and 5.

5.3.2 Petrographic thin section

For calcite and dolomite minerals, the petrographic thin sections (Figure 5.5) confirm the presence of the mineral with their well-known characteristics. Calcite shows rhombohedral cleavage planes and poor vugular porosity. Moreover, dolomite shows rhombohedral cleavage with fractures and signs of recrystallization, which can be observed as lighter zones with differentiated texture.

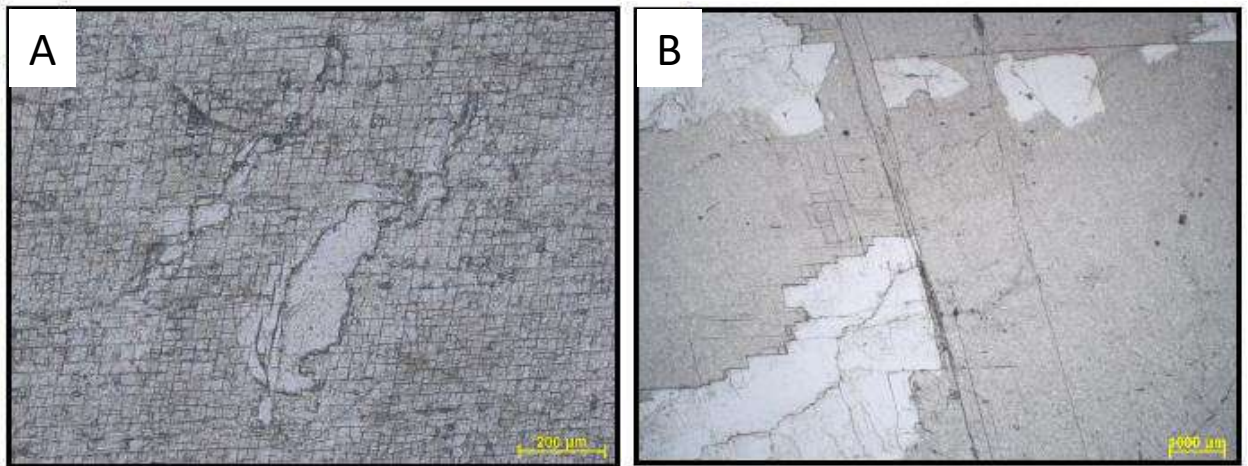


Figure 5.5. Thin layer microscopic analysis of calcite (A) and dolomite (B) minerals.

Three cores from the coquina block in orthogonal directions (x, y and z) were drilled, and thin layers were performed in all of them. The analysis of images in Figure 5.6 retrieved that major grains of the framework are bioclasts (mainly bivalves and other no identified) and minor grains are quartz and feldspar. Also, they showed abundant inter and intraparticle cementation of calcite blocks. Muscovite and pyrite appeared as accessories. These characteristics are in agreement to the detailed description of other samples from this quarry in the literature (SEYYEDI; SOHRABI; FARZANEH, 2015).

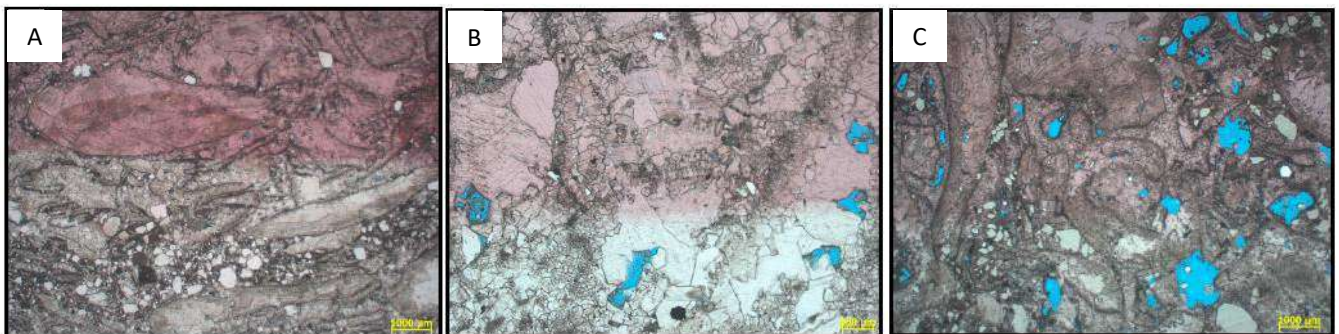


Figure 5.6. Thin layer microscopy of coquina x (A), y (B) and z (C) cores.

Figure 5.7 shows the images of thin layer analysis for two samples from the same well in Field D. Although both of them correspond to carbonates, they present distinct characteristics. Image A shows branching stromatolite structure based on optical calcite with rare spherulites of less than 1 mm and accessories of pyrite. Clays are present with their matrix partially replaced by dolomite and quartz crystals. Both micro (<0.03 mm) and macropores (up to 0.84 mm), which occur in channels. Nevertheless, Image B

consists of spherulites of up to 0.05 mm with some substitution by dolomite crystals resulting in poor interparticle and microporosity. Other constituents include quartz and muscovite.

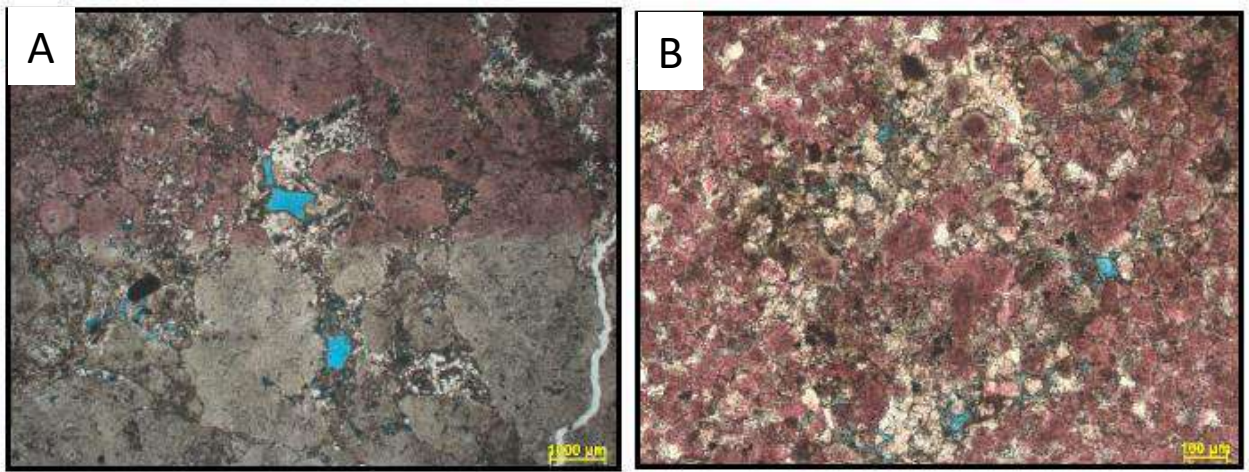


Figure 5.7. Thin layer microscopy of D reservoir rocks showing optical calcite (A) and spherulites (B).

5.3.3 Scanning Electron Microscopy (SEM)

SEM with EDS was performed to get a more detailed idea of the surface morphology of the samples and to identify individual components and their structures on the rock surface. Images of calcite (top) and dolomite (bottom) are shown in Figure 5.8. Homogeneous rhombohedral structure characteristic of calcite is visible. On the other hand, the bottom images show a more heterogeneous structure containing mainly dolomite and some dolomitized calcite.

Figure 5.9 contains SEM images of coquina samples where a macropore with its dimensions is visible. In addition, the presence of perfectly shaped calcite crystals with no signs of corrosion or abrasion is evident. Moreover, the results of EDS analysis to show the main elements on the surface are included. The results are in agreement with the petrographical description for these coquinas samples indicating calcite (Ca), quartz (Si) and pyrite (S and Fe not colored) as primary constituents of the surface.

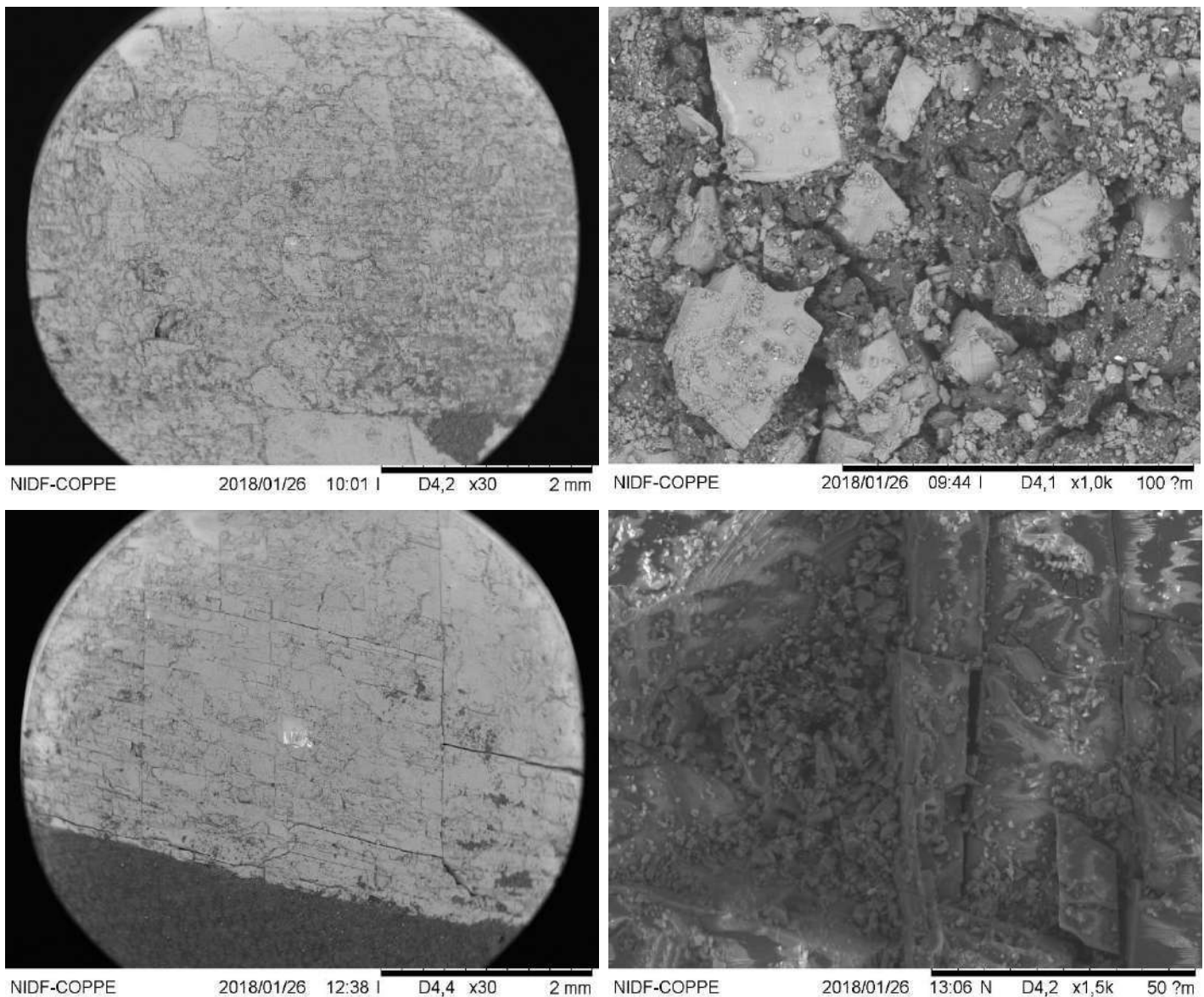


Figure 5.8. SEM images of calcite (top) and dolomite (bottom).

SEM images of D reservoir rocks including EDS analysis are shown in Figure 5.10. It can be observed that these rocks heterogeneous containing minerals of different types, clays and fiber forming materials. EDS identified calcium, silicon and magnesium as main elements indicating the presence of calcite, dolomite and quartz.

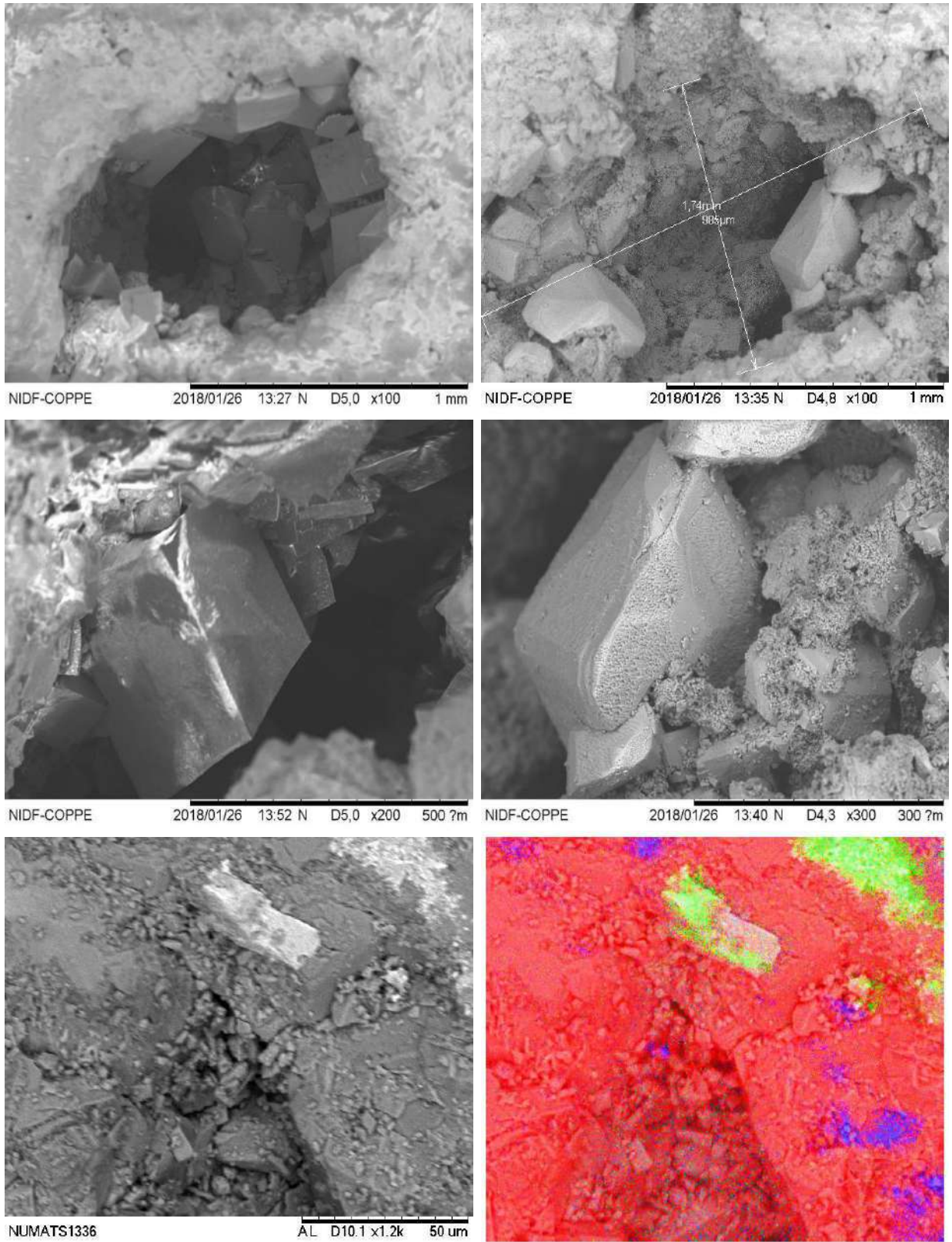


Figure 5.9. SEM images of coquinas samples. Last image shows EDS results showing calcium (red), silicon (blue) and sulfur (green) as main elements.

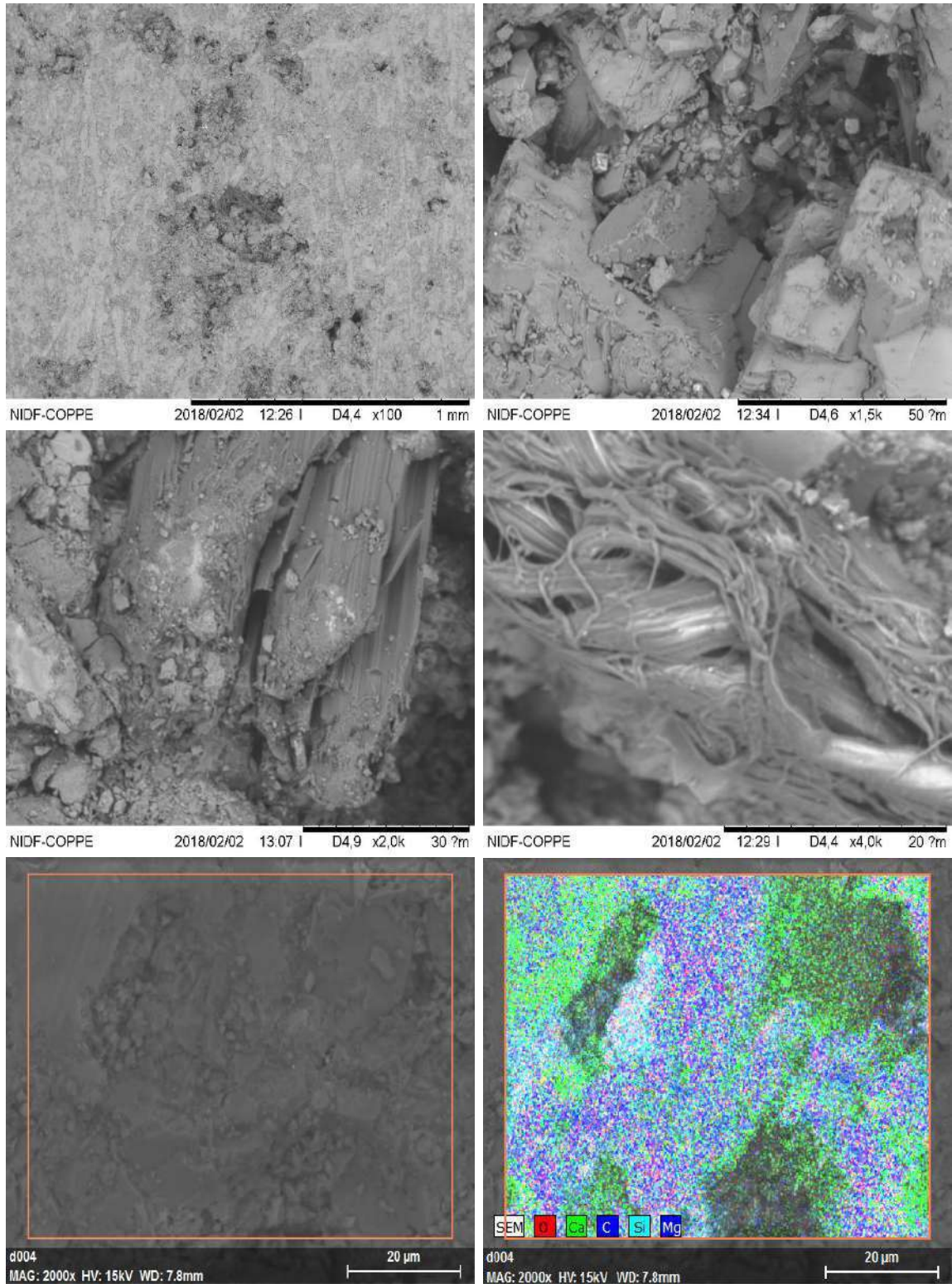


Figure 5.10. SEM/EDS images of D reservoir rocks.

Nevertheless, spotting different regions of several samples from the same well identified the presence of different fractions of other constituents. Sulfur, aluminum, iron, potassium and sodium appeared as secondary constituents indicating the presence of pyrite, muscovite, magnetite feldspar and halite. Figure 5.11 shows some EDS analyses of the same rock sample of reservoir D where the aforementioned elements are identified. It is noticeable that these reservoir rocks contain a high degree of heterogeneity containing a complex surface mineralogy. A list of the most relevant minerals with their formula and description is included in Appendix C.

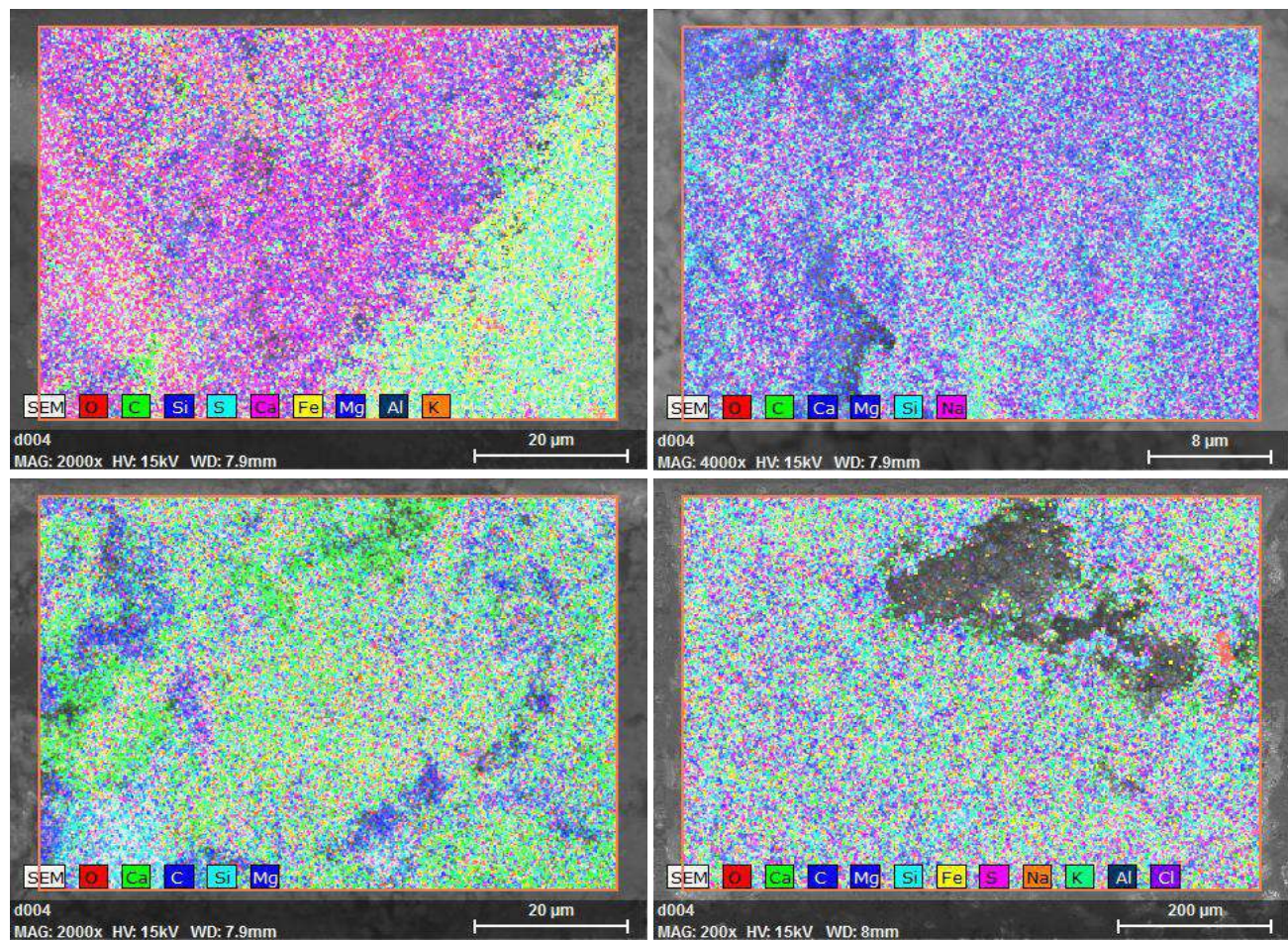


Figure 5.11. EDS analysis of a single D rock sample showing primary and secondary elements.

5.3.4 Surface roughness

Macroscopic roughness was measured using a profilometer as described in 4.1.3. The objective of these measurements, which are carried out on segments of 1 cm, is to analyze the effects of contact with carbonated water at HPHT conditions on surface profile. The consequences of reaction with CO₂ on calcite surface were qualitatively observed in previous works (BUTT; GRAF; KAPPL, 2006).

The average roughness and standard deviation values for the clean slabs of different materials are shown in Table 5.5. Optical quartz has the flattest surface. The other materials have higher greater macroscopic roughness after the cutting and polishing during slab preparation. The higher standard deviation of more complex coquinas and D rocks indicate the greater degree of heterogeneity for these materials.

Table 5.5. Profilometer average roughness and standard deviation of clean rock slabs.

| | R ave (nm) | SD (nm) |
|----------|------------|---------|
| Quartz | 4 | 1 |
| Calcite | 1096 | 283 |
| Dolomite | 3186 | 442 |
| Coquina | 2762 | 613 |
| Rock D | 3522 | 559 |

Microscopic roughness was assessed by AFM covering an area of 15x15 μm per measurement. The purpose of these measurements is to evaluate the degree of roughness that could affect CA measurement. The results are shown in Table 5.6. It can be observed that coquina samples have the greatest roughness in agreement with their greater porosity and wider pore distribution reported in the characterization techniques previously discussed. Nevertheless, surface roughness in the order of 1 μm are considered mild enough for the application of Wenzel approach for the effects of surface roughness on the apparent CA (JAEGER; ALOTAIBI; NASR-EL-DIN, 2010). Significant CA measurements have been reported for minerals, outcrops and reservoir rocks with average roughness of up to 20 μm (BUCKLEY, 1996).

It should be pointed out that the higher microscopic roughness obtained for calcite and dolomite (when compared to D rocks and Indiana Limestone) has a different origin from that of reservoir rocks. For the minerals, the roughness comes from polishing and uneven regions on the different planes of the mineral. For Indianal Limestone, roughness arises from being porous rocks. Therefore, it should not be considered that the surface area of the pure minerals is greater than that of the reservoir rocks, which most likely is not the case.

Table 5.6. AFM root mean square roughness and standard deviation of clean rock slabs.

| | RMS (nm) | SD (nm) |
|-------------------|----------|---------|
| Quartz | 1.4 | 0.09 |
| Calcite | 506 | 65 |
| Dolomite | 543 | 160 |
| Coquina | 1363 | 433 |
| D rocks | 332 | 71 |
| Indiana Limestone | 146 | 16 |

5.3.5 X-ray Diffraction (XRD)

XRD results for Indiana limestone, coquinas and Pre-Salt D rock are showed in Table 5.7. As expected, Indiana limestone consists basically of calcite with some quartz impurities. Moreover, coquinas are rich in calcite and contain variables amounts of quartz and some k-feldspar contents.

Finally, Pre-Salt reservoir rock had a greater concentration of dolomite (and Ca-dolomite) with calcite as second component. Quartz and dawsonite traces were also detected. It should be considered that the actual surface Ca and Mg content for these samples is not known. The SEM/EDS results presented in this chapter showed higher calcium concentrations at the surface indicating that a Ca/Mg ratio greater than 1 is likely. Furthermore, being heterogeneous reservoir rocks, this composition may differ among the different slabs. The analysis could not be performed in a greater number of samples due to limited number of samples.

Table 5.7. XRD results for different rocks. Results in wt%.

| | S# | Quartz | K-Feldspar | Calcite | Dolomite* | Dawsonite | Clays |
|--------------|----|--------|------------|---------|-----------|-----------|-------|
| I. Limestone | 1 | 0.7 | - | 99.3 | - | - | - |
| | 1 | 13 | 4 | 83 | - | - | - |
| | 2 | 1 | - | 99 | - | - | - |
| Coquina | 3 | 2 | Tr | 98 | - | - | - |
| | 4 | 7.5 | Tr | 92.5 | Tr | - | - |
| | 5 | 12.8 | 3 | 82.2 | Tr | - | 2 |
| Pre-Salt D | 1 | 6.4 | Tr | 30.0 | 63.6 | Tr | - |
| rock | 2 | 6.6 | 1.1 | 34.7 | 56.7 | 0.9 | - |

* Includes Ca-Dolomite (with a Ca/Mg ratio greater than 1:1).

** Tr means “traces” (i.e. lower than 1%).

CHAPTER 6: STUDY OF INITIAL WETTABILITY EVALUATION

This chapter presents the results and discussions related to the study of initial wettability for different rocks (minerals, outcrops and reservoir rocks). The initial sections of the chapter are dedicated to analyze how different processes of the method (i.e. aging, bulk oil removal method) influence the CA results. Furthermore, initial wettability of different type of rocks is studied for two Pre-Salt fields scenario (Field B and Field D). Final sections of the chapters discuss changes in oil and brine composition, such as the use of injection water instead of formation water and a model oil with no presence of asphaltenes or resins.

6.1 Development of the initial wettability evaluation technique

6.1.1 Excess bulk oil removal method

As discussed in Chapter 4, after aging the rock an excess bulk oil is deposited on the surface. This bulk oil is not adsorbed on the solid; it remains on the surface due to the fact that its viscosity is higher than that of the other fluids (i.e. brine). Contact angle (CA) cannot be measured without the removal of this bulk oil because it would not represent the three-phase line between the rock, the oil and the brine. Thus, to succeed in measuring the CA of aged rock samples, the excess oil needs to be removed from the surface. However, the method of removal is not trivial since excessive cleaning of the rock would also reverse the aging process. In addition, cleaning methods that would significantly alter the rock properties are also undesired.

As described in Chapter 4, this work considers two different methods for bulk oil removal reported in previous research. First, the solvents method consists of cleaning the rock surface with a fixed volume of solvents with different chemical characteristics. The challenge of this method is to find the right fluid that will rinse the bulk oil without removing the aging effects on the rock (SEYYEDI; SOHRABI; FARZANEH, 2015). The second method uses centrifugation, which has the advantage of rendering on physical effects rather

than chemical effects. The drawback could be that when the oil-solid interaction is very strong oil may still remain on the surface even after centrifugation (SEYYEDI; SOHRABI; FARZANEH, 2015). Comparison of these methods on different minerals is discussed in the following paragraphs.

Formation brine, n-hexane, n-hexadecane, cyclohexane and toluene were used as solvents for bulk oil removal. The first was used since it is the environment fluid where the CA measurements are run. In addition, the two normal alkanes are tested as two non-polar solvents with different carbon chain lengths, and cyclohexane is a hydrocarbon of intermediate polarity. Finally, toluene is used as an aromatic of higher polarity which is a well-known solvent for intermediate, heavy oils and asphaltene dissolution.

In these solvent screening tests, minerals were aged for 1 day in formation brine (B) and for 3 days in crude oil (B) at 60 °C. All measurements were carried out at 60 °C and 1000 psi. Experiments using centrifugation are also included. In addition, the results on non-aged rocks are added for comparison. Figure 6.1 sums up the results for calcite, dolomite and quartz.

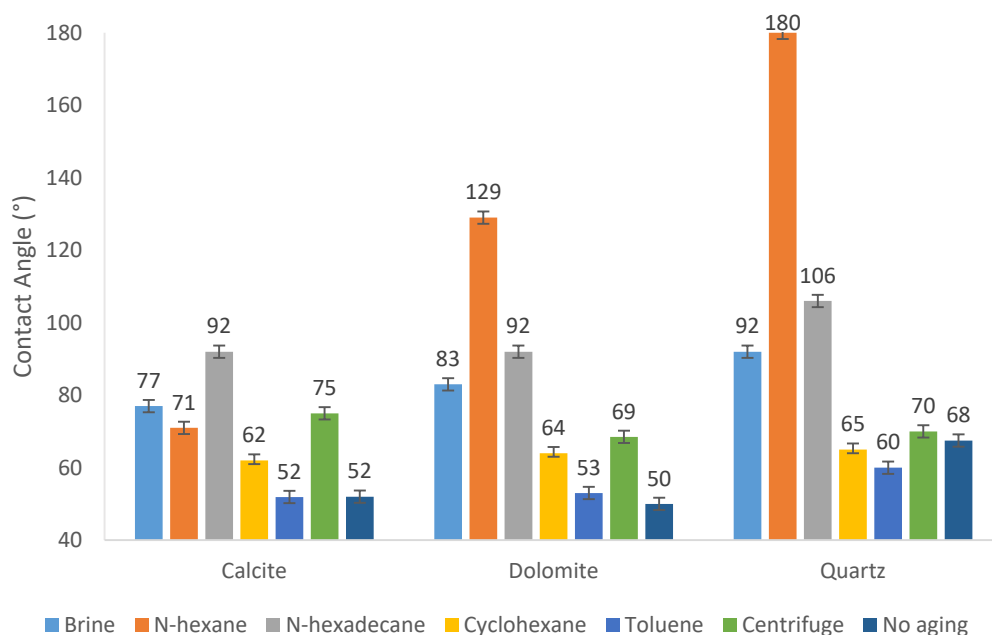


Figure 6.1. Contact angle measurements for three minerals using solvents and centrifuge for bulk oil removal. Aging time: 1-3. Conditions: 60 °C and 1000 psi.

The results indicate that using formation brine results in intermediate wetting for all three minerals. This indicates, as expected, poor oil removal by brine due to the poor interaction between both fluids. For the two n alkanes an increase in the oil-wet behavior is observed. This could be associated with asphaltene precipitation by the addition of a non-polar solvent. This effect will be discussed further in this section. In the case of calcite, n-hexane rendered an intermediate-wet result suggesting that consistency may be an issue in the use of these solvents because of the uncontrolled interaction between the solvent and the oil.

Cyclohexane and toluene resulted in more water-wet or intermediate-wet behaviors which are likely for aging times of a few days only (BARTON, 1991; BUSTAMANTE et al., 2011). However, toluene resulted in lower CA values representing that greater amount of bulk oil is removed by this solvent. Nevertheless, cyclohexane produced greater values that still are in the intermediate or weakly water-wet region.

The use of centrifuge gave similar trends to that of cyclohexane in the way that CA values were higher than for the non-aged rocks but still in the intermediate or weakly water-wet region. This method has also the advantage of being less user-dependent and simpler to repeat as it relies on time and rotational speed which are set on the instrument. In addition, it avoids possible undesirable interactions between the rinsing solvent and the bulk oil, such as asphaltene deposition.

To discuss the conditions for asphaltene precipitation using solvents, the molar fraction of each solvent required for asphaltene precipitation in Oil B at room conditions was calculated. For this, the solubility parameter (δ) was applied. This parameter depends on the cohesive energy density of a solvent and is used to measure polarity of a solvent (SANTOS et al., 2017). Therefore, δ has been used to predict the scenarios for asphaltene precipitation. In this work, the theoretical concentration of solvent for asphaltene precipitation in crude B was calculated using a model recently developed for Brazilian oils (CORRERA et al., 2005). This model is based on the calculation of a critical flocculation parameter from experimental correlations. The solubility parameter of crude B was calculated using two different models to crosscheck the results. Model 1 (VARGAS; CHAPMAN, 2010) uses physical properties

of the oil (density and viscosity) as input data. On the other hand, Model 2 relates the solubility parameter to the density of the crude oil using a proportionality constant, namely the One-Third rule (HANSEN, 2007). In addition, the solubility parameters of the different solvents were searched in the literature (KOSMULSKI, 2011; WALID AL SHALABI EMAD ; SEPEHRNOORI, 2017). The maximum volume fraction of each solvent that can be added to crude B without asphaltene precipitation at room conditions calculated with Model 1 and 2 is shown in Table 6.1.

Table 6.1. Maximum solvent volume fraction that can be mixed with crude B without asphaltene precipitation.

| | Model 1 | Model 2 |
|--------------|---------|---------|
| N-hexane | 0.4 | 0.5 |
| Cyclohexane | 1.0 | 1.0 |
| N-hexadecane | 0.7 | 0.8 |
| Toluene | >1 | >1 |

For the purpose in this work, values in Table 6.1 are considered in a qualitative way. There is agreement between the results obtained for both models. The volume fractions of one or higher than one prove that toluene and cyclohexane will not carry asphaltene precipitation when mixed at any proportion with Oil B. On the other hand, the n-alkanes will favor asphaltene precipitation. For n-hexadecane this happens at higher volume fractions of the solvent (0.7 or 0.8), but for n-hexane lower concentrations (0.4 or 0.5) cause this effect. These results support the idea that asphaltene precipitation while rinsing with the solvent may be an important cause of the change in CA observed for the different solvents. Greater oil-wet behavior obtained for the n-alkanes could be associated with the deposition of asphaltenes on the rock surface as the solvent is dripped on the rock slab. Therefore, n-hexane and n-hexadecane are not recommended as rinsing solvents for bulk oil removal when the crude oil presents risk of asphaltene precipitation.

To analyze the solvation capacity of the reagents regarding Oil B, another test was performed. Coquinas rock slabs were aged 1 day in brine and 30 days in Oil B at 60 °C. Slabs were separated in two groups, one of them was rinsed with the individual solvents as in the

CA measurement tests described before. The rinsing droplets carrying dissolved oil were collected and stored. An additional second rinse was carried out, and the washing droplets were also collected. The second group was initially centrifuged using the same conditions as in the CA measurement procedure (Chapter 4). Then, the slab was rinsed with solvents in a similar fashion as the first group. N-hexane was eliminated from this analysis due to its tendency to destabilize asphaltenes at volume fractions below 0.5.

The goal of these tests is to get a qualitative idea of the relative volume of oil that is removed by rinsing with each solvent. The inclusion of a second rinsing cycle informs if excess solvent would remove additional oil after the first rinsing. In addition, experiments starting with a centrifuging step show the effect of the centrifuge compared to that of the first solvent rinsing step. The stored fluids were analyzed using Gas Chromatography (GC) as described in Chapter 4. It should be considered that these tests are qualitative indicators of the oil removal by each solvent; however, no information about asphaltene precipitation or phase separation can be concluded from these results.

The GC areas obtained for the first rinsing with the three solvents is shown in Figure 6.2. Toluene was the most effective solvent removing Oil B from the rock surface followed by cyclohexane, and n-hexadecane resulted in the lowest oil removal. These results discourage the use of n-hexadecane for excess bulk oil cleaning on the rock's surface due to its poor interaction with Oil B, particularly in the extraction of lighter fractions. On the other hand, toluene was very efficient on dissolving Oil B. However, this does not indicate it is the best solvent for this application. The fact that Oil B is readily dissolved by toluene indicate that controlling the rinsing volume of toluene may be critical complicated. A slight volume excess of toluene may result in removal of not only bulk oil, but also adsorbed molecules on the surface which cause the effects of aging. Thus, cyclohexane was the chosen solvent due its intermediate dissolution of Oil B at all molecular weights and its consistent CA results in the screening tests.

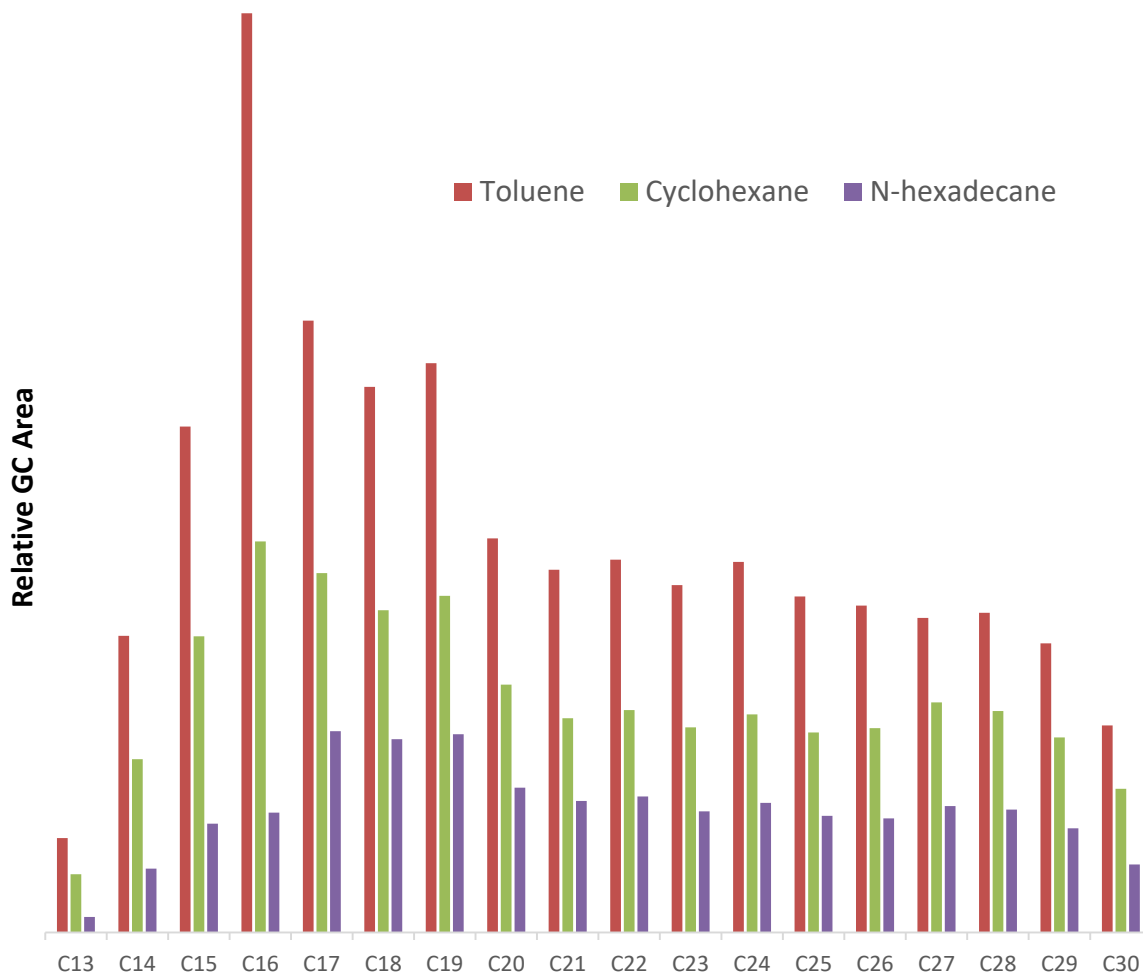


Figure 6.2. Relative GC areas on the analysis of the rinsing with toluene, cyclohexane and n-hexadecane.

Then, the effects of centrifugation were tested by analyzing the cyclohexane rinsing effluents after a centrifuge step (as described in Chapter 4). Figure 6.3 shows the relative GC areas for the effluents of the first and second rinsing cycles both with and without centrifugation. It is evident that centrifugation is very effective in the removal of bulk oil resulting in greater extraction than the first rinsing with cyclohexane. In addition, this trend is consistent for all molecular weights. As a result, centrifugation is the most adequate method for the removal of bulk oil due to its effectiveness combined to its greater controllability and less user dependence. Rendering on physical interactions and not chemically altering the aged surface of the rock makes it more suitable for this specific purpose. Therefore, for all the

experiments in the next sections of this text, centrifuge is used as the bulk removal method unless specified otherwise.

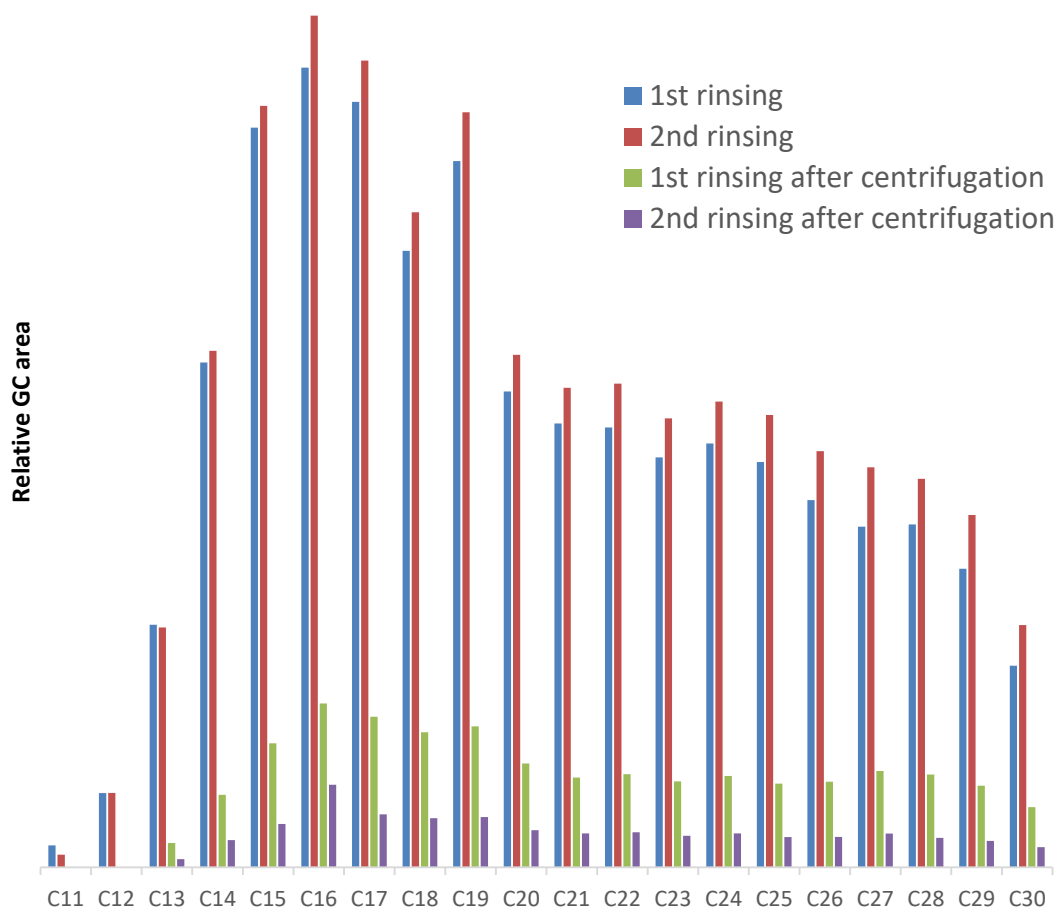


Figure 6.3. Relative GC areas of rinsing with cyclohexane with and without centrifugation.

6.1.2 Aging time

As discussed in the previous chapters, the aging process is fundamental for restoring the initial wettability of reservoir rocks. In this section, the effect of aging time in oil on the wettability of minerals and coquina outcrops is analyzed. For this, slabs of calcite, dolomite, quartz and coquina were aged 1 day in Brine B and 3, 15 and 30 days in Oil B at 60 °C. After bulk oil removal by centrifugation, CA was measured at 60 °C and 1000 psi using Brine B as the external phase and Oil B as the drop phase.

The results are shown in Figure 6.4 evidencing that substrates can be divided in two groups. First, calcite and coquina show increasing CA with aging time. For this group, experiments with 40 days aging time in oil were included. On the other hand, dolomite and quartz show no change in wettability with aging time.

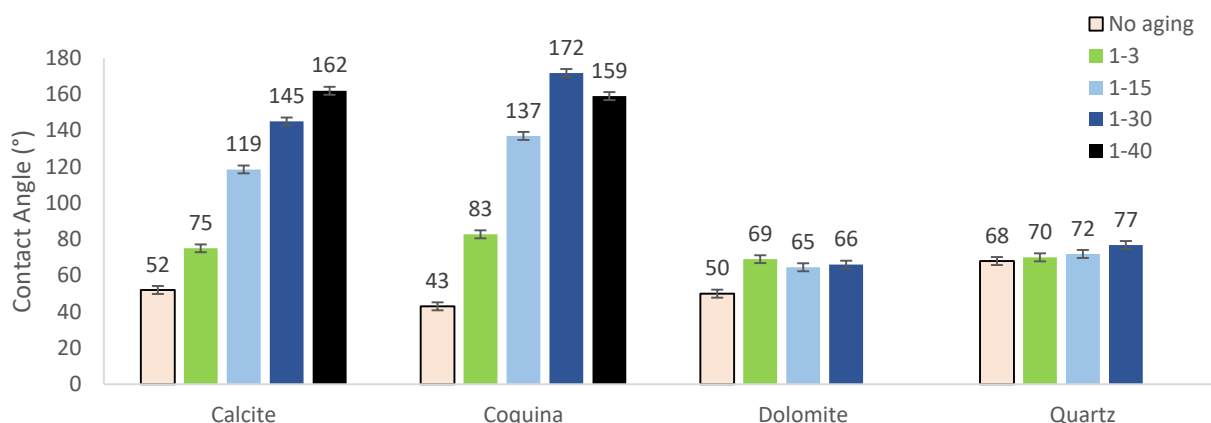


Figure 6.4. Contact angle measurement for minerals and coquinas using 1 day aging in Brine B and different aging times in Oil B. Conditions: 60 °C and 1000 psi.

It is interesting to first compare the results for the unaged slabs. Quartz has the greatest CA followed by dolomite, both in the weakly water-wet region. Unaged calcite and coquina are strongly water wet, and the latter resulted in an even lower CA in agreement with the effects of roughness on hydrophilic substrates discussed before (BUTT; GRAF; KAPPL, 2006; QUÉRÉ, 2002). These results indicate that, in the absence of wettability alteration effects, Oil B has greater instant interaction with quartz which possesses a more acid and negatively charged surface in agreement with its TAN/TBN lower than 1.

As the aging time increases, the wettability of both calcite and coquina shifts towards oil-wet. The images of several drops on different time aged coquinas are shown in Figure 6.5. After 3 days aging, both are neutral-wet, and 15 days are enough to obtain weakly oil-wet surfaces. After aging 30 days, both coquina and calcite show strongly oil-wet behavior. Calcite's wettability towards oil was further increased by using 40 days aging time. Nevertheless, no further increase in CA was observed for coquinas with the same aging time. The effect of aging time on these substrates suggests that wettability alteration occurs through processes that are dependent on time. For coquinas, aging for 30 days was required to achieve

the equilibrium wettability. For calcite, longer times could be necessary due to its lower surface area and concentration of active sites. In addition, as coquina's surface roughness is greater than that of calcite (Table 5.6), the higher CA values found for aged coquina are in agreement to the trends discussed in Chapter 2 (BUTT; GRAF; KAPPL, 2006; QUÉRÉ, 2002). The subjects enunciated in this section will be discussed in Section 6.4.

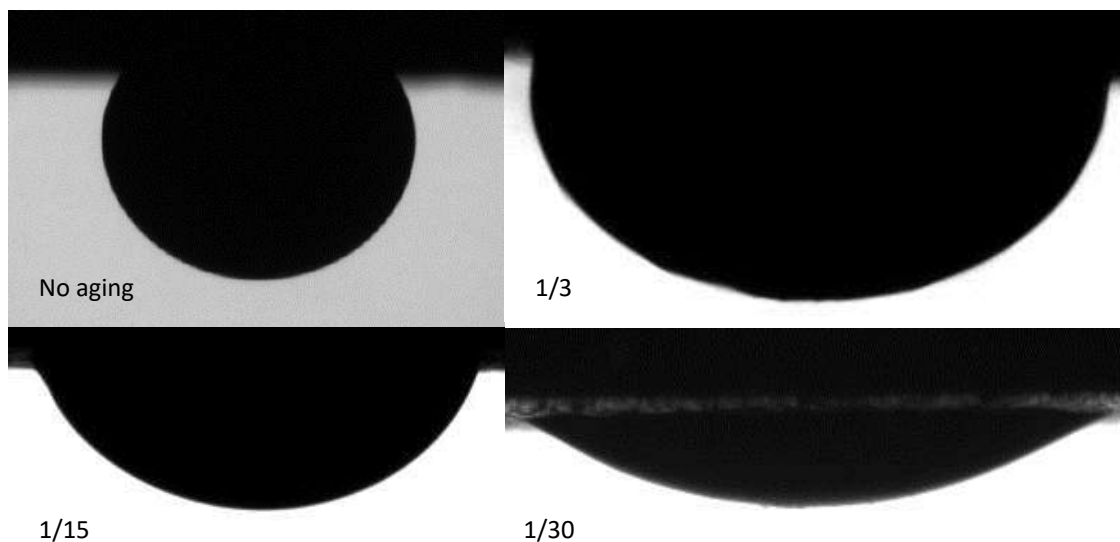


Figure 6.5. Images of Oil B drops surrounded by Brine B on coquinas slab using 1 day aging in brine and 3,15 and 30 days aging in oil. No aged slab is also included.

6.1.3 Effect of pressure

Pressure is not expected to have a major effect on wettability when dead fluids (with no dissolved gas) are used. This is because most of the effects that determine wettability presented in Chapter 3 have a weak or no dependency on pressure in liquid and solid phases. To test this hypothesis, experiments were run using fluids from reservoir B and coquinas at 60 °C, 1 day aging in Brine B and 15 days aging in Oil B. The pressure was raised from 1000 to 5000 psi. In addition, tests pressurizing the chamber at 3000 and 5000 psi and injecting a new drop for each pressure were carried out to compare the effects of increasing pressure prior and after drop deposition. The procedure for these tests is explained in Section 4.1.1.

The results are shown in Figure 6.6. For the same drop experiment, CA changed 2.2%, and for the new drop experiment the difference was 4.1%. The maximum difference between both methods at the same pressure is 6.2%. In addition, the average standard error of the mean for these experiments is 2.0%. Therefore, the effect of pressure on the initial wettability of dead fluids can be considered negligible regarding wettability shifts or major changes in the rock-fluid interactions.

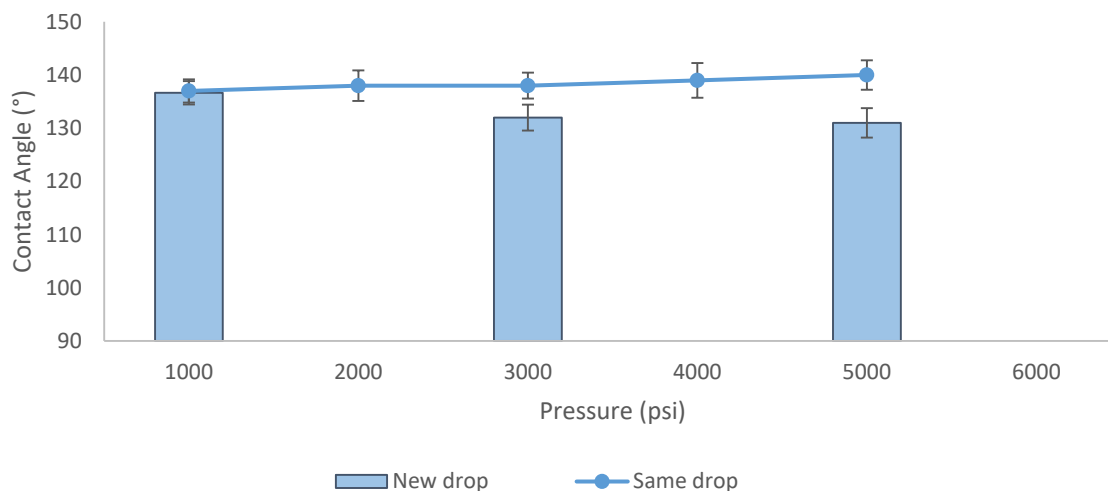


Figure 6.6. Contact angle measurements versus pressure using the same drop and a new drop for coquina with Field B fluids and 15 days aging in oil. Conditions: 60 °C and 1000 psi.

6.1.4 Effect of aging oil reutilization

Reutilization of aging oil can be useful when there are limitations regarding the available volume of the oil of a specific well. To evaluate the effect of aging the slabs in oil which was previously used with this purpose for the same rock, coquina and calcite were aged 1 day in Brine B and 15 or 30 days in reutilized Oil B (Oil B2) at 60 °C.

The properties of Oil B2 are shown in Table 5.2, 5.3 and 5.4. It is clear that, even when the aging process is carried out in a closed recipient minimizing the volume of air, the composition and properties of the oil are dramatically affected by the aging process at 60 °C. The Gas Chromatography analysis shows that most of the lighter compounds (below C16) were practically eliminated from the liquid oil by vaporization. In addition, the API gravity

was reduced from 26.14 to 18.6, and the viscosity at 60 °C was increased over 5.7 times. This altered properties evidence that Oil B2 is much heavier than Oil B resulting in differences between the effects of aging effects with both oils.

CA was of slabs aged with Oil B2 were measured at 60 °C and 1000 psi using Brine B as the ambient phase and Oil B as the drop phase. Centrifugation was used as the oil removal method. However, due to Oil B2’s high viscosity and adherence to the rock surface, the use of cyclohexane after centrifugation was also applied.

The results are shown in Figure 6.7 including the values for tests using slabs aged with unused (new) oil. The first trend that is obvious is that when reutilized oil is employed, centrifugation alone is not efficient in removing bulk oil from the surface. The strongly oil-wet behavior showed for 15 days aged slabs, and the fact the drops spread completely on the 30 days aged slabs prove that an oil layer remains after centrifugation.

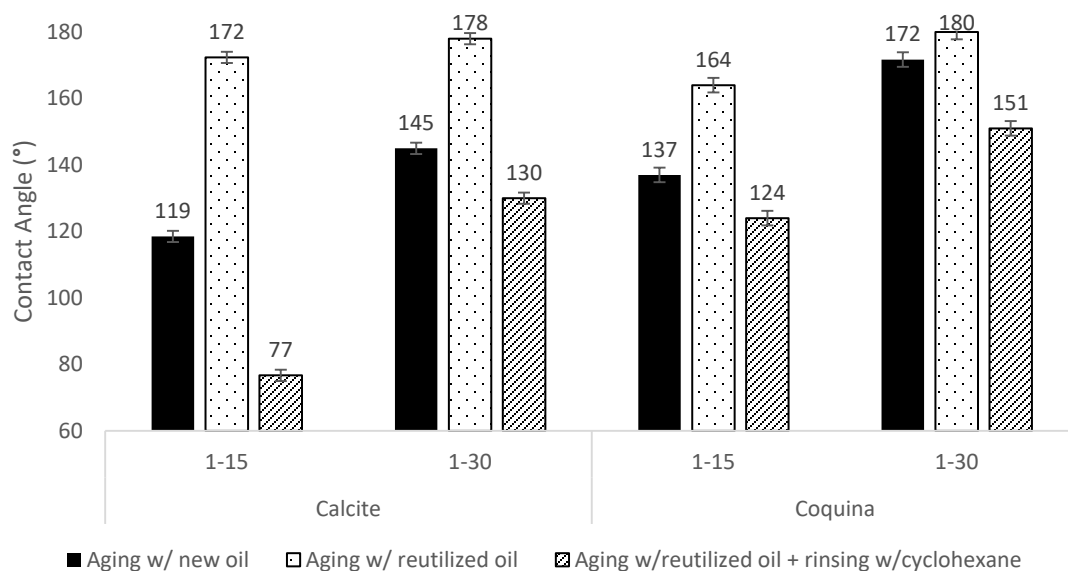


Figure 6.7. Effect of reutilization of the aging oil in the contact angle between Oil B and Brine B on calcite and coquinas aged 1 day in brine and 15/30 days in oil.

Rinsing the surface aged with reutilized oil with cyclohexane was effective in removing the bulk oil and obtaining consistent CA trends. It can be observed that the wettability behavior of these experiments is in agreements with that of the tests aging with new oil. Nevertheless, the CA values obtained using cyclohexane are systematically lower.

This suggests that the use cyclohexane interacts with adsorbed compounds reducing the oil-wet behavior of the rock. This is more evident when the interaction between the oil and the substrate is less strong (i.e. for 15 days aged calcite).

6.2 Wettability of pure minerals

According to the discussion above, under Pre-Salt scenario conditions, 15 days aging is required to shift the initial wettability of carbonate rocks from water to intermediate or slightly oil-wet. Moreover, after 30 days aging carbonates showed oil-wet behavior with different strengths according to their composition and the presence of defects and active sites. For aging times longer than 30 days, no major changes in wettability were observed.

Next, the wettability of the same minerals and coquinas using oils and brines of two different Pre-Salt fields (B and D) were compared for 15 and 30 days aging times. All tests were carried out at 60 °C and 1000 psi. Figure 6.8 shows the results for these tests. It is clear than both fields follow the same trends. Dolomite and quartz show slightly water-wet behavior at all aging times, and calcite is oil-wet. From 15 to 30 days, wettability towards oil increases for the latter. Images of Oil B drops on 30 days aged minerals are shown in Figure 6.9. Coquinas are also shown for comparison.

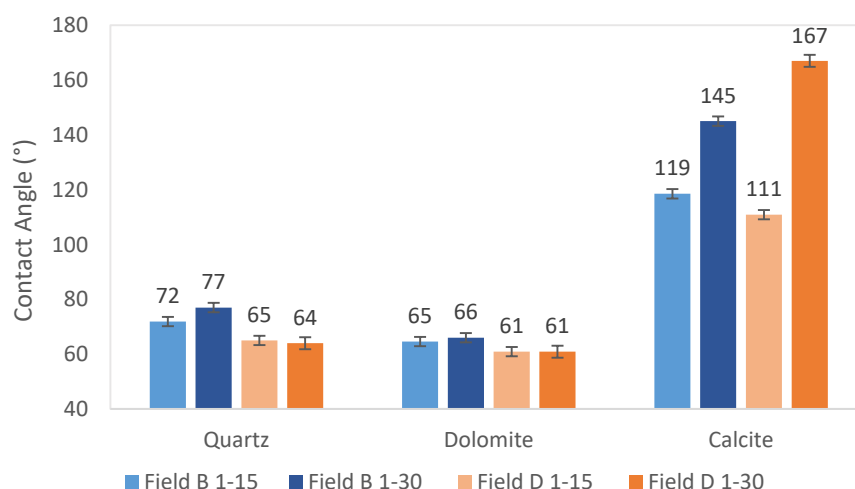


Figure 6.8. Contact angle measurements for pure minerals using Field B and Field D fluids and 15 and 30 days aging in oil. Conditions: 60 °C and 1000 psi.

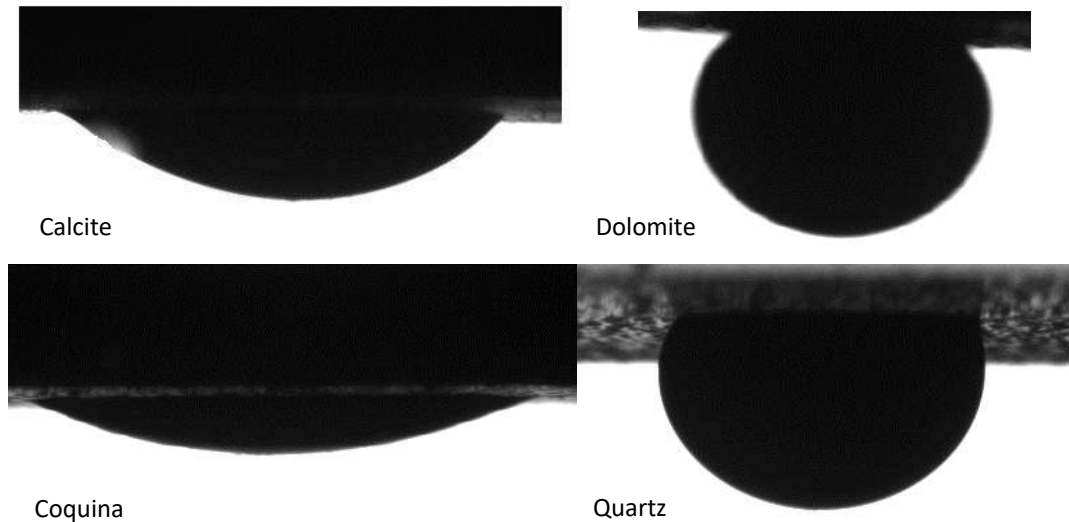


Figure 6.9. Images of Oil B drops in Brine B on different substrates. Aging: 1 day in Brine B 30 days in Oil B.

As reported in the characterization in Chapter 5, both fields consist in similar scenarios regarding the major characteristics that affect wettability. Field D has slightly higher pH (6.1 over 5.7). However, the points of zero charge (pzc) reported in the literature are 9.5 at 20 °C for calcite, 7.0 at 20 °C for dolomite and 3.0 at 20 °C for quartz (AUSTAD et al., 2008). Thus, the aforementioned difference in pH is not significant to greatly affect surface charge on the minerals. In addition, Brine B has greater salinity than Brine D (226000 over 200000 ppm), but both of them are considered of very high ionic force for intermolecular interaction purposes. Both brines contain divalent cations (i.e. Ca^{2+}) which can act as wettability modifiers (GENEROSI et al., 2017).

Regarding the oils, there is no great difference on TAN and TBN of both fields. Field D has a greater concentration of resins (11 over 8%) and aromatics (30 over 26%). This could be a reason for the higher oil-wettability presented by Field D after 30 days aging on calcite. Nevertheless, further research is required to clarify these topics.

The results in Figure 6.8 indicate that the trends obtained for Field B are repeated for the oil and brine compositions of another Pre-Salt field. This shows consistency of the experimental results and suggests that 30 days aging are required to establish wettability on calcite. Quartz being the base of siliciclastic rocks interacts weakly with these oils during the

aging process, resulting in slightly water-wet behavior. Dolomite, which is a carbonate rock, has also a weak interaction with both Pre-Salt oils more likely due to the presence of magnesium. This will be discussed in Section 6.4.

6.3 Wettability of carbonate outcrops and Pre-Salt reservoir rock

A similar analysis to that of the previous section was carried out using coquinas outcrops. CA experiments were run at 60 °C and 1000 psi using 1 day aging in brine and 15 or 30 days aging in oil. Fluids from both Field B and Field D were used to compare the scenarios of these reservoirs as in the previous section. The results are illustrated in Figure 6.10.

The trends obtained for coquinas follow that of calcite for fluids of both reservoirs. Both samples show an increase in oil wettability when aging time is augmented from 15 to 30 days. This results in a shift from initially weakly oil-wet to strongly oil-wet. Moreover, CA values are similar for both types of rocks, but coquinas resulted in higher values with differences between 3 and 27°. These differences are not relevant regarding the initial wettability trends, which were consistent for both materials. A cause for this increased CA values could be the higher microscopic roughness of coquinas (Table 5.6), which may increase the apparent CA of the already oil-wet rock as discussed in Chapter 2 (SEYYEDI; SOHRABI; FARZANEH, 2015). Moreover, the presence of defects and increased surface area on the coquinas rocks can enhance the adsorption of surface-active compounds in the oil.

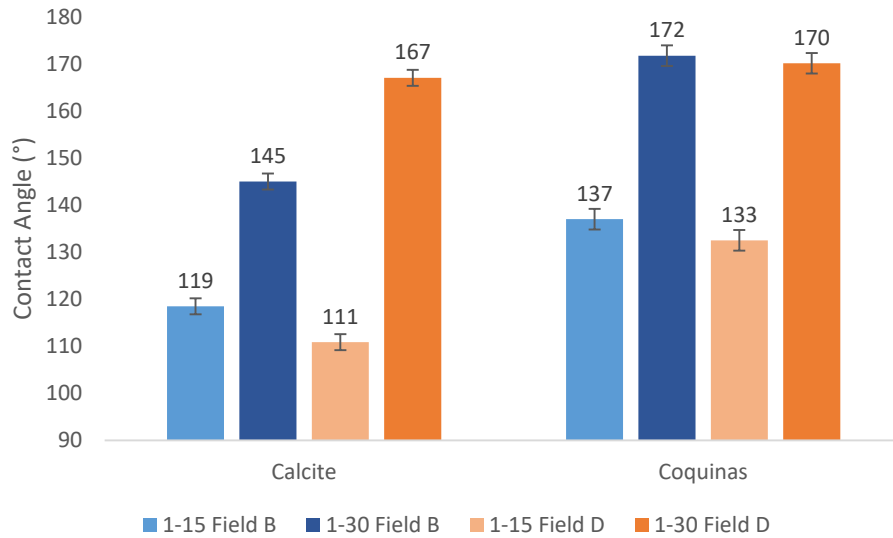


Figure 6.10. Contact angle measurements for calcite and coquina outcrops using Field B and Field D fluids and 15 and 30 days aging in oil. Conditions: 60 °C and 1000 psi.

The next step consisted in comparing the initial wettability of Field D Pre-Salt reservoir rock with that of carbonate outcrops. Tests were carried out at the same conditions as in the previous series using Field D oil and brine. Indiana limestone was added as a reference carbonate outcrop for comparison. The results are included in Figure 6.11. The obtained CA values decreased as the heterogeneity and complexity of the rock increased. The decreased oil-wettability for the Pre-Salt rock could be caused by the presence of chunks of minerals which have weaker interactions with the oil, such as feldspar and pyrite. Nevertheless, the results obtained for this rock are still higher than those for calcite, showing that reservoir rocks with increased roughness result in greater CA values.

The three complex rocks considered showed oil-wet behavior. Indiana limestone, which is the most homogeneous and richest in calcite, is strongly oil-wet. The CA value for coquinas is moderate oil-wet, and the reason it has an intermediate value between the other two could be due to multiple effects. The increased roughness favors oil-wettability, but the presence of quartz and k-feldspar reduce the interaction with active components of the oil. Finally, Rock D is weakly oil-wet. This could be attributed to the greater dolomite content on these heterogeneous rocks. In addition, its decreased surface roughness and more heterogeneous composition could also lead to a reduction of the apparent contact angle.

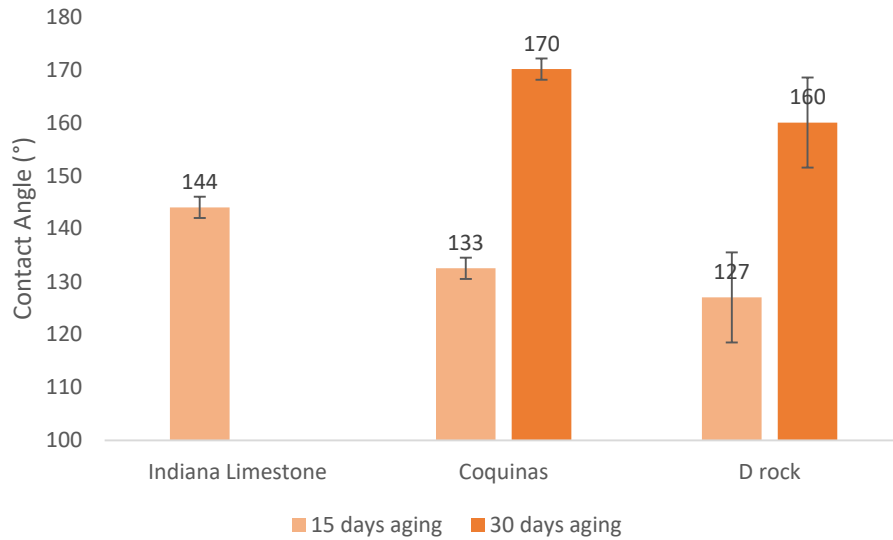


Figure 6.11. Contact angle measurements for Indiana limestone, coquina outcrops and Field D rock using Field D fluids 15 and 30 days aging in oil. Conditions: 60 °C and 1000 psi.

6.4 Discussion: Initial wettability of different minerals and rocks under Pre-Salt reservoir conditions

The results presented up to this point of the chapter encourage the discussion regarding the initial wettability of pure minerals, outcrops and Pre-Salt rock. It is interesting to analyze similarities and differences between the minerals that compound the more complex outcrops, and also between the outcrop analogues and the actual reservoir rock. The following paragraphs contrast the results obtained in terms of rock type, aging time and reservoir fluids. They also propose supporting facts to understand the causes for such differences.

All carbonate rocks (with the exception of dolomite) showed to be oil-wet if sufficient aging time is allowed. Before discussing the difference interactions that could favor this shift in wettability during the aging process, the presence of oil on the rock surface after aging was checked through SEM. For this, calcite and coquina rock slabs were aged for 1 day in Brine B and 30 days in Oil B both at 60 °C. The slabs were then centrifuged and rinsed with

cyclohexane as described in Chapter 4. The analysis of this pictures aimed to observe the effects of aging on the rock surface. The images for calcite are shown in Figure 6.12.

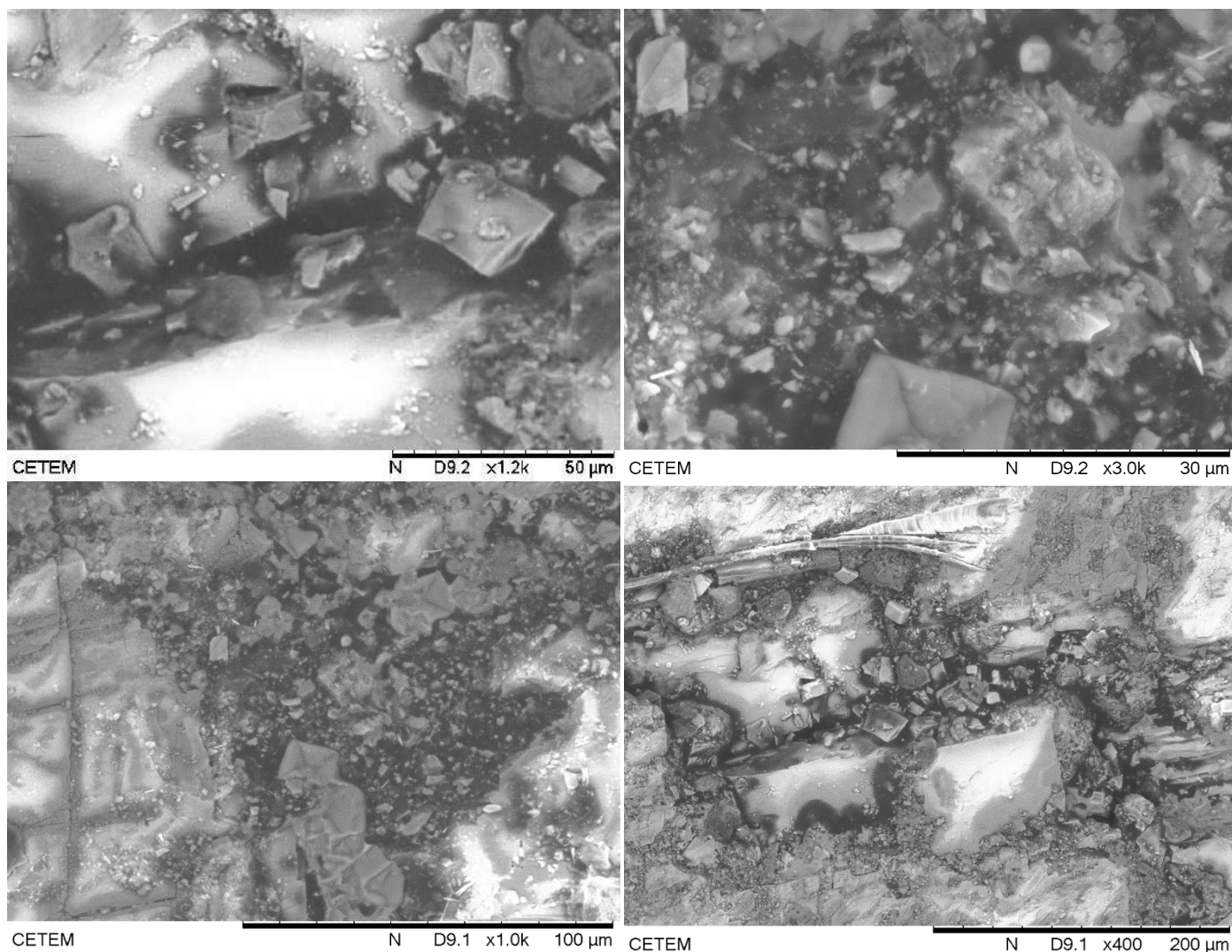


Figure 6.12. SEM images of calcite aged 1 day in Brine B and 30 days in Oil B after centrifugation and rinsing with cyclohexane.

When these images are compared to those for clean calcite (Figure 5.8), the appearance of darker areas in the background and surrounding the calcite rhombohedra is evident. These areas, which are clearly not pores, correspond to oil layers on the rock surface. To support this idea, EDS analysis was implemented in different regions. The results for a selected image are shown in Figure 6.13. The maps of the three main elements that compose calcite (Ca, O and C) is also included. Observation of these images indicate that the areas

corresponding to lower concentration of calcium match the darker regions observed in the SEM image. In addition, these areas correspond to the sections where carbon concentration dominates the spectra of elements. This is a qualitative indicator of the presence of oil covering the calcium carbonate at the matrix of the mineral.

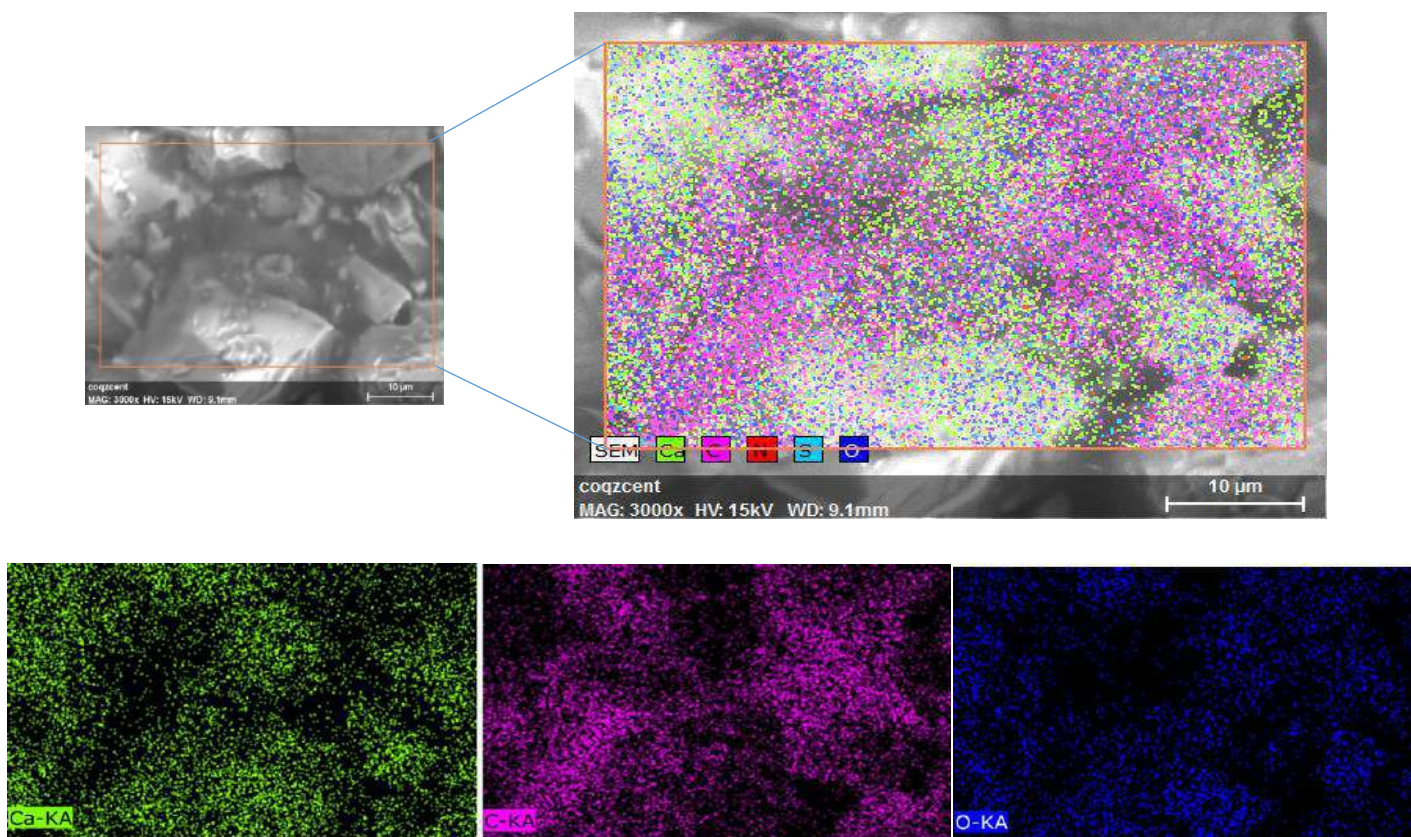


Figure 6.13. EDS analysis of the selected image showing concentration maps of calcium, carbon and oxygen.

A quantitative spot analysis was run at the areas containing higher concentration of aging oil, and the results are in Figure 6.14. The spectra for the selected spot detected almost 60% carbon and 24% oxygen, as opposed to 40% calcium, 48% oxygen and 12% carbon typical of calcite. This result also indicates the presence of aging oil on the surface of the mineral.

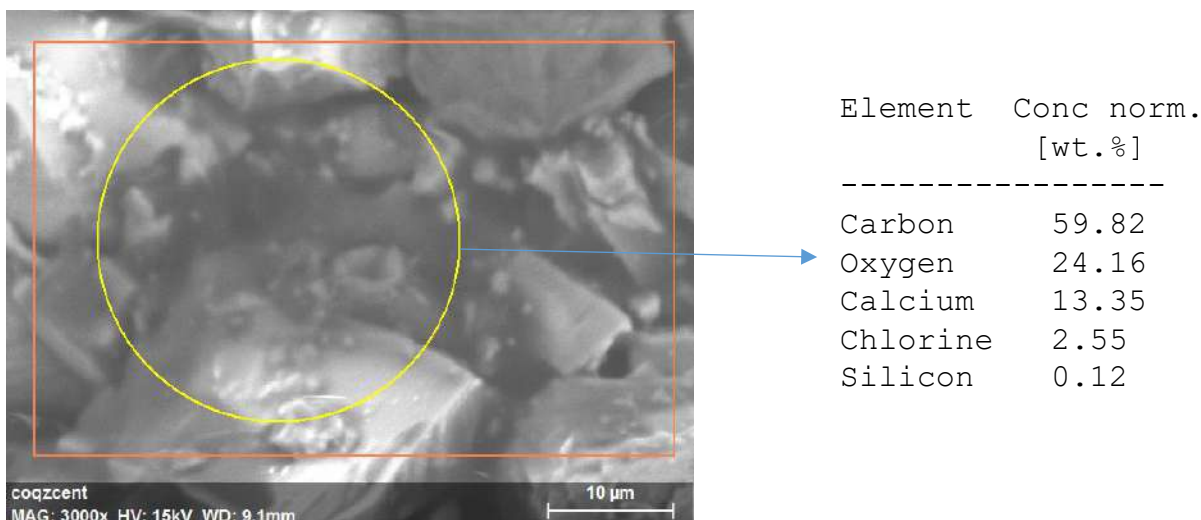


Figure 6.14. Spot EDS analysis of aged calcite showing the %wt. of the detected elements.

The same analysis was carried out for a coquina sample, which is a more complex rock. Figure 6.15 shows the SEM images of the aged rock. These images, compared to those of Figure 5.9, clearly indicate the presence of aged oil on the rock surface. Qualitatively, this is even more evident than in the images of calcite.

EDS analysis including maps of carbon, calcium and oxygen concentration are shown in Figure 6.16. The darker areas of the SEM image are clearly associated with higher concentrations of carbon, and lower concentrations of calcium as observed for the calcite slab. The reader should compare Figure 6.16 to the EDS of analysis of a clean coquina sample (Figure 5.9), which shows greater domination of calcium throughout the rock surface with exception of pyrite and quartz chunks.

Quantitative spot analysis of an area showing the presence of oil was carried out (Figure 6.17). In this case, elemental composition of the rock is not as straightforward due to the heterogeneity of the rock. Nevertheless, these results show almost 70%wt. of carbon in agreement to the presence of aging oil in the selected spot.

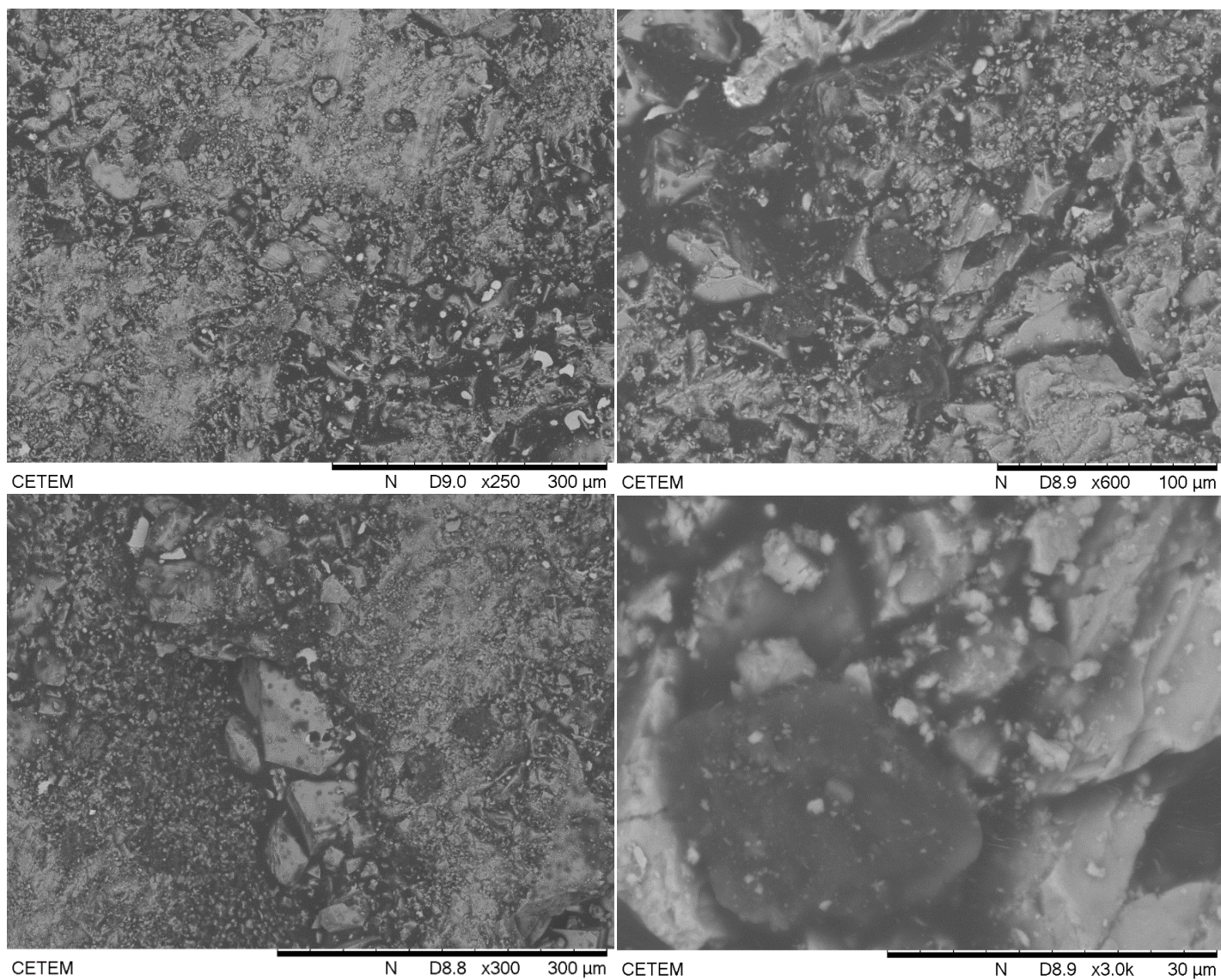


Figure 6.15. SEM images of coquina aged 1 day in Brine B and 30 days in Oil B after centrifugation and rinsing with cyclohexane.

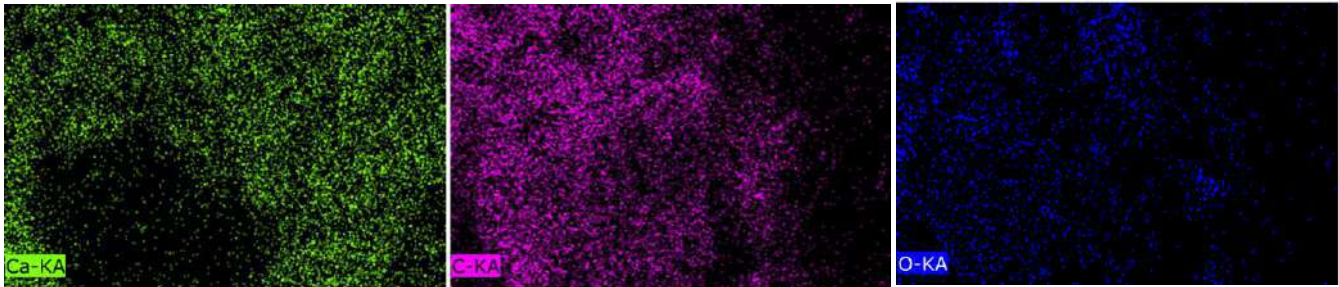
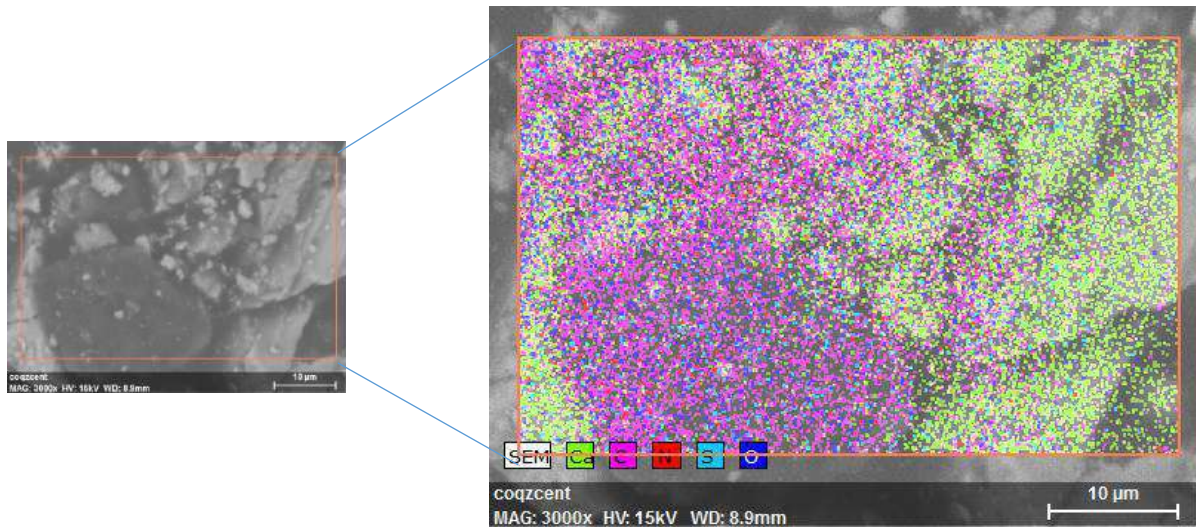
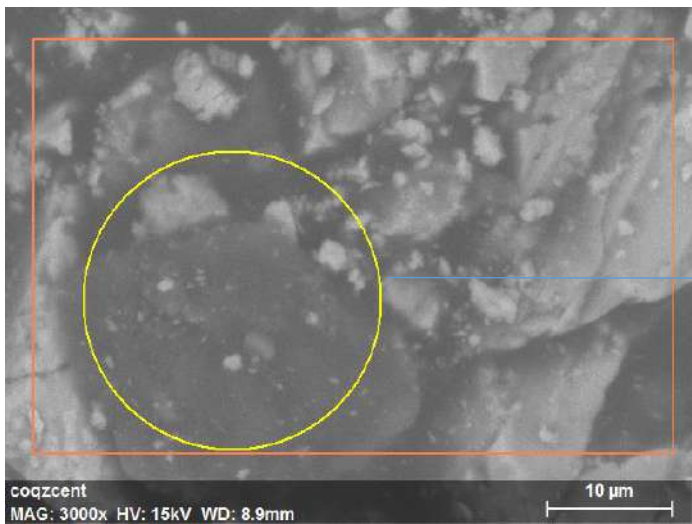


Figure 6.16. EDS analysis of the selected image showing concentration maps of calcium, carbon and oxygen.



| Element | Conc. norm. [wt.%] |
|-----------|-----------------------|
| Carbon | 69.67 |
| Oxygen | 21.34 |
| Calcium | 7.42 |
| Chlorine | 1.20 |
| Aluminium | 0.19 |
| Silicon | 0.19 |

Figure 6.17. Spot EDS analysis of aged coquina showing the %wt. of the detected elements.

As showed in Section 6.1.2, the CA obtained for unaged quartz was greater than that of unaged calcite or coquina. This indicates that the basic compounds in Oil B present stronger interaction with the acidic negatively charged surface of quartz at the slightly acidic and high-salinity environment that Brine B represents. However, aging in oil does not shift quartz wettability proving that these interactions are weak and independent of time.

On the other hand, the results acquired for calcite presented the opposite behavior. Unaged calcite was initially water-wet with weak interaction with Oil B. Aging calcite in oil continuously shifted its wettability towards oil-wet as the aging time increased. This wettability alteration with aging occurs through adsorption of active species in the oil (i.e. asphaltenes, resins or aromatic compounds). Evidence of this was given in the beginning of this section. As opposed to instantaneous acid-base or electrostatic forces, the process that shift calcite wettability depends on time critically, and increase in the obtained CA was observed even after 40 days of aging. As discussed in Chapter 3, one of the most commonly accepted mechanisms of wettability alteration in carbonates is through adsorption of the carboxylic anions ($R-COO^-$) on the positively charged active sites on the rock. The carboxylic groups are contained in the acid fractions of the oil. Since oils B and D present TAN/TBN ratios lower than 1, the acidic compounds are diluted in comparison to the basic compounds. This could be a cause of the prolonged aging times needed to shift wettability as acid compounds have to diffuse and accumulate at the interface to build the required concentration.

Dolomite had a differentiated behavior. The unaged mineral had a wettability in between that of quartz and calcite. This fits its surface properties as its point of zero charge and concentration of acid sites also follows between those minerals (SEYYEDI; SOHRABI; FARZANEH, 2015). Even though it is a carbonate, aging in oil did not shift its wettability. The interaction between oils B and D and the mineral were not strong enough to disrupt the water film at any aging time. The weak interaction of dolomite with basic compounds was previously reported (MORROW; CRAM; MCCAFFERY, 1973). The same authors altered dolomite wettability towards oil-wet with acidic compounds, but the interaction was not strong enough and wettability was reversed during the experiments. The effect of acid compounds in the oil, as discussed for calcite, also applies for dolomite. Nevertheless, Mg^{2+} is ten times less reactive towards carboxylic acids than Ca^{2+} due to their differences in ion

size and hydration energy. This results in a weaker interaction between dolomite and the acid groups of the oil than that of calcite (SHARIATPANAH et al., 2016). This weaker interaction and the low concentration of acid groups in oils B and D could be the reason for the dolomite remaining water-wet at all conditions.

Coquina and limestones outcrops showed similar results both following the trends of calcite. Coquina rocks should show stronger oil-wet behavior than that of calcite for both oils considered in this work. In addition, the shift of wettability through aging occurred at shorter times reaching the final wettability at 30 days aging. The CA obtained for coquinas is induced by their greater reactivity and also by roughness effects. First, they are more reactive due to the increased surface area and the presence of clusters active for adsorption. However, a complete surface characterization should be carried out to conclude about the potential for chemical adsorption of different species on the surface of these rocks. In addition, surface roughness in coquinas decreased its apparent contact angle for the unaged (hydrophilic) rock, and augmented it for the aged (hydrophobic) rocks.

Finally, the Pre-Salt reservoir rock from Field D was also weakly oil-wet after 15 days aging and strongly oil-wet after 30 days aging. The lower CA values compared to coquinas could be related to the lower surface roughness of the D reservoir rocks (Table 5.6), which may induce a lower apparent CA. However, the wettability behavior of both rocks matches for both aging times considered. Therefore, since the difference in the obtained CA is not relevant regarding the wettability behavior of the rocks, it can be concluded that coquinas are good analogues for Reservoir D rocks in terms of initial wettability if sufficient aging time is provided.

6.5 Effect of asphaltenes and resins on changing initial wettability

Asphaltenes and resins are considered as the responsible compounds that alter rock wettability during the aging process. As it was evidenced in the previous sections, Pre-Salt crudes B and D have strong interaction with carbonate rocks shifting their wettability towards oil-wet if enough aging time is allowed. Both crudes have asphaltene contents lower than 3%, but higher resin contents (i.e. 8% for crude B) as showed in Table 5.2. These polar species are believed to be very surface active as it will be discussed in Chapter 8.

To prove that asphaltenes and resins are responsible for changing the wettability during the aging process, CA measurements were carried out using a synthetic Model Oil composed of n-hexadecane and toluene keeping the same ratio of saturates over aromatics of Oil B (71.1 wt% C16, Table 5.2). Hexadecane was chosen as the heaviest hydrocarbon which would give the most approximate API to Oil B while being liquid at room temperature.

Coquina and calcite were aged for 1 day in Brine B and 30 days in Model Oil, and the CA was measured at 1000 psi and 60 °C. The results compared to that of Oil B are shown in Figure 6.18. It is clear from these results that the interaction between Model Oil and both carbonates is very weak as both rocks had water-wet behavior. These results indicate that surface active species (i.e. asphaltenes and resins) are responsible for the interaction with the carbonates rocks shifting their wettability towards oil-wet during the aging process.

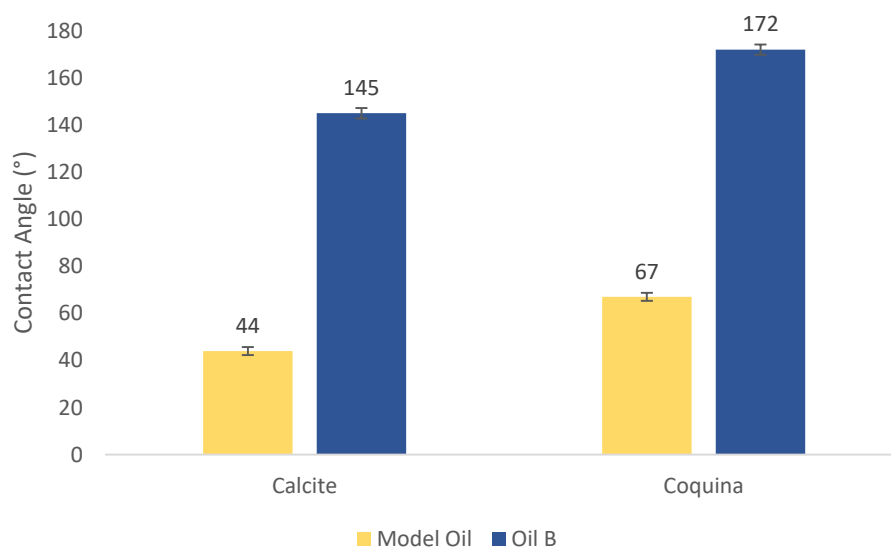


Figure 6.18. Contact angle measurements for calcite and coquina using Oil B / Model Oil and Brine B. Conditions: 60 °C and 1000 psi and 30 days aging in oil.

Asphaltene fractions from Oils B and D were separated using *n*-heptane following the procedure found elsewhere (FRANCO et al., 2013). After drying the samples, Fourier-transform infrared spectroscopy (FTIR) and elemental analysis were performed (as described in Section 4.1.3) to characterize the obtained materials.

The FTIR spectra of asphaltenes fractions from both Oils are included in Appendix D. Both spectra have a similar aspect to those reported in the literature (WILT; WELCH; GRAHAM RANKIN, 1998). The resemblance between both spectra indicates that both oils contain similar functional groups on their asphaltenes. Some characteristic functional groups were identified and compared to the ones reported in Wilt et al. to verify the separated samples correspond to asphaltenic fractions of the oil.

The aromatic carbon-carbon double bond stretching vibration is found at 1604 cm^{-1} . In addition, the CH_2 bending modes are found in 1461 cm^{-1} . The 1376 cm^{-1} peak corresponds to the methyl bending vibrations. Also, the 1031 cm^{-1} may represent ester linkage on asphaltene structure. The characteristic four bands between 871 and 719 cm^{-1} , which represent out of plane bending vibration of carbon-hydrogen bonds, were also found. Finally, the broad area around 3400 cm^{-1} corresponds to the presence of water.

The elemental (CHN) analysis for two asphaltene samples from oils B and D is shown in Table 6.2. The results show that the H/C ratio of all samples is in the characteristic range for asphaltenes between 1 and 1.3 (SPIECKER et al., 2003). In addition, all samples have values lower than 1.15 indicating high aromaticity (POVEDA-JARAMILLO et al., 2016). The aromaticity of asphaltenes from Oil D is even higher than that of Oil B, this could be the reason of its higher increased wettability changing effects.

Table 6.2. CHN (wt.%) for asphaltene samples of Oils B and D.

| Oil | Sample | N % | C% | H% | H/C |
|-----|--------|------|-------|------|------|
| B | 1 | 0.00 | 80.39 | 9.03 | 1.12 |
| | 2 | 0.00 | 80.58 | 9.07 | 1.13 |
| D | 1 | 0.00 | 83.49 | 8.92 | 1.07 |
| | 2 | 0.00 | 84.10 | 9.01 | 1.07 |

It is also important to remark that none of the samples contained nitrogen, showing the absence of basic groups on the asphaltene composition (LASHKARBOLOOKI; AYATOLLAHI, 2018). This suggests that the asphaltenes may play important part in changing the wettability through interaction with the basic surfaces (i.e. calcite and coquinas). Therefore, long aging times are required to obtain wettability alteration through the aging process. Since acid asphaltenic samples are more active at higher pH, these results

also support the idea of weaker interaction between the crude and the rock at higher pH, as discussed in the following chapter. Nevertheless, further characterization is required to quantify the acid behavior of the asphaltene samples.

6.6 Initial wettability under injection brine

The effects of injection brine on the initial wettability of calcite and coquinas was tested by aging the slabs 1 day in desulphated seawater (DSW) and 30 days in Oil B. CA was measured using DSW and Oil B at 1000 and 60 °C. DSW has 0.15 times the salinity of Brine B and basic pH of 8.6 (while Brine B's pH is 5.7). These experiments do not intend to evaluate dynamic effects of waterflooding, as water advancing CA measurements should be carried out for this purpose. In addition, it is not the scope of this work to evaluate wettability changes with brine composition in detail. The objective of these tests is to understand how this environment would affect the initial wettability of the aged rocks regarding the solid-fluid interactions.

The results of these experiments are compared to those using Brine B in Figure 6.19. Even though both solids had oil-wet behavior for both brines, a decrease of 5% for coquina and 11% for calcite is observed. This slight decrease in wettability towards oil could be induced by the changes induced in electrostatic and acid-base interactions when DSW is employed, which will be briefly discussed as follows.

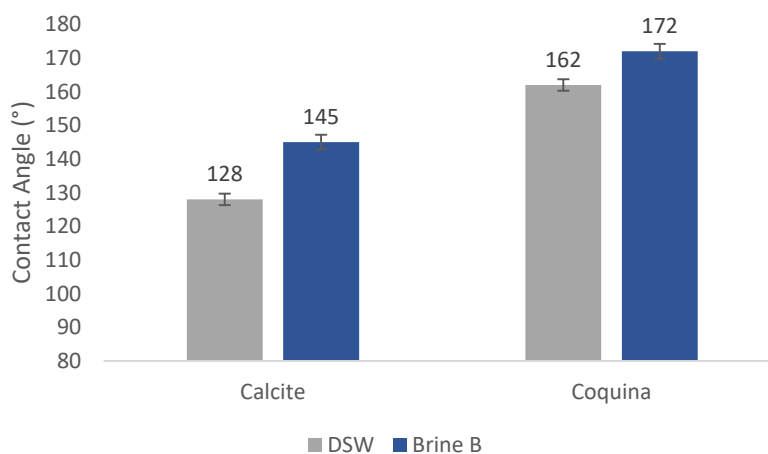
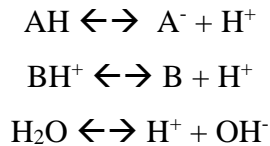


Figure 6.19. Contact angle measurements for calcite and coquina using Oil B and Brine B / DSW. Conditions: 60 °C and 1000 psi and 30 days aging in oil.

The decrease in salinity induces a reduction in the screening effect of the high ionic force induced in a high salinity environment as Brine B. As a result, the effects of electrostatic interactions and pH on surface charges and adsorption is augmented. When DSW is used, the pH is increased; thus, the positive charge on the surface of carbonate rocks is reduced. In addition, the equilibrium of acid and basic compounds in the oil is shifted according to the reactions below:



The ionic form of the acidic species prevails, and the bases tend to deionize. If the acidic species have the greatest interaction with the rock surface, as the charge of calcite turns more negative this interaction will be weakened.

Nevertheless, the effect of pH is not the only difference between Brine B and DSW. The lower salinity favors the partitioning of surface-active species. As a result, greater concentration of these species may be desorbed from the rock surface and diffuse to the oil-brine interface reducing the interaction between the oil and the rock.

Another important mechanism for wettability alteration that could be changed is asphaltene deposition. Nevertheless, a robust characterization of the asphaltenes including their predominant surface charge in contact with Brine B and BSW is needed to interpret if this could be a cause for the decrease in CA obtained for the DSW.

6.7 Highlights of this chapter

- Rock-fluid interaction of Pre-Salt crudes B and D is greater with unaged quartz than with unaged calcite and coquinas caused by the low TAN/TBN ratio.
- Aging shift the initial wettability of calcite, coquina, Indiana limestone and Pre-Salt rock D towards oil-wet due to adsorption of active species from the oil on the rock surface. This process depends on time, and a possible cause is the diffusion of surface active species to reach high enough concentration to disrupt the water film.

- 30 days were required to achieve the final wettability on outcrops. Calcite required even longer times due to its reduced surface area.
- Dolomite interacts weakly with Pre-Salt crudes, and these interactions are not enhanced by rock aging.
- Roughness had the effect reported in the literature decreasing the apparent CA of hydrophilic solids and increasing that of hydrophobic solids.
- Asphaltenes and resins are responsible for the wettability alteration of Pre-Salt oils in carbonates.
- Asphaltenes from Oils B and D have high aromaticity and no basic behavior resulting in stronger interaction with positively-charged calcite, limestone and Pre-Salt rock surfaces.

CHAPTER 7: CO₂ EFFECT ON INITIAL WETTABILITY

This chapter of the text is based on the analysis of the impact of CO₂ on the initial wettability of the different rocks included in this work. The first parts compare the “Gas cap” and “Pre-equilibrated fluids” methods described in Section 4.1.1. Results are first presented for different rocks, and the consequences of CO₂ on each one is discussed afterwards. Then, the effect of CO₂ concentration on the initial wettability is evaluated. Finally, the presence of CO₂ in different scenarios including changes in oil and brine compositions is analyzed.

7.1 CO₂ injection method

As described in Section 4.1.1, two different methods for injecting CO₂ in the system were studied. The “Gas cap” consisted in placing a gas cap of controlled volume on top of the brine after drop deposition. In contrast, the “Pre-equilibrated fluids” method used carbonated brine (saturated) and CO₂-saturated oil.

The differences between both methods were described before. In summary, the “Gas cap” methods compares the effects of CO₂ mass transfer during the measurements. On the other hand, in “Pre-equilibrated fluids” the interaction between carbonated brine and the rock happens prior to drop deposition. Thus, the initial CA value corresponds to the contact of oil with the rock surface after the effects of CO₂ dissolved in the brine phase. In addition, in this method the CO₂ transfer between the oil and brine phases is minimized.

7.1.1 Calcite

The results of CA measurements as a function of pressure using Field B on calcite fluids and 15 and 30 days of aging in oil are shown in Figure 7.1. It clear that the injection of pre-saturated carbonated brine changed the wetting behavior of calcite. In the 1-15 plot this behavior turned from neutral-wet (when no CO₂ was applied) to water-wet (contact angle

lower than 70°). For the 30 days aged mineral, the decrease in contact angle is even greater turning from strongly oil-wet (145°) to water-wet (CA lower than 70°).

The effect of injecting a gas cap after drop deposition, on the other hand, has no such effect on the CA at the initial pressure. For 15 days aging the decrease in contact angle is only noticeable as the pressure increases. This may be due to the higher solubility of the CO₂ cap as the pressure increases. For the 30 days aged rock the decrease in CA was not sufficient to change the wettability of the rock from oil-wet to neutral-wet.

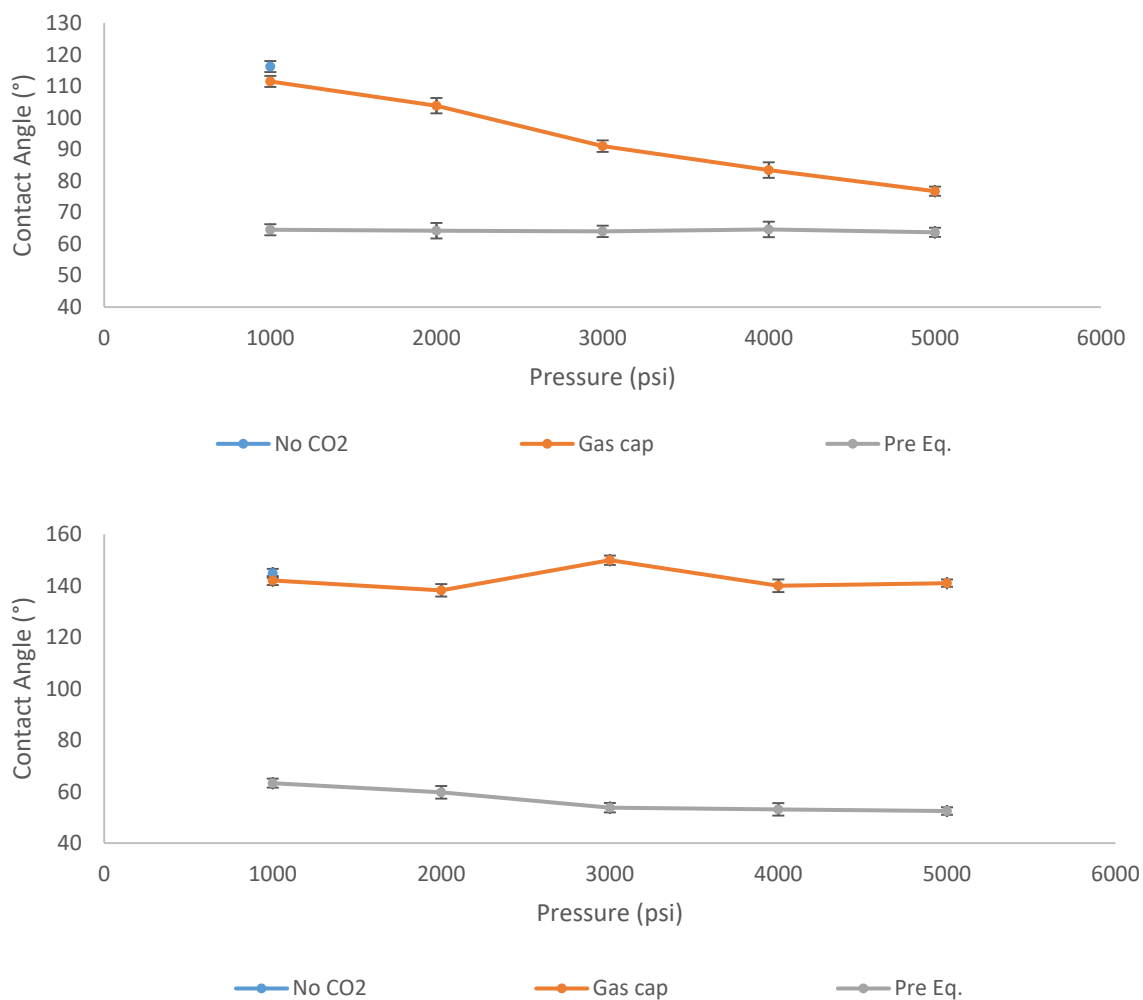


Figure 7.1. Effect of different CO₂ injection methods for calcite using Field B fluids at 60 °C. Top: 15 days aging in oil. Bottom: 30 days aging in oil.

The behavior observed for the “Gas cap” experiments is a consequence of mass transfer during the experiments, which cause not only the interaction of CO₂ with the aged rock, but also swelling of the oil drop. Moreover, it is important to remark that in this method CO₂ is introduced in the system only after the oil drop is equilibrated on the rock surface. Therefore, after pinning of the three-phase line it is possible than the effects of CO₂ on wettability may be less pronounced than other mass transfer effects such as oil swelling.

Similar experiments in were carried out using Field D oil and formation brine. The results (Figure 7.2) show the same trends. The agreement between the results using fluids from both fields indicate consistence in the effect of the two methods considered in this work.

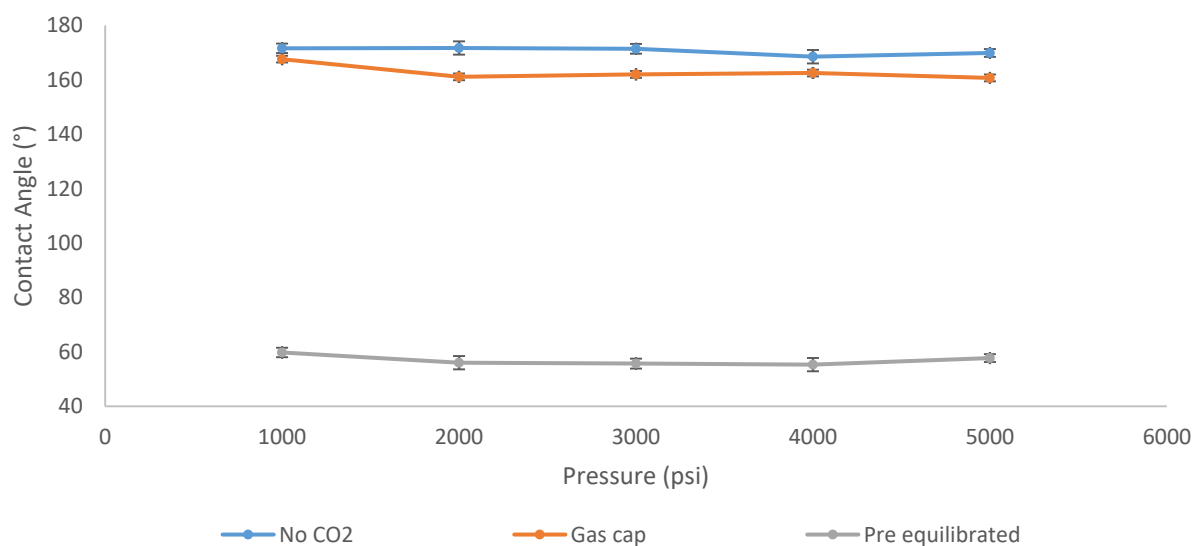


Figure 7.2. Effect of different CO₂ injection methods for calcite using Field D fluids at 60 °C and 30 days aging in oil.

7.1.2 Dolomite

Similar approach was employed for dolomite mineral samples, and the results for Field B fluids and 30 days of aging are shown in Figure 7.3. It is clear than the effect of CO₂ in this case is less relevant than for calcite resulting in a decrease of 20° for the injection of pre-saturated carbonated brine. For the gas cap injection, the change in CA is not relevant oscillating in +/- 10° from the value with no CO₂ supporting the idea of the instability of this method due to mass transfer effects. These experiments were run using Field D fluids, and

the effects were practically negligible obtaining a decrease from 60° (no CO₂) to 55° (Pre-equilibrated fluids). Therefore, the complete plots are not shown in this text.

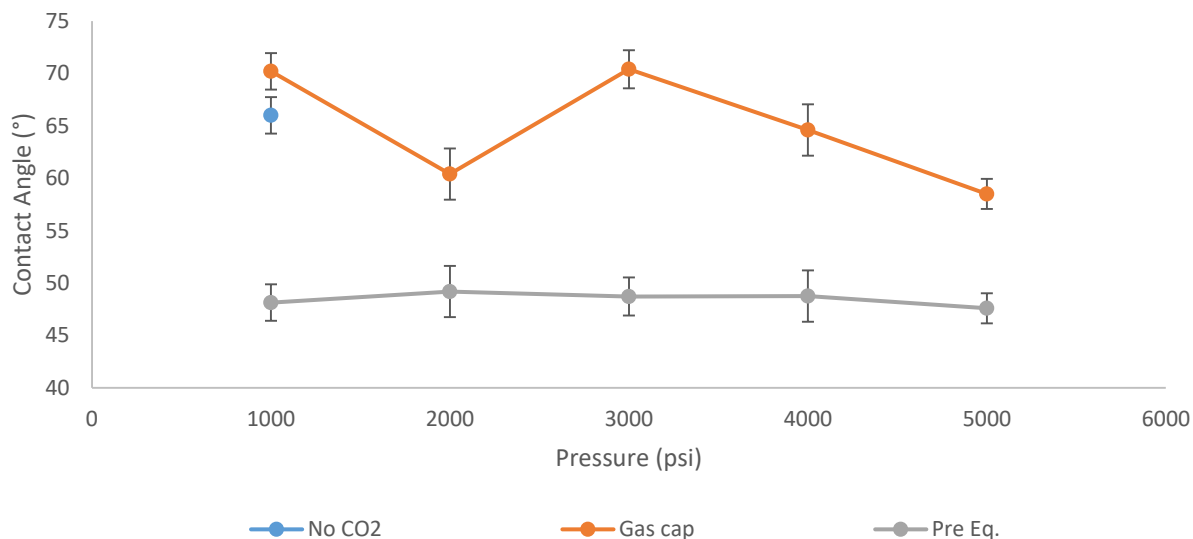


Figure 7.3. Effect of different CO₂ injection methods for dolomite using Field B fluids at 60 °C and 30 days aging in oil.

7.1.3 Quartz

The effect of injection CO₂ using the same methods as before on 30 days aged quartz surface using Field B fluids is represented in Figure 7.4. The “Gas cap” experiment did not show an effect on the CA value. Nevertheless, the “Pre-equilibrated” experiment showed an increase of over 30° in agreement with previous results for carbonated water on this mineral (GRIBANOVA, 1992). It should be noticed that this effect is less critical than the decrease in CA found for calcite. This will be discussed in more detail in Section 7.5.

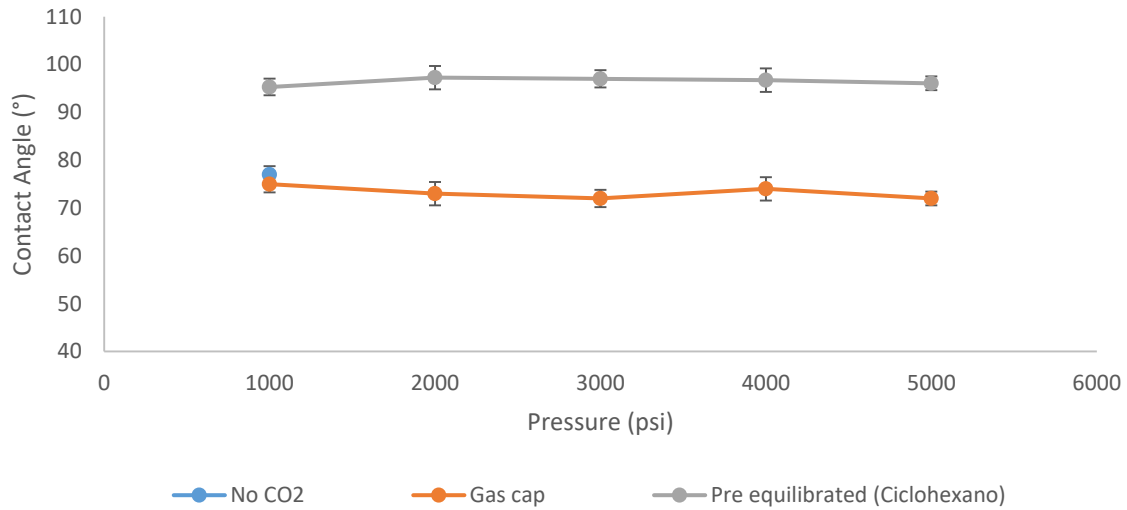


Figure 7.4. Effect of different CO₂ injection methods for quartz using Field B fluids at 60 °C and 30 days aging in oil.

The results of similar tests for Field D fluids resulting in an initial value of 65° for the experiment without CO₂, 67° for the “Pre-equilibrated” experiment and 59° for the “Gas cap”. Since the effect of CO₂ is less significant for this mineral, the complete plots for this field and for 1-15 aging time were not included in this text.

7.1.4 Coquinas

The results of the same experiments for Field B fluids using 15 and 30 days aged coquinas is shown in Figure 7.5. It is evident that the curves follow a similar trend than that for calcite (Figure 7.1) with slight differences in the initial values. Nevertheless, the wetting behavior is the same having oil-wet behavior in the absence of CO₂ and neutral to water-wet behavior after carbonated water injection.

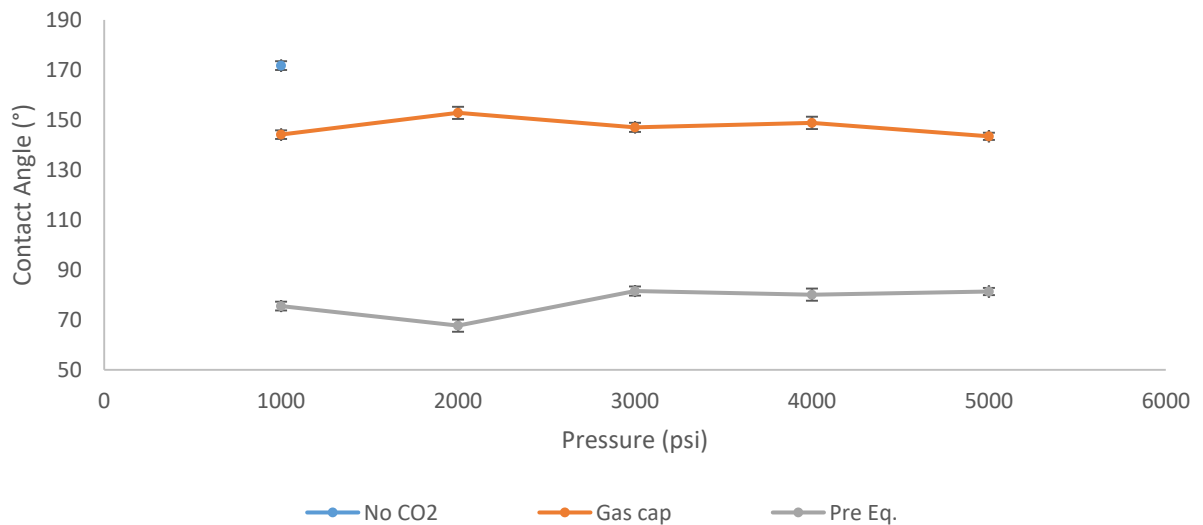
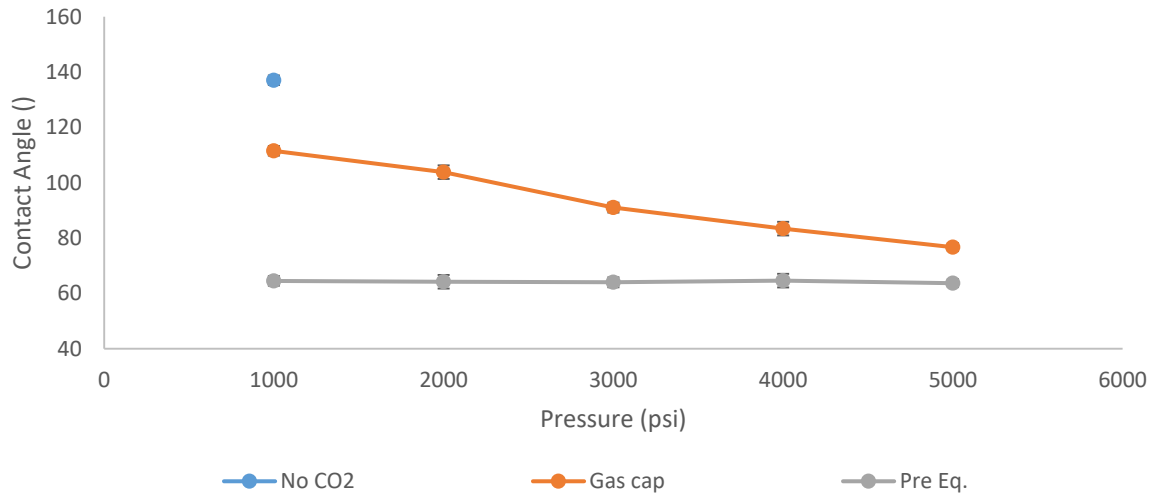


Figure 7.5. Effect of different CO₂ injection methods for coquinas using Field B fluids at 60 °C. Top: 15 days aging in oil. Bottom: 30 days aging in oil.

As with calcite, the tests were also carried out using Field D fluids and 30 days aging time in oil, and the results are plotted in Figure 7.6. As stated before, these curves indicate that the obtained effects of CO₂ injection are consistent for the scenario of both Pre-Salt fields considered in this work. The similarities and differences between the results for both calcite and coquinas will be discussed in Section 7.5.

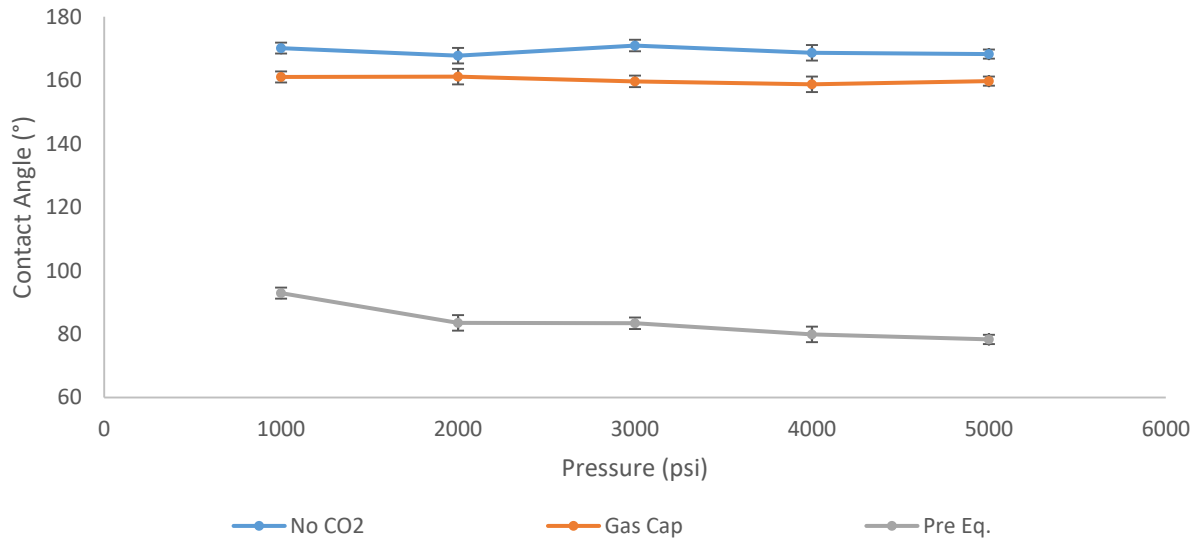


Figure 7.6. Effect of different CO₂ injection methods for coquinas using Field D fluids at 60 °C and 30 days aging in oil.

7.1.5 Pre-Salt Field D reservoir rock

The analysis of CO₂ effect on Field D Pre-Salt rock was carried out using 30 days aging and Field D fluids, and the results are on Figure 7.7. The Pre-equilibrated fluids experiment results reduces the CA in a similar fashion than on calcite and coquinas. As in those rocks, in this case the decrease is from strongly-wet (160°) to neutral-wet (105°) behavior.

For comparison, the test was repeated for a different Field D rock sample using 15 days aging in oil and fluids from the same field. Figure 7.8 shows that saturated carbonated water injection reduced the CA more than 40°. In this case the Pre-Salt reservoir rock changed from slightly oil-wet to neutral-wet getting a final value similar to that of Figure 7.7. Both results presented in this section indicate that, if for certain Pre-Salt field formation brine is originally saturated with CO₂, neutral to slightly water-wet behavior could be expected to represent their initial wettability.

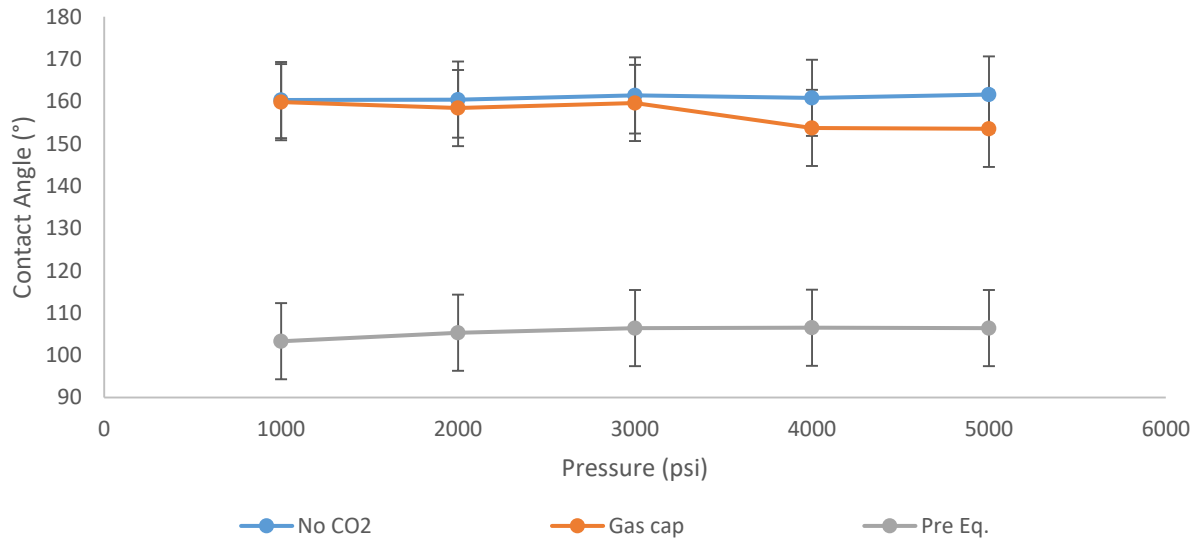


Figure 7.7. Effect of different CO₂ injection methods for Field D Pre-Salt rock using Field D fluids at 60 °C and 30 days aging in oil.

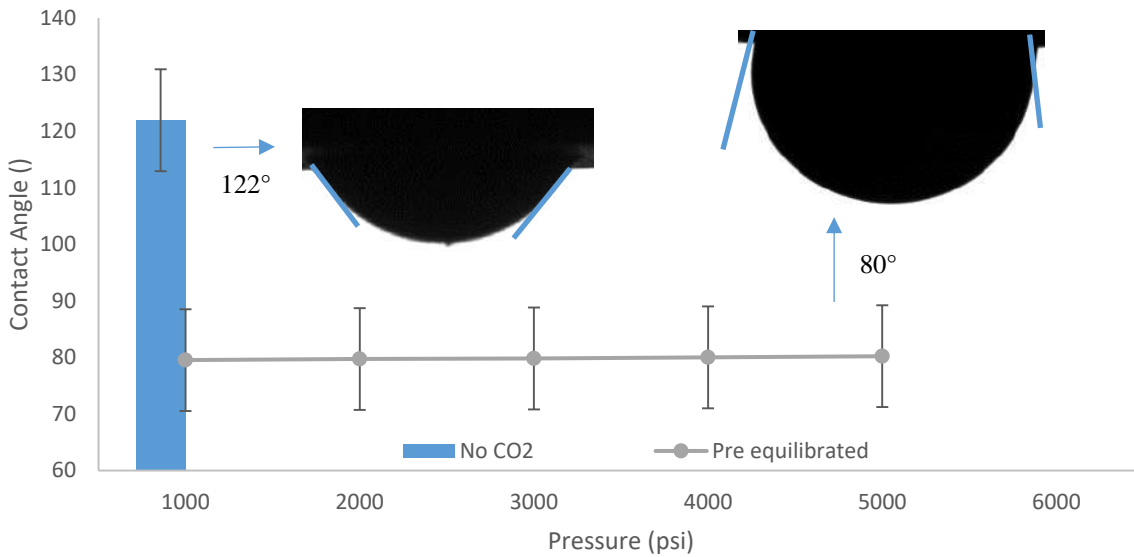


Figure 7.8. Effect of carbonated water injection for Field D Pre-Salt rock using Field D fluids at 60 °C and 15 days aging in oil.

7.2 Pre-equilibration of the gas cap

As presented in the previous section, the injection of a gas cap after drop deposition did not affect the previously established equilibrium of rock-fluid interactions. To study the effects of injecting a gas cap prior to oil-rock contact, the methods described in Section 4.1.1 were implemented for both rocks that were more reactive to CO₂ injection, calcite and coquinas.

In summary, two additional types of experiments were carried out. The “New drop gas cap” experiment consisted in carrying out separate independent tests on different aged rock slabs for each pressure. On each test, a drop was injected in the same fashion as in the “Gas cap experiment”, but each test was run in a single pressure (i.e. 1000, 3000 or 5000 psi). In the “Equilibrated gas cap” procedure, each test was run at a single pressure too. The difference was that the gas cap was injected and set to equilibrate with the brine in which the rock slab was immersed for over 12 hours. After this equilibration time, the oil drop was injected as in the other methods.

The objective of comparing these methods is to understand the differences in the results obtained between the “Gas cap” and “Pre-equilibrated” experiments in previous sections. Having CO₂ dissolved in brine prior to drop deposition may be required to observe wettability alteration using static CA measurement. In addition, it is not clear if the dynamics of CO₂ dissolution, its diffusion through the brine and reaction with the surface and removal of adsorbed oil compounds during the aging is a process that will require considerable amount of time or if it can be considered an instantaneous process in practical terms.

Finally, the changes in CA found for different pressures using the same method have the purpose of evaluating the effect of pressure on initial wettability for CO₂ saturated systems. As previously discussed, static CA measurements are not sensitive to dynamic effects due to pinning of the three-phase contact line. Heterogeneities on the solid, roughness or mass transfer between phases can favor this effect. As the purpose of these experiments is to account for the possible variations on the initial wettability depending on the system pressure at which CO₂ is injected, the injection of a new drop is the most sensible way to observe this by static CA measurements.

In other words, by comparing “New drop gas cap” and “Equilibrated gas cap”, information about the time required for wettability effects by CO₂ dissolution should be retrieved. Moreover, the differences (or similarities) between the “Pre-equilibrated” and “Equilibrated gas cap” experiments will give an insight on the effect of pressure when measurements are carried out on the same drop or using individual drops for each pressure.

The results of the experiments using the previously discussed methods for calcite (Figure 7.9) and coquina (Figure 7.10) are included below:

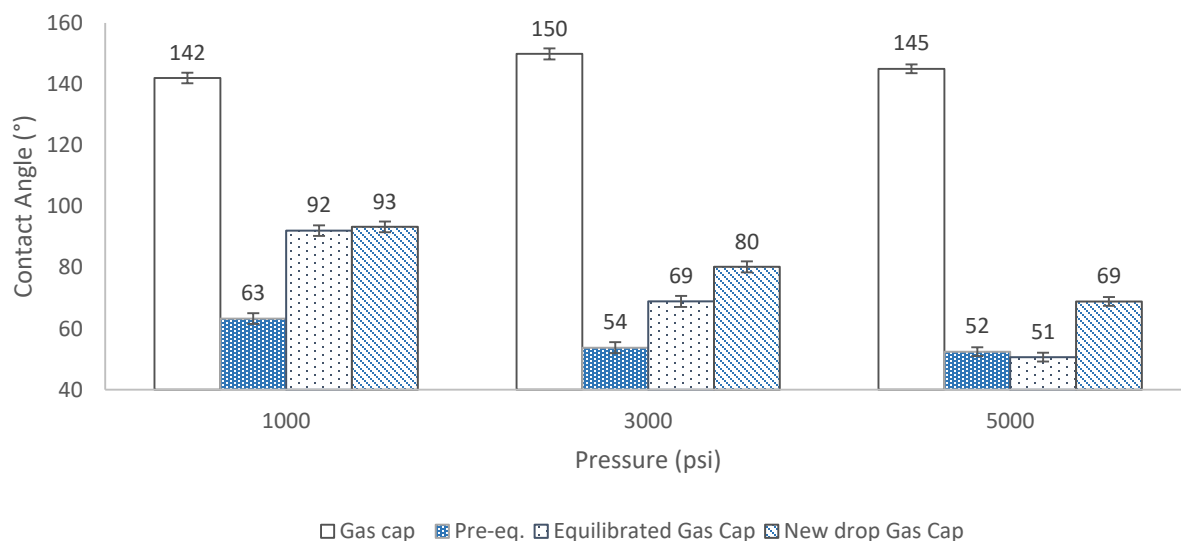


Figure 7.9. Contact angle on 30 days aged calcite measured for CO₂ injection using separate drops at different pressures or varying the pressure on the same drop. Field B fluids at 60 °C.

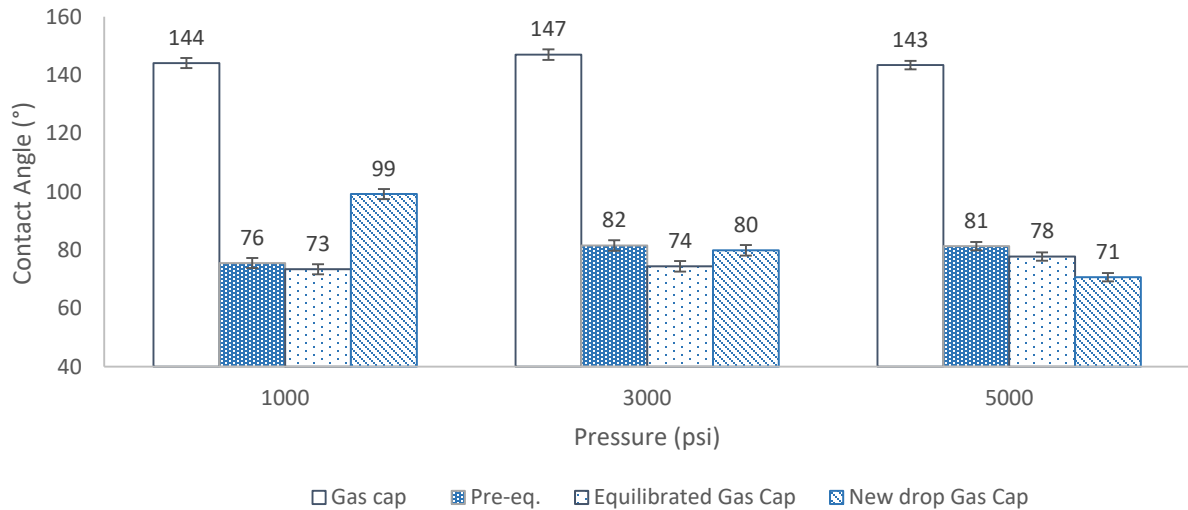


Figure 7.10. Contact angle on 30 days aged coquina measured for CO₂ injection using separate drops at different pressures or varying the pressure on the same drop. Field B fluids at 60 °C.

Looking at the previous pictures, it is evident that the “Gas cap” experiment shows the greatest difference with the other methods at all pressure values. In fact, “Gas cap” is the only method that results in opposite wetting behavior. This proves that, after drop deposition, injecting the CO₂ cap won’t affect the oil-brine-rock contact line as it is already equilibrated. Thus, “Gas cap” method is not adequate to observe wettability changes on the rock, and the variation in CA found by this method may be the result of other mass transfer mechanisms, such as drop swelling.

Another visible effect is that the other methods result in neutral or water-wet behavior showing a clear trend on the impact of CO₂ on the wettability of these carbonate rocks. The difference in the values obtained with the different procedures is decreased as pressure increase, indicating that shorter time is required to reach equilibrium at higher pressures. It should be considered that at 1000 psi the gas cap is below CO₂ critical point resulting in poorer dissolution and mass transfer in the aqueous phase.

Both the “Equilibrated gas cap” and “Pre-equilibrated” results show similar wettability trends at all conditions indicating that pre-saturating both phases prior contact with the solid phase or dissolving CO₂ in the brine where the rock is immerse have an impact on its wettability. However, for calcite discrepancy between both methods is noticeable at

1000 psi, at which “Pre-equilibrated” shows water-wet and “Equilibrated gas cap” has intermediate or neutral-wet value. As pressure increases, this difference vanishes. For coquinas, both methods result in similar values at all pressures obtaining a maximum difference of 3° between them. This disparity between both rocks could indicate that pre-saturated brine may react more readily with calcite, which is more reactive than the heterogeneous coquinas. Therefore, the in “Equilibrated gas cap” method similar effect is found at higher pressures, at which mass transfer is enhanced. Despite these differences, in terms of wettability trends both methods showed wettability alteration and only the experiment for calcite at 1000 psi indicated a difference in the wetting behavior.

In the “New drop gas cap”, on the other hand, the drop is injected right after gas cap injection. Thus, no equilibration time for dissolution and mass transfer is allowed. It can be acknowledged that this method results in lower CA values at higher pressure at which mass transfer is accelerated. Moreover, the difference between this method and the “Equilibrated gas cap” has opposite trends in calcite and coquinas. This supports the discussion in the previous paragraph. Further reaction with calcite reactive surface favors the lower CA values observed for the “Equilibrated gas cap” at high pressure. For coquinas, this difference is not as relevant as its surface is less attacked by CO₂ than that of calcite.

Previous discussions comment on the contrast found for different equilibration times and sequences in the injected fluids. To study time effects and dynamic variations on wettability, advancing and receding CA should be measured as pressure is increased using the “Gas cap” or “Pre-equilibrated” fluids. The objective of the previous discussion was to evaluate how initial wettability could be assessed by using independent measurements at different pressures, as opposed to changing pressure on the same drop. The most relevant conclusion is that, when using independent drops on each measurement, injecting a gas caps allows to observe wettability changes by CO₂. Thus, at pressure higher than CO₂ critical point, the methods give similar trends showing consistent shift of wettability towards water-wet.

7.3 Effect of CO₂ concentration

The effect of CO₂ concentration in carbonated water on rock wettability was studied using the “Pre-equilibrated” method. For this, different concentrations of CO₂ were dissolved in brine B using the procedure in Section 4.1.4. The properties of the resulting carbonated brines are detailed in Table B.6. These tests were carried out for calcite and coquinas using 30 days aging in reutilized oil after aging. As discussed in the previous chapter, since reutilized oil is more viscous and heavier, cyclohexane must be used to aid in bulk oil removal after centrifugation. The results are shown in Figure 7.11 and 7.12.

In both cases it is noticeable that the higher the CO₂ concentration, the greater the reduction in CA. To get a straightforward visualization of this, Figure 7.13 shows the CA as a function of CO₂ concentration at 1000 psi. This proves that at very low CO₂ concentrations (i.e. lower than 10 mol%), the effects of CO₂ are negligible. As CO₂ concentration increases, the augmented in water-wet behavior indicates that the effect of carbonated water on carbonate rock wettability is proportional to CO₂ concentration. The main reasons for this are the reactivity of calcium carbonate as CO₂ is dissolved in brine (Chapter 3) and the decrease in pH, which increases the charge of the system which weakens the interaction between the active sites on the rock and the polar molecules in the oil that cause oil wettability during aging.

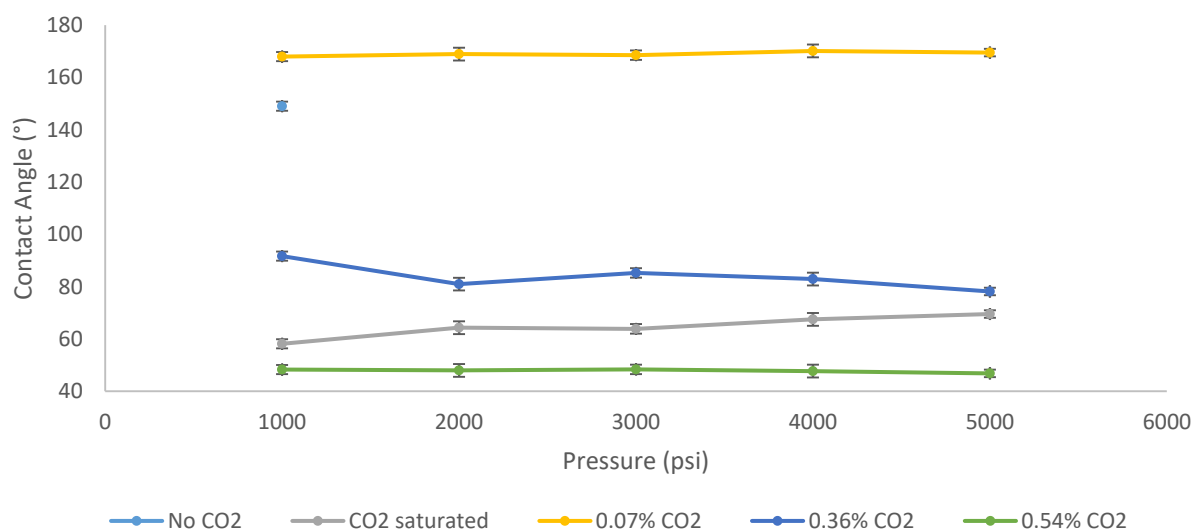


Figure 7.11. Contact angle versus pressure for 30 days aged calcite (in reutilized oil) using Field B fluids at 60 °C.

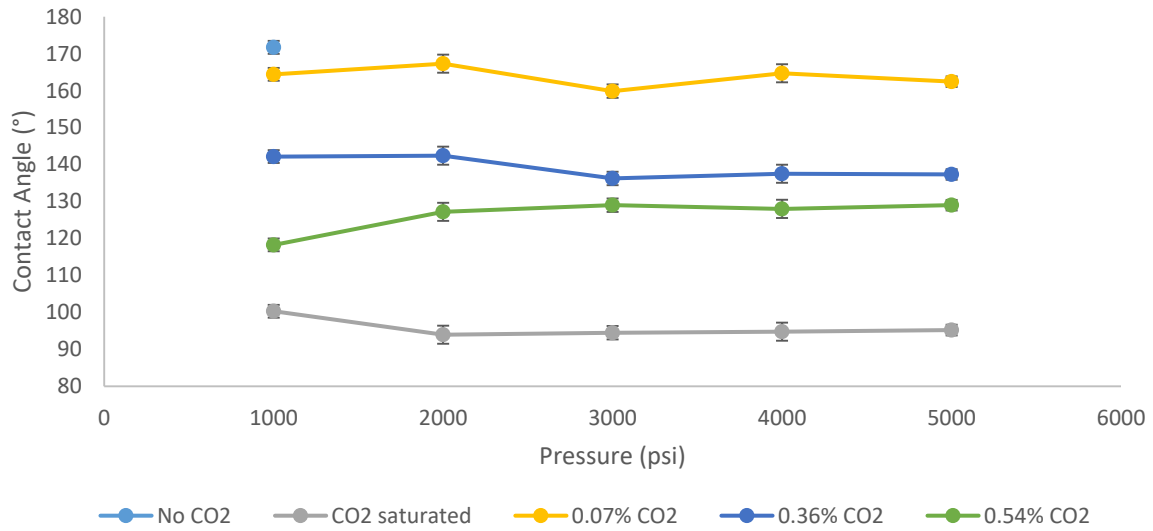


Figure 7.12. Contact angle versus pressure for 30 days aged coquina (in reutilized oil) using Field B fluids at 60 °C.

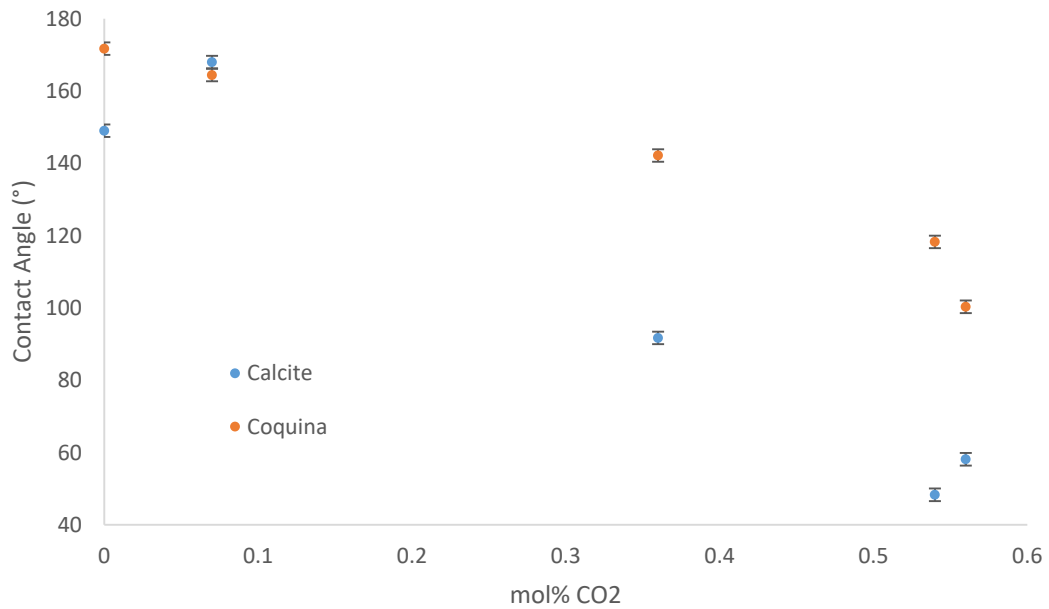


Figure 7.13. Contact angle versus CO₂ concentration in brine for 30 days aged (in reutilized oil) calcite and coquina using Field B fluids at 60 °C and 1000 psi.

Nevertheless, it should be pointed out that the decrease in CA does not follow a proportional trend with the reduction of pH. Figure B.2 shows the pH as a function of pressure

for Brine B with the concentrations of CO₂ considered in this section. Considering LB1 with a concentration of 0.07 mol% CO₂, while pH is 3.3 at 1000 psi, the initial CA is still in the oil-wet region for both calcite and coquina. For LB2 (0.35 mol% CO₂) the pH is 2.8 and the wettability is in the intermediate or oil-wet region. However, for LB3 pH is slightly reduced (2.7) and a major shift in wettability of calcite towards water-wet is observed.

Two important conclusions can be drawn from this experiment. First, dramatic wettability changes with carbonated brine seem to occur when CO₂ concentration overpasses a threshold value rather than as a direct function of pH reduction. This gives the idea that carbonate reactivity causing desorption of the organic molecules is the main promotor of this shift in wettability. Secondly, wettability changes in calcite takes place at lower concentrations of CO₂ in agreement with the presented idea as calcite is expected to be more reactive than coquina rocks. Experimental analysis of the effects of carbonated brine on these solid phases is presented in Section 7.5 to support these ideas.

7.4 Effect of pressure

In the previous chapter, it was shown that the effect of pressure on the initial wettability is negligible when dead fluids are used. To study the effect of pressure in CO₂ saturated fluids, a set of experiments using pre-equilibrated fluids in which the drop was deposited either at 3000 or 5000 psi and 60 °C were carried out. These tests included calcite and coquinas aged 1 day in Brine B and 15 days in Oil B. The results (Figure 7.14. Contact angle versus pressure for tests with pre-saturated fluids using the same drop (line) or a new drop (bars). Conditions: 1 day aging (Brine B), 15 days aging (Oil B) and 60 °C. Top: calcite. Bottom: coquina.) were compared to those in which the pressure was raised from 1000 to 5000 psi after drop deposition to observe the effect of pressure prior and after drop deposition.

It is clear that after drop deposition, no effect of pressure is observed. This indicates that pinning of the three-phase line hinders the displacement of the drop, a well-known limitation for static contact angle measurements. For the tests injecting a new drop at each pressure, a decrease in CA with pressure is shown. This effect is more relevant for calcite, which is the most reactive mineral resulting in a difference of 18° at 5000 psi. For coquinas,

the maximum difference was of 6° supporting the idea that this outcrop rock is less reactive with carbonated water than calcite.

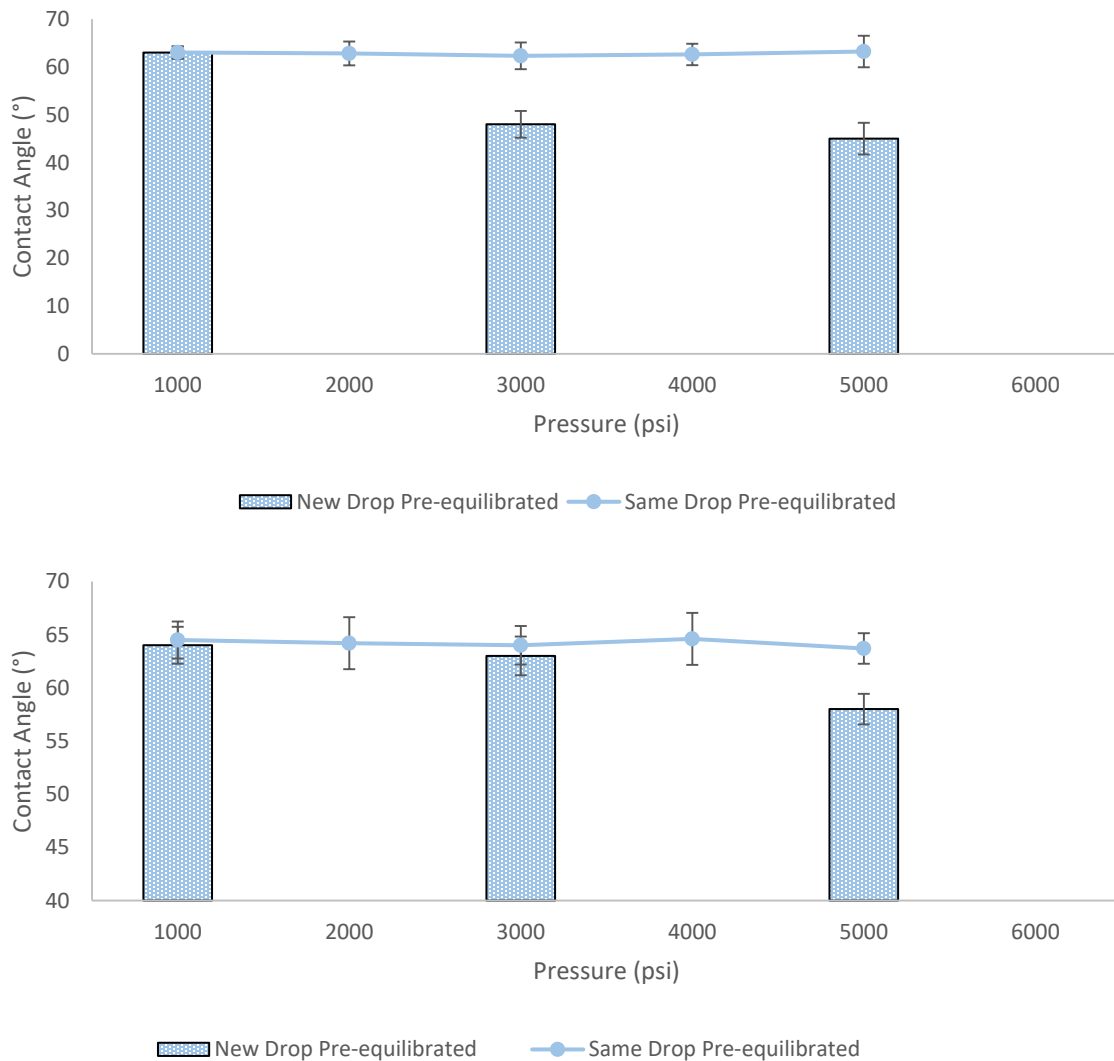


Figure 7.14. Contact angle versus pressure for tests with pre-saturated fluids using the same drop (line) or a new drop (bars). Conditions: 1 day aging (Brine B), 15 days aging (Oil B) and 60 °C. Top: calcite. Bottom: coquina.

Differently to what was found for fluids with no dissolved gas, a trend was found for fluids pre-saturated with CO₂. Higher pressure resulted in increased water-wet behavior tending to the wettability of the unaged rocks. Nevertheless, at the lowest test pressure (1000 psi), the wettability behavior of both carbonate rocks had already been shifted towards water-wet.

7.5 Discussion: Effect of CO₂ on the wettability of the different rocks

The following paragraphs will discuss the effect of CO₂ on the wettability for the different rocks employed in this work. The results of 15 and 30 days aged rocks using Field B fluids without CO₂ injection and with pre-equilibrated fluids at 60 °C and 1000 psi are summed up in Figure 7.15. Moreover, the same analysis was done for tests with fluids from Field D on all pure minerals and rocks used in this work. The results are condensed in Figure 7.16 (minerals) and Figure 7.17 (rocks). The effect of CO₂ on the rocks can be divided into two broad groups. On the one hand, carbonate reactive rocks including calcite, coquinas, limestone and Pre-Salt reservoir rock, which showed oil-wet behavior in the absence of CO₂. On the other hand, initially water-wet rocks (dolomite and quartz) were not as critically affected by CO₂ dissolution in brine.

a) Quartz

The wettability of quartz depends on the formation of a water adsorption film which is stabilized by electrostatic interactions. As discussed in Section 2.4.4, quartz's negative surface charge at neutral pH is the result of the protonation equilibrium of silanol and silanoic acid. The thermodynamics of water wetting on glass surface were studied (CHIQUET; BROSETA; THIBEAU, 2007). The authors stated that lower equilibrium CA values (and increasing water-wet behavior) were associated to decreasing free energies of activation of wetting. This represents that when the water film is more stable, it will not be disrupted by the charges present on the other interfaces.

The dissolution of CO₂ decreases pH reducing the negative charge on quartz. This weakens the repulsion between the solid-brine and brine-oil interfaces that stabilize the water film. As water-wet behavior of quartz is promoted by the stability of the water film, the decrease in pH favors its disruption resulting in a less water-wet (or more neutral or oil-wet) behavior. This was previously discussed in the literature (BUCKLEY; TAKAMURA; MORROW, 1989). At pH between 2 and 3, which corresponds to carbonated brine B, surface charge is reduced to close to zero (AL-YASERI et al., 2017).

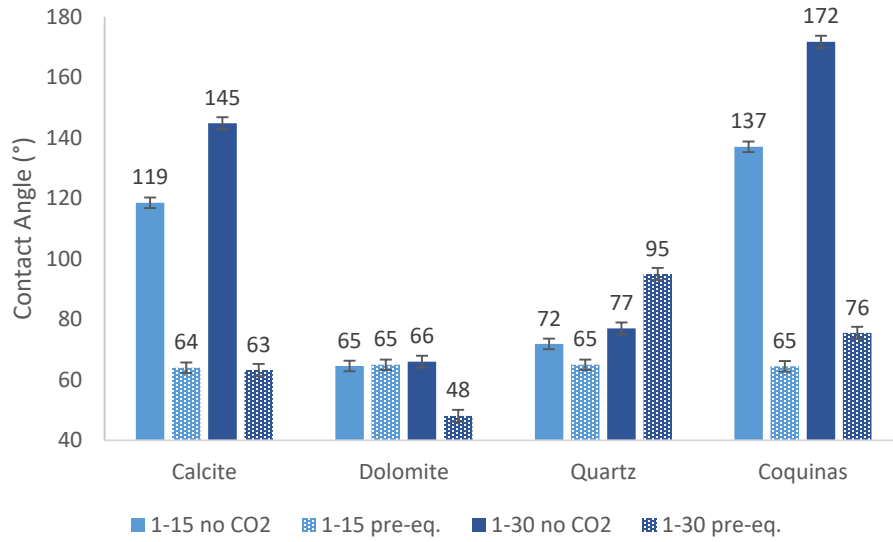


Figure 7.15. Effect of CO₂ injection on the wettability of different rocks using Field B fluids. Aging time: 15 or 30 days. Field B fluids at 60 °C and 1000 psi.

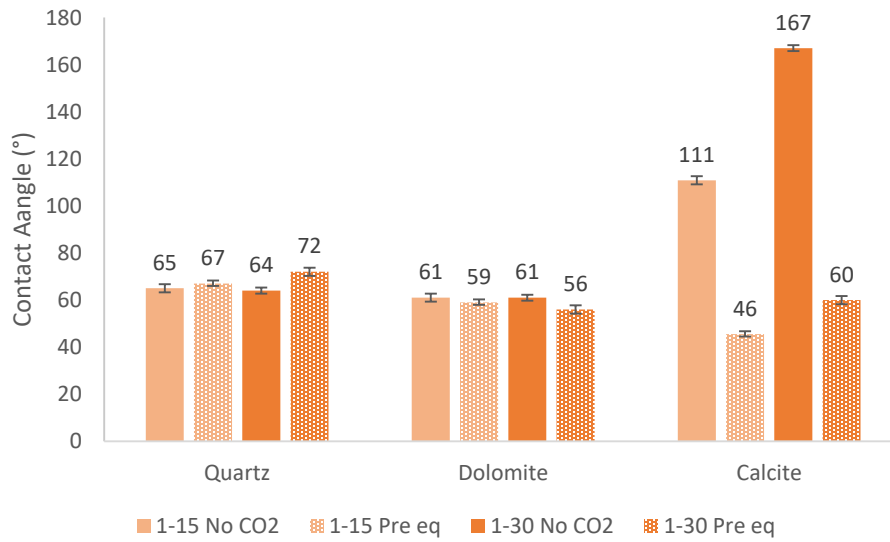


Figure 7.16. Effect of CO₂ injection on the wettability of pure minerals using Field D fluids. Aging time: 15 days. Field D fluids at 60 °C and 1000 psi.

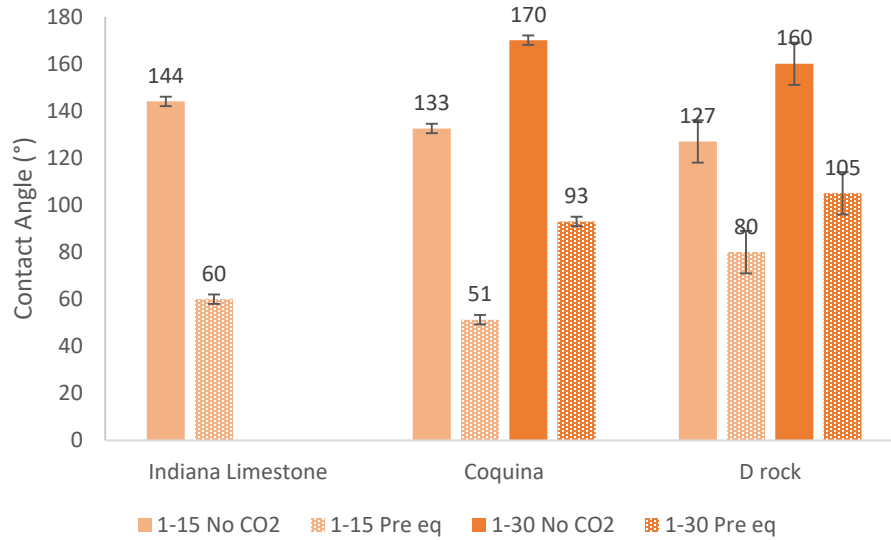


Figure 7.17. Effect of CO₂ injection on the wettability of pure minerals using Field D fluids. Aging time: 30 days. Field D fluids at 60 °C and 1000 psi.

Buckley et al. (1989) performed adhesion tests of three crude oils on quartz changing brine pH and NaCl salinity. They obtained that acid pH (lower than 4) favored oil adhesion to the solid surface indicating disruption of the water film. They also measured the isoelectric point (pI), pH at which the negative charge of acid groups and positive charge of acid groups is balanced on the oil-brine interface, as a function of salinity. For the oils and NaCl brines they used, they obtained values between 3.5 and 5. Thus, at the pH values corresponding to saturated carbonate water, the electrostatic repulsion could be overcome by van der Waals attractive forces resulting in negative disjoining pressure, as previously discussed in Section 2.3.2.

These considerations support the results for quartz in Figure 7.15. The injection of pre-saturated carbonated brine reduces the pH below 3, and the charge on quartz's surface becomes less negative. At lower pH the acid groups on the oil-brine interface become protonated, also reducing its negative charge. As a result, the water film is destabilized, and the aged quartz presents neutral-wet behavior.

b) Dolomite

The effect of pressure on the CA of a brine droplet in a CO₂ atmosphere on dolomite before and after aging with triethoxy(octyl)silane was recently studied (ROSHAN et al., 2016). In both cases, CA increased with pressure. The authors related this effect to the decrease in density difference as the pressure increases (MORROW; CRAM; MCCAFFERY, 1973). They concluded that, for weakly charged surfaces, the effects of density difference, fluid-fluid interfacial tension and van der Waals forces between the fluids and the solid are critically affected as temperature, pressure and pH are modified.

As discussed in the previous chapter, the presence of Mg on the structure of dolomite weakens the interaction between the active groups in crude oil and its surface. The increase in water-wet behavior of dolomite by acidification with octanoic acid was reported elsewhere (KOSMULSKI, 2011). The point of zero charge (pzc) for dolomite at 20 °C was reported as close to 7 (SEYYEDI; SOHRABI; FARZANEH, 2015); thus, a slightly positive charged surface is expected when immerse in Brine B. Dissolution of CO₂ weakens even more the interaction of the polar groups in the oil resulting in more water-wet behavior. Nevertheless, this effect is less pronounced than in the other carbonate rocks because the interaction between oil and dolomite was already weak even before CO₂ injection.

c) Calcite, coquinas, Indiana limestone and Pre-Salt rock

The effect of carbonated brine on wettability of these rocks is very clear (Figure 7.18), the decrease in pH produced a decrease in CA shifting wettability from oil-wet to neutral or water-wet. This trend is in agreements with the results found by Seyyedi et al. (2015) for aged calcite plates using CO₂ injection in brine with a salinity below 55000 ppm at 38 °C and pressures up to 3000 psi. The authors stated that this change in wettability is caused to dissolution of the organic molecules adsorbed in the aging process, which cause wettability towards oil. As pH decreases, the interaction between the polar compounds and the active sites on the solid are weakened in a similarly as with dolomite. However, as calcite is more reactive with carbonated brine (Section 3.3, the impact of CO₂ injection on the surface of this mineral is more dramatic, reversing its wetting behavior to that of the unaged mineral.

Another fact that plays an important role in wettability alteration of calcite is dissolution, represented by the chemical reactions in Section 3.3. The dissolution of active

sites increases the concentration of Ca^{2+} cations (AUSTAD et al., 2008). The presence of these divalent cations were reported as wettability modifiers of carbonates, shifting wettability towards water-wet (YAKHSHI-TAFTI; KUMAR; CHO, 2011).

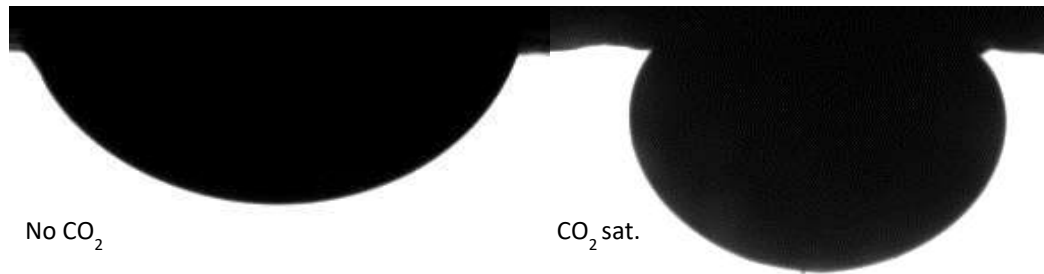


Figure 7.18. Oil B drop in Brine B on 15 days aged coquinas using dead fluids and CO_2 saturated fluids.

These combined factors cause the great effects in calcite wettability found in Figure 7.15. Other carbonates such as limestone, coquinas and Pre-Salt rocks present the same behavior at different degrees which depend on presence of heterogeneities and more complex mineralogy and surface roughness among others. As presented in Chapter 5, coquinas and Pre-Salt rocks contain quartz, feldspar and other minerals among their constituents. Thus, the lower reactivity of these rocks with carbonated are expected compared to that of calcite.

Seyyedi et al. (2015) qualitatively identified effects of carbon dissolution such as increased surface roughness. In the following paragraphs, the effects of CO_2 on the wettability of different carbonates are described using different techniques.

The roughness of the new rock slabs before the test and after test with CO_2 pre-saturated brine were measured using a profilometer as described in Chapter 4. In both cases, samples were cleaned with toluene and methanol prior to the measurement. The results including the difference after the test with carbonated brine are shown in Table 7.1.

Table 7.1. Effect of CO₂ on average roughness of different rocks.

| | Ave. R (nm) | | % Difference |
|----------|-------------|---------|--------------|
| | New | Pre-eq. | |
| Quartz | 4 | 3.92 | -2% |
| Calcite | 1096 | 27036 | 2367% |
| Dolomite | 3186 | 4126 | 30% |
| Coquina | 2762 | 3987 | 44% |
| Rock D | 2207 | 2740 | 24% |

After the test with carbonated brine, all carbonate rocks showed an increase in the macroscopic roughness. Nevertheless, the surface of calcite was visible attacked by carbonated water, which is confirmed by the increase in its surface roughness of over 20 times.

The surface topography was qualitatively analyzed using confocal microscopy. The images for the calcite slab before test and after test are shown in the next two figures. The severe signs of rock dissolution in Figure 7.20 are remarkable when compared to the flatter and smoother surface in Figure 7.19.

The same comparison for coquinas and Pre-Salt rock is set in Figures 7.21 – 7.24. In these cases, despite visible differences on the surface, the effects are less critical than in the case of calcite. This was expected due to the increased heterogeneity of these reservoir rocks, and also since calcite is the most reactive mineral in their composition. Thus, these images support the results in the previous sections of this chapter.

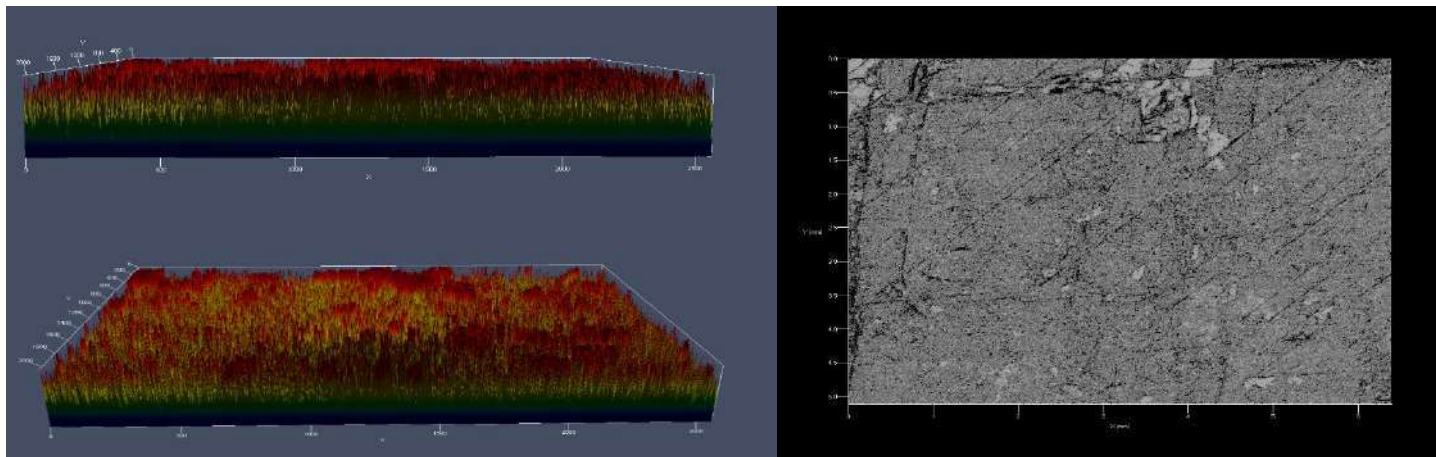


Figure 7.19. Confocal microscopy showing surface topography of new calcite slab.

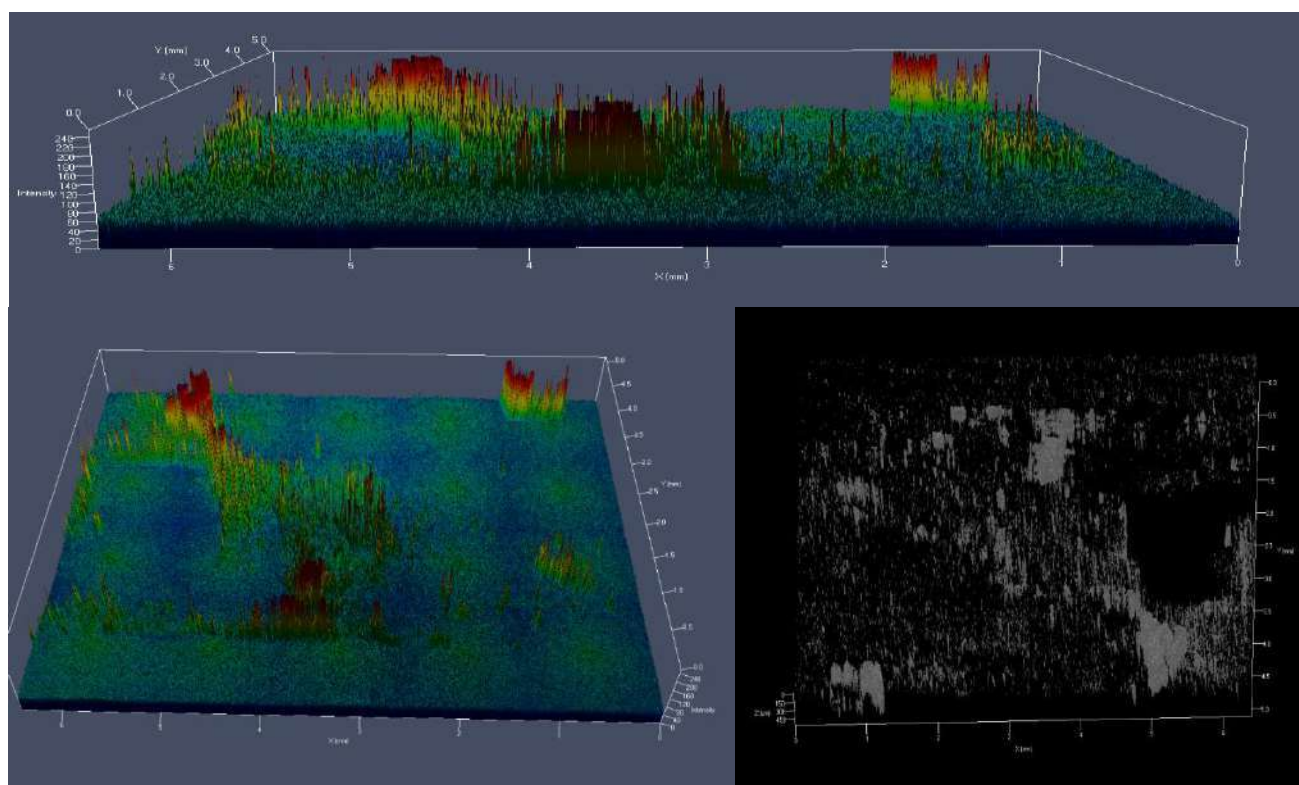


Figure 7.20. Confocal microscopy showing surface topography of calcite slab after test with carbonated brine.

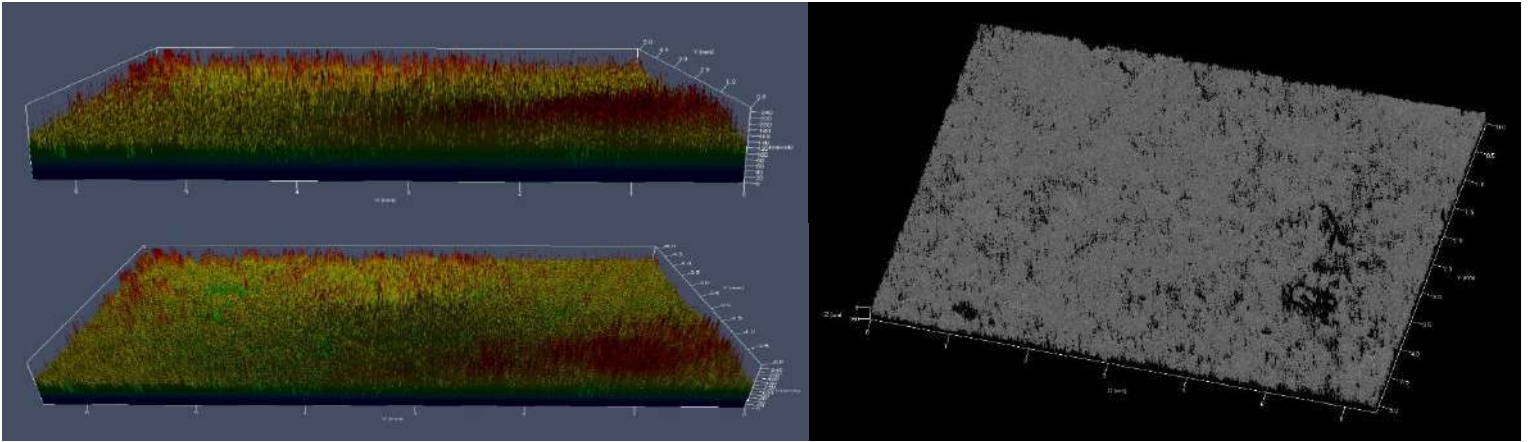


Figure 7.21. Confocal microscopy showing surface topography of new coquina slab.

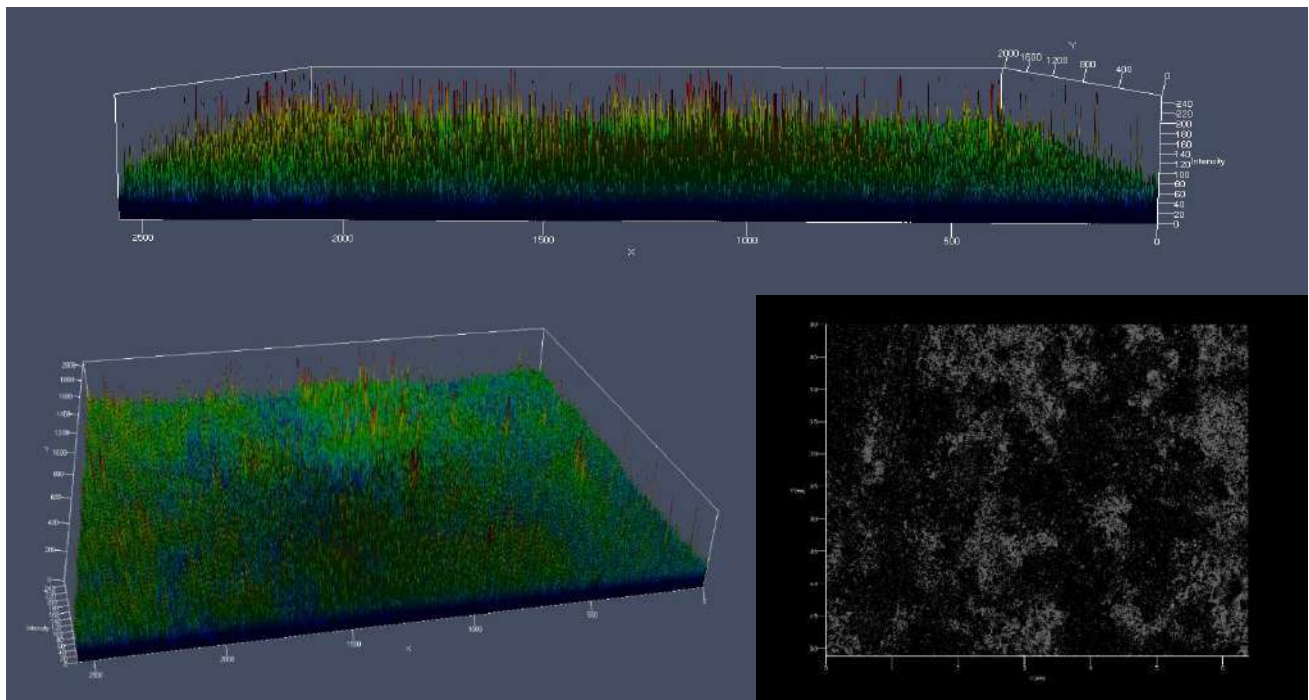


Figure 7.22. Confocal microscopy showing surface topography of coquina slab after test with carbonated brine.

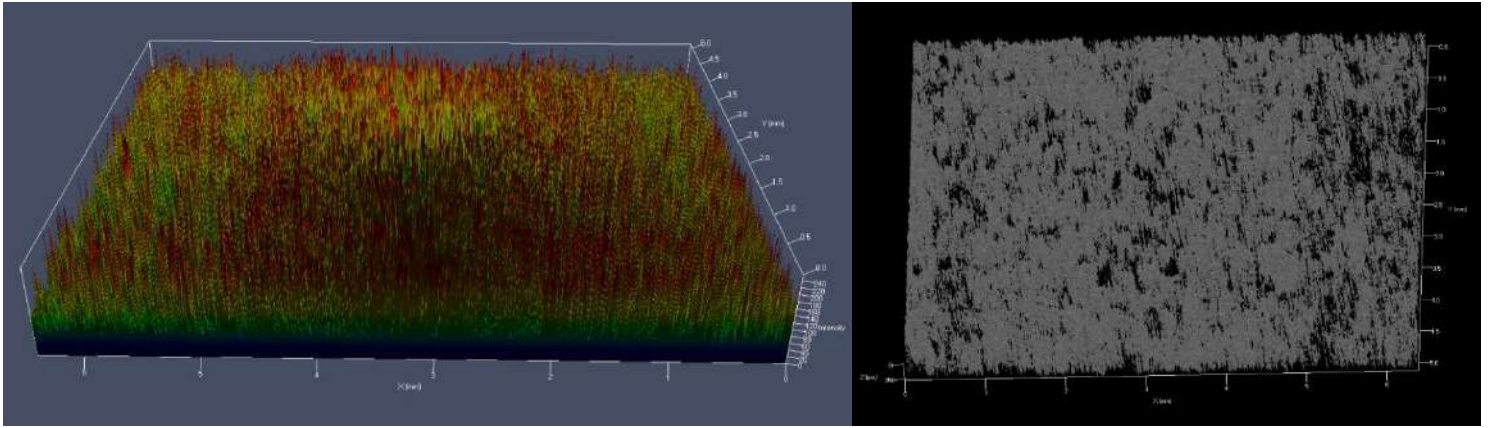


Figure 7.23. Confocal microscopy showing surface topography of new Field D rock slab.

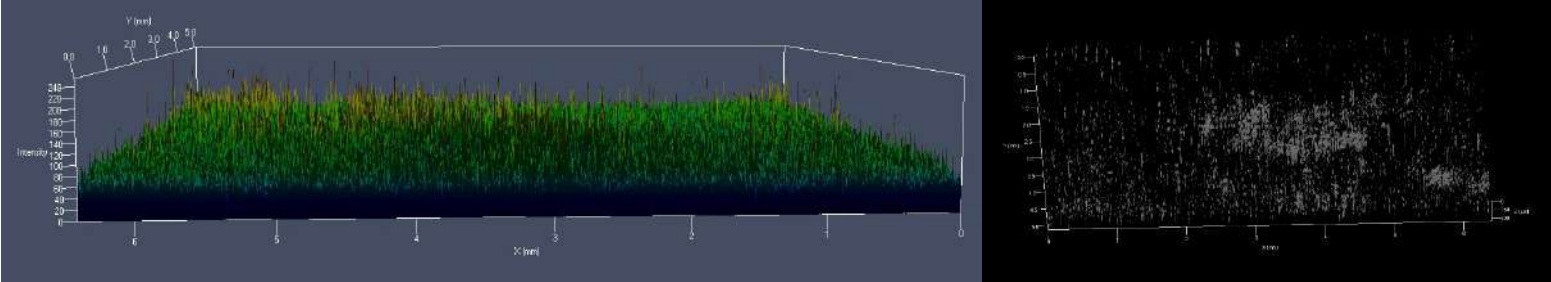


Figure 7.24. Confocal microscopy showing surface topography of Field B slab after test with carbonated brine.

Optical microscopy was also carried out on the same rock samples. The contrast between the new and after test images is shown in Figures 7.25 – 7.27.

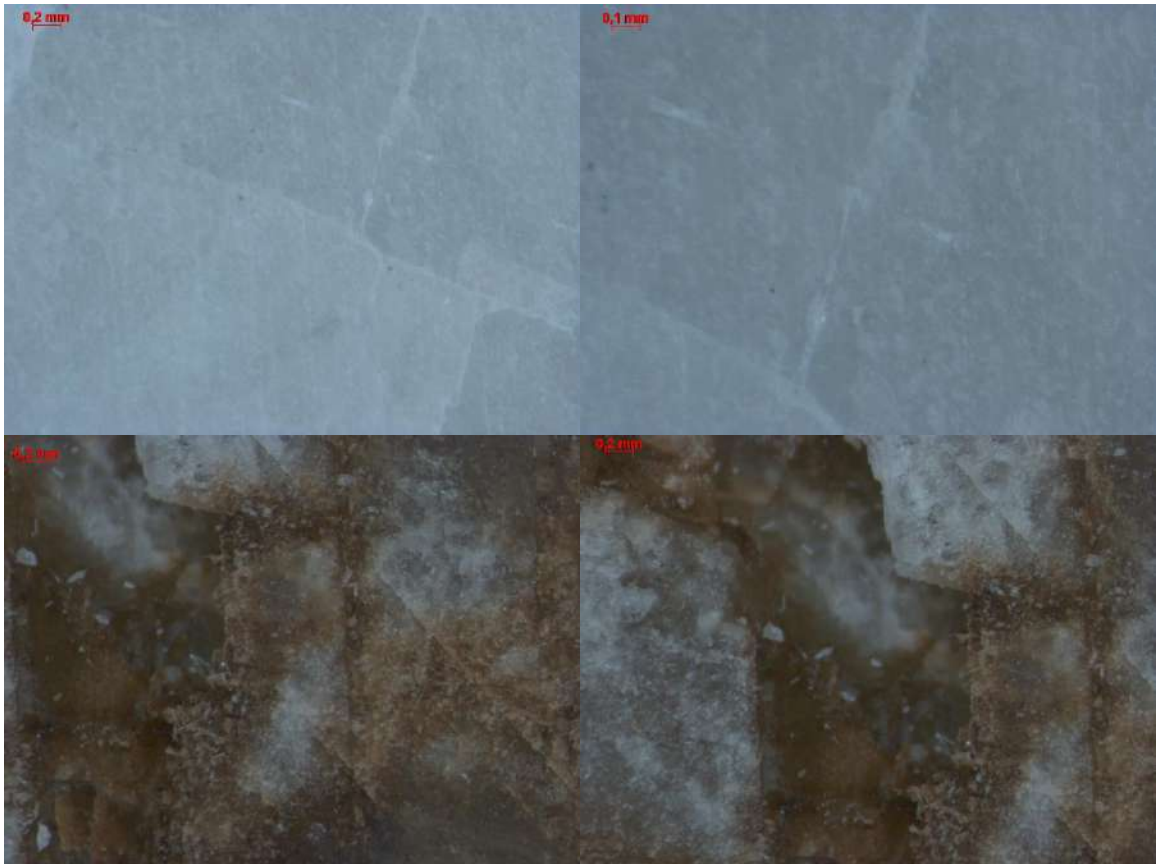


Figure 7.25. Optical microscope of a calcite sample. Top: new sample. Bottom: sample after test with carbonated brine.

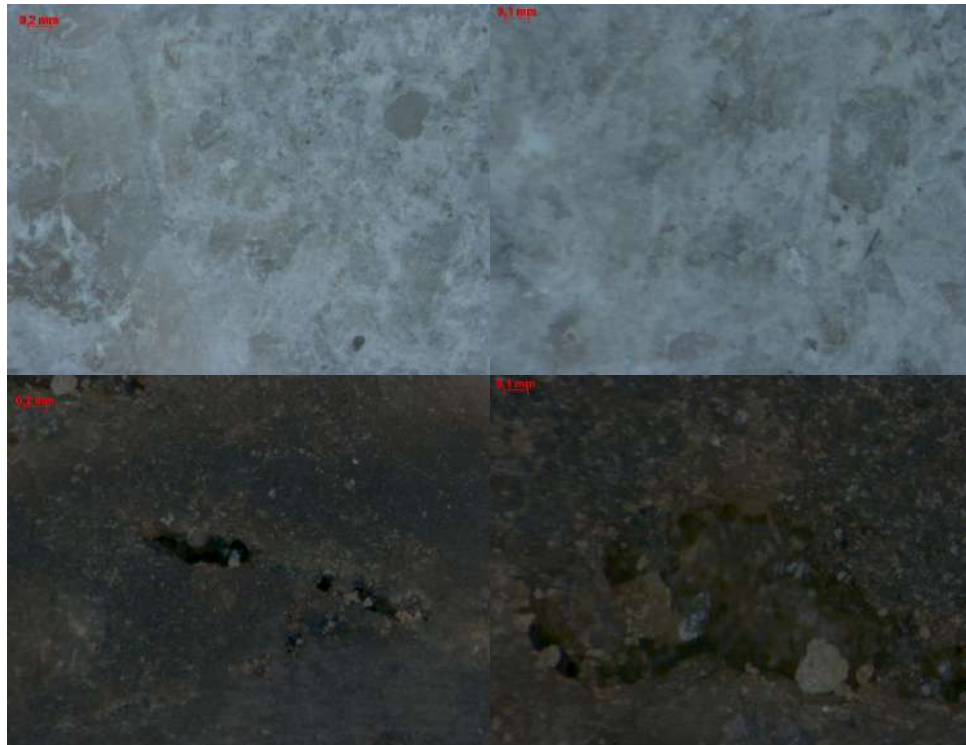


Figure 7.26. Optical microscope of a coquina sample. Top: new sample. Bottom: sample after test with carbonated brine.

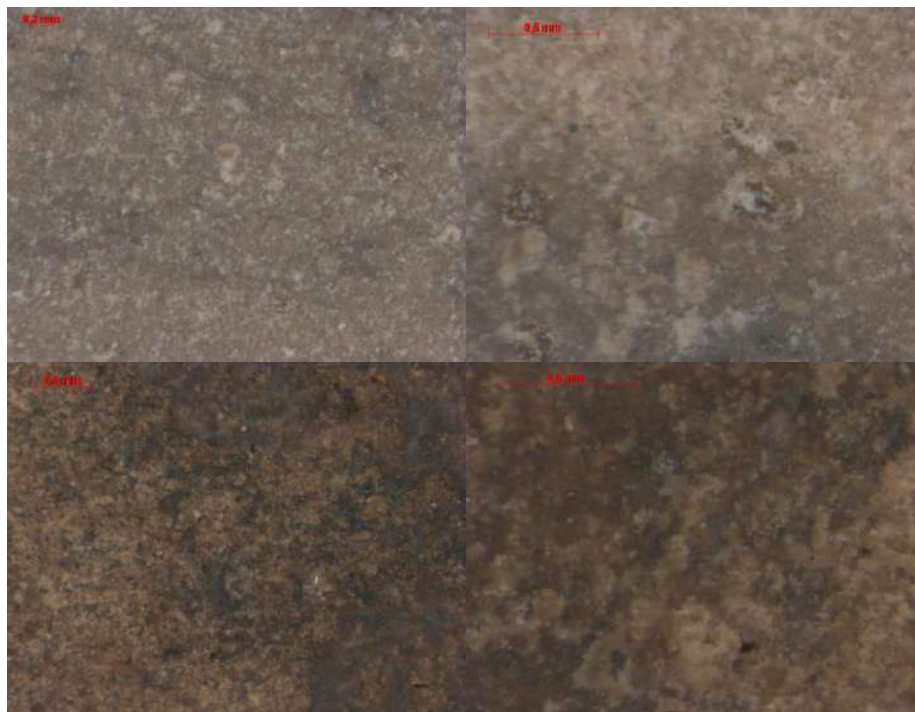


Figure 7.27. Optical microscope of a Pre-Salt Field D rock sample. Top: new sample. Bottom: sample after test with carbonated brine

For calcite (Figure 7.25), corrosion created a height difference between the planes which is visible in the images in agreement to the results of confocal microscopy. In the case of coquinas, pores already existed on the new sample before the test. However, Figure 7.26 illustrates signs of dissolution such as rougher edges on the pore walls and scale precipitation.

In Figure 7.27, augmented surface roughness is visible. However, the signs of CO₂ attack for Field D rock are less critical than for the other samples. This confirms the higher stability of this rock to carbonate water injection in agreement with the discussions in the previous sections.

SEM images of the samples before and after the test with Pre-equilibrated carbonated brine were obtained to observe the effects of CO₂ on the surface morphology in greater detail. Figures 7.28 – 7.30 show the results.

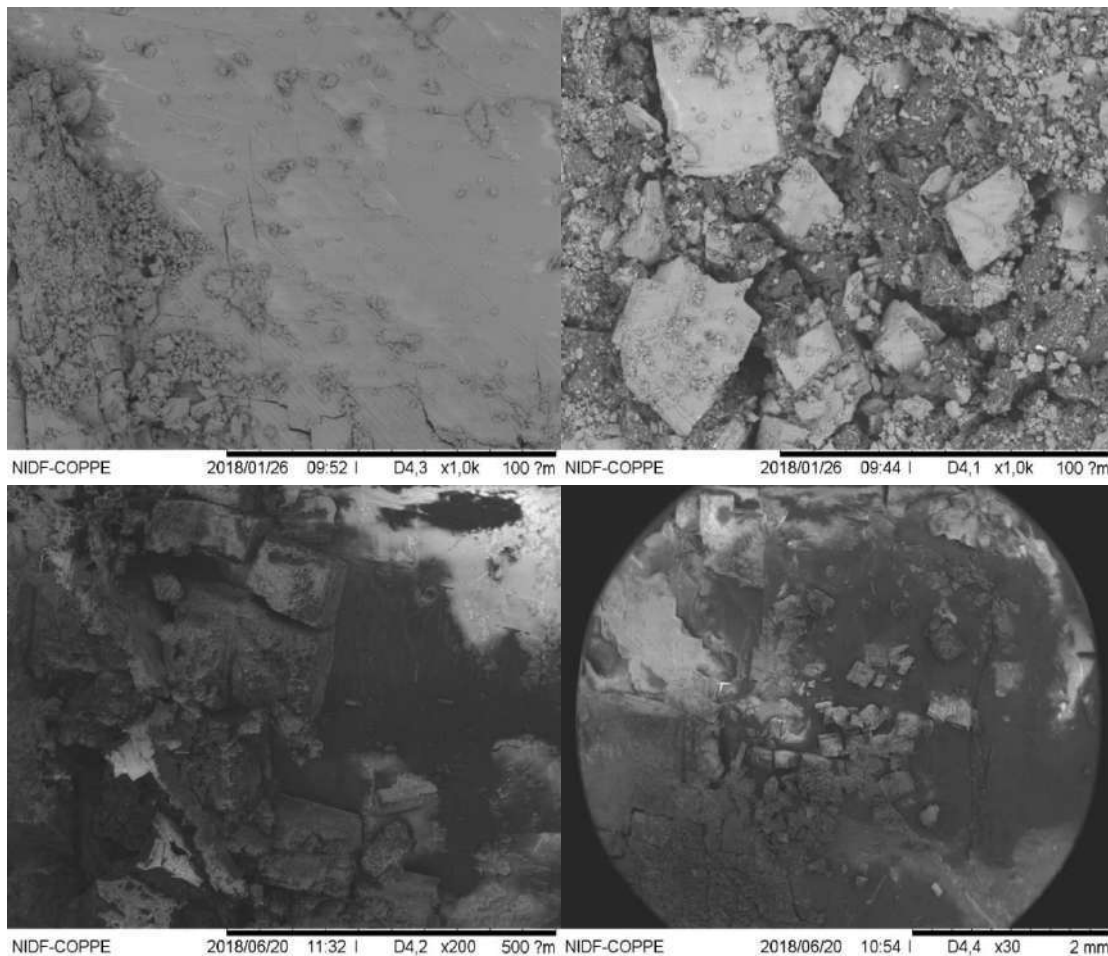


Figure 7.28. SEM images of calcite. Top: new sample. Bottom: sample after test with pre-saturated carbonated brine.

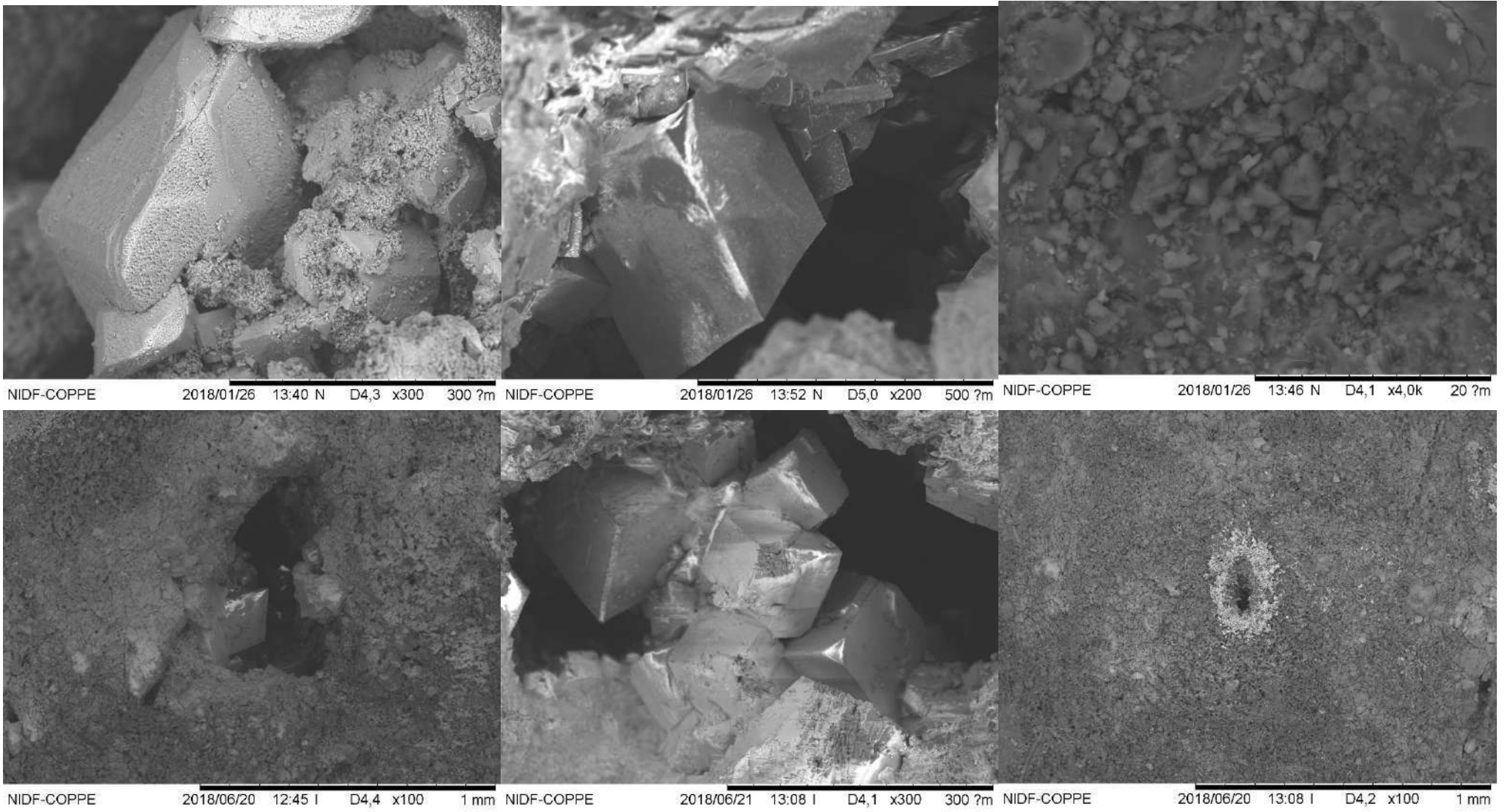


Figure 7.29. SEM images of coquinas. Top: new sample. Bottom: sample after test with pre-saturated carbonated brine.

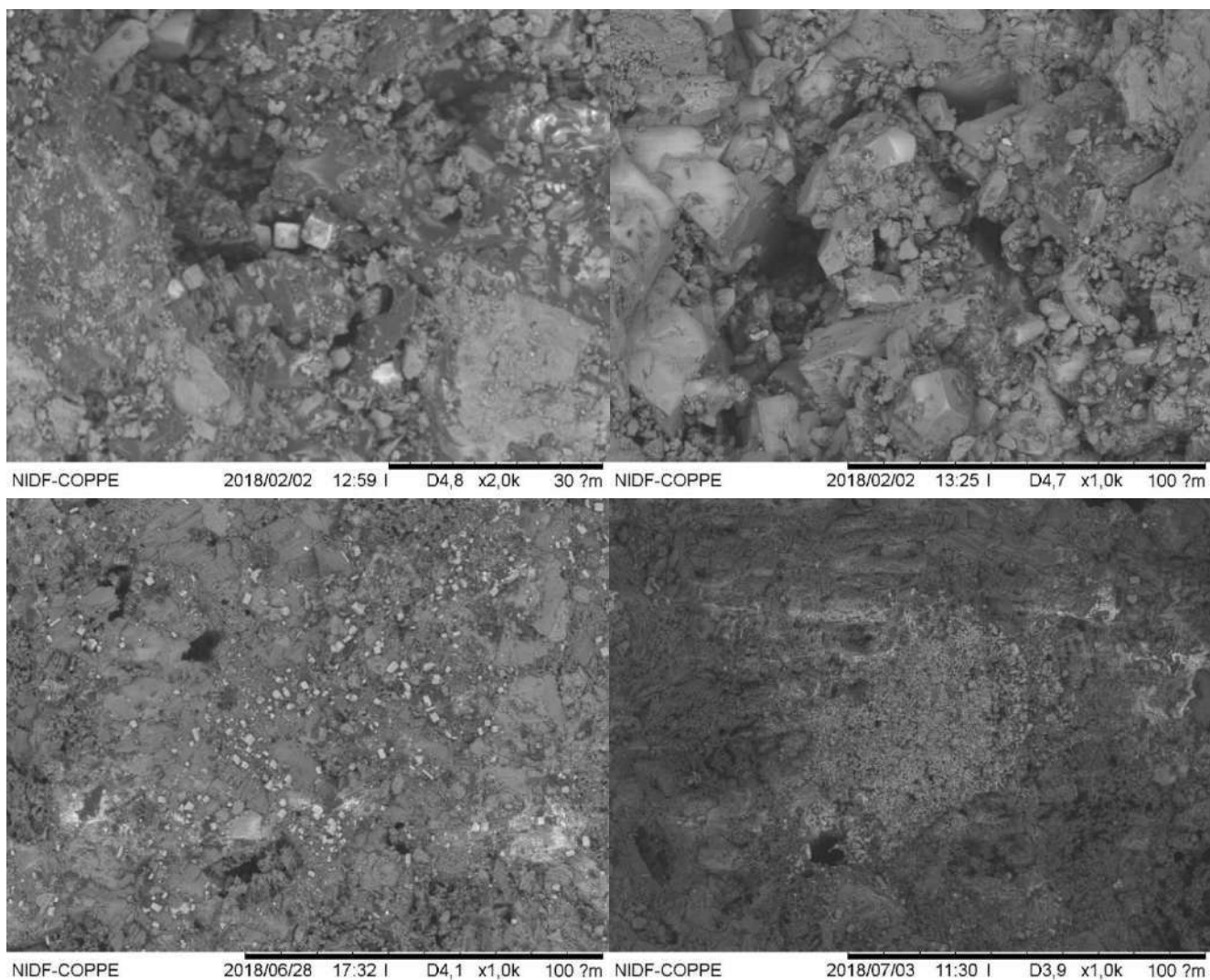


Figure 7.30. SEM images of Pre-Salt Field D sample. Top: new sample. Bottom: sample after test with pre-saturated carbonated brine.

The SEM images show clear signs of reaction with CO₂ on the different carbonate rocks. These are more noticeable for calcite (Figure 7.28). The flat surface that is observed at lower magnification for the new sample is replaced by a surfaces with steps and valleys. In addition, the rhombohedral structure of calcite shows evidence of abrasion as a result of CO₂ attack.

For coquinas (Figure 7.29), even though the surface of the new sample is more heterogeneous, still signs of corrosion by CO₂ are observed on the borders of the pore and on the integrity of the mineral structure. The creation of microposity due to acid attack is also

visible. Furthermore, the lower right-hand picture shows the precipitation of scales which is common after rock dissolution. This could take part during the experiment due to the increased concentration of calcium ions (calcite or other calcium salts) or during depressurization due to evaporation and CO₂ release (halite).

The Pre-Salt reservoir sample (Figure 7.30), which is also a heterogeneous rock, has similar effects than coquinas. The shape of calcite is particularly affected showing signs of reaction. Moreover, the macroscopic topography has a worn-out appearance evidencing an increase of microporosity. Finally, halite and deposition of other scales is also present for the samples after the test with CO₂ saturated brine.

Finally, a common effects on all these carbonate rocks is the weaker interaction of the asphaltene fractions of Oils B and D with the surface as the pH is decreased. As showed in the previous chapter, the asphaltenic fractions of these crudes do not contain basic groups. Therefore, they are more surface-active as the pH is increased (LASHKARBOLOOKI; AYATOLLAHI, 2018). The decrease in their charge (and activity) as pH turns acidic could contribute to the more water-wet behavior found for all these carbonate rocks when CO₂ saturated fluid are employed.

7.6 Effect of CO₂ on wettability of synthetic Model Oil

As discussed in the previous chapter (Section 6.5), the synthetic oil containing the same saturates over aromatics ratio as Oil B but no asphaltenes and resins interacts poorly with carbonate rocks. The saturation of brine with CO₂ produced major changes in the carbonate rocks tested in this work, with the exception of dolomite. The tests included in this section aimed to evaluate the effects of carbonated water on the wettability of calcite and coquinas (representing carbonate mineral and outcrop rock) using Model Oil compared to that of Oil B.

A set of experiments was carried out using calcite and coquinas as substrates. They were aged 1 day in Brine B and 60 days in Model Oil at 60 °C. Then, the tests were carried out using pre-equilibrated fluids with CO₂. As Model Oil is totally miscible with CO₂ at 1000 psi, the same volume of CO₂ as in the pre-equilibration of Oil B was added. The results for

the same fluids with no CO₂ addition is included for comparison. The reader can find the simulated density and phase behavior of both oils recombined with CO₂ in Appendix B.

The results (Figure 7.31) show that for Model Oil, the effect of carbonated brine is less critical than for Pre-Salt oil. For coquinas, the exact average value was obtained remaining at the weakly water-wet condition. For calcite even an increase of 23% in the CA was observed. This increase may be caused by effects other than wettability alteration because the mineral still remains in the water-wet region. A possible cause of this is the decrease in the interfacial tension between Model Oil and Brine B when the concentration of fluids is raised. The effects of CO₂ on the fluid-fluid interactions for both systems will be discussed in Chapter 8.

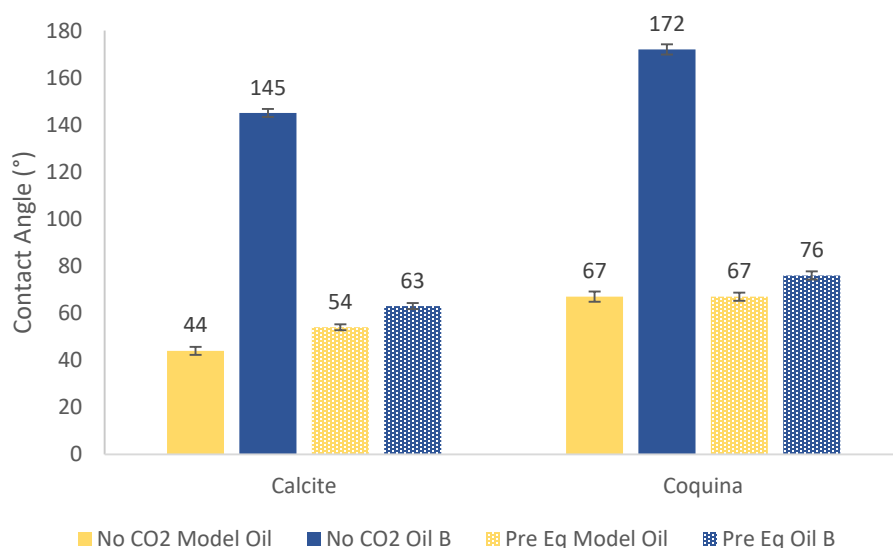


Figure 7.31. Contact angle values for experiments using Model Oil and Oil B. Full bars are tests with no CO₂ and patterned bars are pre-saturated tests. Conditions: 60 °C, 1000 psi, 1 day aging in Brine B, 30 days aging in oil.

7.7 Effect of CO₂ dissolution on wettability using injection brine

The final set of results of wettability using carbonated brine was carried using desulphated seawater DSW. In the previous chapter it was reported that, even though DSW has much lower salinity and higher pH than Brine B, the effects on wettability were not enough to shift the initial wettability of calcite and coquinas.

Similar tests using the same substrates were carried with CO₂ pre-saturated Oil B and DSW. Rocks were aged 1 day in brine and 30 days in oil, and the test conditions were 60 °C and 1000 psi and all tests used Oil B. Figure 7.32 illustrates the results evidencing that the use of pre-saturated DSW has the same impact on wettability of both calcite and coquina than that of Oil B, shifting wettability towards neutral or water-wet.

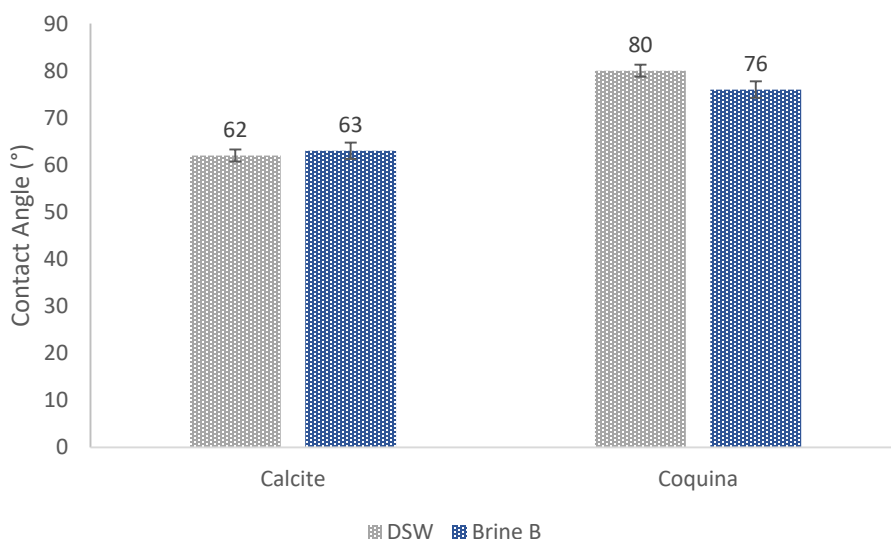


Figure 7.32. Contact angle values for experiments using DSW / Brine B and Oil B. Conditions: 60 °C, 1000 psi, 1 day aging in brine, 30 days aging in Oil B.

The dissolution of CO₂ in both DSW and Brine B decreases to acidic values (3.45 and 2.54 respectively) as shown in Figure B.1. In the case of calcite the results for carbonated DSW were practically the same as with carbonated Brine B. CO₂ solubility in DSW is even higher than in Brine B (Table B.1). Thus, equal or higher of reactivity with calcite and other carbonates is expected. For coquinas, carbonated brine resulted in neutral wettability in a similar fashion as carbonated Brine B.

These facts are in agreement with the idea that pH is not the main variable in shifting wettability in these high salinity brine environments. The reactivity of both systems to attack calcite and desorb organic groups on its surface seems to be the key for this wettability change. Both CO₂ saturated brines have high enough concentration to shift wettability towards water-wet.

7.8 Highlights of this chapter

- CO₂ dissolution in the brine shifts the wettability of aged calcite, coquina, Indiana limestone and Pre-Salt rock D from oil to water-wet.
- Calcite is the most reactive substrate, showing clear signs of acid attack and the greatest CA reduction. Coquina is still attacked by carbonated brine, but with less critical effects. Pre-Salt rock D showed milder effects of carbonate dissolution and wettability alteration.
- For dolomite, the effect of CO₂ was negligible, and for quartz it weakened the interaction with the crude oil.
- CO₂ concentration plays an important role on the wettability alteration by carbonated brine. The reduction of oil wettability of aged rocks does not seem to be linked solely to acidic pH values in the brine.
- CO₂ caused desorption of the adsorbed oil, corrosion on calcite's rhombohedral structure, increase of microporosity, increase of macroscopic roughness and appearance of scale deposition.

CHAPTER 8: CO₂ EFFECT ON THE FLUID-FLUID INTERACTIONS

Interfacial tension (IFT) is one of the most relevant properties in terms of fluid-fluid interactions as it determines the capillary effects at the pore scale (as reviewed in Chapter 2). The dissolution of CO₂ in the reservoir fluids has a direct impact on their bulk properties (i.e. density or viscosity). Nevertheless, the effect of CO₂ partitioning in the oil and brine phases has a more complex effect on the interfacial properties.

The dead Pre-Salt crudes considered in this work have a high concentration of resins and asphaltenes (Table 5.2), which are compounds with interfacial activity. Thus, their interfacial tension is hardly represented by a simple mixture of hydrocarbons. This chapter aims to evaluate the interfacial tension of the dead Pre-Salt crude oil and to observe the effects of CO₂ dissolution as a function of pressure.

8.1 Validation of the technique

The DSA technique for IFT measurement was validated by reproducing values in the literature for n-alkanes and deionized water. For this, the IFT between n-hexane, n-heptane and n-octane (purity 99.9%+) and deionized water (conductivity below 1 $\mu\text{S}/\text{cm}$ at 25 °C) were measured at 40, 60 and 80 C and pressures from atmospheric to 6000 psi. Each measurement was repeated five times, and data was acquired every 30 seconds until the relative difference between 50 subsequent measurements was lower than 1%. The densities, required for the calculation of the IFT as discussed in Chapter 2, were obtained from the NIST website (NIST, 2017). The recorded value was the average of the last 50 measurements. The average standard error of the mean of all measurements was 0.04 mN/m. The results are shown in Appendix E.

The values at atmospheric pressure were contrasted to that in the literature (ZEPPIERI; RODRÍGUEZ; LÓPEZ DE RAMOS, 2001). Table 8.1 shows that the maximum

relative difference obtained was 7.36%. This difference (for n-octane which is the heavier n-alkane considered) is attributed to the difference in purification methods between the work in the literature and this work.

Table 8.1. Comparison of interfacial tension measured at atmospheric pressure with the results in the literature (ZEPPIERI; RODRÍGUEZ; LÓPEZ DE RAMOS, 2001).

| T (°C) | N-heptane – water | | | N-octane – water | | |
|-------------------------|-------------------|-------|-------|------------------|-------|-------|
| | 40 | 50 | 60 | 40 | 50 | 60 |
| IFT this work (mN/m) | 48.25 | 47.89 | 47.09 | 47.94 | 46.48 | 45.84 |
| IFT literature (mN/m) | 49.38 | 48.55 | 48.82 | 49.84 | 48.95 | 49.21 |
| Relative difference (%) | 2.34 | 1.38 | 3.68 | 3.96 | 5.31 | 7.36 |

To verify if the obtained trends matched those accepted in the literature, a statistical analysis was conducted assuming a normal distribution of probabilities with a 95% confidence interval as described in Section 4.2. The objective was to evaluate the impact of pressure, temperature and number of carbon atoms in the molecule on the interfacial tension output variable.

Figure 8.1 shows the surface plots of the IFT as a function of temperature and alkane carbon number (at fixed pressure) and as a function of pressure and alkane carbon number (at fixed temperature). It is evident that temperature has a much important impact on the IFT than pressure as represented for the minimal inclination on the plane obtained for variable pressures. This results confirms the expected trends for the IFT between liquid hydrocarbons and water. The IFT was reported to decrease with temperature (MEDEIROS, 2015; TIAN et al., 2014; ZEPPIERI; RODRÍGUEZ; LÓPEZ DE RAMOS, 2001) and increase with pressure (CAI; YANG; GUO, 1996; MCCAFFERY; MUNGAN, 1970; WIEGAND; FRANCK, 1994). Nevertheless, the effect of pressure is weak compared to that of temperature.

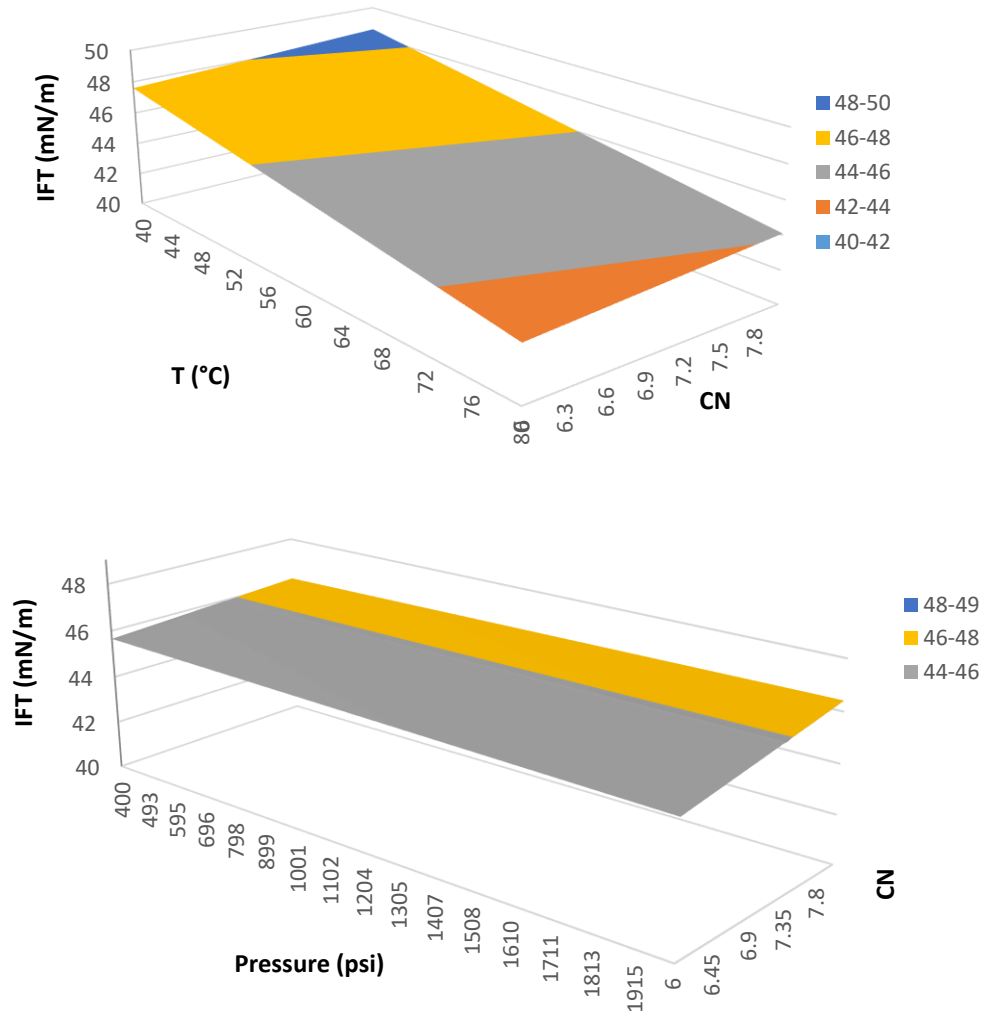


Figure 8.1. Surface plots showing the interfacial tension (IFT) dependence on Temperature (T), Alkane Carbon Number (CN) and Pressure (P). Top: IFT as a function of T and CN at fixed 1200 psi. Bottom: IFT as e function of P and CN at 60°C.

8.2 Dynamic behavior of IFT

When two phases are put in contact mass transfer tends to equilibrate the chemical potential of the different components in both phases. Surface active species diffuse to the interface to minimize the free energy of the system (ROSEN; KUNJAPPU, 2012). A common example of this an aqueous solution of a surfactant in contact with an immiscible fluid. When in solution, the hydrophobic tails of the surfactant, which interact poorly with the water molecules, are surrounded by a solvation layer. This reduction in the degrees of

freedom of a large amount of water molecules decreases the entropy of the system resulting in an increase of the Gibbs free energy. As a result, the surfactant molecules adsorb at the interface with the hydrophilic head towards the aqueous phase and the hydrophobic tail oriented to the less polar phase. This reduces the interfacial tension by enhancing the intermolecular interactions across the interface, as the surfactant's head interacts with the water molecules and its tail with the non-polar molecules in the hydrophobic phase. After saturation of the interface, an increase in surfactant concentration results in the formation of organized structures called micelles. In these structures, the contact of the hydrophobic tails with water molecules is minimized as they are located in the interior of the micelles. Surfactants were used as an example of adsorption of surface active components on interfaces. The self-assembly characteristics of surfactants are out of the scope of this text.

When an organic liquid phase is in contact with water, a similar process takes place. The compounds with amphiphilic characteristics diffuse towards the interface minimizing the free energy. In the case of pure hydrocarbons or solutions of non-polar hydrocarbons, these surface active species can be impurities. For crude oils, the compounds with surface activity are mainly the resins and the asphaltenes. Some aromatic molecules can also have interfacial properties.

Diffusion and adsorption increase the concentration of the surface active species at the interface. As a result, the IFT decreases with time as mass transfer proceeds. This effect takes place until reaching mass transfer equilibrium, which is achieved by the chemical potential equality of the species that partition in both phases and by the maximization of the concentration of amphiphilic species at the interface minimizing the free energy. At this point, the IFT reaches its equilibrium value. Thus, the IFT decays dramatically during the first period after the formation of the interface because of the massive increase in surface active species at the interface. Afterwards, it plateaus as the adsorption of surface active species equilibrates.

The decay of IFT with time caused by impurities was extensively reported in the literature. Most of the authors informed the equilibrium values by either performing measurements for sufficiently long periods or adjusting the data with a mathematical model (AVEYARD; HAYDON, 1965; GOEBEL; LUNKENHEIMER, 1997; ZEPPIERI;

RODRÍGUEZ; LÓPEZ DE RAMOS, 2001). Others calculated dynamic values set as specific times that depend on the rate of decay of the IFT with time (GEORGIADIS; TRUSLER; BISMARCK, 2011; SUSNAR; HAMZA; NEUMANN, 1994).

As described in Section 4.3, in this work both equilibrium and dynamic IFT values were calculated. The dynamic IFTs are the average of the values at 150 and 900 seconds as adopted in the literature for the water-CO₂-decane system. Furthermore, the equilibrium values were obtained by fitting the data with a logarithmic curve using a rate of decay lower than 0.01 mNm⁻¹h⁻¹ as the equilibrium condition. Experiments with dissolved CO₂ were carried out in a similar fashion as the CA measurements as indicated in Chapter 4.

As described before, the DSA measurement of the IFT is linearly dependent on the density difference between the phases. The density values used in the calculation for dead oils and brines and fluids with different concentrations of CO₂ (saturated or unsaturated) are included in Appendix B. For the dynamic values containing CO₂, the density of the corresponding phases with dissolved CO₂ were used from the initial time. The maximum difference between the density of the dead fluids and the CO₂ saturated fluids at the same conditions is below 2%. Thus, the error for density correction of the transient mass transfer effect is below 0.01 mN/m. This is expected as minimal concentrations have great impact on surface properties as IFT and little impact on bulk properties as density.

This section presents the IFT as a function of time for the oils and brines used in this work in the absence of CO₂ and under CO₂ saturation conditions at 60 °C and 1000 and 5000 psi. The discussion will not focus in the comparison between the IFT values of different systems as that is the objective of the following section.

The IFT values as a function of time for Oil and Brine B are presented in Figure 8.2. It is evident that mass transfer effects are more visible for the systems with no dissolved CO₂. The IFT decay is steeper and takes a longer time to stabilize. The actual plateau of both curves is not showed in the plot to preserve the scale. This decay is even more critical at higher pressure (5000 psi). For the CO₂ saturated fluids, the slope of the IFT decay curve is diminished. Moreover, the curves plateau at shorter times (i.e. about 400 seconds). In this case, the highest pressure reaches stable values even at shorter times.

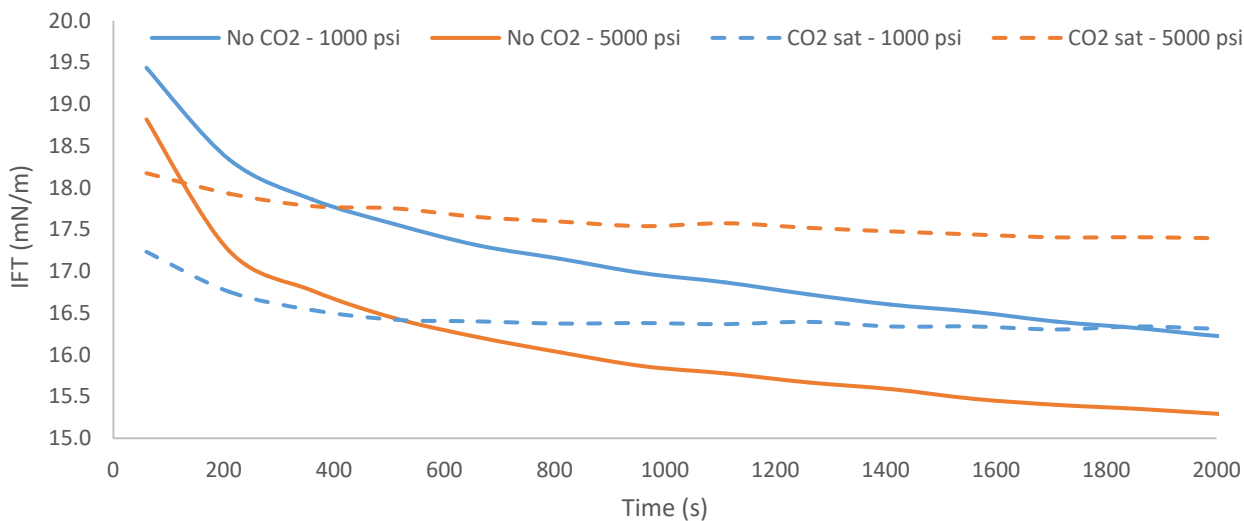


Figure 8.2. Interfacial tension between Oil B and Brine B as a function of time with no CO₂ and with CO₂ saturated fluids. Conditions: 60 °C, 1000 or 5000 psi.

These results indicate that in the absence of CO₂, mass transfer of surface active species from Oil B to the interface is of paramount importance. This is in agreement with the high content of resins and asphaltenes reported for Oil B (Table 5.2). The initial IFT values are higher for the dead fluids. However as the concentration of asphaltenes and resins at the interface increases, the IFT decays considerably dropping below that of the CO₂ saturated fluids.

These results indicate that, as CO₂ partitions in both phases, it decreases the initial IFT. Higher pressure, which mean higher CO₂ concentration, results in an even lower initial value. Nevertheless, CO₂ is not an efficient surface active component, and its effect on IFT is lower than that of polar fractions of the oil. Thus, the mass transfer of these components produce a greater reduction of IFT with time. The fact that the IFT plateaus at a higher value for the CO₂ saturated fluids suggest that CO₂ dissolution in both phases reduce the effect resins and asphaltenes at the interface. It appears that, when the fluids are saturated in CO₂, the surface-active components from the oil are less efficient in decreasing the IFT. A probable reason for this is, as pH decreases, the acid species in the oil are protonated reducing their potential as surfactants. This would also suggest that bases in the oil are less effective reducing the IFT; however, further studies are required to conclude about these possibilities.

Tests under the same conditions were carried out for the Model Oil (71.1 wt% C16 and 28.9 wt% toluene) employed in the previous chapters. The measured IFT as a function of time is plotted in Figure 8.3. There is a clear difference with the results for Oil B (Figure 8.2). As Model Oil does not contain resins or asphaltenes, the decrease of the IFT between the dead fluids (no CO₂) plateaus at an earlier time that in Oil B. This time is shorter at the highest pressure (5000 psi).

The presence of CO₂ favors a faster stabilization of the IFT value, as observed for Oil B. Nevertheless, the IFT for CO₂ saturated remains lower than that of the dead fluids at all times. This indicates that, in the absence of surface-active compounds, CO₂ partitioning between the oil and brine phases enhances the interactions at the interface reducing the IFT as reported in previous works for the decane-water system (GEORGIADIS; TRUSLER; BISMARCK, 2011). This effect is greater at higher pressure, as CO₂ solubility increases with pressure for both oil and brine (Appendix B).

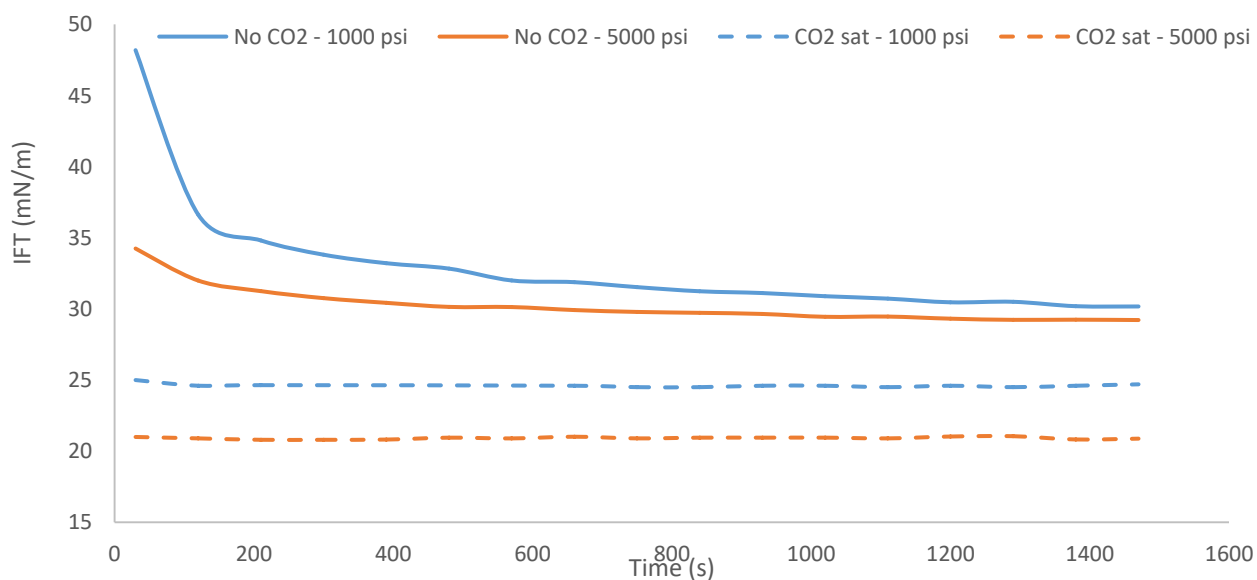


Figure 8.3. Interfacial tension between Model Oil and Brine B as a function of time with no CO₂ and with CO₂ saturated fluids. Conditions: 60 °C, 1000 or 5000 psi.

The results presented in this section confirm the importance of resins and asphaltenes as surface-active components reducing the IFT. They affect the equilibration of the interface

and the IFT changes as mass transfer takes place. The effect of CO₂ was shown to depend on the concentration of surface-active species. This will be discussed in the following section.

8.3 Effect of CO₂ for different oils

The effect of CO₂ on oil-brine IFT was analyzed for the three oils considered in this work using dynamic and equilibrium measurements (the procedures for calculation are in Section 4.3). The results for Oil B are in Figure 8.4 evidencing the important effect of surface-active components as the equilibrium values for dead fluids (no dissolved CO₂) are 40% lower than dynamic values.

However, when the fluids are saturated with CO₂, the equilibrium values are 5% lower at the highest pressure confirming the reduced decay in IFT for these fluids. CO₂ saturated fluids result in higher equilibrium IFT values. This indicates that the effect of CO₂ partitioning in both phases hinders the surface-active effect of the asphaltenes and resins on crude B. A reason for this could be the decrease of pH, as CO₂ is dissolved in brine. As a future work, characterization and quantification of the asphaltenes and resins in this crude oil could contribute to the understanding of this mechanism.

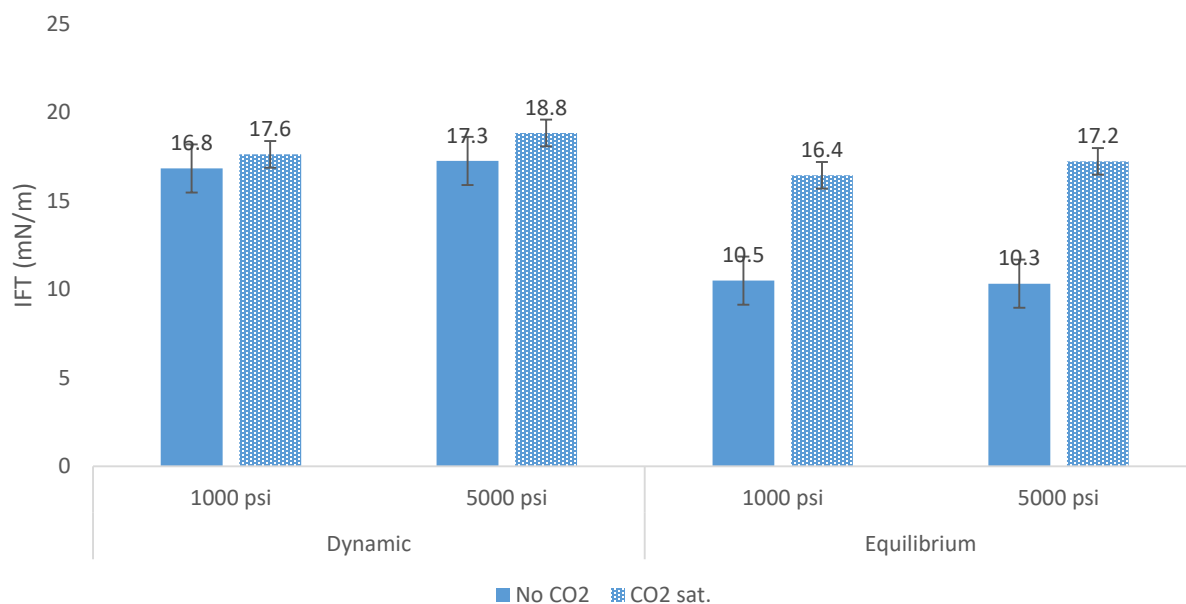


Figure 8.4. CO₂ effect on the dynamic and equilibrium interfacial tension between Oil B and Brine B. Conditions: Conditions: 60 °C, 1000 or 5000 psi.

The same analysis was carried out for Model Oil (Figure 8.5). In this case, CO₂ partitioning reduces the IFT up to 30% as suggested in the previous section. In the absence of compounds with strong surface behavior in Model Oil, the presence of CO₂ at the interface reduces the energy difference for compounds at both sides on the interface resulting in a decrease of the IFT. This effect is in agreement to the results found for a paraffinic oil with no reported asphaltenes and resins (SUN; CHEN, 2005).

This difference is greater for the dynamic measurements, suggesting the effect of impurities contribute to a slow decrease of the IFT as reported in the literature (GEORGIADIS; TRUSLER; BISMARCK, 2011; MICHAELS; HAUSER, 1951; SUSNAR; HAMZA; NEUMANN, 1994).

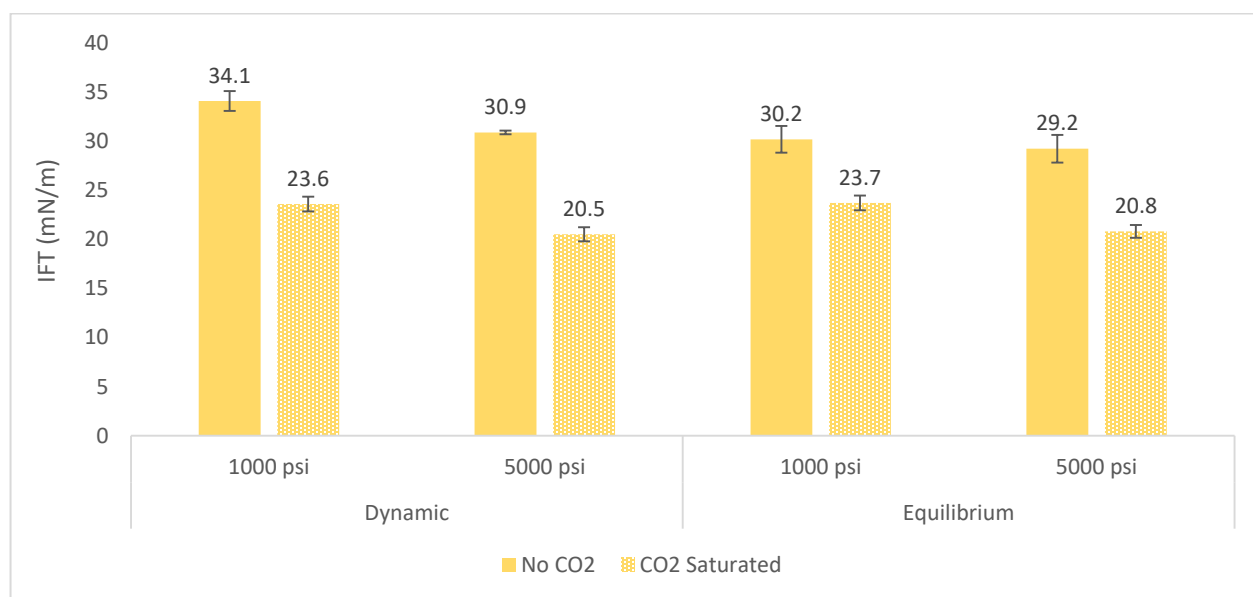


Figure 8.5. CO₂ effect on the dynamic and equilibrium interfacial tension between Model Oil and Brine B. Conditions: Conditions: 60 °C, 1000 or 5000 psi.

Experiments under the same conditions were carried out for Oil D and Brine D, and the results are shown in Figure 8.6. As for Oil B, the effect of CO₂ is not significant for these Pre-Salt fluids. Oil D has a greater content of asphaltenes and resins, but there was no difference between the results with and without CO₂ at all pressures. To understand if there

is a difference between the interfacial properties of both crudes, characterization of the asphaltenes and resins in both crudes is recommended as a future step.

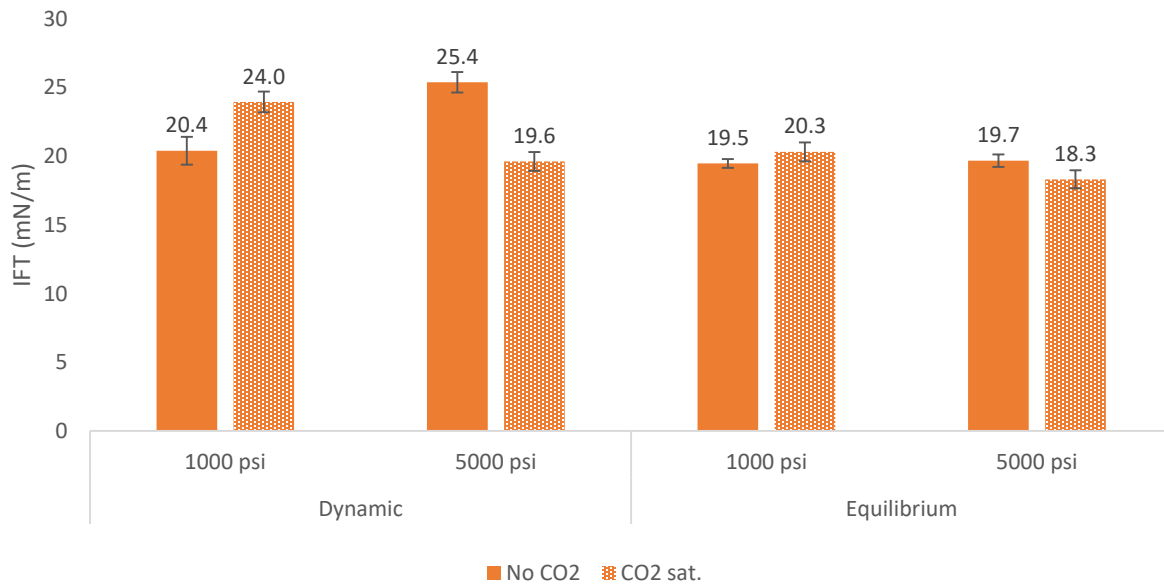


Figure 8.6. CO₂ effect on the dynamic and equilibrium interfacial tension between Oil D and Brine D. Conditions: Conditions: 60 °C, 1000 or 5000 psi.

8.4 Effect of pressure and CO₂ concentration

Tests at different pressures and using the same CO₂ concentrations as in the previous chapters (L1 – L4) were carried out for Oil B and Brine B. The densities of all fluids, required for IFT calculation, are reported in Appendix B. The CO₂ concentrations indicated in the figures correspond to those in the brine. It should be remarked that, in all cases, CO₂ was injected in the oil prior to deposition to keep the same proportionality ratio with its solubility as that used in the brine.

The IFT as a function of pressures with and without CO₂ using dynamic and equilibrium calculation is illustrated in Figure 8.7. For the pressures considered (over 1000 psi), there is no relevant effect of pressure on the IFT as the results maintain the same trends at all pressures. In addition, the differences between the same tests at different pressures have

the same order of magnitude as the uncertainty indicated by the error bars (average of ± 0.75 mN/m).

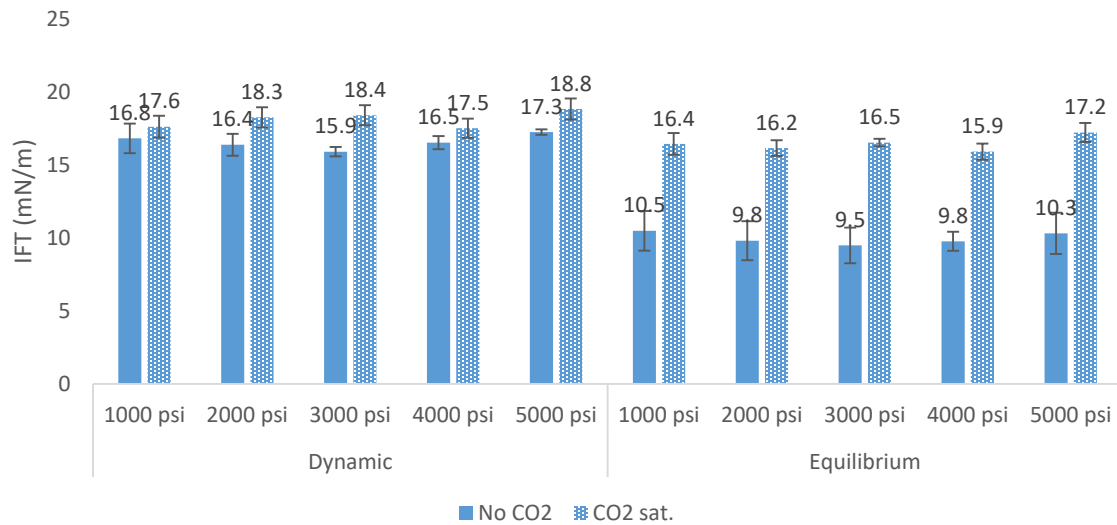


Figure 8.7. Interfacial tension versus pressure using dynamic and equilibrium measurements in Oil B and Brine B with and without CO₂. Temperature: 60 °C.

The results for a series of experiments using the concentrations of CO₂ in oil and brine in Section 7.3 are shown in Figure 8.8. As with pressure, no major changes on IFT were found with CO₂ concentration, as even the lowest concentration had similar impact than the saturated fluids. This is an indication that even at low concentrations, CO₂ tends to accumulate at the interface interfering the diffusion of surface-active species.

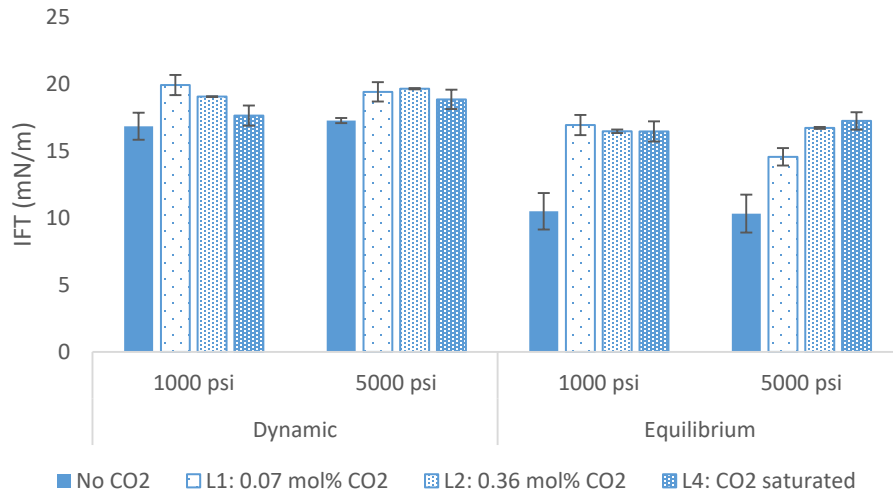


Figure 8.8. Interfacial tension between Oil B and Brine B for different CO₂ concentrations. Conditions: 60 °C, 1000 or 5000 psi.

8.5 Highlights of this chapter

- Dynamic decay of interfacial tensions is caused by mass transfer of surface-active components towards the interface. Since low concentrations of these components have great impact on the interfacial tension, this dynamic variation can take long times to reach equilibrium (i.e. more than 24 hours).
- These effects difficult the acquisition of equilibrium interfacial tension in unpurified systems, as reported in the literature.
- Pre-Salt crude B contains high concentrations of surface-active components (i.e. resins and asphaltenes), having relatively low values of interfacial tension with formation brine. Oil D still has high concentration of these compounds, but the IFT is higher.
- CO₂ dissolution in Pre-Salt oil and brine does not aid to decrease the interfacial tension. As these oils high concentration of surfactant-type molecules that dominate the interface, CO₂ dissolution reduces their activity.
- This reduced action of the surface-active compounds results in shorter equilibration times for the CO₂ saturated fluids.
- For the model oil, which does not contain asphaltenes nor resins, CO₂ dissolution reduces de interfacial tension.

CHAPTER 9: CONCLUSIONS AND FUTURE WORK

This work is a pioneer research effort considering both fluid-fluid and rock fluid-interactions at the Pre-Salt scenario. It is innovative in customizing experimental techniques to achieve a representative description of this unique environment, characterized by high salinity brine, oil with high concentration of surface-active compounds and high basic number, heterogeneous carbonate rocks and elevated dissolved CO₂ concentration. In this regard, its scope is to provide reliable experimental data and consistent evidence to analyze the complex phenomena involved in the phase equilibrium in the porous medium.

The approach used in this research is based on two pillars to evaluate the rock-fluid and fluid-fluid interactions with regard to the Displacement Efficiency, which determines the Enhanced Oil Recovery and Recovery Factor under different conditions. First, there is wettability, which determines phase distribution in the pores and relative permeabilities, establishing how the fluids are displaced throughout the porous medium. As described in Chapter 2, wettability is the result of complex interactions including intermolecular forces, electrostatic attraction or repulsion and acid/base equilibrium. Containing multicomponent phases with a wide range of compositions, wettability in oil reservoirs is far from being a property with linear characteristics. It is not only phase composition that plays an important part in defining wettability. Other effects, such as contact time between the phases, phase saturation history changes and mass transfer effects, can also be critical.

Several wettability studies including sandstone and carbonate reservoirs and different crudes and brines exist in the literature (BROWN; FATT, 1956; BUCKLEY, 1998; BUCKLEY et al., 1997; LIN; HUANG, 1990; SEYYEDI; SOHRABI; FARZANEH, 2015). Nevertheless, since Pre-Salt reservoirs present specific challenges, extrapolation of the results found for other carbonates is not viable. In addition, available experimental data with high CO₂ content on reservoir rocks is very limited. Therefore, it is critical to provide experimental results to contribute with the reservoir description of these important assets. In

this context, this work aims to supply discussions and tools oriented to the Pre-Salt environment to address unanswered topics like the required aging time for rocks, the analogy between minerals, outcrops and reservoir rocks, the most adequate procedure to introduce CO₂ in the contact angle experiments and the role of CO₂ in the initial wettability.

The second property considered in this work is the interfacial tension as a representation of the fluid-fluid interactions. Capillary forces, and thus residual oil saturation, are linked to the interfacial tension. As a result, the importance of this variable cannot be neglected when modeling a reservoir. Chapters 2 and 3 reviewed the challenges of measuring the interfacial tension in complex scenarios. To the best of the author's knowledge, there are no works available in the literature describing the effects of CO₂ partitioning in the Pre-Salt environment. This research provides dynamic and equilibrium interfacial tensions for Pre-Salt fluids in the presence and absence of CO₂ at high temperature and pressure.

The following paragraphs will review the main results and conclusions from Chapters 6, 7 and 8 and their implications to oil displacement and EOR scenarios for the Pre-Salt. The initial results presented in Chapter 6 evaluated different factors to obtain reliable contact angle measurements when crude oil, high salinity brine and different rocks at high pressure and temperature are used. One important step in contact angle measurement is rock preparation. Aging time is critical as it affects the results dramatically. For the Pre-Salt oil and brine systems tested in this work, aging time of unaged rocks differed from that of aged rocks. The oils, which have greater basic than acid number, interacted more with unaged quartz than calcite. This is an indication of the instantaneous effect of the highly concentrated basic compounds as previously suggested for basic oil at ambient conditions (FACANHA, 2017). In addition, aging effects were different for the different minerals and rocks. All carbonate rocks tested, with the exception of dolomite, presented a shift towards oil-wet behavior with aging time. This indicates that other long-term effects such as asphaltene precipitation or adsorption of more diluted surface-active components take place during the aging process. Coquinas, Indiana limestone and Pre-Salt Field D rock were more sensitive to this effect due to their higher surface area and presence of active sites for adsorption. In addition, the greater surface roughness of these rocks can contribute to the higher apparent contact angle, as reported in the literature (Chapter 2). As a result, they achieved equilibrium wettability after 30 days aging. Calcite, on the other hand, showed increased contact angles

up to 40 days aging. Longer aging times were not employed in this work to verify if 40 days were sufficient to achieve equilibrium. The similar behavior for these substrates in equilibrium contact angle measurements suggest that analogue responses in terms of initial wettability in the absence of CO₂ can be expected if equilibrium values with sufficient aging time are employed in this technique. This confirms the application of the previously proposed analogue coquinas from Morro de Chaves at least in terms of initial wettability by contact angle measurement.

Dolomite showed a differentiated behavior than that of calcite and other carbonates. Unaged dolomite was slightly more oil-wet than calcite. Nevertheless, dolomite was not affected by aging, and the contact angle of aged dolomite did not show considerable change. Initially, dolomite interacts weakly with these basic oils due to its point of zero charge close to 7 and its basic nature. As aging times proceeds, interaction between of the solid surface and the charged compounds in the oil remains weak due to the reduced surface charge. Magnesium is also thought to provide a water-wet behavior to the mineral as reported in works studying ion exchange on the rock (GENEROSI et al., 2017; SAKUMA et al., 2014) as described in Chapter 6. As a result, when aged dolomite is surrounded by formation brine, the oil-solid interactions are not strong enough to disrupt the water film resulting in a slightly water-wet behavior.

Regarding the excess bulk oil removal after aging, centrifugation proved to be the most adequate method as it does not alter the physics and chemistry of the surface and it is independent of the operator. Nevertheless, for very viscous and heavy oils, such as reutilized crude B2, solvent rinsing may be required as centrifugation alone may not remove the oil layer. For the oils tested, cyclohexane was the most adequate solvent to avoid asphaltene precipitation and excessive removal of the aging oil.

The results in Chapter 7 include CO₂ in the scenario. It is important to remark that these tests evaluate the effects of CO₂ on the equilibrium initial wettability, instead of the dynamic effects of CO₂ flooding as formation brine is replaced by carbonated water. For all initially oil-wet carbonates, CO₂ dissolution rendered the rocks more water-wet. From the different forms of injecting CO₂ in the system, pre-saturating oil and brine with CO₂ resulted the most consistent method. Gas cap injection is not recommended because it is widely affected by oil drop swelling and pinning of the three-phase line giving unstable result.

However, pre-equilibrating the gas cap before each independent measurement resulted similar effects than injecting pre-saturated fluids. In addition, forming injecting a new drop with a non-pre-equilibrated gas cap for each pressure gave the same trends at higher pressures, condition at which CO₂ dissolution is enhanced. This leads to two conclusions. First, the mechanism that leads to oil-wet reduction (i.e. desorption of organic compounds) occurs instantaneously and does not need long pre-equilibration times. Also, that in the case of the gas cap injection with pressure increase on the same drop, three-phase line pinning plays an important role avoiding reaching the equilibrium wettability.

Considering the effect of CO₂ dissolution on the different solid substrates, calcite was the most sensitive shifting from strongly oil-wet to water-wet for a 30 days aged mineral. This is caused by the higher reactivity of calcite to the acid attack that results from CO₂ dissolution in brine. Coquinas, Indiana limestone and Pre-Salt rock also presented reductions in the contact angle, varying from strongly oil-wet to intermediate-wet. The lower reactivity of these rocks was expected due to their heterogeneous compositions, which contains non-reactive minerals such as quartz. This result is of paramount importance since it suggests that, under reservoir conditions, fields that contain high production of CO₂ may be initially intermediate or even water-wet and should be modeled representing this behavior.

For dolomite, CO₂ dissolution weakened the already weak interaction with crude oil, giving a slight reduction in the contact angle. In contrast, carbonated water rendered quartz more oil-wet to some degree, in agreement to some results previously reported (SEYYEDI; SOHRABI; FARZANEH, 2015).

Several effects of CO₂ dissolution can render the initially oil-wet carbonates more water-wet. First, the decrease of pH plays a major role on surface charge and acid/base behavior of minerals and rocks. These effects could be diminished by the high ionic force in the Pre-Salt formation brines. Also, carbonates are reactive with brine with dissolved CO₂. This reactivity can also desorb organic molecules adsorbed during the aging process rendering a “clean” unaged surface. The results in Chapter 7 indicate that, if carbonate water is in contact with the rock before oil deposition, the surface will be intermediate to water-wet even if the rock contains previously adsorbed organic matter.

The data collected for different CO₂ concentrations suggests that at very low concentrations (i.e. 0.07 mol% in brine), the effect of CO₂ dissolution on wettability is

negligible. This shows that wettability alteration is not linear with pH decrease, as this concentration was enough to reduce pH below 3. It is likely that a threshold CO₂ concentration is required to obtain a dramatic shift in wettability either by desorption or chemical reaction. However, a detailed study including pH and ionic concentration measurements as a function of contact angle should be carried out to get a more precise idea of these effects.

Finally, Chapter 8 studied the effect of CO₂ on the interfacial tension between crude oils and formation brines. It is important to remark that high surface-activity of asphaltenes and resins was evidenced by the low measured equilibrium interfacial tensions (i.e. 10 mN/m). This produced relevant dynamic effects, and long equilibration times are required to obtain a plateau on the interfacial tension curve. Capillary effects of this type of oils are less disadvantageous for fluid displacement than in paraffinic crudes.

CO₂ dissolution is expected to reduce the interfacial tension between hydrocarbons and water due to its partitioning in both phases (GEORGIADIS et al., 2011). Nevertheless, for the Pre-Salt crudes and brines tested in this work, CO₂ dissolution either did not affect or either increased the equilibrium interfacial tension. The main reason for this is that CO₂ concentration in the proximities of the interface hinders the action of the asphaltenes and resins, which are the promoters of the decrease in interfacial tension. This is in agreement with the shorter equilibration times found for CO₂ saturated systems, indicating reduced mass transfer of surface-active compounds at the interface. These results suggest that, in terms of Capillary Number reduction, no relevant benefits of CO₂ injection are expected.

The expected impact of CO₂ dissolution on the Displacement Efficiency are summed up as follows. First, carbonated water has a major impact on carbonate rock wettability. The augmented water or intermediate-wet behavior contributes positively in the displacement of oil by increasing its relative permeability and reducing residual oil saturation. Analysis of rock dissolution, scale precipitation and formation of preferential paths (i.e. wormholes) is recommended to assess the effects on the Sweep Efficiency. Moreover, no considerable effect on interfacial tension is expected if the oil contains surface-active species as Oils B and D. Other positive effects of CO₂ dissolution than can contribute to oil recovery, such as viscosity reduction and oil swelling, should also be addressed.

Some recommendations for future works include the following:

- Compositional analysis of the surface-active groups in these Pre-Salt crudes.
- Phase partitioning studies for these compounds between the oil and the brine phases in the presence and absence of CO₂.
- High pressure aging of the rock slabs in the presence and absence of CO₂.
- Contact angle hysteresis using dynamic measurements to assess WAG injection.
- Amott Index wettability measurements in cores to cross-match the wettability.
- High pressure viscosity measurements and swelling effects of CO₂ saturated fluids.
- Core flood experiments to correlate the results.

CHAPTER 10: BIBLIOGRAPHY

2017 OPEC World Outlook. Disponível em: <www.opec.org>. Acesso em: 29 jul. 2018.

ADYANI, W. N. et al. **A Systematic Approach to Evaluate Asphaltene Precipitation During CO₂ Injection** SPE Enhanced Oil Recovery Conference Kuala Lumpur, Malaysia Society of Petroleum Engineers, , 2011. Disponível em: <<https://doi.org/10.2118/143903-MS>>

AHMED, T. H. **Reservoir engineering handbook.** 4th. ed. Burlington, MA, USA: Gulf Professional Publishing, 2010.

AL-MUTAIRI, S. M.; ABU-KHAMSIN, S. A.; HOSSAIN, M. E. **A Novel Approach to Handle Continuous Wettability Alteration during Immiscible CO₂ Flooding Process** Abu Dhabi International Petroleum Conference and Exhibition Abu Dhabi, UAE Society of Petroleum Engineers, , 2012.

AL-YASERI, A. Z. et al. Effect of the Temperature on CO₂/Brine/Dolomite Wettability: Hydrophilic versus Hydrophobic Surfaces. **Energy and Fuels**, v. 31, n. 6, p. 6329–6333, 2017.

ALI, M.; DAHRAJ, N. U. H.; HAIDER, S. A. **Study of Asphaltene Precipitation during CO₂ Injection in Light Oil Reservoirs** SPE/PAPG Pakistan section Annual Technical Conference Islamabad, Pakistan Society of Petroleum Engineers, , 2015. Disponível em: <<https://doi.org/10.2118/181130-MS>>

ALVES, D. R. et al. Influence of the salinity on the interfacial properties of a Brazilian crude oil-brine systems. **Fuel**, v. 118, p. 21–26, 2014.

AMOTT, E. Observations Relating to the Wettability of Porous Rock. **Petroleum Transactions AIME**, v. 216, p. 156–162, 1959.

ANASTASIADIS, S. H. et al. The determination of interfacial tension by video image processing of pendant fluid drops. **Journal of Colloid And Interface Science**, v. 119, n. 1, p. 55–66, 1987.

ANDERSON, W. Wettability Literature Survey- Part 2: Wettability Measurement. **Journal of Petroleum Technology**, v. 38, n. 11, p. 1246–1262, 1986.

ANDREAS, J. M.; HAUSER, E. A.; TUCKER, W. B. Boundary tension by pendant drops. **The Journal of Physical Chemistry**, v. 42, n. 8, p. 1001–1019, 1 jan. 1937.

ATKINS, P.; DE PAULA, J. **Atkins' Physical Chemistry**. [s.l.] Oxford University Press, 2010.

AUSTAD, T. et al. Seawater in Chalk: An EOR and Compaction Fluid. **SPE Reservoir Evaluation & Engineering**, v. 11, n. 4, p. 648–654, 2008.

AVEYARD, R.; HAYDON, D. A. Thermodynamic properties of aliphatic hydrocarbon/water interfaces. **Trans. Faraday Soc.**, v. 61, n. 0, p. 2255–2261, 1965.

BACCI, G.; KORRE, A.; DURUCAN, S. An experimental and numerical investigation into the impact of dissolution/precipitation mechanisms on CO₂ injectivity in the wellbore and far field regions. **International Journal of Greenhouse Gas Control**, v. 5, n. 3, p. 579–588, 1 maio 2011.

BARTA, C. **ENSCO: The First 20 Years**. [s.l.] Elsevier Science, 2008.

BARTON, A. F. M. **CRC Handbook of Solubility Parameters and Other Cohesion Parameters**. 2nd. ed. Boca Raton, FL, USA: CRC Press,

1991.

BASHFORTH, F.; ADAMS, J. C. **An attempt to test the theories of capillary action by comparing the theoretical and measured forms of drops of fluid. With an explanation of the method of integration employed in constructing the tables which give the theoretical forms of such drops** Cambridge, UK Cambridge University Press, , 1883. Disponível em: <file://catalog.hathitrust.org/Record/007060245>

BHAUMIK, D.; JAFFÉ, H. H.; MARK, J. E. Calculated polarizabilities for some aliphatic and aromatic hydrocarbons. **Journal of Molecular Structure: THEOCHEM**, v. 87, n. 1, p. 81–86, 1982.

BLOCK, A.; SIMMS, B. B. Desorption and exchange of adsorbed octadecylamine and stearic acid on steel and glass. **Journal of Colloid And Interface Science**, v. 25, n. 4, p. 514–518, 1967.

BO, J.; ZHANG, Y.; ZHANG, Y. Solubility of Nesquehonite and Calcite in Pressurized Carbonated Water from 293.15 to 343.15 K. **Journal of Chemical & Engineering Data**, v. 63, n. 8, p. 2868–2874, 2018.

BOYD, A. et al. Presalt Carbonate Evaluation for Santos Basin , Offshore Brazil. **Petrophysics**, v. 56, n. 6, p. 577–591, 2015.

BROCK, W. R.; BRYAN, L. A. **Summary Results of CO₂ EOR Field Tests, 1972-1987**. Low Permeability Reservoirs Symposium. **Anais...** Denver, CO, USA: Society of Petroleum Engineers, 1989

BROWN, R. J. S.; FATT, I. **Measurements Of Fractional Wettability Of Oil Fields' Rocks By The Nuclear Magnetic Relaxation Method**. Fall Meeting of the Petroleum Branch of AIME. **Anais...** Los Angeles, CA, USA: Society of Petroleum Engineers, 1956

BUCKLEY, J. S. **Mechanisms and Consequences of Wettability Alteration by Crude Oils**. [s.l.] Heriot Watt University, 1996.

BUCKLEY, J. S. et al. Asphaltenes and Crude Oil Wetting - The Effect of Oil Composition. **SPE Journal**, v. 2, n. 2, p. 107–119, 1997.

BUCKLEY, J. S. Wetting Alteration of Solid Surfaces By Crude Oils and Their Asphaltenes. **Revue de l'Institute Francais du Petrole**, v. 53, n. 1, p. 303–312, 1998.

BUCKLEY, J. S.; LIU, Y.; MONSTERLEET, S. Mechanisms of Wetting Alteration by Crude Oils. **SPE Journal**, v. 3, n. 1, p. 54–61, 1998.

BUCKLEY, J. S.; TAKAMURA, K.; MORROW, N. R. Influence of Electrical Surface Charges on the Wetting Properties of Crude Oils. **SPE Reservoir Engineering**, v. 4, n. 3, p. 332–340, 1989.

BUCKLEY, K.; UEHARA, R. **Subsea Concept Alternatives for Brazilian Pre-Salt Fields**. Offshore Technology Conference Brasil. **Anais...**Rio de Janeiro, Brazil: Society of Petroleum Engineers, 2017

BUSTAMANTE, P. et al. Hildebrand solubility parameter to predict drug release from hydroxypropyl methylcellulose gels. **International Journal of Pharmaceutics**, v. 414, n. 1–2, p. 125–130, 2011.

BUTT, H. J.; GRAF, K.; KAPPL, M. **Physics and Chemistry of Interfaces**. Berlin, Germany: WILEY-VCH Verlag GmbH & Co., 2006.

CAI, B.-Y.; YANG, J.-T.; GUO, T.-M. Interfacial Tension of Hydrocarbon + Water / Brine Systems under High Pressure. **J. Chem. Eng. Data**, v. 41, p. 493–496, 1996.

CAMARA, R. et al. **Carbonate coquina reservoirs: New insights for petrophysical reservoir characterisation**. 76th EAGE Conference and

Exhibition 2014. **Anais...**Amsterdam, Netherlands: 2014

CASSIE, A. B. D. Contact angles. **Discussions of the Faraday Society**, v. 3, n. 0, p. 11–16, 1948.

CASTELLAN, G. W. **Physical chemistry**. 2nd. ed. Reading, MA, USA: Addison-Wesley Pub. Co., 1971.

CEZAR, A. S. P. et al. Subsea Solutions in the Pre-Salt Development Projects. **Offshore Technology Conference**, 2015.

CHANG, H. L. et al. Advances in Polymer Flooding and Alkaline/Surfactant/Polymer Processes as Developed and Applied in the People's Republic of China. **Journal of Petroleum Technology**, v. 58, n. 2, p. 84–91, 2006.

CHIQUET, P.; BROSETA, D.; THIBEAU, S. Wettability alteration of caprock minerals by carbon dioxide. **Geofluids**, v. 7, n. 2, p. 112–122, 2007.

CORBETT, P.; BORGHI, L. Lacustrine Carbonates - For the Purpose of Reservoir Characterization Are They Different? **Offshore Technology Conference**, p. 1–23, 2013.

COREY, A. T. The Interrelation Between Gas and Oil Relative Permeabilities. **Producers Monthly**, v. 19, n. 1, p. 38–41, 1954.

CORRERA, S. et al. Estimation of the solvent power of crude oil from density and viscosity measurements. **Industrial and Engineering Chemistry Research**, v. 44, n. 24, p. 9307–9315, 2005.

CRAIG, F. F. **The Reservoir Engineering Aspects of Waterflooding**. Richardson, TX, USA: H. L. Doherty Memorial Fund of AIME, 1971.

CUIEC, L. E. **Restoration of the Natural State of Core Samples**. Fall

Meeting of the Society of Petroleum Engineers of AIME. **Anais...**Dallas, TX, USA: Society of Petroleum Engineers, 1975Disponível em: <<https://doi.org/10.2118/5634-MS>>

D'SOUZA, R. et al. **A Universal Field Development Approach for Advancing Stalled GOM Deepwater Projects**. Offshore Technology Conference. **Anais...**Houston, TX, USA: Society of Petroleum Engineers, 2018

DANOV, K. D.; BASHEVA, E. S.; KRALCHEVSKY, P. A. Effect of ionic correlations on the surface forces in thin liquid films: Influence of multivalent coions and extended theory. **Materials**, v. 9, n. 3, p. 1–23, 2016.

DE ALMEIDA, A. S. et al. **CCGS opportunities in the Santos Basin pre-salt development**. SPE International Conference on Health, Safety and Environment in Oil and Gas Exploration and Production 2010. **Anais...**Rio de Janeiro, Brazil: Society of Petroleum Engineers, 2010Disponível em: <<http://www.scopus.com/inward/record.url?eid=2-s2.0-77954229090&partnerID=tZOtx3y1>>

DE FREITAS FILHO, R. D. G. **Dissolution of Carbonate Rocks in High Pressure CO₂/Brine Systems: Effects on Porosity and Permeability**. [s.l.] Universidade Estadual de Campinas, 2017.

DE MORAES CRUZ, R. O. et al. Lula NE Pilot Project - An Ultra-Deep Success in the Brazilian Pre-Salt. **Offshore Technology Conference**, p. 1–21, 2016.

DEL RÍO, O. I.; NEUMANN, A. W. Axisymmetric Drop Shape Analysis: Computational Methods for the Measurement of Interfacial Properties from the Shape and Dimensions of Pendant and Sessile Drops. **Journal of Colloid and Interface Science**, v. 196, n. 2, p. 136–147, 15 dez. 1997.

DERJAGUIN, B. V; CHURAEV, N. V; MULLER, V. M. The Derjaguin—Landau—Verwey—Overbeek (DLVO) Theory of Stability of Lyophobic Colloids BT - Surface Forces. In: DERJAGUIN, B. V; CHURAEV, N. V; MULLER, V. M. (Eds.). . Boston, MA: Springer US, 1987. p. 293–310.

DONALDSON, E. C.; ALAM, W. **Wettability**. Houston, TX, USA: Gulf Publishing Company, 2008.

DONALDSON, E. C.; CHILINGARIAN, G. V.; YEN, T. F. **Enhanced Oil Recovery, II: Processes and Operations**. Amsterdam, Netherlands: Elsevier Science, 1989.

DONALDSON, E. C.; THOMAS, R. D.; LORENZ, P. B. Wettability Determination and Its Effect on Recovery Efficiency. **Society of Petroleum Engineers Journal**, v. 91, n. 1, p. 18–20, 1969.

DREXLER, S. et al. **Statistical Analysis to Evaluate the key Parameters Affecting Wettability of a Brazilian Pre-Salt Crude and Brine on Different Mineral Rocks**. Rio Oil & Gas. **Anais...**Rio de Janeiro, Brazil: IBP, 2018

EDERTH; CLAEISSON. Forces between Carboxylic Acid Surfaces in Divalent Electrolyte Solutions. **Journal of colloid and interface science**, v. 229, n. 1, p. 123–128, set. 2000.

EMERA, M. K.; SARMA, H. K. Prediction of CO₂ Solubility in Oil and the Effects on the Oil Physical Properties. **Energy Sources, Part A: Recovery, Utilization, and Environmental Effects**, v. 29, n. 13, p. 1233–1242, 2007.

FACANHA, J. M. F. **Fundamentals of Wettability Applied to Brazilian Pre-Salt Reservoirs and Wettability Alteration Evaluation in Low Salinity Water Injection**. [s.l.] Heriot-Watt University, 2017.

FJELDE, I.; ASEN, S. M. **Wettability alteration during water flooding**

and carbon dioxide flooding of reservoir chalk rocks. SPE EUROPEC/EAGE Annual Conference and Exhibition. **Anais...**Barcelona, Spain: Society of Petroleum Engineers, 2010

FORMIGLI, J. M.; CAPELEIRO PINTO, A. C.; ALMEIDA, A. S. **SS: Santos Basin's Pre-Salt Reservoirs Development: The Way Ahead.** Offshore Technology Conference. **Anais...**Houston, Texas: Offshore Technology Conference, 2009

FORMIGLI FILHO, J. M.; CAPELEIRO PINTO, A. C.; ALMEIDA, A. S. **SS: Santos Basin's Pre-Salt Reservoirs Development: The Way Ahead.** Offshore Technology Conference. **Anais...**Houston, Texas, USA: Offshore Technology Conference, 2009

FRANCO, C. A. et al. Nanoparticles for inhibition of asphaltenes damage: Adsorption study and displacement test on porous media. **Energy and Fuels**, v. 27, n. 6, p. 2899–2907, 2013.

FREITAG, N. P. Similarity of the Effect of Different Dissolved Gases on Heavy-Oil Viscosity. **SPE Reservoir Evaluation & Engineering**, v. 21, n. 3, p. 747–756, 2018.

GAO, L.; MCCARTHY, T. J. How Wenzel and Cassie Were Wrong. **Langmuir**, v. 23, n. 7, p. 3762–3765, 1 mar. 2007.

GARDNER, J. W.; ORR, F. M.; PATEL, P. D. The Effect of Phase Behavior on CO₂-Flood Displacement Efficiency. **Journal of Petroleum Technology**, v. 33, n. 11, p. 2067–2081, 1981.

GAVISH, N.; PROMISLOW, K. Dependence of the dielectric constant of electrolyte solutions on ionic concentration: A microfield approach. **Physical Review E**, v. 94, n. 1, p. 12611, 13 jul. 2016.

GENEROSI, J. et al. Calcite wettability in the presence of dissolved Mg²⁺ and SO₄²⁻. **Energy and Fuels**, v. 31, n. 1, p. 1005–1014, 2017.

GEORGIADIS, A. et al. Interfacial Tension Measurements of the (H₂O + CO₂) System at Elevated Pressures and Temperatures. **Journal of Chemical & Engineering Data**, v. 55, n. 10, p. 4168–4175, 2010.

GEORGIADIS, A. et al. Interfacial tension measurements of the (H₂O + n -decane + CO₂) ternary system at elevated pressures and temperatures. **Journal of Chemical and Engineering Data**, v. 56, n. 12, p. 4900–4908, 2011.

GEORGIADIS, A.; TRUSLER, J. P. M.; BISMARCK, A. Interfacial Tension Measurements of the (H₂O + n -Decane + CO₂) Ternary System at Elevated Pressures and Temperatures. p. 4900–4908, 2011.

GIBBS, J. W. **The Collected Works of J. Willard Gibbs**. [s.l.] Yale University Press, 1948.

GOEBEL, A.; LUNKENHEIMER, K. Interfacial Tension of the Water/n-Alkane Interface. **Langmuir**, v. 13, n. 2, p. 369–372, 1997.

GONÇALVES REIS VIANNA FILHO, F.; NAVEIRO, J. T.; DE OLIVEIRA, A. P. **Developing Mega Projects Simultaneously: The Brazilian Pre-Salt Case**. Offshore Technology Conference. **Anais...**Houston, Texas, USA: Offshore Technology Conference, 2015

GRAHAME, D. C. The Electrical Double Layer and the Theory of Electrocapillarity. **Chemical Reviews**, v. 41, n. 3, p. 441–501, 1 dez. 1947.

GRAUE, D. J.; BLEVINS, T. R. **Sarcoc Tertiary CO₂ Pilot Project**. SPE Symposium on Improved Methods of Oil Recovery. **Anais...**Tulsa, OK, USA: Society of Petroleum Engineers, 1978

GRETTIE, D. P.; WILLIAMS, R. J. The adsorption of organic compounds

on hydrous oxides and fuller's earth. **Journal of the American Chemical Society**, v. 50, n. 3, p. 668–672, 1928.

GRIBANOVA, E. V. Dynamic contact angles: Temperature dependence and the influence of the state of the adsorption film. **Advances in Colloid and Interface Science**, v. 39, p. 235–255, 1992.

GU, Y.; YANG, D. **Interfacial Tensions and Visual Interactions of Crude Oil-Brine-CO Systems Under Reservoir Conditions**. Canadian International Petroleum Conference. **Anais...**Calgary, Canada: Petroleum Society of Canada, 2004

HAMAKER, H. C. The London—van der Waals attraction between spherical particles. **Physica**, v. 4, n. 10, p. 1058–1072, 1 out. 1937.

HANSEN, C. M. **Hansen Solubility Parameters: A User's Handbook**. 2nd. ed. Boca Raton, FL, USA: CRC Press, 2007.

HIEMENZ, P. C.; RAJAGOPALAN, R. **Principles of Colloid and Surface Chemistry, Third Edition, Revised and Expanded**. New York, NY, USA: CRC Press, 1997.

HOLM, L. W. CO₂ Flooding: Its Time Has Come. **Journal of Petroleum Technology**, v. 34, n. 12, p. 2739–2745, 1982.

HONARPOUR, M.; KOEDERITZ, L.; HARVEY, A. H. **Relative permeability of petroleum reservoirs**. Boca Raton, FL, USA: C.R.C. Press, 1986.

HOORFAR, M.; KURZ, M. A.; NEUMANN, A. W. Evaluation of the surface tension measurement of axisymmetric drop shape analysis (ADSA) using a shape parameter. **Colloids and Surfaces A: Physicochemical and Engineering Aspects**, v. 260, n. 1–3, p. 277–285, 2005.

HUANG, E. T. S.; HOLM, L. W. Effect of WAG Injection and Rock Wettability on Oil Recovery During CO₂ Flooding. **SPE Reservoir Engineering**, v. 3, n. 1, p. 119–129, 1988.

HUNTER, R. J. **Zeta Potential in Colloid Science: Principles and Applications**. London: Academic Press, 1988.

ISRAELACHVILI, J. N. **Intermolecular and Surface Forces**. 3rd. ed. Burlington, MA, USA: Elsevier Science, 2015.

IZGEC, O. et al. **CO₂ Injection in Carbonates**. SPE Western Regional Meeting. **Anais...**Irvine, CA, USA: Society of Petroleum Engineers, 2005

JAAFAR, M. Z.; NASIR, A. M.; HAMID, M. F. **Measurement of Isoelectric Point of Sandstone and Carbonate Rock for Monitoring Water Encroachment****Journal of Applied Sciences**, 2014.

JACKSON, D. D.; ANDREWS, G. L.; CLARIDGE, E. L. **Optimum WAG Ratio vs. Rock Wettability in CO₂ Flooding**. SPE Annual Technical Conference and Exhibition. **Anais...**Las Vegas, NV, USA: Society of Petroleum Engineers, 1985

JAEGER, P. T.; ALOTAIBI, M. B.; NASR-EL-DIN, H. A. Influence of Compressed Carbon Dioxide on the Capillarity of the Gas - Crude Oil - Reservoir Water System. **Journal of Chemical and Engineering Data**, v. 55, p. 5246–5251, 2010.

JHA, N. K. et al. **Analysis of CO₂ Swelling and Modeling of PVT Properties of Reservoir Fluid of an Onland Field of Gujarat, India****Carbon Management Technology Conference**Sugar Land, TX, USA**Carbon Management Technology Conference**, , 2015.

KATZ, D. L. Possibilities of Secondary Recovery for the Oklahoma City

Wilcox Sand. **Transactions of the AIME**, v. 146, n. 1, p. 28–53, 1942.

KOSMULSKI, M. The pH-dependent surface charging and points of zero charge. V. Update. **Journal of Colloid and Interface Science**, v. 353, n. 1, p. 1–15, 2011.

LANSANGAN, R. M.; SMITH, J. L. Viscosity, Density, and Composition Measurements of CO₂/West Texas Oil Systems. **SPE Reservoir Engineering**, v. 8, n. 3, p. 175–182, 1993.

LASHKARBOLOOKI, M.; AYATOLLAHI, S. The effects of pH, acidity, asphaltene and resin fraction on crude oil/water interfacial tension. **Journal of Petroleum Science and Engineering**, v. 162, n. December 2017, p. 341–347, 2018.

LEACH, R. O. et al. A Laboratory and Field Study of Wettability Adjustment in Water Flooding. **Journal of Petroleum Technology**, v. 14, n. 2, p. 206–212, 1962.

LIN, E. C.; HUANG, E. T. S. The Effect of Rock Wettability on Water Blocking During Miscible Displacement. **SPE Reservoir Engineering**, v. 5, n. 2, p. 205–212, 1990.

LOCHTE, H. L. Petroleum Acids and Bases. **Industrial & Engineering Chemistry**, v. 44, n. 11, p. 2597–2601, 1952.

LONDON, F. The general theory of molecular forces. **Trans. Faraday Soc.**, v. 33, n. 0, p. 8b–26, 1937.

LOWE, A. C.; PHILLIPS, M. C.; RIDDIFORD, A. C. On the Wetting of Carbonate Surfaces By Oil And Water. **Journal of Canadian Petroleum Technology**, v. 12, n. 2, p. 9, 1973.

LOWELL, S.; SHIELDS, J. E. Hysteresis, entrapment, and wetting angle

in mercury porosimetry. **Journal of Colloid and Interface Science**, v. 83, n. 1, p. 273–278, 1 set. 1981.

LU, X.; SUN, S.; DODDS, R. **Toward 70% Recovery Factor: Knowledge of Reservoir Characteristics and IOR/EOR Methods from Global Analogs**. SPE Improved Oil Recovery Conference. **Anais...**Tulsa, OK: 2016Disponível em: <<http://www.onepetro.org/doi/10.2118/179586-MS>>

MAITLAND, G. C. **Intermolecular forces: their origin and determination**. New York, NY, USA: Oxford University Press, 1981.

MANCIU, M.; RUCKENSTEIN, E. Role of the hydration force in the stability of colloids at high ionic strengths. **Langmuir**, v. 17, n. 22, p. 7061–7070, 2001.

MANRIQUE, E. J.; MUCI, V. E.; GURFINKEL, M. E. **EOR Field Experiences in Carbonate Reservoirs in the United States**. SPE/DOE Symposium on Improved Oil Recovery. **Anais...**Tulsa, OK, USA: Society of Petroleum Engineers, 2006

MARSDEN, S. S.; KHAN, S. The wettability of the Bradford sand. **Producers Monthly**, v. 26, n. 5, p. 2–5, 1962.

MATIAS, H. C. et al. **Unlocking Pandora - Insights from Pre-salt Reservoirs in Campos and Santos Basins (Offshore Brazil)**. 77th EAGE Conference and Exhibition 2015. **Anais...**Madrid, Spain: 2015

MCCAFFERY, F. G.; MUNGAN, N. Contact Angle And Interfacial Tension Studies of Some Hydrocarbon-Water-Solid Systems. **Journal of Canadian Petroleum Technology**, v. 9, n. 3, p. 13, 1970.

MEDEIROS, M. Liquid-liquid interfacial tensions of binary water-hydrocarbons mixtures via gradient theory and CPA equation of state. **Fluid**

Phase Equilibria, v. 392, p. 65–73, 2015.

MICHAELS, A. S.; HAUSER, E. A. Interfacial Tension at Elevated Pressure and Temperature. II. Interfacial Properties of Hydrocarbon–Water Systems. **The Journal of Physical Chemistry**, v. 55, n. 3, p. 408–421, 1 mar. 1951.

MORROW, N. R.; CRAM, P. J.; MCCAFFERY, F. G. Displacement Studies in Dolomite With Wettability Control by Octanoic Acid. **Society of Petroleum Engineers Journal**, v. 13, n. 4, p. 221–232, 1973.

NING, S. X. et al. **Viscosity Reduction EOR with CO₂ & Enriched CO₂ to Improve Recovery of Alaska North Slope Viscous Oils** SPE Western North American Region Meeting Anchorage, AK, USA Society of Petroleum Engineers, , 2011. Disponível em: <<https://doi.org/10.2118/144358-MS>>

NIST. **Thermophysical Properties of Fluid Systems**. Disponível em: <<https://webbook.nist.gov/chemistry/fluid/>>. Acesso em: 2 set. 2018.

NUTTING, P. G. Some Physical and Chemical Properties of Reservoir Rocks Bearing on the Accumulation and Discharge of Oil. In: WRATHER, W. E.; LAHEE, F. H. (Eds.). . **Problems of Petroleum Geology**. [s.l.] American Association of Petroleum Geologists, 1934. p. 825–832.

ONISHI, K. et al. Measuring Electrical Resistivity Variations in a Sandstone Specimen Injected with Gas, Liquid, and Supercritical CO₂. In: GROBE, M.; PASHIN, J. C.; DODGE, R. L. (Eds.). . **Carbon Dioxide Sequestration in Geological Media—State of the Science**. Tulsa, OK, USA: American Association of Petroleum Geologists, 2009. p. 609–618.

OPEC Share of World Proven Reserves. Disponível em: <https://www.opec.org/opec_web/en/data_graphs/330.htm>. Acesso em: 29

jul. 2018.

PADDAY, J. F.; PITT, A. Axisymmetric meniscus profiles. **Journal of Colloid And Interface Science**, v. 38, n. 2, p. 323–334, 1972.

PARDINI DE SOUZA, F. **Análise Estatística e Determinação Experimental de Ângulos de Contato e Molhabilidades de Sistemas Óleo-Salmoura-Mineal Análogos ao Pré-sal Brasileiro**. [s.l.] Universidade Federal do Rio de Janeiro, 2018.

PÉNELOUX, A.; RAUZY, E.; FRÉZE, R. A consistent correction for Redlich-Kwong-Soave volumes. **Fluid Phase Equilibria**, v. 8, n. 1, p. 7–23, 1 jan. 1982.

PEPIN, A. et al. **Pre-Salt Carbonate Reservoir Analog Selection for Stimulation Optimization**. International Petroleum Technology Conference. **Anais...**Kuala Lumpur, Malaysia: 2014

PINDER, G. F.; GRAY, W. G. **Essentials of Multiphase Flow and Transport in Porous Media**. Hoboken, NJ, USA: John Wiley & Sons Inc., 2008.

PIZARRO, J. O. D. S.; BRANCO, C. C. M. **Challenges in Implementing an EOR Project in the Pre-Salt Province in Deep Offshore Brasil**SPE EOR Conference at Oil and Gas West AsiaMuscat, OmanSociety of Petroleum Engineers, , 2012. Disponível em: <<https://doi.org/10.2118/155665-MS>>

POTTER, G. F. **The Effects of CO₂ Flooding on Wettability of West Texas Dolomitic Formations**SPE Annual Technical Conference and ExhibitionDallas, TX, USASociety of Petroleum Engineers, , 1987.

POVEDA-JARAMILLO, J.-C. et al. Chemical Characterization of the Asphaltenes from Colombian Colorado Light Crude Oil. **CT&F - Ciencia**,

Tecnologia y Futuro, v. 6, p. 105–122, 2016.

QUÉRÉ, D. Rough ideas on wetting. **Physica A: Statistical Mechanics and its Applications**, v. 313, n. 1–2, p. 32–46, 2002.

RAIMONDI, P.; TORCASO, M. A. Distribution of the Oil Phase Obtained Upon Imbibition of Water. **Society of Petroleum Engineers Journal**, v. 4, n. 1, p. 49–55, 1964.

RAO, D. N.; GIRARD, M.; SAYEGH, S. G. **Interfacial Phenomena in Miscible Gas Processes**. SPE Annual Technical Conference and Exhibition. **Anais...**San Antonio, TX, USA: Society of Petroleum Engineers, 1989

RAO, N. D.; GIRARD, M.; SAYEGH, S. G. Impact of Miscible Flooding on Wettability, Relative Permeability, and Oil Recovery. **SPE Reservoir Engineering**, v. 7, n. 2, p. 204–212, 1992.

REBELLO, L.; SIEPMAN, T. **Desenvolvimento de Metodologia Experimental para Determinação do TDS de Amostras de Salmoura do Pré-Sal Brasileiro**. [s.l.] Universidade Federal do Rio de Janeiro, 2018.

ROELOFSEN, J.; BASTIAN, B. **Recovery Factors and Production Technology - An Overview**. 70th EAGE Conference and Exhibition incorporating SPE EUROPEC 2008. **Anais...**Rome, Italy: 2008

ROSEN, M. J.; KUNJAPPU, J. T. **Surfactants and Interfacial Phenomena**. [s.l.] Wiley, 2012.

ROSHAN, H. et al. On wettability of shale rocks. **Journal of Colloid and Interface Science**, v. 475, p. 104–111, 2016.

RUIDIAZ, E. M.; WINTER, A.; TREVISAN, O. V. Oil recovery and wettability alteration in carbonates due to carbonate water injection. **Journal of Petroleum Exploration and Production Technology**, v. 8, n. 1, p. 249–258,

2018.

RUSSEL, W. B. et al. **Colloidal Dispersions**. Cambridge, UK: Cambridge University Press, 1991.

SAAD, S. M. I. et al. Range of validity of drop shape techniques for surface tension measurement. **Langmuir**, v. 26, n. 17, p. 14004–14013, 2010.

SAKUMA, H. et al. Surface tension alteration on calcite, induced by ion substitution. **Journal of Physical Chemistry C**, v. 118, n. 6, p. 3078–3087, 2014.

SALATHIEL, R. A. Oil Recovery by Surface Film Drainage In Mixed-Wettability Rocks. **Journal of Petroleum Technology**, v. 25, n. 10, p. 1216–1224, 1973.

SANTOS, D. C. et al. Asphaltene flocculation parameter in Brazilian crude oils and synthetic polar and nonpolar mixtures: Experimental and modeling. **Fuel**, v. 199, p. 606–615, 2017.

SANTOS NETO, E.; CERQUEIRA, J. R.; PRINZHOFER, A. **Origin of CO₂ in Brazilian Basins**. Proceedings of the AAPG Annual Convention and Exhibition. **Anais...**Long Beach, CA, USA: 2012

SCAIFE, W. G. The relative permittivity of the n alkanes from n pentane to n decane as a function of pressure and temperature. **Journal of Physics A: General Physics**, v. 5, n. 6, p. 897–903, 1972.

SCHRAMM, L. L. **Surfactants: Fundamentals and Applications in the Petroleum Industry**. Cambridge, UK: Cambridge University Press, 2000.

SCHWARTZ, L. W.; GAROFF, S. Contact angle hysteresis and the shape of the three-phase line. **Journal of Colloid and Interface Science**, v. 106, n. 2, p. 422–437, 1 ago. 1985.

SEYYEDI, M.; SOHRABI, M.; FARZANEH, A. Investigation of Rock Wettability Alteration by Carbonated Water through Contact Angle Measurements. **Energy and Fuels**, v. 29, n. 9, p. 5544–5553, 2015.

SHARIATPANAHI, S. F. et al. Water Based EOR by Wettability Alteration in Dolomite. **Energy and Fuels**, v. 30, n. 1, p. 180–187, 2016.

SHAW, D. J. **Introduction to Colloid and Surface Chemistry**. 4th. ed. Oxford, UK: Butterworth-Heinemann, 1992.

SHEDID, S. A.; GHANNAM, M. T. Factors affecting contact-angle measurement of reservoir rocks. **Journal of Petroleum Science and Engineering**, v. 44, n. 3–4, p. 193–203, 2004.

SHENG, J. **Modern Chemical Enhanced Oil Recovery: Theory and Practice**. Burlington, MA: Gulf Professional Publishing, 2010.

SHENG, J. **Enhanced Oil Recovery Field Case Studies**. Waltham, MA, USA: Gulf Professional Publishing, 2013.

SHOAIB, S.; HOFFMAN, B. T. **CO₂ Flooding the Elm Coulee Field**. SPE Rocky Mountain Petroleum Technology Conference. **Anais...** Denver, CO, USA: Society of Petroleum Engineers, 2009

SIMON, R.; GRAUE, D. J. Generalized Correlations for Predicting Solubility, Swelling and Viscosity Behavior of CO₂ -Crude Oil Systems. **Journal of Petroleum Technology**, v. 17, n. 1, p. 102–106, 1965.

SPIECKER, P. M. et al. Effects of petroleum resins on asphaltene aggregation and water-in-oil emulsion formation. **Colloids and Surfaces A: Physicochemical and Engineering Aspects**, v. 220, n. 1–3, p. 9–27, 30 jun. 2003.

SRIVASTAVA, R. K.; HUANG, S. S.; DONG, M. Asphaltene Deposition

During CO₂ Flooding. **SPE Production & Facilities**, v. 14, n. 4, p. 235–245, 1999.

STALKUP, F. I. Displacement of oil by Solvent at High Water Saturation. **Society of Petroleum Engineers Journal**, v. 10, n. 4, p. 337–348, 1970.

STEPHANOS, J. J.; ADDISON, A. W. **Electrons, Atoms, and Molecules in Inorganic Chemistry: A Worked Examples Approach**. [s.l.] Elsevier Science, 2017.

STEWART, J. V. **Intermediate Electromagnetic Theory**. Singapore: World Scientific, 2001.

STONE, A. **The Theory of Intermolecular Forces**. 2nd. ed. Oxford, UK: Oxford University Press, 2013.

SUN, C.-Y.; CHEN, G.-J. Measurement of Interfacial Tension for the CO₂ Injected Crude Oil + Reservoir Water System. **Journal of Chemical & Engineering Data**, v. 50, n. 3, p. 936–938, 2005.

SUSNAR, S. S.; HAMZA, H. A.; NEUMANN, A. W. Pressure dependence of interfacial tension of hydrocarbon-water systems using axisymmetric drop shape analysis. **Colloids and Surfaces A: Physicochemical and Engineering Aspects**, v. 89, n. 2–3, p. 169–180, 1994.

SVENSSON, U.; DREYBRODT, W. Dissolution kinetics of natural calcite minerals in CO₂-water systems approaching calcite equilibrium. **Chemical Geology**, v. 100, n. 1–2, p. 129–145, 1992.

SZILAGYI, I.; SADEGHPOUR, A.; BORKOVEC, M. Destabilization of colloidal suspensions by multivalent ions and polyelectrolytes: from screening to overcharging. **Langmuir : the ACS journal of surfaces and colloids**, v. 28, n. 15, p. 6211–6215, abr. 2012.

TAVARES, A. C. et al. Facies and depositional environments for the coquinas of the Morro do Chaves Formation, Sergipe-Alagoas Basin, defined by taphonomic and compositional criteria. **Brazilian Journal of Geology**, v. 45, n. 3, p. 415–429, 2015.

TELES, A. P. et al. Analysis of subterranean Pre-salt carbonate reservoir by X-ray computed microtomography. **Journal of Petroleum Science and Engineering**, v. 144, p. 113–120, 1 ago. 2016.

TERRA, J. G. S. et al. Classificações Clássicas De Rochas Carbonáticas. **B. Geoci. Petrobras, Rio de Janeiro**, v. 18, n. 1, p. 9–29, 2010.

THAKUR, G. Spectrum: Moving Toward 70% Recovery Factor: Multiple Disciplines, Different Methods, One Goal. **Journal of Petroleum Technology**, v. 64, n. 6, p. 14–15, 2012.

THIESSEN, D. B. et al. Robust digital image analysis of pendant drop shapes. **Journal of Colloid and Interface Science**, v. 177, n. 2, p. 658–665, 1996.

THOMPSON, D. L.; STILWELL, J. D.; HALL, M. Lacustrine carbonate reservoirs from Early Cretaceous rift lakes of Western Gondwana: Pre-Salt coquinas of Brazil and West Africa. **Gondwana Research**, v. 28, n. 1, p. 26–51, 1 ago. 2015.

TIAB, D.; DONALDSON, E. C. **Petrophysics: Theory and Practice of Measuring Reservoir Rock and Fluid Transport Properties**. 4th. ed. Waltham, MA, USA: Gulf Professional Publishing, 2015.

TIAN, Y. et al. Comparison Study on Temperature Dependence of the Interfacial Tension of *n* -Alkane–Water and *n* -Alcohol–Water Two Binary Systems. **Journal of Chemical & Engineering Data**, v. 59, n. 11, p. 3495–

3501, 2014.

TIFFIN, D. L.; YELLIG, W. F. Effects of Mobile Water on Multiple-Contact Miscible Gas Displacements. 1983.

TIPLER, P. A.; LLEWELLYN, R. **Modern Physics**. 5th. ed. New York, NY, USA: W. H. Freeman and Company, 2007.

TREIBER, L. E.; OWENS, W. W. A Laboratory Evaluation of the Wettability of Fifty Oil-Producing Reservoirs. 1972.

US Energy Information Administration Spot Price. Disponível em: <https://www.eia.gov/dnav/pet/pet_pri_spt_s1_m.htm>. Acesso em: 29 jul. 2018.

VARGAS, F. M.; CHAPMAN, W. G. Application of the One-Third rule in hydrocarbon and crude oil systems. **Fluid Phase Equilibria**, v. 290, n. 1–2, p. 103–108, 2010.

VERWEY, E. J. W.; OVERBEEK, J. T. G.; VAN NEE, K. **Theory of the Stability of Lyophobic Colloids: The Interaction of Sol Particles Having an Electric Double Layer**. Eindhoven, Netherlands: Elsevier Publishing Company, 1948.

WALID AL SHALABI EMAD ; SEPEHRNOORI, K. **Low Salinity and Engineered Water Injection for Sandstone and Carbonate Reservoirs**. [s.l.] Elsevier Science, 2017.

WEAST, R. C. **Handbook of Chemistry and Physics: A Ready-reference Book of Chemical and Physical Data**. 49th. ed. Cleveland, OH, USA: Chemical Rubber, 1968.

WENZEL, R. N. Resistance of solid surfaces to wetting by water. **Industrial and Engineering Chemistry**, v. 28, n. 8, p. 988–994, 1936.

WENZEL, R. N. Surface roughness and contact angle. **Journal of Physical & Colloid Chemistry**, v. 53, n. 9, p. 1466–1467, 1949.

WIEGAND, G.; FRANCK, E. Interfacial-tension between water and nonpolar fluids up to 473-K and 2800-bar. **Ber Bunsen-Gesellschaft-Phys Chem**, v. 98, n. 6, p. 809–817, 1994.

WILLHITE, G. P. **Waterflooding**. Richardson, TX, USA: Society of Petroleum Engineers, 1986.

WILT, B. K.; WELCH, W. T.; GRAHAM RANKIN, J. Determination of asphaltenes in petroleum crude oils by fourier transform infrared spectroscopy. **Energy and Fuels**, v. 12, n. 5, p. 1008–1012, 1998.

YAKHSHI-TAFTI, E.; KUMAR, R.; CHO, H. J. Measurement of Surface Interfacial Tension as a Function of Temperature Using Pendant Drop Images. **International Journal of Optomechatronics**, v. 5, n. 4, p. 393–403, 2011.

YOUNG, T. **Miscellaneous works of the late Thomas Young ...** [s.l.] J. Murray, 1855.

YU, L.; BUCKLEY, J. S. Evolution of Wetting Alteration by Adsorption From Crude Oil. **SPE Formation Evaluation**, v. 12, n. 1, p. 5–12, 1997.

YUAN, Y.; LEE, T. R. Contact Angle and Wetting Properties. In: BRACCO, G.; HOLST, B. (Eds.). . **Surface Science Techniques**. Berlin, Germany: Springer Berlin Heidelberg, 2013. p. 3–34.

ZEPPIERI, S.; RODRÍGUEZ, J.; LÓPEZ DE RAMOS, A. L. Interfacial tension of alkane + water systems. **Journal of Chemical and Engineering Data**, v. 46, n. 5, p. 1086–1088, 2001.

ZHANG, K. Experimental and Numerical Investigation of Oil Recovery from Bakken Formation by Miscible CO₂ Injection. **SPE Annual Technical**

Conference and Exhibition, v. 1, p. 1–23, 2016.

ZHU, J. et al. **Ultra Heavy Oil Production Experience in China** **SPE Kingdom of Saudi Arabia Annual Technical Symposium and Exhibition** Dammam, Saudi Arabia Society of Petroleum Engineers, , 2018.
Disponível em: <<https://doi.org/10.2118/192302-MS>>

APPENDIX A: EQUATIONS INVOLVED IN THE DROP SHAPE ANALYSIS METHOD

For a pendant (or sessile) drop, the Young-Laplace Equation (Equation 2.1) describes the pressure difference between the internal and external phases at any point of its interface. If the drop is in static equilibrium, this pressure drop must be equal to the difference in hydrostatic pressure between both fluids at the same point of the interface, which basically depends on the density difference between both phases. This is expressed in Equation A.1 where the z coordinate corresponds to the axis of the drop and is parallel to the gravity, and x and y are the other orthogonal coordinates.

$$g\left(\frac{1}{R_1} + \frac{1}{R_2}\right) = \Delta P = \Delta\rho gz + C \quad (\text{A.1})$$

where ΔP is the pressure difference at both sides of the interface, γ is the interfacial tension between the fluids, R_1 and R_2 are the main radii of curvature, $\Delta\rho$ is the density difference between the fluids, z is the height of the point considered with respect to the origin of coordinates, C is a constant that depends on the location of the origin of coordinates and g is the acceleration of gravity.

If b is defined as the radius of curvature at the droplet apex (where $R_1 = R_2$), the application of Equation A.1 at the apex (using the apex as origin of coordinates, then $z = 0$) allows to obtain the integration constant $C = (2\gamma)/b$. In addition, if ϕ is the angle between the axis of the drop (z) and the normal to the surface of the drop at a given point, the radius of curvature of the cross-section contained on the plane $x - z$ can be written as: $R_2 = x/\sin(\phi)$. A scheme of these parameters is shown in Figure A.1. Applying these substitutions in Equation A.1 gives place to Equation A.2.

$$\frac{1}{R_1} + \frac{\sin(j)}{x} = \frac{Drgz}{g} + \frac{2}{b} \quad (\text{A.2})$$

where γ is the interfacial tension between the fluids, R_l is the radius of curvature in a drop cross section at a plane that includes z , φ is the angle between the axis of the drop and the normal to its surface, $\Delta\rho$ is the density difference between the fluids, z is the height of the point considered with respect to the apex of the drop, b is the radius of curvature at the apex of the drop and g is the acceleration of gravity.

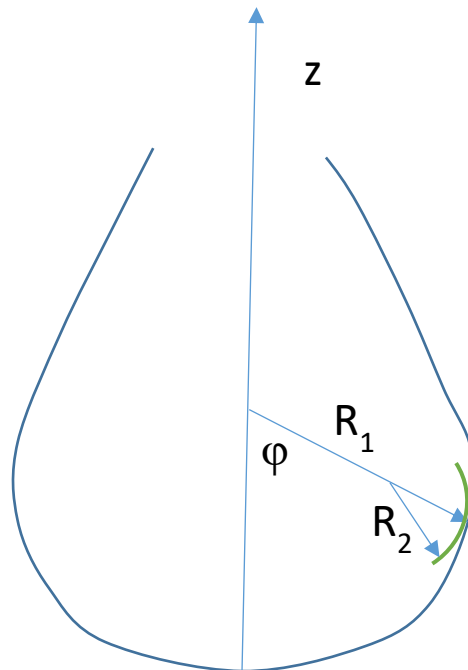


Figure A.1. Scheme of the parameter used to characterize the equations involved in DSA measurements.

The dimensionless parameter β is defined as showed in Equation A.3. The physical meaning of this parameter, which is referred to as Bond Number, is the gravitational over the interfacial tension forces.

$$b = \frac{Drgb^2}{g} \quad (\text{A.3})$$

By expressing R_l and φ as a function of the coordinates x and z applying the geometrical relations A.4 and A.5, a parametrization of Equation A.2 is achieved obtaining the expression showed in Equation A.6.

$$\frac{1}{R_l} = \frac{\frac{d^2z}{dx^2}}{\left[1 + \left(\frac{dz}{dx}\right)^2\right]^{3/2}} \quad (\text{A.4})$$

$$\sin(j) = \frac{\frac{dz}{dx}}{\left[1 + \left(\frac{dz}{dx}\right)^2\right]^{1/2}} \quad (\text{A.5})$$

$$\frac{d^2z}{dx^2} + \left[1 + \left(\frac{dz}{dx}\right)^2\right] \frac{1}{x} \frac{dz}{dx} = (2 + bz) \left[1 + \left(\frac{dz}{dx}\right)^2\right]^{3/2} \quad (\text{A.6})$$

Equation A.6 gives the profile of the drop that is immerse in an external fluid in terms of the coordinates x and z . Two boundary conditions must be applied to solve this second order differential equation. Typically, the apex of the drop is chosen as the origin of coordinates which results in the first, and more evident, boundary condition: $x = 0$ for $z = 0$. The second boundary condition is less obvious and requires that the radius of curvature at the apex as an input for the resolution, this is: $R_l = b$ when x tends to zero. This can be converted into an expression that depends on x , z and b alone by using the geometrical relation above. There are different approaches to solve this equation using numerical methods. This is out of the scope of this work, but further information about the numerical resolution of this problem can be found elsewhere ((YAKHSHI-TAFTI; KUMAR; CHO, 2011)).

APPENDIX B: SIMULATIONS OF FLUID'S PROPERTIES

The results regarding phase behavior of oil brines and fluids recombined with CO₂ are summarized in this appendix. The simulations were carried out using the software and specifications detailed in Section 4.2.

a) Brines

CO₂ solubility in the brines used in this work as a function of pressure at 60 °C is represented in Table B.1. As expected, the solubility of CO₂ increases with pressure. However, the decreasing slope indicates that for higher pressures, the augment in solubility is reduced with a tendency to plateau.

In addition, CO₂ solubility tends to decrease as the salinity of the brine increases. As a result, DSW presents the maximum solubility and Brine B the minimum. This has to be taken into account since a higher CO₂ solubility represents greater effect on the properties on the brine and increased partitioning of CO₂ between the oil and the brine phases.

Table B.1. CO₂ solubility in the brines used in this work at 60 °C.

| Pressure (psi) | Brine B | | Brine D | | DSW | |
|-------------------|---------|-------|---------|-------|-------|-------|
| | g/lit | mol% | g/lit | mol% | g/lit | mol% |
| 1000 | 14.06 | 0.56% | 20.70 | 0.83% | 31.79 | 1.34% |
| 2000 | 17.79 | 0.67% | 28.68 | 1.15% | 44.19 | 1.87% |
| 3000 | 19.72 | 0.74% | 31.85 | 1.28% | 49.19 | 2.09% |
| 4000 | 21.21 | 0.80% | 34.18 | 1.38% | 52.84 | 2.26% |
| 5000 | 22.42 | 0.85% | 36.27 | 1.47% | 56.04 | 2.40% |

A vital effect of CO₂ dissolution in brine is the decrease of pH. As discussed throughout the text, the acid – base equilibrium is affected by the dissolution of CO₂. This effect impacts on surface charges, the most stable acidic or basic species and dissolution of

carbonate rocks. The pH of the brines used in this work with no CO₂ addition and CO₂ saturated are plotted at 60 °C and pressures from 1000 to 5000 psi in Figure B.1.

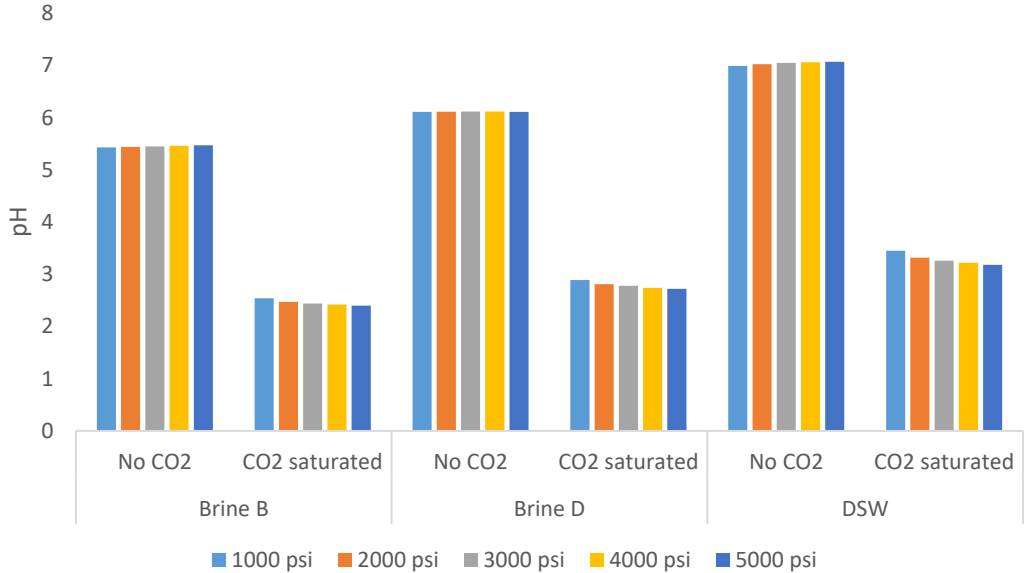


Figure B.1. pH of Brine B, D and DSW with no CO₂ and CO₂ saturated at 60 °C.

The results show the expected trends as the decrease in pH follows the solubility of CO₂. It is important to point out that CO₂ has a paramount effect on the pH of the aqueous phase. Even at 1000 psi, CO₂ dissolution reduces the pH of reservoir brines to values below 3 and that of DSW to 3.45.

The pH of Brine B with the concentrations of CO₂ used in Section 7.3 is plotted in Figure B.2. The addition of CO₂ in the formation brine has a dramatic impact on CO₂. It can be observed that even for the lowest pressure and minimum concentration, the pH shifts from 5.43 to 2.93. The decrease is even greater for the CO₂ saturated brine. These results show how pH is strongly affected by CO₂ dissolution in formation brine even at low concentrations.

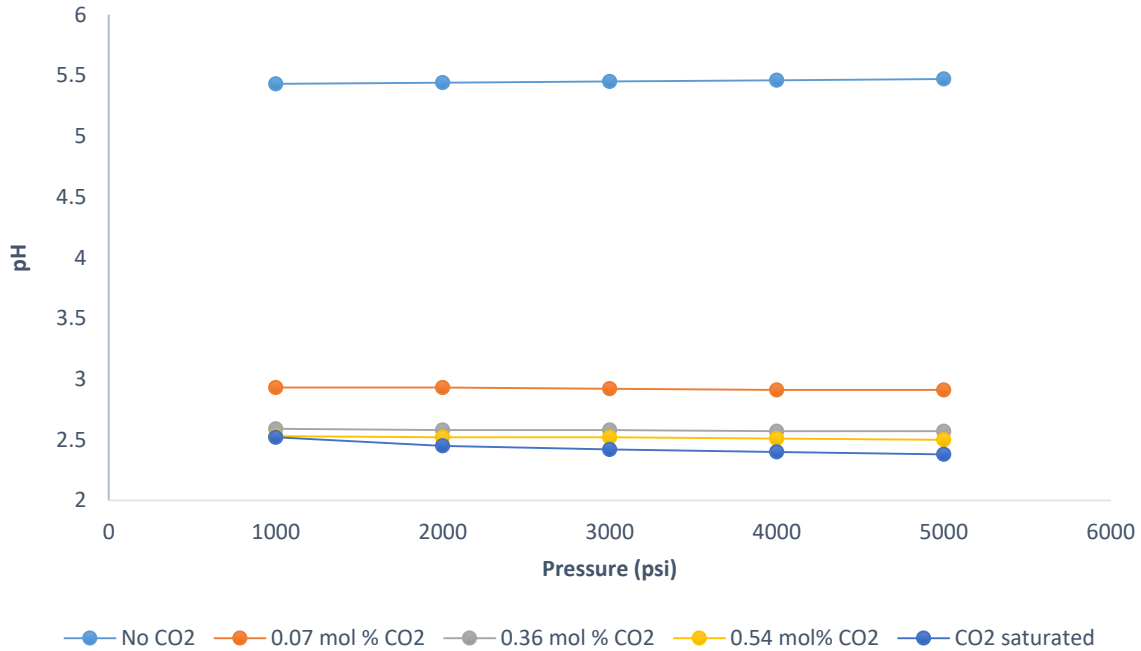


Figure B.2. pH for Brine B at 60 °C with different concentrations of CO₂ used in this work.

The density of formation brines is important not only due to material balance and gravity segregation reasons, but also is a required input for interfacial tension calculation using the Drop Shape Analyzer. The density of the brines used in this work at 60 °C and different pressures is shown in Table B.2 including the brine with no added CO₂ and the CO₂ saturated brine. Density increases with pressure for all brines. For the heavier brines (B and D), CO₂ reduces the density at lower pressures. However, at higher pressures, the density of supercritical CO₂ is greatly increased and the density of the carbonated brines levels or overpasses that of the dead brine. For the injection water (DSW), the carbonated brine is heavier than the dead one even at 1000 psi.

Table B.2. Density (g/ml) of the brines used in this work with no CO₂ and CO₂ saturated. Temperature = 60 °C.

| Pressure (psi) | Brine B | | Brine D | | DSW | |
|----------------|---------|---------------|---------|---------------|--------|---------------|
| | No CO2 | CO2 saturated | No CO2 | CO2 saturated | No CO2 | CO2 saturated |
| 1000 | 1.182 | 1.183 | 1.098 | 1.098 | 1.014 | 1.021 |
| 2000 | 1.184 | 1.185 | 1.100 | 1.102 | 1.017 | 1.027 |

| | | | | | | |
|------|-------|-------|-------|-------|-------|-------|
| 3000 | 1.186 | 1.188 | 1.102 | 1.105 | 1.020 | 1.030 |
| 4000 | 1.189 | 1.192 | 1.105 | 1.109 | 1.022 | 1.034 |
| 5000 | 1.193 | 1.197 | 1.110 | 1.112 | 1.025 | 1.037 |

The density of the recombined mixtures of brine B with different concentrations of CO₂ (mixtures LB1 – LB4) is a required input data for IFT calculation. Table B.3 shows the values obtained for the mixtures L1, L2 and L3 for the range of pressures used in this work at 60 °C, including the corresponding CO₂ concentration for each mixture. The saturated data was crosschecked with the experimental measured values using the procedure in Section 4.1.3 (data not showed) obtaining a maximum relative error of 1.3%.

Table B.3. Concentration and simulated density data for brine B recombined with CO₂.

| Mixture | LB1 | LB2 | LB3 | LB4 (Saturated) |
|------------------------|-------------------------|-------|-------|-----------------|
| CO ₂ mol% | 0.07% | 0.36% | 0.54% | 0.56%* |
| g CO ₂ /lt* | 1.85 | 9.05 | 13.33 | 14.06* |
| Pressure [psi] | Density at 60 °C (g/ml) | | | |
| 1000 | 1.182 | 1.183 | 1.183 | 1.183 |
| 2000 | 1.184 | 1.185 | 1.185 | 1.185 |
| 3000 | 1.187 | 1.187 | 1.188 | 1.188 |
| 4000 | 1.190 | 1.191 | 1.191 | 1.192 |
| 5000 | 1.195 | 1.196 | 1.196 | 1.197 |

* At 60 °C and 1000 psi.

b) Oils

The density of CO₂ saturated oil B at 60 °C was simulated for pressures from 1000 to 5000 psi. Also, the data for oil B with no added CO₂ was included. The results are shown in Figure B.3. Interestingly, CO₂ decreases the density of the oil phase at lower pressure. Nevertheless, for pressures greater than 3000 psi, the CO₂ saturated mixture is heavier than crude B. The cause of this is that the density of supercritical CO₂ increases steeply with pressure overcoming the density of the crude. This effect an gravity segregation was discussed elsewhere (TIAB; DONALDSON, 2015).

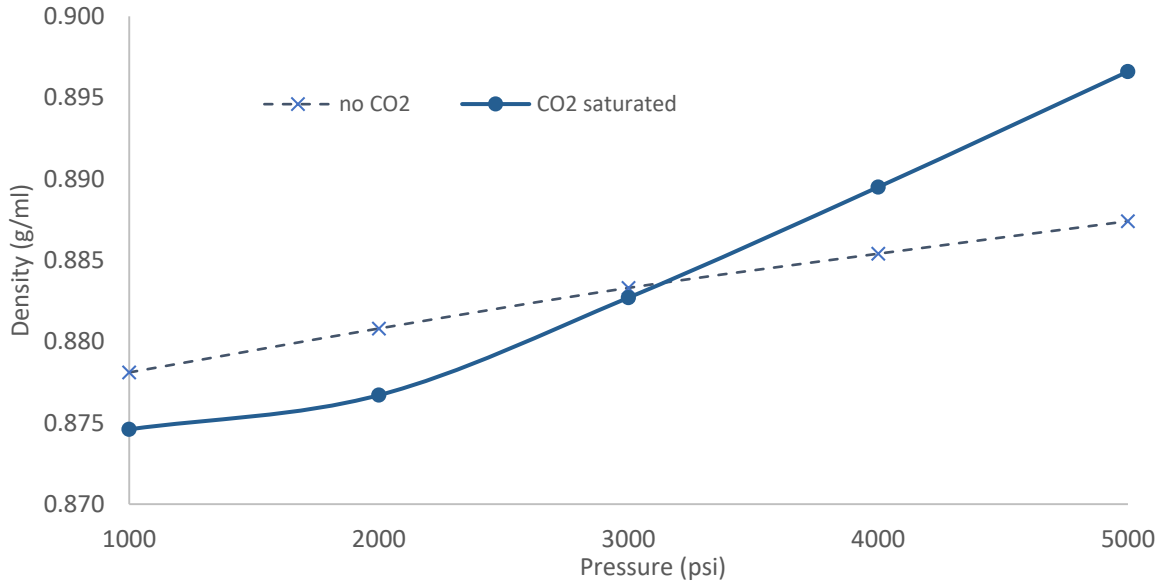


Figure B.3. Density of crude B and CO₂ saturated mixture.

Phase behavior of dead oil B and of the mixtures corresponding to the actual volumes injected in the different recombination procedures (L1 – L4) employed in this work were modelled. Table B.4 indicates the injected volumes of oil and CO₂ at recombination conditions (1000 psi and 25 °C).

Table B.4. Volumes injected for each recombination at 1000 psi and 25 °C.

| Recombination | V oil (ml) | V CO ₂ (ml) |
|---------------|------------|------------------------|
| L1 | 50 | 1.92 |
| L2 | 38 | 7.33 |
| L3 | 30 | 8.20 |
| L4 | 50 | 18.8 |

The flash of the mixtures in Table B.4 was carried out to obtain the number of resulting phases and the composition of the heavier liquid phase which is injected to the DSA equipment. The results are shown in Table B.5. It can be observed that the mixtures L1 and

L2 result in a liquid single phase. L3 and L4, which have excess CO₂, results in a heavy oil phase with 61.6 mol% of CO₂ and in light a liquid phase with 99.5 mol% CO₂.

Table B.5. Composition (mol%) of the phases after recombination at 25 °C and 1000 psi.

| | L1 | L2 | L3 | | L4 | |
|--|--------|--------|--------|--------|--------|--------|
| | liquid | liquid | light | heavy | light | heavy |
| CO ₂ | 22.926 | 59.106 | 99.482 | 61.631 | 99.505 | 61.631 |
| m-c-C ₅ | 0.162 | 0.086 | 0.033 | 0.073 | 0.030 | 0.065 |
| c-C ₆ | 0.146 | 0.078 | 0.027 | 0.067 | 0.024 | 0.060 |
| m-c-C ₆ | 0.370 | 0.196 | 0.070 | 0.168 | 0.062 | 0.151 |
| Toluene | 0.023 | 0.012 | 0.003 | 0.011 | 0.003 | 0.010 |
| et-Benzene | 0.062 | 0.033 | 0.008 | 0.029 | 0.007 | 0.027 |
| p-Xylene | 0.035 | 0.018 | 0.004 | 0.016 | 0.004 | 0.015 |
| m-Xylene | 0.035 | 0.018 | 0.004 | 0.016 | 0.004 | 0.015 |
| o-Xylene | 0.039 | 0.020 | 0.004 | 0.018 | 0.004 | 0.017 |
| iC ₄ +nC ₄ | 0.016 | 0.008 | 0.003 | 0.007 | 0.003 | 0.006 |
| iC ₅ +nC ₅ +C ₆ | 0.601 | 0.319 | 0.068 | 0.284 | 0.063 | 0.266 |
| C ₇ -C ₂₄ | 35.647 | 18.914 | 0.288 | 17.735 | 0.285 | 17.723 |
| C ₂₅ -C ₃₆ | 18.717 | 9.931 | 0.006 | 9.346 | 0.006 | 9.386 |
| C ₃₇ -C ₅₂ | 12.910 | 6.850 | 0.000 | 6.447 | 0.000 | 6.476 |
| C ₅₃ -C ₈₀ | 8.313 | 4.411 | 0.000 | 4.151 | 0.000 | 4.170 |

The density of the heavy liquid phase (LO1 – LO4) corresponding to each recombination process (L1 – L4) was calculated at 60 °C and pressures from 1000 to 5000 psi (Table B.6). This data is required for the calculation of the interfacial tension.

Table B.6. Density (g/ml) of the liquid oil phase at 60 °C after recombination flash at 25 °C and 1000 psi.

| Pressure (psi) | LO1 | LO2 | LO3 | LO4 |
|----------------|--------|--------|--------|--------|
| 1000 | 0.8770 | 0.8745 | 0.8746 | 0.8746 |
| 2000 | 0.8806 | 0.8775 | 0.8770 | 0.8771 |
| 3000 | 0.8837 | 0.8837 | 0.8835 | 0.8837 |
| 4000 | 0.8865 | 0.8891 | 0.8893 | 0.8894 |
| 5000 | 0.8890 | 0.8939 | 0.8944 | 0.8945 |

Solubility of CO₂ in crude oil B at 60 °C and pressures up to 10000 psi was modelled obtaining the plot in Figure B.4. This curve confirms that mixtures from L2 – L4 correspond to CO₂ saturated oil phases at recombination conditions.

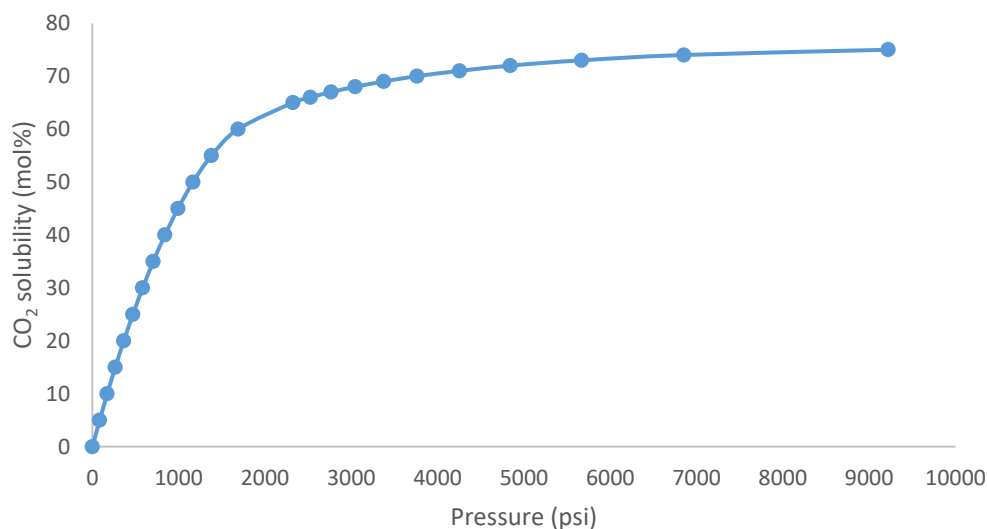


Figure B.4. Solubility of CO₂ in crude B at 60 °C and pressures up to 10000 psi.

The same approach was used to solve the flash at 25 °C and 1000 psi of the mixtures of 50 ml Oil D and 18.8 ml CO₂ (used in the pre-saturated fluids). The results, in Table B.7, are similar to those of the saturated B oil LO4 (Table B.7). For the model oil, the mixture resulted in full miscibility with a composition of 60 mol% CO₂, 20 mol% toluene and 20 mol% hexadecane.

As for Oil B, the density and CO₂ solubility was calculated for Oil D and Model Oil (71.1 wt% n-hexadecane and 28.9% toluene). The results are plotted in Figures B6 – B8. For Oil D, the results are similar to that of Oil B. The density of the CO₂ saturated oil is equal to that of the dead crude at a higher pressure than for Oil B (4000 psi instead of 3000). CO₂ solubility in the same order of magnitude for both Pre-Salt oils. For Model Oil, the density of CO₂ saturated and dead oil are equal even at lower pressure (2500 psi). In addition, CO₂ solubility is higher and the mixture is completely miscible at pressures over 1700 psi.

Table B.7. Composition (mol%) of the phases after recombination of 50 ml Oil D and 18.8 ml CO₂ at 25 °C and 1000 psi.

| | light liquid | heavy liquid |
|--|--------------|--------------|
| CO ₂ | 98.577 | 64.280 |
| m-c-C ₅ | 0.059 | 0.114 |
| Benzene | 0.003 | 0.012 |
| c-C ₆ | 0.051 | 0.110 |
| m-c-C ₆ | 0.137 | 0.288 |
| Toluene | 0.020 | 0.054 |
| et-Benzene | 0.019 | 0.056 |
| p-Xylene | 0.016 | 0.048 |
| m-Xylene | 0.016 | 0.049 |
| o-Xylene | 0.015 | 0.050 |
| iC ₅ +nC ₅ +C ₆ | 0.102 | 0.388 |
| C ₇ -C ₁₈ | 0.929 | 16.764 |
| C ₁₉ -C ₂₉ | 0.056 | 9.262 |
| C ₃₀ -C ₄₉ | 0.001 | 5.282 |
| C ₅₀ -C ₈₀ | 0.000 | 3.244 |

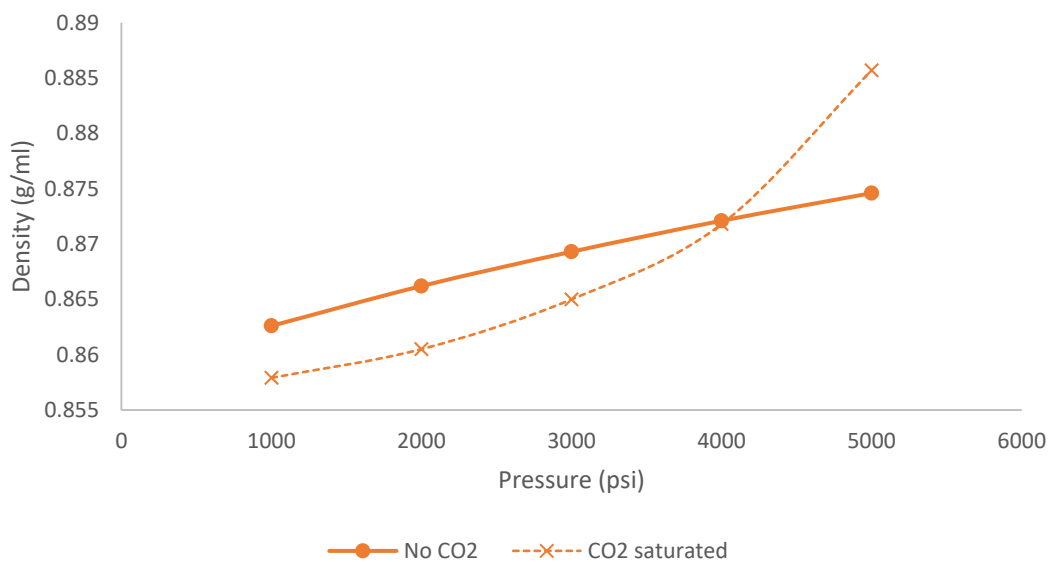


Figure B.5. Density of crude D and CO₂ saturated mixture at 60 °C.

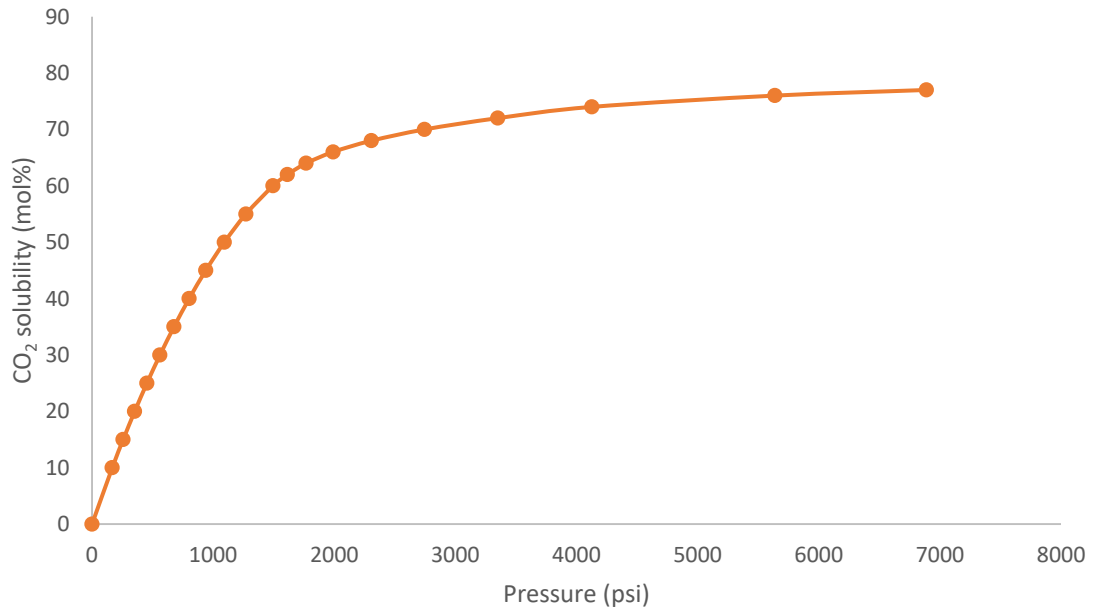


Figure B.6. CO₂ solubility in crude B at 60 °C and pressures up to 7000 psi.

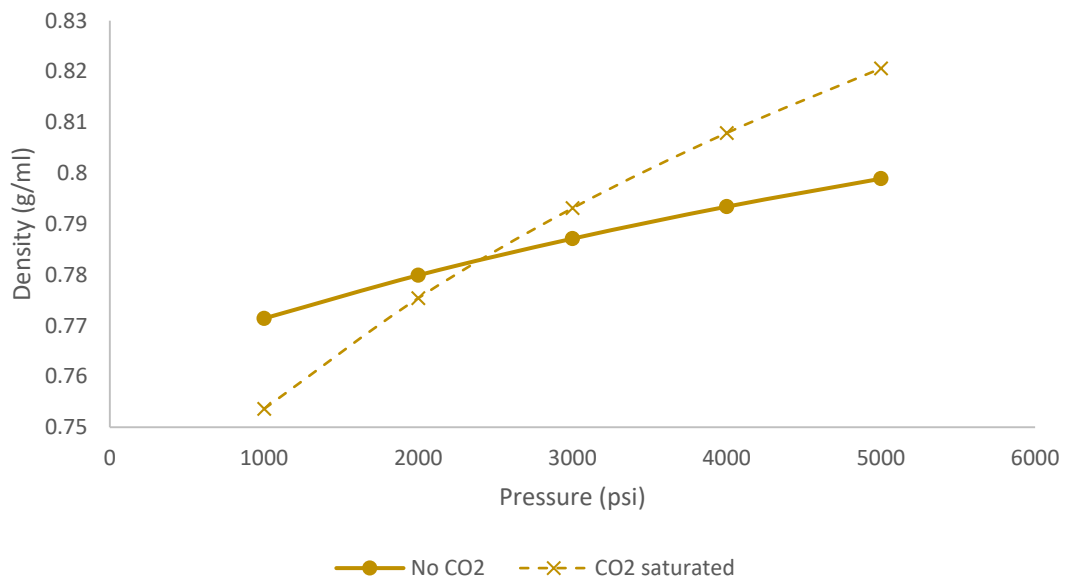


Figure B.7. Density of Model Oil and CO₂ saturated mixture at 60 °C.

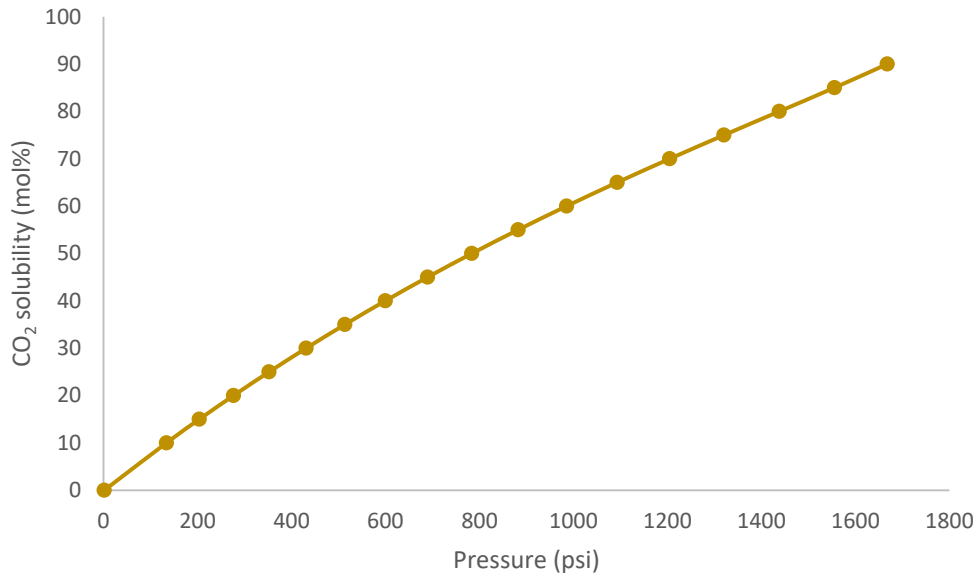


Figure B.8. CO₂ solubility in Model Oil at 60 °C and pressures up to reaching a critical mixture.

To have a qualitative idea of the phase behavior of the different oil-CO₂ mixtures prepared under several pressure and temperature conditions, the phase envelope was simulated in PVT-Sim for Oil B and the total mixtures L1-L4 (Table B.4). The results are shown in Figures B.9 – B.17. The red dots represent the critical points.

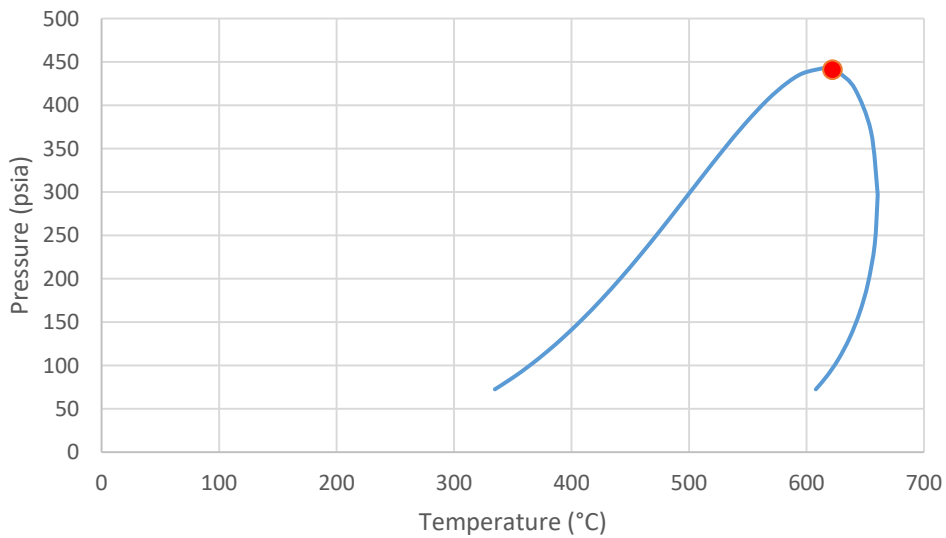


Figure B.9. Phase diagram for dead Oil B.

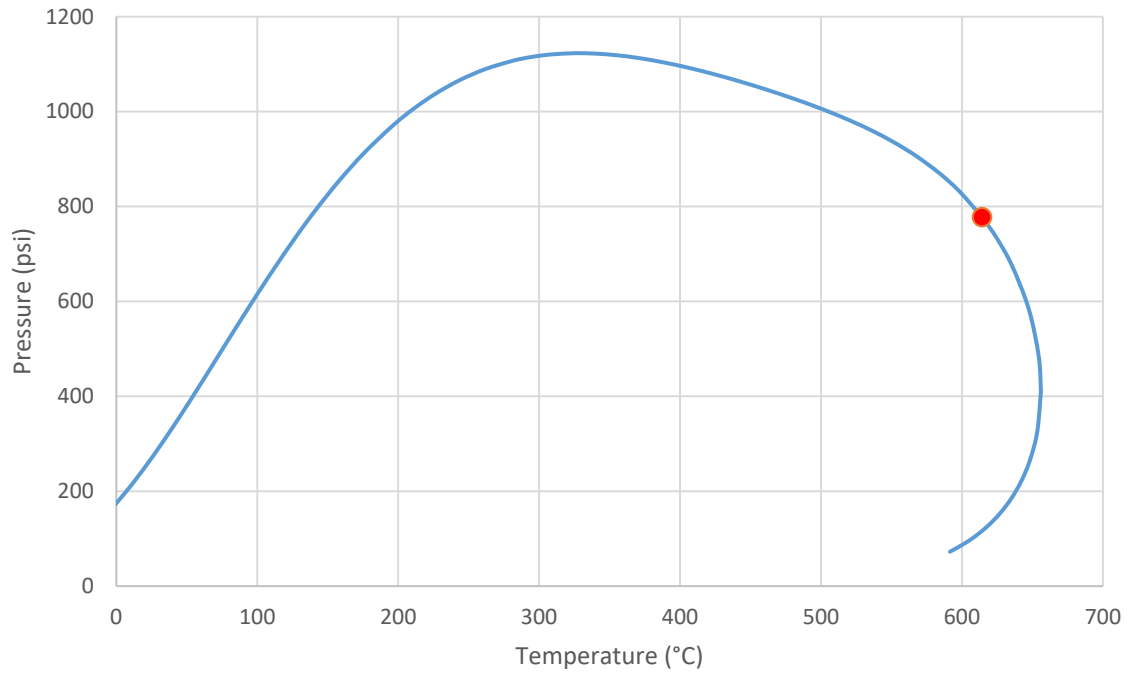


Figure B.10. Phase diagram for mixture L1.

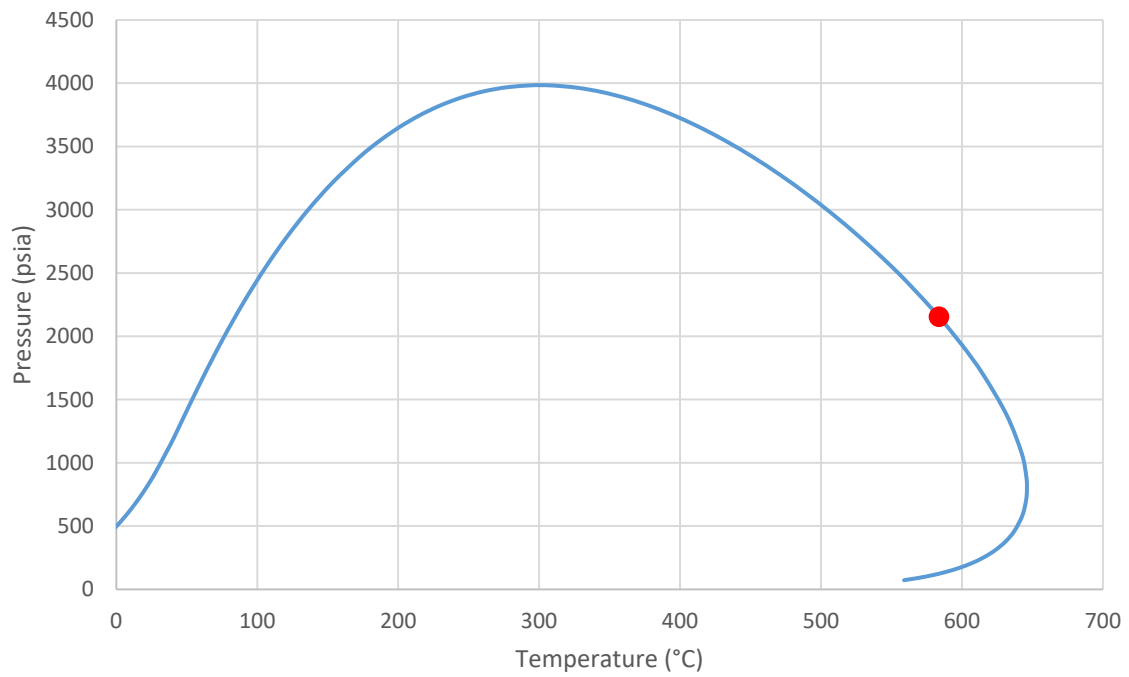


Figure B.11. Phase diagram for mixture L2.

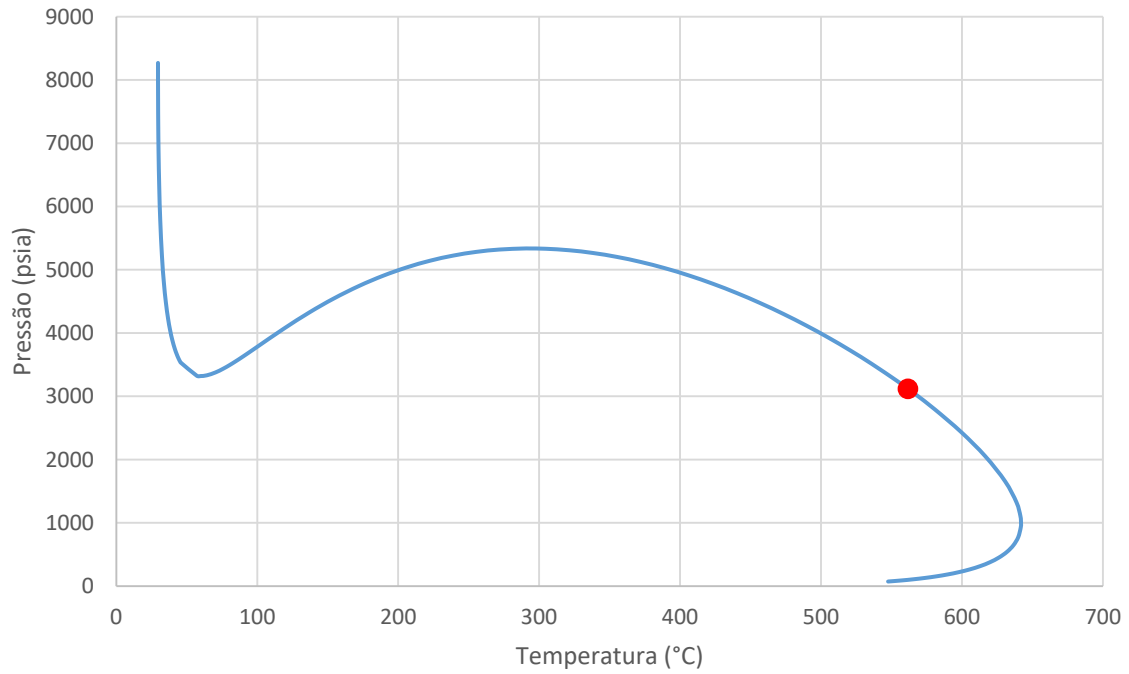


Figure B.12. Phase diagram for mixture L3.

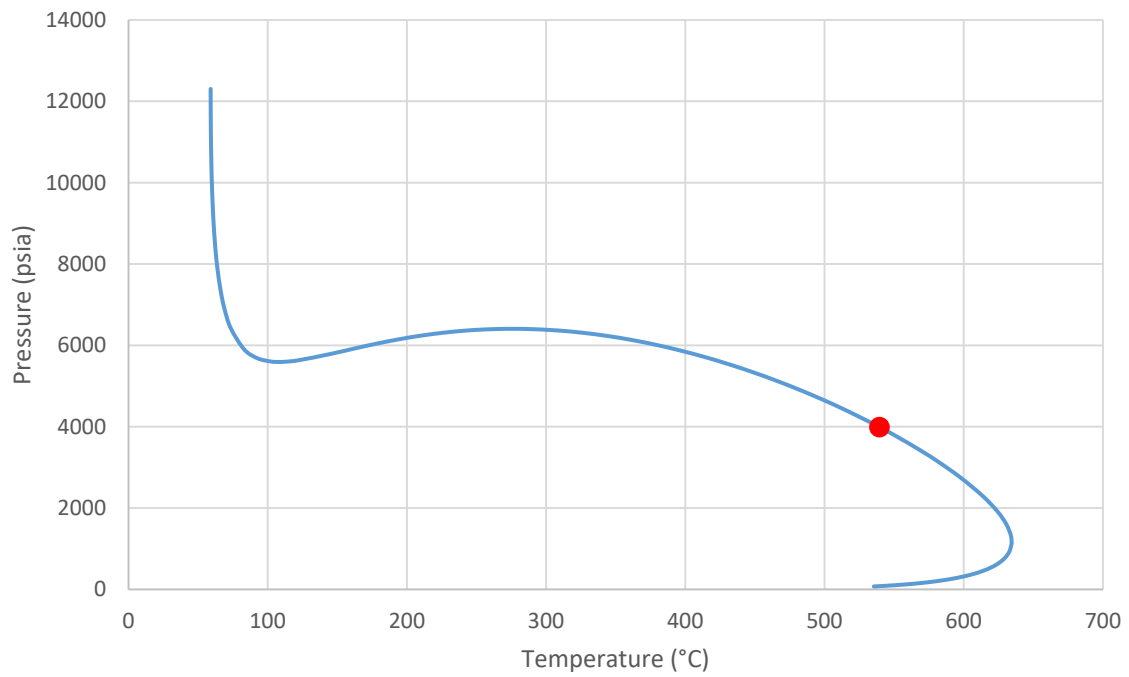


Figure B.13. Phase diagram for mixture L4.

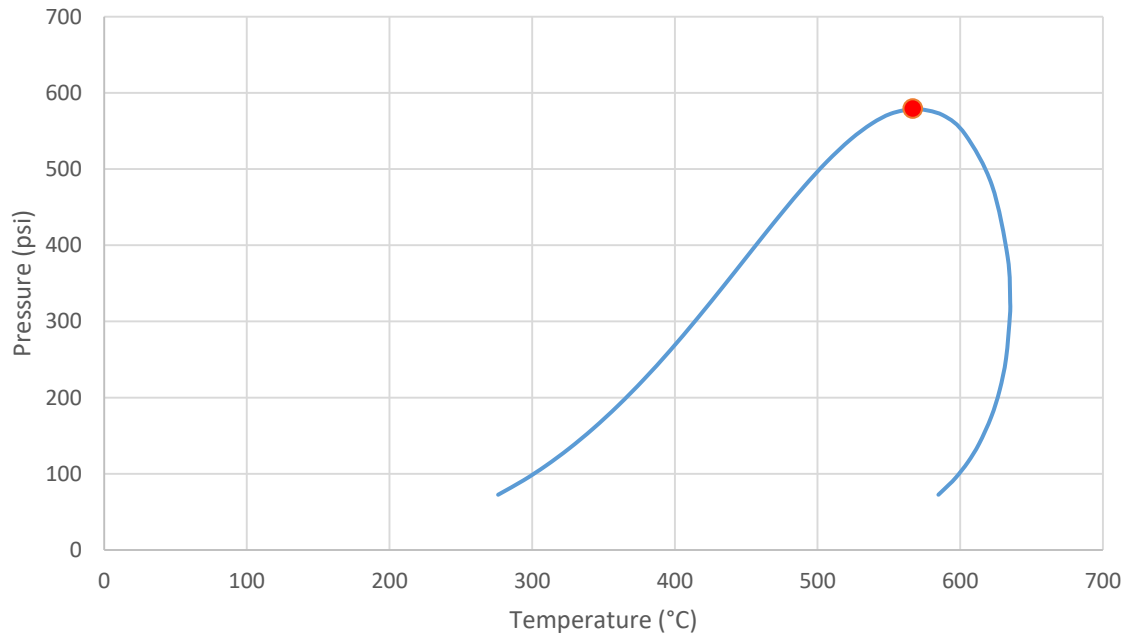


Figure B.14. Phase diagram for dead Oil D.

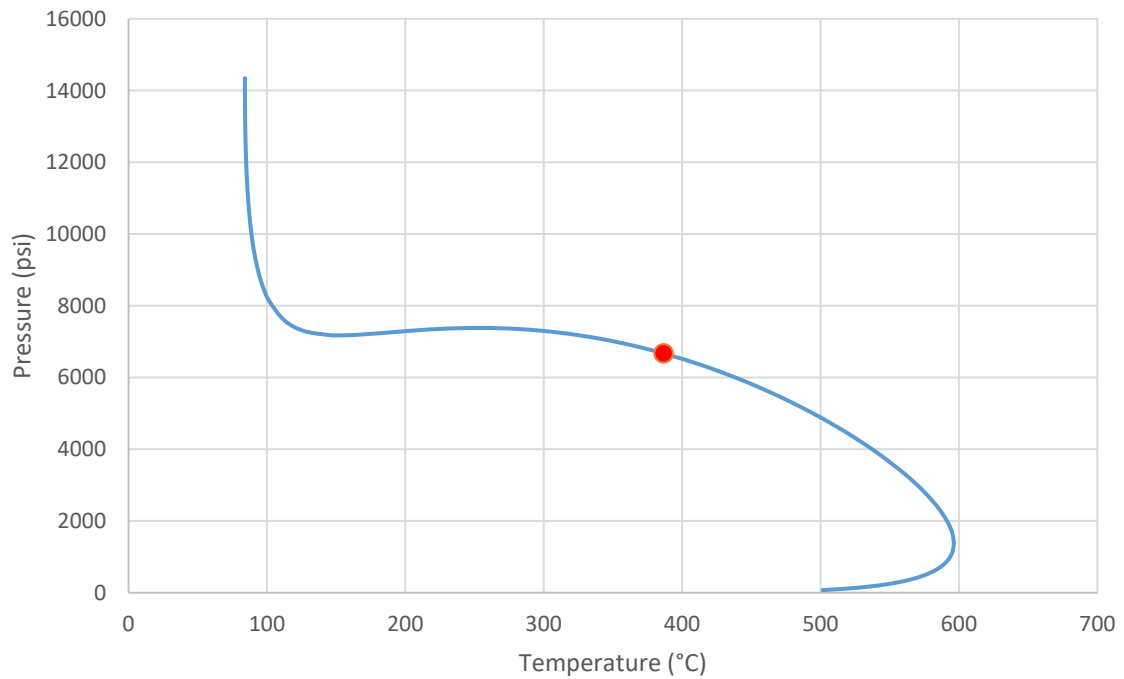


Figure B.15. Phase diagram for mixture with equivalent volumes to L4 using Oil D.

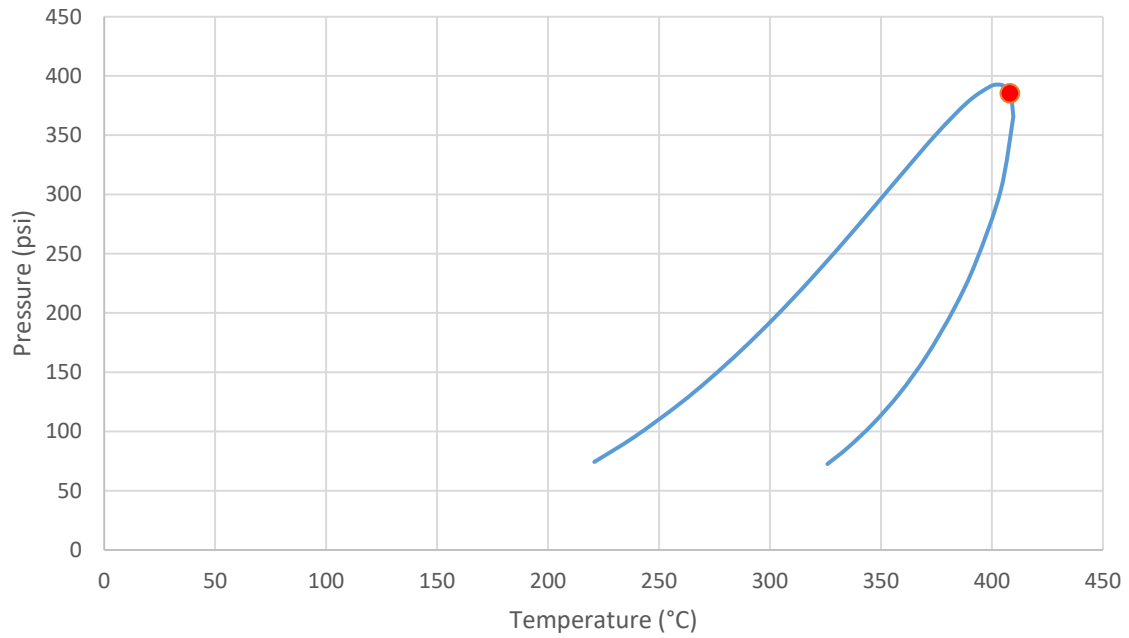


Figure B.16. Phase diagram for dead Model Oil.

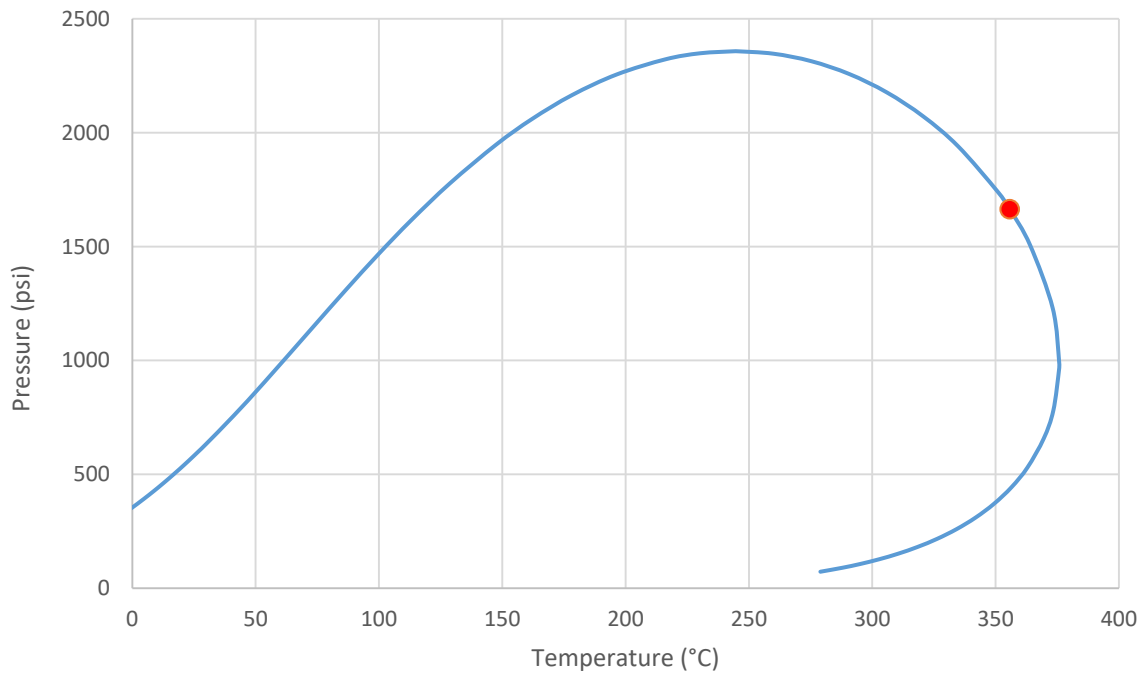


Figure B.17. Phase diagram for mixture with equivalent volumes to L4 using Model Oil.

APPENDIX C: MINERAL COMPOSITIONS AND DESCRIPTIONS

The composition and description of the minerals used throughout this text are exposed below. A complete list of minerals can be found elsewhere (TIAB; DONALDSON, 2015). H represents hardness with the following scale (1-3 can be scratched by a fingernail, 4-5 by a copper coin, 5-6 by a knife, 6-8 by a piece of quartz, 9-10 by any of the previously mentioned). Parenthesis in the formulas represent that those elements may be present in different amounts.

- Anhydrite: CaSO_4 ; white-gray; H=2.
- Barite: BaSO_4 ; white, blue, yellow or red; H=3.
- Biotite: $\text{K}(\text{Fe,Mg})_3(\text{AlSi}_3\text{O}_{10})(\text{OH})_2$; dark green to black; H=3.
- Calcite: CaCO_3 ; white to light brown; H=3.
- Dolomite: $\text{CaMg}(\text{CO}_3)_2$; pink or light brown; H=3.
- Dawsonite: $\text{NaAlCO}_3(\text{OH})_2$
- Feldspar (Orthoclase): KAlSi_3O_8 ; pink or light brown; H=6.
- Feldspar (Plagioclase): $\text{CaAl}_2\text{Si}_2\text{O}_8$ and $\text{NaAlSi}_3\text{O}_8$; white to green; H=6.
- Halite: NaCl ; colorless to white; H=2.
- Illite (Muscovite): $\text{KAl}_2(\text{AlSi}_3\text{O}_{10})(\text{OH})_2$; clear to light green; H=2.5.
- Magnetite: Fe_3O_4 ; black; H=6.
- Pyrite: FeS_2 ; pale yellow; H=6.
- Quartz: SiO_2 ; clear or with a variety of colors imparted from impurities; H=7.
- Siderite: FeCO_3 ; light colored to brown; H=3-4.

APPENDIX D: ASPHALTENE CHARACTERIZATION

Fourier-transform infrared (FTIR) spectra of the asphaltene samples from Oils B and D are shown in Figures D.1 and D.2.

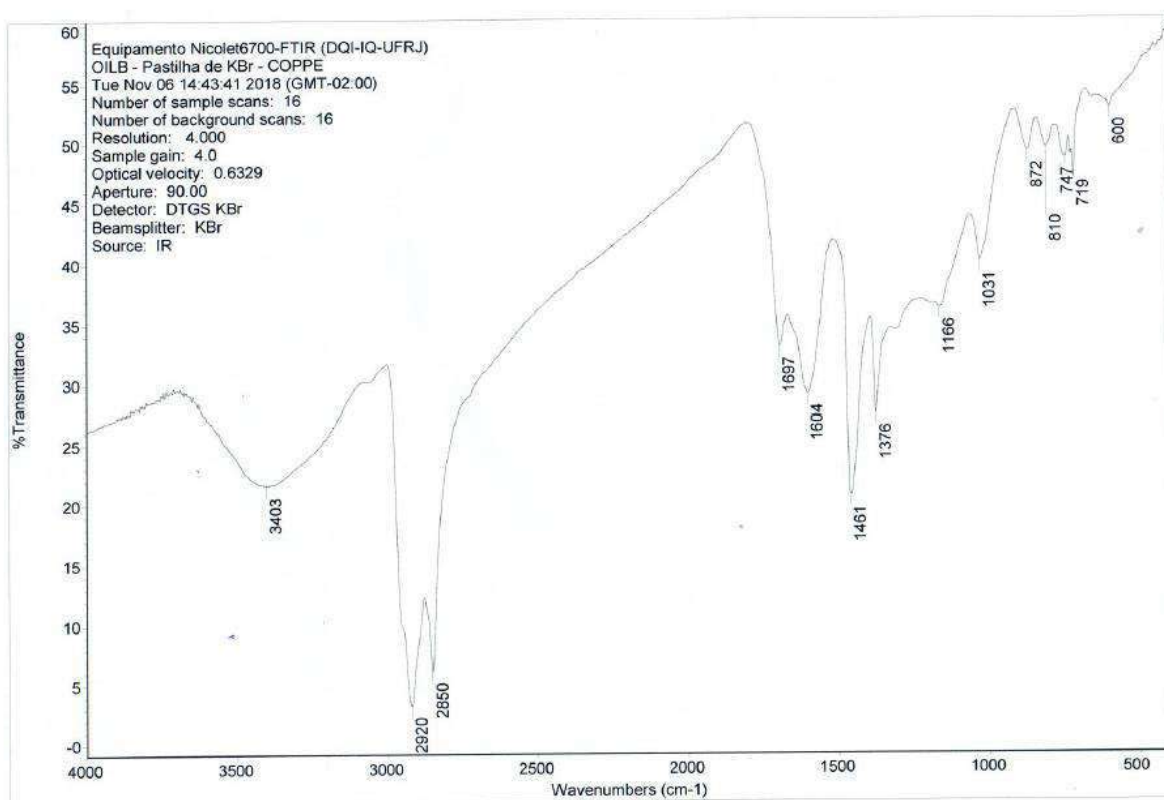


Figure D.1. FTIR spectra of asphaltene sample from Oil B.

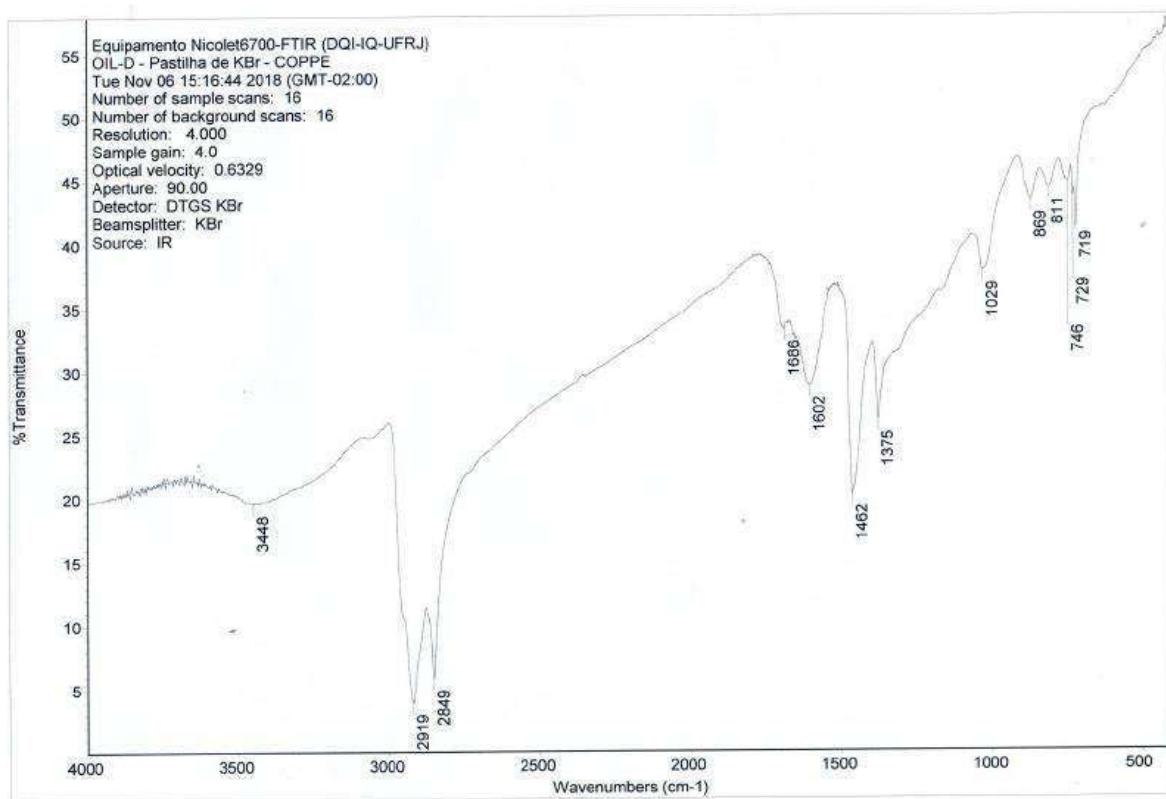


Figure D.2. FTIR spectra of asphaltene sample from Oil D.

APPENDIX E: ALKANE-WATER IFT

RESULTS

The mean of the five measurements at each conditions are included in Table E.1. The average standard error of the mean was 0.04 mN/m.

Table E.1. Interfacial tension measurements between n-alkanes and water.

| Interfacial Tension (mN.m ⁻¹) | | | | |
|---|----------------|----------------|-----------------|----------------|
| Temperature (°C) | Pressure (psi) | hexane + water | heptane + water | octane + water |
| 26.0 | 14.7 | 47.61 | 48.91 | 48.75 |
| | 400 | 47.94 | 48.71 | 48.79 |
| | 800 | 48.12 | 49.00 | 49.21 |
| | 1200 | 48.32 | 49.24 | 49.25 |
| | 2000 | 48.57 | 49.23 | 50.71 |
| | 4000 | 48.98 | 50.13 | 50.23 |
| | 6000 | 49.04 | 50.61 | 50.37 |
| 40.0 | 14.7 | 45.85 | 48.25 | 47.94 |
| | 400 | 47.37 | 48.12 | 48.14 |
| | 800 | 47.39 | 47.48 | 48.24 |
| | 1200 | 47.40 | 47.82 | 48.34 |
| | 2000 | 47.41 | 48.07 | 48.43 |
| | 4000 | 47.82 | 48.47 | 48.75 |
| | 6000 | 48.48 | 48.48 | 49.34 |

| | | | | |
|------|------|-------|-------|-------|
| | 14.7 | 45.33 | 47.89 | 46.48 |
| | 400 | 45.50 | 48.26 | 47.13 |
| | 800 | 45.27 | 47.79 | 47.15 |
| 50.0 | 1200 | 45.14 | 48.20 | 47.31 |
| | 2000 | 45.39 | 48.24 | 47.53 |
| | 4000 | 45.86 | 48.90 | 48.67 |
| | 6000 | 46.65 | 49.46 | 48.33 |
| | 14.7 | - | 47.09 | 45.84 |
| | 400 | 47.02 | 47.30 | 46.06 |
| | 800 | 46.67 | 47.24 | 46.34 |
| 60.0 | 1200 | 46.55 | 46.35 | 46.36 |
| | 2000 | 47.00 | 46.44 | 46.36 |
| | 4000 | 47.44 | 46.28 | 46.40 |
| | 6000 | 48.19 | 46.68 | 47.01 |
| | 14.7 | - | 45.38 | 44.88 |
| | 400 | 44.46 | 44.99 | 44.99 |
| | 800 | 44.15 | 45.13 | 45.31 |
| 70.0 | 1200 | 43.98 | 45.25 | 45.15 |
| | 2000 | 43.78 | 45.34 | 45.24 |
| | 4000 | 44.06 | 46.01 | 45.45 |
| | 6000 | 44.58 | 46.65 | 46.04 |
| | 14.7 | - | 44.47 | 43.52 |
| 80.0 | 400 | 43.53 | 45.30 | 43.79 |

| | | | |
|------|-------|-------|-------|
| 800 | 43.58 | 44.88 | 43.70 |
| 1200 | 43.24 | 45.39 | 43.78 |
| 2000 | 42.57 | 45.37 | 43.99 |
| 4000 | 43.02 | 45.92 | 44.43 |
| 6000 | 43.52 | 46.27 | 44.93 |
